THE PROCEEDINGS OF
THE PHYSICAL SOCIETY

Section A

Vol. 63, Part 10 1 October 1950 No. 370 A

A Magnetic Cosmic-Ray Spectrograph with Counter Recording

By B. D. HYAMS, M. G. MYLROI, B. G. OWEN and J. G. WILSON
University of Manchester

Communicated by P. M. S. Blackett; MS. received 24th March 1950

ABSTRACT. An instrument is described in which the momentum of single cosmic-ray particles is measured, the particles leaving the instrument in a sufficiently collimated beam for use in subsequent experiments. The 'maximum detectable momentum' of the apparatus is about 3×10^{10} ev/c., almost all particles are collected within 10° of the zenith and in directions individually defined to $\pm 1°$, the output is about 400 particles/day, and the proportion of spurious records is of the order of, or less than, 0·1%.

§ 1. INTRODUCTION

The instrument briefly referred to in an earlier publication (Owen and Wilson 1949), and described here in greater detail, measures the momentum of fast charged particles by recording the deflection of their trajectories passing through a magnetic field.

The scope of the apparatus is essentially determined by the requirement that the measured particle must pass unaccompanied through the measuring rows of Geiger counters. Accordingly the measurement of particles which exist closely associated with others is not possible, nor is it possible to measure in the spectrograph the momentum both of a primary particle and of the secondary particles arising from any interaction in which it takes part. If, however, it is possible to separate any experiment which it is intended to perform with a particle from the process of momentum measurement, our apparatus shows to advantage compared with the widely applied cloud chamber technique in which the particle trajectory in a uniform magnetic field is photographed and measured.

Much of the advantage of our instrument arises from a very marked improvement in the efficiency with which the available magnetic field is used, for in cloud chamber experiments the field consists only of the region of more or less uniform field, while most even of this portion is inaccessible to particles on account of the geometrical limitations of camera optics. We may consider the efficiency of use of a magnetic field in terms of the deflecting power, that is to say, of $\int H\,dl$ measured along a representative particle trajectory, and of the area perpendicular to this direction over which particles may be received. The efficiency with which the available magnetic field is used is thus of the form

$$\int_{(1)} H\,dv \Big/ \int_{(\infty)} H\,dv,$$

where the volume integration (1) is carried out over the volume usefully accessible to particles for purposes of measurement, and the volume integration (∞) is carried out over the whole space. In cloud chamber measurements this factor rarely exceeds about 5%; in our instrument it is about 50%.

Similar instruments, which however do not follow the symmetrical design which we have adopted, have been used extensively by Alikhanian and his co-workers (1947 a, b, 1948 a, b). The early form used by these workers was considerably smaller than our apparatus and of low resolution; the more recent apparatus is considerably more massive than that described here although the resolution is probably not quite so great.

The spectrograph as described here represents the first stage in the development of an instrument of very high resolution, and the probable requirements of this extension have determined certain details of design. Other features, notably the large vertical separation of the two magnets, have been adopted with a view to improving the flexibility of the equipment as a whole and with other possible applications in view.

§ 2. PRINCIPLE OF THE SPECTROGRAPH

A fast charged particle moves in a vertical plane through a horizontal magnetic field perpendicular to this plane and having significant values of field only in restricted similar regions H_1 and H_2 (Figure 1).

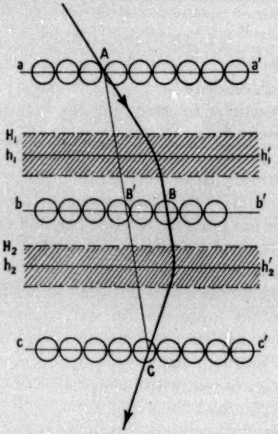

Figure 1.

The deflection of the trajectory of the particle is described by reference to the intersections A, B, C of the trajectory with horizontal lines in the plane of the trajectory, aa', bb', cc', which are symmetrically placed relative to the field regions H_1 and H_2. The angular deflection θ of the particle trajectory in each field region is given by

$$\theta = \int dl/\rho = \left(300 \int H\, dl\right) \Big/ p,$$

where ρ is the radius of curvature in centimetres from point to point of the trajectory of a (singly charged) particle of momentum p ev/c., and the integral $\int H\,dl$ is taken through the whole of the region H_1 or H_2 from which significant contributions arise. If the whole deflection in H_1 be considered as occurring at a point in h_1h_1', and the whole deflection in H_2 at a point in h_2h_2', and if the vertical separations are $ah_1 = h_2c = d_0$, $h_1b = bh_2 = d_1$, then BB′, the displacement of the intersection B of the particle trajectory with the line bb′ from the intersection B′ of the line joining A and C with bb′, is given by

$$BB' = \Delta = d_0\theta = \left(300\, d_0 \int H\,dl\right)\Big/p. \qquad \ldots\ldots(1)$$

In our instrument, operating at maximum field, $d_0 = 149$ cm., $\int H\,dl = 6{\cdot}5 \times 10^5$ gauss.cm., and thus

$$\Delta = 2{\cdot}9 \times 10^{10}/p \text{ cm.} \qquad \ldots\ldots(2)$$

The order of accuracy which is expected from the system of deflection measurement which is described below is never closer than within about 5%. It is therefore unnecessary to define the deflection arm, d_0, to better than, say, 2 cm. in 149 cm., and substantially the whole of this variation can be tolerated in the location of h_1h_1', h_2h_2'. Measurements show that the magnetic fields are symmetrical about the central horizontal plane in the pole gaps to within 2%; we therefore consider only movements of h_1h_1', h_2h_2', in so far as they arise as a function of track curvature in the pole gap and of inclination of trajectory. To a first approximation, the vertical displacement of h_1h_1' from the plane of symmetry is then

$$\frac{\int H\,dl}{2H_{\max}} \tan \tfrac{1}{2}\theta \sin \bar{\phi},$$

where $H_{\max}$ is the almost uniform deflecting field, which extends over the greater part of the geometrical pole gap, θ is the angular deflection of the particle trajectory and $\bar{\phi}$ is its mean inclination to the vertical in the region of deflection. In our apparatus, for the extreme deflection, this displacement is less than 1 cm. and is in the sense to reduce the effective value of d_0. Under these conditions it is therefore in a direction to oppose the increase of deflection arising from the extra length of trajectory which lies in the field (§4.1). We conclude that to the precision of the existing arrangement, the lines h_1h_1', h_2h_2' are adequately defined by the horizontal planes of symmetry of the magnetic fields.

The intersections A, B, C are, at the present stage of development, determined by the discharge of one Geiger counter of a closely spaced row placed parallel to the magnetic field at each of the levels aa′, bb′, cc′ (Figure 1). The measurements do not give a continuous range of momentum values, but assign particles to certain 'momentum categories' and the application of the instrument can yield information only about the average behaviour of the particles falling into a single momentum category. It is therefore necessary to know the momentum spectrum of the particles falling into a given category in any particular experiment.

It is convenient to consider, in the first place, the ideal spectrum of a single momentum category, ignoring disturbing factors such as the scattering of particles in the instrument, and lack of uniformity of the magnetic deflecting field. The modification of the spectrum in the presence of these factors will be considered later in terms of the actual performance and construction of the instrument.

2.1. *The Ideal Spectrum of a Single Momentum Category*

We identify a momentum category by Δ_n, the measured deviation, BB′, for a track passing through the axes of the three detecting counters concerned (Figure 2 (*a*)). The deflection spectrum of this category, $S_n(\Delta)$, is then given by the product

$$S_n(\Delta) = S(\Delta)P(\Delta - \Delta_n), \qquad \ldots\ldots(3)$$

where $S(\Delta)$ is the incident particle spectrum, and $P(\Delta - \Delta_n)$ is a purely geometrical expression giving the relative collecting efficiency of a set of three counters as a function of the difference of deviation from the normal deviation Δ_n of the counter geometry. While in application we will as a rule be concerned with the *momentum* spectrum of each category, it is more convenient at this stage to work in terms of the deflection spectrum. The momentum spectrum and the deflection spectrum are connected by the relation

$$S(\Delta) \sim p^2 s(p). \qquad \ldots\ldots(4)$$

In order to determine $P(\Delta - \Delta_n)$, consider deviations from the nominal trajectory (Figure 2 (*a*)) defined by the axes of the describing counters, ψ corresponding to a difference of deviation at each field region, and hence to a difference of momentum, and ϕ corresponding to a difference of direction of the trajectory in the central part of the apparatus. (Although used in practice in a particular sense the spectrograph is essentially symmetrical about the line bb′ (Figure 1) and hence the direction of any trajectory is conveniently also defined symmetrically.) Then, in Figure 2 (*b*), in which the situation shown in Figure 2 (*a*) is simplified by the omission of the nominal deflection, the probability of operation by a particle of the group defined by (ψ, ϕ) is proportional to $b_0 - a_1$ or $b_0 - a_2$, whichever is smaller, that is to say, to the aperture perpendicular to the counter axes within which particles of the group can be accepted, where b_0 is the effective diameter of each counter, and the probability of operation by a particle of the momentum defined by ψ is proportional to the integral of $(b_0 - a_{1,2})$ over the accessible values of ϕ.

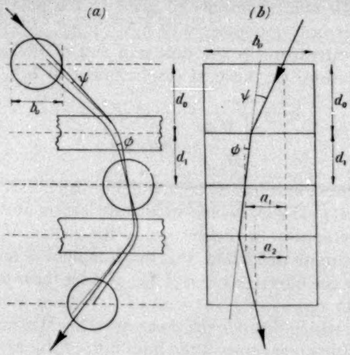

Figure 2.

The quantities a_1, a_2 given by

$$\left.\begin{aligned} a_1 &= (d_0+d_1)\phi + d_0\psi, \\ a_2 &= 2(d_0+d_1)\phi, \end{aligned}\right\}$$

are equal when

$$(d_0+d_1)\phi = d_0\psi,$$

and reach the maximum possible value, b_0, when

$$\phi = \frac{b_0 - d_0\psi}{d_0+d_1}, \quad \text{and when} \quad \phi = \frac{b_0}{2(d_0+d_1)},$$

respectively. The probability, $P(\psi)$, depends only on a_1 when

$$\begin{aligned} &d_0\psi > (d_0+d_1)\phi_{\max} = (d_0+d_1)\frac{b_0-d_0\psi}{d_0+d_1} = b_0 - d_0\psi, \\ &\psi > \tfrac{1}{2}b_0/d_0; \end{aligned}$$

thus

$$\begin{aligned} P(\psi) &= A\int_0^{\frac{b_0-d_0\psi}{d_0+d_1}} \{(b_0-d_0\psi)-(d_0+d_1)\phi\}\,d\phi \\ &= \tfrac{1}{2}A\frac{(b_0-d_0\psi)^2}{(d_0+d_1)}. \end{aligned}$$

When $\psi < \frac{1}{2}b_0/d_0$,

$$\begin{aligned} P(\psi) &= A\int_0^{\frac{d_0\psi}{d_0+d_1}} \{(b_0-d_0\psi)-(d_0+d_1)\phi\}\,d\phi + A\int_{\frac{d_0\psi}{d_0+d_1}}^{\frac{b_0}{2(d_0+d_1)}} \{b_0-2(d_0+d_1)\phi\}\,d\phi \\ &= A\{\tfrac{1}{4}b_0^2 - \tfrac{1}{2}(d_0\psi)^2\}/(d_0+d_1). \end{aligned}$$

At

$$\psi = \tfrac{1}{2}b_0/d_0, \quad P(\psi > \tfrac{1}{2}b_0/d_0) = P(\psi < \tfrac{1}{2}b_0/d_0).$$

Simplifying, if we write

$$P(0) = \tfrac{1}{2}, \quad d_0\psi/b_0 = f,$$

$$\left.\begin{aligned} P(f<\tfrac{1}{2}) &= (\tfrac{1}{2}-f^2) \\ P(f>\tfrac{1}{2}) &= (1-f)^2 \end{aligned}\right\}.$$

Here, clearly,

$$(\Delta - \Delta_n) = fb_0.$$

Thus,

$$\left.\begin{aligned} P(|(\Delta-\Delta_n)| < b_0/2) &= \left\{\tfrac{1}{2} - \left(\frac{\Delta-\Delta_n}{b_0}\right)^2\right\}, \\ P(|(\Delta-\Delta_n)| > b_0/2) &= \left\{1 - \left(\frac{|\Delta-\Delta_n|}{b_0}\right)\right\}^2. \end{aligned}\right\} \quad \ldots\ldots(5)$$

The function $P(|\Delta-\Delta_n|)$ is shown in Figure 3. The half breadth of the distribution is at $(\Delta-\Delta_n)/b_0 = 0{\cdot}26$.

2.2. *Relationships between Momentum Categories*

In the preceding section we have made use of b_0 the effective (internal) diameter of each counter in the three rows. Even in tight packing the centres of successive counters are separated by a distance greater than b_0, say b_1, on account of the finite thickness of the counter walls.

The apparatus is aligned so that the nominal deviation $\Delta_n = 0$ occurs for a particular selection of counters. Then further categories of nominal deviation

$\frac{1}{2}b_1 n$ occur, where n is integral and takes all values up to a limit set by the number of counters used in the various rows. In our apparatus $n_{\max}=22$.

Thus, when disturbing factors are ignored, the deviation interval between successive momentum categories is $\frac{1}{2}b_1$ while the extreme deviation spread of a single momentum category is $\pm b_0$ where b_0 is somewhat smaller than b_1. Particles of a particular momentum are therefore to be found in three successive momentum categories.

We have shown (equation (1)) that the deviation corresponding to momentum p is $\Delta=(300\,d_0\int H\,dl)/p$. The momentum category n therefore corresponds to the nominal momentum

$$np_n=\left(600\frac{d_0}{b_1}\int H\,dl\right)\text{ ev/c.} \qquad \ldots\ldots(6)$$

In our apparatus,

$$d_0=149\text{ cm.,}\qquad b_1=3{\cdot}9\text{ cm.,}\qquad \left(\int H\,dl\right)_{\max}=6{\cdot}5\times10^5\text{ gauss.cm.}$$

Thus $$(np_n)_{\max}=1{\cdot}5\times10^{10}\text{ ev/c.}$$

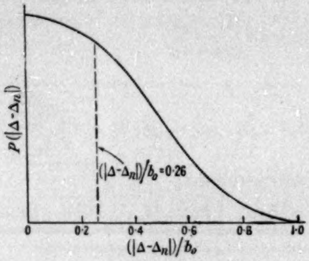

Figure 3.

2.3. *The Maximum Detectable Momentum*

The resolution of the instrument may be defined by a quantity analogous to the *maximum detectable momentum* of cloud chamber practice.

In the cloud chamber, the maximum detectable momentum, p_0, is defined as that momentum of a singly charged particle which, in the conditions of operation, yields a magnetic field curvature equal to the probable spurious curvature arising from the uncorrected sources of disturbance. In particular, the probable uncertainty of a measured momentum p, say δp, is given by $\delta p/p=p/p_0$.

In the spectrograph the probable difference between the deflection Δ of a particle and the nominal deflection Δ_n of the category to which it is assigned is $0{\cdot}26\,b_0$, and the maximum detectable momentum is defined as that momentum which leads to a true deflection (equation (6)) of this magnitude. Hence the maximum detectable momentum of our instrument is given by

$$p_0=(300\,d_0/0{\cdot}26b_0)\int H\,dl$$

or, since $d_0=149$ cm., $b_0=3{\cdot}6$ cm., $\left(\int H\,dl\right)_{\max}=6{\cdot}5\times10^5$ gauss.cm.,

$$p_0=3{\cdot}1\times10^{10}\text{ ev/c.}$$

It will be observed that the first deflected momentum category is at nominal momentum

$$p_1 = 600(d_0/b_1)\int H\,dl \text{ ev/c.} \qquad \ldots\ldots(7)$$

$$= 0{\cdot}52(b_0/b_1)p_0 = 0{\cdot}48p_0. \qquad \ldots\ldots(8)$$

Thus there is no category of nominal momentum greater than about half of the maximum detectable momentum. This, however, is in no way a serious limitation, on account of the very restricted interpretation which may properly be placed on a statement that any single particle has a measured momentum equal to the maximum detectable momentum of the apparatus with which the measurement has been made.

Following equations (7) and (8),

$$(\delta p/p)_n = p_n/p_0 = 0{\cdot}48/n; \qquad \ldots\ldots(9)$$

for example, for $n=10$, $p_n = 1{\cdot}5\times 10^9$ ev/c., $(\delta p/p)_n = 0{\cdot}05$.

§ 3. DESCRIPTION OF THE SPECTROGRAPH

An account will now be given of the design features of the spectrograph in so far as they affect the actual operation and application; the electronic and recording equipment which is involved, its performance and the problems of its testing and maintenance are discussed in a separate paper by one of us (Owen 1950).

3.1. *Magnets*

The general construction of the apparatus is shown in Figure 4*. Two large electromagnets are supported on a girder structure with pole faces of like polarity coplanar. The pole faces are of area 30 cm. × 40 cm., with the smaller dimension vertical, and are separated by a distance 9·5 cm. The magnets follow closely in design and performance that described by Blackett (1936) except in so far as the method of support requires modification. The pole pieces are conical, tapering near the field gap to 40 cm. diameter, then passing in a further 5 cm. to the rectangular form of the pole faces. The rectangular pieces together with the transition sections are separate, and are mounted by means of bolts passing axially down the respective pole pieces. The orientation of the pole pieces is thus adjustable. The performance of the magnets is summarized below (§ 4.1).

3.2. *Counter Arrays*

The three systems of counters which determine the points of intersection of a particle trajectory with the three planes aa′, bb′, cc′ (Figure 1) consist respectively of 16 (upper), 8 (middle) and 16 (bottom) counters of conventional pattern, with cathodes of length 15 cm., internal diameter 3·6 cm., and wall thickness 0·1 cm. Each group forms an almost tightly packed row. Slight variations of counter-tube diameter make necessary a small amount of spacing in order to maintain the required geometrical relation between counter centres.

---

* This diagram may be compared with the photograph of the spectrograph already published (Owen and Wilson 1949).

3.3. *Defining Counters*

The measuring counters are made longer than the breadth of the pole gap in order to collect particles traversing the field regions but diverging above and below the magnet poles. It therefore becomes necessary to exclude particles which in any part of their trajectory pass through the iron of the pole faces. This is done by placing 'defining counters' in each pole gap and accepting, for measurement, only particles which traverse a defining counter in each pole gap. The *accepted event* of the spectrograph is thus a five-fold counter coincidence, comprising discharges from one counter from each of the three measuring rows and from the two defining counters, one in the pole gap of each deflecting magnet.

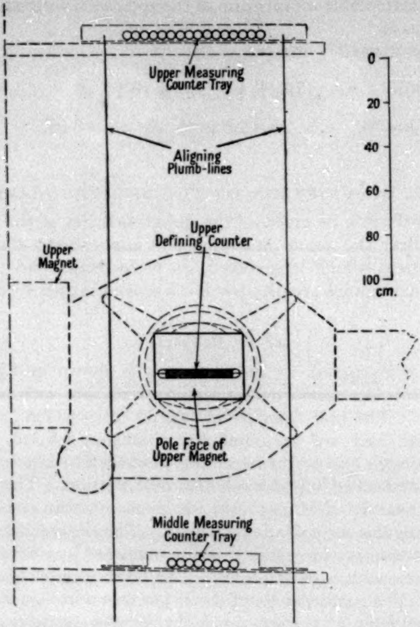
Upper Measuring Counter Tray
Aligning Plumb-lines
Upper Defining Counter
Upper Magnet
Pole Face of Upper Magnet
Middle Measuring Counter Tray
0
20
40
60
80
100
cm.

Figure 4. Geometry of spectrograph. (The upper half of the instrument, which is symmetrical about the middle counter tray, only is shown.)

For the highest efficiency in collecting particles it is desirable that the defining counters shall fill as large a fraction as possible of the magnet air gap subject to the following restrictions: (i) no straight trajectory shall exist that passes through five counters and the iron of the pole faces, (ii) no particle shall be scattered from the defining counters into the iron, and then be scattered back into the beam.

These counters have been placed between the pole faces about 12 cm. from the pole edge nearest the centre of the system, and filling 80% of the gap width. With this arrangement the probability of scattering in the iron is less than 1 in

1,000 for particles of momentum 5×10^8 ev/c., and correspondingly less for higher momenta.

In requiring accepted particle trajectories to pass through defining counters in the pole gaps, we have adopted an exactly opposite policy to that described by Alikhanian and his co-workers (1948 a), who place a row of narrow counters close to the pole faces of their magnet and reject particles which, by traversing these counters, are shown to pass near enough to the pole faces to have the possibility of entering the pole face and subsequently re-emerging as a result of scattering. The advantage of the Alikhanian arrangement lies in the fact that the additional scattering which takes place in the walls of our defining counters is avoided, although some particles, which may be appreciable in number, suffer the more severe scattering arising from tangential traversal of the counter wall without entering the sensitive volume within (the wall thickness for these particular counters in the Alikhanian experiment is not quoted).

We consider scattering in detail later (§ 4.8) and it will appear that the position of the defining counters in our arrangement reduces the importance of scattering in them compared with that of the central array (bb′, Figure 1). The number of particles excluded by Alikhanian's protective counters on each pole face ($\sim 45\%$) appears excessive. The use of a five-fold counter coincidence, however, exhibits a most valuable property which is to be found in the increased discrimination against spurious operation by showers of particles. The markedly lower rate of spurious operation which is obtained in our instrument as compared with that of Alikhanian probably depends mainly upon this feature (§ 4.6), which we regard as the significant difference between the two systems.

3.4. *Alignment of the Measuring Counter Arrays*

The counters in each of the three rows are mounted on a carriage allowing horizontal motion in two directions and are located on each carriage with reference to two aligning holes 4 mm. in diameter. Through these holes plumb lines are hung from pegs which fit closely in the aligning hole of the top tray; the carriages are adjusted until the lines hang centrally in the holes of the two remaining carriages.

The accuracy of alignment is open to a fairly precise internal check. Consider, when the apparatus is operated without magnetic field, particle trajectories of momentum categories ± 1. (We ignore, in this statement, the scattering of these particles, for since it leads to a small and essentially symmetrical set of deviations it is of no importance to the present argument.) Typical channels of categories ± 1 are defined by upper and middle counters, n, and lower counters $n-1$, $n+1$.

In correct alignment the number of counts in categories $+1$ and -1 will be equal, apart from statistical variations, but if the apparatus is misaligned by a distance δb at the middle tray it may be shown that the counts will differ in the ratio $(1+8\,\delta b/b_0)$, where $b_0 = 3{\cdot}6$ cm. is the effective internal diameter of the counters. A misalignment, δb, of 1 mm. thus leads to a $(+1/-1)$ ratio $1{\cdot}22$, and a statistically significant departure from the ratio unity is to be expected for about 250 counts in each category. Even if account is taken of scattering, the great majority of counts in zero magnetic field fall into categories -1, 0, $+1$ in the approximate ratios $1:2:1$; thus a 1-mm. misalignment gives rise to a significant difference between the counts in categories $+1$, -1 in a total of about 1,000 counts.

§4. PERFORMANCE OF THE SPECTROGRAPH

Factors determining the practical performance and application of the spectrograph will now be discussed under the heads: (1) the magnetic fields, (2) the rate of operation, the relative efficiency of different momentum categories and the angular distribution of collected particles, (3) the occurrence of spurious records simulating normal operation, and (4) the modification of precision of measurement by scattering of recorded particles in counters and in the air column of the instrument.

4.1. *Magnetic Fields*

The magnets are operated at a pole separation of 9·5 cm. A three-dimensional plot was made of the variations of the component of magnetic field parallel to the axes of the magnets over the pole gap and over the adjacent regions accessible to particles traversing the spectrograph. A typical field distribution, which was measured in the central plane of the pole gap, is given in Figure 5.

The integrated deflecting field, $\int H\,dl$, was also measured for vertical trajectories covering the whole gap in a series of direct vertical traverses of the search coil.

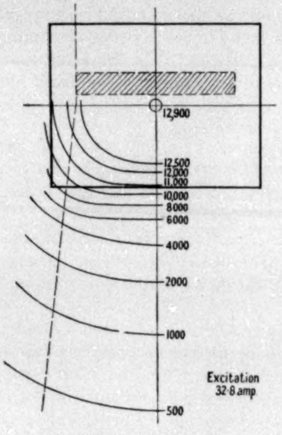

Figure 5. Field plot (gauss) in the central plane of the pole gap of the lower magnet. Shaded area, defining counter; broken line, limit of accessible area.

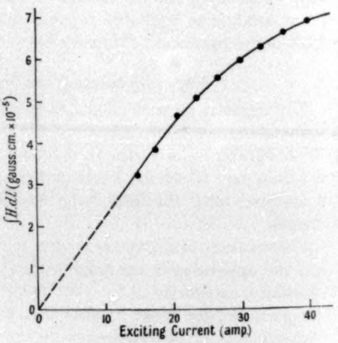

Figure 6. $\int H\,dl$ as a function of excitation for vertical trajectory through centre of pole gap.

Vertical traverses through the central point of the pole gap were carried out at a range of magnet excitations to calibrate the integrated deflecting field in terms of the exciting current in the magnets: the results of this calibration are given in Figure 6. In Figure 7 the variations of $\int H\,dl$ measured along vertical trajectories at various parts of the pole gap are shown for the excitation corresponding approximately to the maximum deflecting field and to half maximum deflecting field. In this diagram the area covered by the defining counters, through which accepted particles must pass, is indicated by a broken line.

It is necessary to consider the effect on the integrated field of the inclination of particle trajectories to the vertical and of the curvature of trajectories in the region of intense field. The extreme mean inclination possible in the pole gap is about $\tan^{-1}0{\cdot}15$, corresponding to an increase of integrated field of the order 1%; moreover this inclination is only possible towards the edge of the pole gap, where there is a much larger field deficiency for vertical trajectories. The maximum curvature in the pole gap is set, by the geometry of the instrument, to be approximately 0·5 m^{-1}. Over a trajectory length in the region of intense field of about 40 cm. this curvature would lead to an increase of deflecting integrated field of 0·5%. This maximum curvature also is only possible in the extreme edges of the accessible region of the pole gap.

The purely geometrical limitation of precision of measurement has been treated in an earlier section and the modification to this result which arises when account is taken of Coulomb scattering of the measured particles in the material of the apparatus is examined below. The effect of variations of magnetic field on the precision of measurement can be introduced in two ways. Ultimately, the section of pole gap traversed by particles in a single counter channel is defined in a direction perpendicular to the field axis, within an extreme variation of $+\frac{1}{2}b_0 = \pm 1{\cdot}8$ cm. It is immediately clear (Figure 7) that the uncertainty of deflecting field for a single channel in isolation is almost always very small compared with the effects of geometry and scattering. If the magnet excitation at the instant of passage is then sufficiently known, variation of magnetic field will make no significant contribution to the uncertainty of momentum which attaches to each individual particle assigned in the spectrograph to a particular momentum category. On the other hand, for many applications the limit of accuracy reached in this procedure is unnecessary, and it is convenient to treat together the large number of channels which contribute to a single momentum

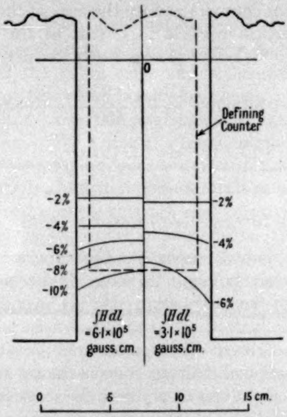

Figure 7. Plan of pole gap, showing variations of deflecting field for vertical trajectories.

category. The practical aperture of the apparatus, set by the dimensions of the defining counters, is a compromise to this purpose, allowing all accepted channels to be treated as of the same deflecting field to an accuracy where the effect of field variations is not large compared with the effect of scattering (which varies with momentum in the same way). The rapid variation of the integrated field shown in Figure 7 near the ends of the defining counters indicates that little choice of aperture is in fact at our disposal.

4.2. *Rate of Operation: Efficiency as Function of Momentum: Distribution*

The counting rate of the spectrograph in the absence of deflecting magnetic fields is a purely geometrical problem, since the vertical cosmic-ray flux at sea level in high geomagnetic latitudes is well known. To a first approximation there are 80 accessible channels for undeflected particles, the counting rate of each being determined by the mean solid angle subtended by a counter of the upper tray at one of the bottom counters and by the area of the receiving counter.

Writing for the vertical particle flux, that of the hard component only, $J_v = 0{\cdot}82 \times 10^{-2}\,\mathrm{cm}^{-2}\,\mathrm{sec}^{-1}\,\mathrm{sterad}^{-1}$ (Rossi 1948), we derive a counting rate

$$r_0 = 0{\cdot}82 \times 10^{-2}\frac{(3{\cdot}6 \times 15)(3{\cdot}6 \times 10)}{500^2}\,80\,\mathrm{sec}^{-1}$$

$$= 5{\cdot}12 \times 10^{-3}\,\mathrm{sec}^{-1} = 19\,\mathrm{hr}^{-1}.$$

If the total vertical flux, on the other hand, is used,

$$J_v' = 1{\cdot}23 \times 10^{-2}\,\mathrm{cm}^{-2}\,\mathrm{sec}^{-1}\,\mathrm{sterad}^{-1}, \quad \text{and} \quad r_0 = 29\,\mathrm{hr}^{-1}.$$

The measured rate is about 24 hour^{-1}. The rate is reduced with increasing magnetic field as successively larger fractions of the incident beam are cut off by the characteristics of the instrument. At the maximum field the measured counting rate is about 16 hour^{-1}.

The exclusion of particles in the magnetic field takes the form of a low energy cut-off. The determination of the exact form of the cut-off is the crucial measurement in the application of the spectrograph to the sea-level momentum spectrum, and will be considered in detail, in this context, elsewhere. It may be noted here, however, that the total counting rate in a particular momentum category (i.e. for a known momentum range) is the sum of the counting rates of possible counter channels which fall into this category. The separate channels suffer no cut-off (except for the zenith angle variation of particle intensity), and the efficiency of a given momentum category depends essentially on the effective number of counter channels which comprise it.

The angle of entry into the spectrograph of a particle is closely defined by the identification of the counter channel traversed.

In the plane containing the axis of the deflecting field the maximum possible angle between the particle trajectory and the vertical is clearly about 15/500 radian (length of measuring counters 15 cm., full length of spectrograph 500 cm.) or less than 2°. In the plane of deflection the maximum angular departure from the angle defined by the counter axes is $b_0/d_0 = 3{\cdot}6/149$ radian, less than $1\frac{1}{2}°$. These figures are extreme values and, except in so far as the direction of approach of a particle is masked by scattering in the first counter of the instrument, the mean departure from the nominal angle of approach is less than 1° in both planes.

The uncertainty of direction due to scattering becomes of comparable magnitude (see equation (15)) for momenta of the order 2×10^8 ev/c., and thus does not become important even at the lowest momenta of the useful range of the instrument.

While the angle of approach corresponding to a single counter channel is closely defined, the total collection into a complete momentum category is spread over a considerable angular range. Typical examples of the collecting range as a function of momentum have been given in an earlier publication (Owen and Wilson 1949). It will be seen that very few particles of any momentum are accepted at angles greater than 10° from the vertical, and it follows that the zenith angle variation of the particle flux is without effect on the collecting rates in different momentum categories until the accuracy of measurement is of the order 3%, a performance which, for the categories of low momentum and correspondingly low intensity which do reach inclinations of this order is, as, a matter of track statistics, unlikely often to be of importance.

4.3. *Spurious Records*

Close attention has been given to various methods by which the frequency of spurious operation of the instrument may be estimated, since this forms a limiting background against which real phenomena must be studied. The suitability of the apparatus for certain applications is entirely determined by the level of spurious operation. We define as a spurious record any record in which one counter only in each measuring layer is shown to have discharged, when the five-fold coincidence forming the master selection has not arisen for the direct passage of a single charged particle through each of the five counter layers.

The sources of spurious counts are of two kinds: (i) where the operation of the five counters involves the casual coincidence in time of two or more particles which individually traverse only some of the five counter layers, the simplest example being the passage of a single particle through four counter layers (but not the fifth), within the resolving time of the system, with the discharge from whatever cause of the fifth counter layer, (ii) where the record arises from the discharge of the various counter layers by different particles of a true particle association (for example, an extensive air shower).

These alternatives will first be discussed.

4.4. *Casual Coincidences*

The rate r_c of casual n-fold operations between n independent counters or counter groups with individual rates $r_1 \dots r_n$ in a recording system of resolving time τ is given by an expression (Jánossy 1948, p. 48) of which the leading term is

$$r_c = n(r_1 r_2 \dots r_n)\tau^{n-1}. \qquad \dots\dots(10)$$

In our apparatus the rates of possible counter groups vary from about 100 sec^{-1} for a single large tray to approximately 0·2, 0·04, and 0·01 sec^{-1} respectively for the various two-, three- and four-fold groups, while the resolving time is 3×10^{-6} second. It follows immediately that two-fold casual operation between the discharge of four counter groups by a single particle and the independent discharge of the fifth group alone need be considered, and that the rates involved will be of the order

$$r_c = 2\tau r_1 r_4 = 2(3 \times 10^{-6})(100)(0{\cdot}01)\,\text{sec}^{-1}$$
$$= 6 \times 10^{-6}\,\text{sec}^{-1} \qquad \text{or} \qquad 1 \text{ in } 50 \text{ hours.}$$

More exactly, the total casual rate arising from the five possible ways in which one particle traversing four counter layers can be in casual coincidence with the discharge of the remaining layer can be written

$$(r_c)_{\text{total}} = \Sigma_m 2\tau r_{1m}(r_4 - r_5)_m \qquad \ldots\ldots(11)$$

to take account of the high probability that a particle traversing four counter layers must of necessity traverse also the fifth layer, and of the different counting rates of the single trays. This rate is approximately evaluated in Table 1.

Table 1. Casual Occurrences of Spurious Records in the Spectrograph ($r_5 = 0{\cdot}005\ \text{sec}^{-1}$)

Counter layer operated independently	r_1 (sec^{-1})	$r_4 - r_5$ (sec^{-1})	Weight	Contribution to r_c (sec^{-1})
Outer	100	0·002	2	$2{\cdot}4 \times 10^{-6}$
Centre	50	0·001	1	$0{\cdot}3 \times 10^{-6}$
Defining	30	0·005	2	$2{\cdot}0 \times 10^{-6}$
			$(r_c)_{\text{total}}$	$4{\cdot}7 \times 10^{-6}$
				=about 1 in 60 hours or 0·08% r_5

4.5. *Operation by Associated Particles*

The main source of associated particles to which the apparatus is subject is constituted by extensive cascade showers in the atmosphere, and the density variation of these showers at sea level is sufficiently established to allow an immediate estimate of their effect to be made.

We require to know the frequency with which one shower particle (and one only) falls upon each of the three measuring counter trays while at least one particle falls upon each pair of defining counters. The treatment of problems of this type is well known (see, for example, Jánossy 1948, p. 257), and we may write down the probability $P(\rho)$ that an extensive shower of density ρ particles/m^2 will give rise to a spurious event in the form

$$P(\rho) = 8 \times 16^2\{1 - \exp(-S\rho)\}^3 \exp\{-(40-3)S\rho\}\{1 - \exp(-S'\rho)\}^2, \qquad \ldots\ldots(12)$$

where S m^2 is the area of each individual counter in the measuring trays, and S' m^2 is the total area of each pair of defining counters. Then, if the rate of occurrence of showers of density between ρ m^{-2} and $(\rho + d\rho)$ m^{-2} is given by

$$r(\rho) = \kappa\rho^{-\gamma} d\rho\ \text{sec}^{-1}, \qquad \ldots\ldots(13)$$

where $\gamma = 2{\cdot}43$ and $\kappa = 880$ (Broadbent, private communication), the rate of spurious records arising from extensive showers will be

$$r_s' = \int_0^\infty P(\rho)\kappa\rho^{-\gamma}\, d\rho\ \text{sec}^{-1}. \qquad \ldots\ldots(14)$$

Now $S = 0{\cdot}0055$ m^2, $S' = 0{\cdot}022$ m^2; then $r_s' \simeq 1{\cdot}6 \times 10^{-5}$ sec^{-1} (1 in 22 hours).

This result may be expected to be considerably too high, for the lower counter trays of the spectrograph receive heavy shielding from the bulk of the deflecting magnets. The magnets cover a large fraction of the solid angle into which the majority of extensive showers fall (up to 30° zenith angle) with about 50 cm. iron, which is a complete absorber for electrons of energy about 10^8 ev. (the critical cascade energy in air). No serious modification of the analysis is to be expected on account of the vertical stacking of the counter trays, since the solid angles subtended by the upper trays at those below is small. The largest angle is subtended by the top tray at the upper defining counter, but this is only 0·04 steradian compared with which extensive showers occur with comparable order of intensity throughout an angle of the order one steradian.

4.6. *Function of the Defining Counters in controlling the Incidence of Spurious Operation*

It is valuable to examine more closely the shower operation of the counter array, whether it leads to a spurious count or whether the operation of several counters in a single tray makes the record recognizably that of a particle association. In particular, the way in which the defining counters modify shower operation is of fundamental importance to the achievement of a low rate of spurious counts.

Each shower counting rate can be written in the form

$$r' = \int_0^\infty P(\rho)\kappa\rho^{-\gamma}\,d\rho \ \mathrm{sec}^{-1},$$

where $P(\rho)$ takes the appropriate value of the particular counter configuration concerned:
for all showers without defining counters,

$$P(\rho, -D) = [1 - \exp(-16S\rho)]^2[1 - \exp(-8S\rho)],$$

for all showers with defining counters,

$$P(\rho, D) = [1 - \exp(-16S\rho)]^2[1 - \exp(-8S\rho)][1 - \exp(-S'\rho)]^2,$$

for '1, 1, 1' showers without defining counters,

$$P(\rho, 1.1.1, -D) = 8 \times 16^2[1 - \exp(-S\rho)]^3 \exp[-(40-3)S\rho],$$

for '1, 1, 1' showers (spurious records) with defining counters,

$$P(\rho, 1.1.1, D) = 8 \times 16^2[1 - \exp(-S\rho)]^3 \exp[-(40-3)S\rho][1 - \exp(-S'\rho)]^2.$$

The corresponding quantities $P(\rho)\kappa\rho^{-\gamma}$ are shown in Figure 8, and the *relative* values of r' are given in column (3) of Table 2. The striking feature of this result is the extent to which the occurrence of spurious counts is controlled by the inclusion of defining counters, which reduces the rate by a factor of nearly 30.

As has already been pointed out, the primary purpose of the defining counters, which is to ensure that the particles recorded travel through the air gap of the magnets only, can be achieved in other ways: for example in the arrangement of Alikhanian, counters close to the pole faces are used in anti-coincidence, particles traversing them being rejected. We consider that the large reduction of spurious counts which arises from the use of defining counters in our instrument greatly outweighs the rather small increase of scattering of particles traversing the counter system.

4.7. *Experimental Tests of Spurious Operation*

(*a*) *Shower recording.*

For the purpose of shower recording the central measuring counter array was displaced in the horizontal plane until it was no longer possible for a single particle traversing the remaining counter system to pass through it.

Records were taken first of normal five-fold coincidences and secondly of three-fold coincidences excluding the defining counters. Each operation then recorded the passage of an extensive shower, while showers in which one counter only of each measuring tray was discharged (' 1, 1, 1 ' showers), and which in normal operation would be incorrectly assigned to single particles, could be recognized. Thus measured ratios were determined for the four shower types for which theoretical expressions are given in the previous section. The measured rates are compared with the *relative* theoretical rates in Table 2.

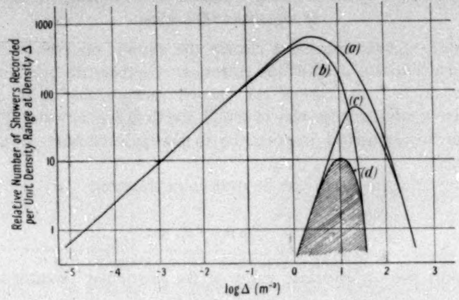

Figure 8. Sensitivity of the counter system of the spectrograph to extensive atmospheric showers.

(*a*) All showers without defining counters.
(*b*) 1,1,1 showers without defining counters.
(*c*) All showers with defining counters.
(*d*) 1,1,1 showers with defining counters (spurious records).

Table 2. Operation of Spectrograph Counter System (with central tray displaced) by Extensive Cascade Showers

	(1)	(2)	(3)	(4)
Defining counters excluded	All showers	4·2±0·4	1	4·2±0·4
	1,1,1, showers	0·63±0·16	0·31	2·0±0·5
Defining counters included	All showers	1·1±0·05	0·24	4·6±0·2
	1,1,1, showers	0·025±0·008	0·012	1·9±0·7

(1) type of shower; (2) experimental rate (hr^{-1}); (3) relative theoretical rate; (4) ratio experimental/theoretical (not normalized).

The constancy of the ratio in the last column of Table 2 is satisfactory since these values refer to shower events which differ in absolute frequency over a range of nearly 200 to 1. Moreover, the variation in this ratio, making ' 1, 1, 1 ' showers relatively less frequent experimentally than would be expected from the theoretical treatment, is exactly the effect to be anticipated from the shielding of the lowest counter tray by the magnet structure. Showers which but for this shielding would be in the category '1, 1, 1' now fail to operate this layer and do not occur; on the other hand, showers reduced at this layer to one particle over the whole tray are likely to be more dense at the upper trays and so do not, as a result of shielding, enter the category '1, 1, 1'. It follows that if we were able to recognize spurious '1, 1, 1', records with the central counter tray in its normal position, where it also is shielded instead of being displaced clear of the magnets as was the case in the test under discussion, the rate of occurrence would be still lower.

If we estimate the random coincidence rate of the displaced central tray with the five-fold operation of the remaining counter system in this test as

$$\begin{aligned} r'' &= 2(3\times10^{-6})\,50\times0{\cdot}005\ \mathrm{sec}^{-1} \\ &= 1{\cdot}5\times10^{-6}\ \mathrm{sec}^{-1} = 0{\cdot}005\ \mathrm{hr}^{-1} \end{aligned}$$

the shower rate with displaced tray is about 0·018 hr^{-1}, and with the actual tray in its normal position and shielded cannot well be more than about 0·01 hr^{-1} leading to about 0·05% of spurious counts.

Comparing this figure with the estimated total spurious counting rate for random coincidences we conclude that the two sources of spurious counts are of comparable importance and together give rise to a background count of the order 0·1% of all counts.

(*b*) *Operation with opposed magnetic fields.*

A direct measurement of the spurious operating rate has been attempted using the normal geometry of the spectrograph but with the two magnetic deflecting fields opposed. With this arrangement all genuine records will show only small deflection arising from any out of balance of the two deflecting fields and from the scattering in the instrument of those particles of momentum sufficiently high to be transmitted.

This test differs from comparable measurements without magnetic field since it reproduces more closely the condition of actual operation, in so far as a lower limit of momentum is imposed excluding particles which in the absence of field would be capable of considerable scattering. A rather low deflecting field was used ($\int H dl \sim 3\times10^5$ gauss.cm.) and the geometry of the apparatus leads immediately to the minimum momentum of transmission, $p_{\min} \sim 2\times10^8$ ev/c. The probable deflection due to scattering at this momentum is (§ 4.8) 2 cm. and hence a scattering deflection greater than about 6 cm. is unlikely. The lack of balance between the deflecting fields might be as large as 5% which would lead to a further deflection of 2 cm. Thus deflections greater than about 8 cm. are expected to be rare, and particles should not occur appreciably beyond momentum category 6 (deflection range 8·1–15·3 cm.).

Spurious operation, whether due to different particles in extensive air showers or to a random association of particles in which the independent counter group is one of the measuring trays, are expected to give combinations of measuring counters in which all possible counter combinations are equally probable.

In Table 3 we give the result of about 5,100 traversals with opposed fields and, in comparable form, the distribution of false counts to be expected for the occurrence of 0·2% of spurious operation.

The results are not easily reconciled with a fraction of spurious counts as large as 0·2%. For 0·2% of spurious counts the statistical probability of recording no counts out of 5,000 in category 8 or greater is 0·025; for 0·1% of spurious counts the corresponding probability is 0·16.

Table 3. Deflection spectrum in opposed fields ($\int H dl = 3\cdot3 \times 10^5$ gauss.cm.) of sea-level meson beam filtered in 1·3 cm. lead, and expected contribution due to 0·2% of spurious records

Momentum category, *n*	0	2	3	4	5	6	7	8	10	12	14
Observed no. of particles category *n* or greater	5123	151	31	11	5	2	1	0			
Expected no. of particles category *n* or greater for 0·2% spurious records	10·2	8·8	7·9	6·9	6·1	5·2	4·4	3·7	2·5	1·6	1·0

Thus this direct estimate of the spurious background agrees completely with that deduced from the measurement of shower rates, and sets the background rate at the order 0·1% or less.

(*c*) *Occurrence of 'forbidden counts' in normal operation.*

Alikhanian and his co-workers (1948 a) make an estimate of the spurious counting rate for their instrument by noting the occurrence of counter combinations which are inconsistent with the field distribution available for particle deflection. This method does not seem to be suitable for our instrument partly because of the extremely low background rate which is to be detected and partly because the distinction between allowed and forbidden counter combinations is extremely vague, depending on the uncertain axial extent of the sensitive regions of the defining counters, thus allowing only a very few counter combinations to be classified as completely forbidden. Even the few combinations which are geometrically completely forbidden in fact refer to particles traversing the insensitive end sections of the defining counters, and the probability that a secondary electron released in the counter wall can pass into the sensitive region and discharge the counters is likely to be greater than the background effect under investigation. The use of these 'forbidden combinations' as a method of measuring the spurious background rate has therefore been rejected.

4.8. *Factors determining the Precision of Measurement*

We have already given an expression for the ideal, purely geometrical, form of the spectrum of particles falling into a single momentum category as the product of the incident particle spectrum with a suitable function representing the collecting efficiency of a single counter channel for particle deflections in the neighbourhood of the nominal deflection of the channel. We now consider the modification of this collecting function which arises from the scattering of particles in the instrument.

Scattering. The mean projected angle of scattering $\bar{\theta}$ in a scattering length t of material with N atoms of atomic number Z per cm^3 may be written (Williams 1939)

$$\bar{\theta} = (19\cdot5 - 3\cdot1 \log Z)^{1/2} \frac{600\, Ze(Nt)^{1/2}}{\beta p} \qquad \ldots\ldots(15)$$

$$= \kappa t^{1/2}/\beta p,$$

where e is measured in E.S.U., and p in ev/C., and $\kappa \times 10^{-6}$ is 3·9 for glass, 9·7 for copper, 0·6 for air. For copper in glass counters of the type used (1 mm. glass wall, 0·003 in. copper foil), $\bar{t}_{\text{glass}} = 0{\cdot}24$ cm., $\bar{t}_{\text{foil}} = 0{\cdot}015$ cm., and thus for a single counter

$$\bar{\theta} = (2{\cdot}2 \times 10^6)/\beta p. \qquad \ldots\ldots(15\,a)$$

We require the lateral displacement of trajectory in the central plane of the apparatus due to the traversal of one counter in the central plane and two counters (the defining counters) at a distance 91·5 cm. from the central plane. This is clearly given by (notation of Figure 2)

$$\begin{aligned}(\overline{\delta\Delta})_s' &= [\{\tfrac{1}{2}\bar{\theta}(d_0 + d_1)\}^2 + 2\{\tfrac{1}{2}\bar{\theta}\, d_0\}^2]^{1/2} \text{ cm.} \\ &= (7{\cdot}2 \times 10^8)/\beta p \text{ cm.} \qquad \ldots\ldots(16)\end{aligned}$$

For the air column the lateral displacement in a column of length t is given by (see, for example, Rossi and Greisen 1941) $\bar{x} = 3^{-1/2} t\bar{\theta}$. Thus the mean displacements at the extreme trays for scattering in the air from the line defined by the tangent at the central tray are $\bar{x} = 3^{-1/2}(d_0 + d)\bar{\theta}_1$, and the mean displacement of the central point from the line joining the extreme points will be

$$(\overline{\delta\Delta})_s'' = (1{\cdot}2 \times 10)^8/\beta p \text{ cm.} \qquad \ldots\ldots(17)$$

Thus the total scattering displacement $(\overline{\delta\Delta})_s$ is

$$\begin{aligned}(\overline{\delta\Delta})_s &= \{(\overline{\delta\Delta})_s'^2 + (\overline{\delta\Delta})_s''^2\}^{1/2} \\ &= (7{\cdot}4 \times 10^8)/\beta p \text{ cm.} \qquad \ldots\ldots(18)\end{aligned}$$

This uncertainty of displacement arising from scattering is to be compared with the geometrical uncertainty which has the 50% breadth, $(\overline{\delta\Delta})_G = 0{\cdot}26 b_0$ cm.; the effects are of similar importance when $p\beta = 8 \times 10^8$ ev/c., and in general we may write the function which represents the efficiency of collection in the neighbourhood of the nominal deflection of a counter channel, to include scattering within the apparatus,

$$P_1(\Delta - \Delta_n) = \int P(\Delta' - \Delta_n) \exp\{-(\Delta' - \Delta_n)^2/(\overline{\delta\Delta})_s^2\} d\Delta' \qquad \ldots\ldots(19)$$

where $P(\Delta - \Delta_n)$ is the purely geometrical function (equation (3)).

In practice the treatment of the variation of collecting spectrum with scattering will depend closely on the particular application in view. Frequently the effect of variations of magnetic field, which also lead to an uncertainty of deflection proportional to $(\beta p)^{-1}$ will be combined with that of scattering. An example of this kind, arising in a consideration of the particle spectrum will be treated in detail elsewhere.

The scattering deflection, equation (18) sets a limit of precision of measurement at low momentum, for since the total deflection (equation (1)) is

$$\Delta = \left(300\, d_0 \int H\, dl\right) \Big/ p,$$

we have, for

$$\beta = 1 \quad \text{and for} \quad (\overline{\delta\Delta})_s \gg (\overline{\delta\Delta})_G$$

$$\begin{aligned}(\overline{\delta\Delta})_s/\Delta &= (7{\cdot}4 \times 10^8) \Big/ \left(300\, d_0 \int H\, dl\right) \\ &= (1{\cdot}65 \times 10^1) \Big/ \int H dl,\end{aligned}$$

and, for the maximum value of deflecting field ($\int H\, dl = 6{\cdot}5 \times 10^5$ gauss.cm.), $(\overline{\delta\Delta})_s/\Delta = 0{\cdot}025$.

§5. OUTPUT OF MEASURED PARTICLES

We shall discuss elsewhere the detailed application of the instrument to direct measurements of the vertical particle spectrum and the ratio of positive to negative particles in it. The apparatus, however, is designed for the additional purpose of supplying a beam of particles of measured momentum which can be used for experimental purposes, and the following summary indicates the main features of the beam produced.

5.1. *Momentum Distribution*

In Table 4 the distribution into momentum categories of the output, normalized to a total of 1,000 particles, is given, for two values of deflecting field which have already been used, together with the mean momentum of the particles forming each category. For the lower momenta the mean values of momentum in each momentum category are taken directly from equation (6); at the higher momenta this value is no longer a good approximation since the incident deflection spectrum is varying greatly over the range of deflection accepted by the instrument. In applications at high momenta, it will usually be necessary to consider the detailed momentum spectrum covered by each category, but for completeness approximate values of momentum are included in brackets in Table 4.

Table 4

Momentum category	$\int H\,dl = 6{\cdot}1 \times 10^5$ gauss. cm. Mean momentum 10^9 ev/c.	 No. of particles per 1000	$\int H\,dl = 3{\cdot}1 \times 10^5$ gauss. cm. Mean momentum 10^9 ev/c.	 No. of particles per 1000
0	(26)	53	(16)	90
1	(12)	126	(7·6)	197
2	(7·1)	148	(4·3)	185
3	(5·0)	137	(2·7)	151
4	3·7	118	2·0	107
5	2·8	94	1·5	72
6	2·3	76	1·3	56
7	2·0	50	1·1	40
8	1·7	42	0·96	28
9	1·5	36	0·83	22
10	1·4	32	0·74	14
11+12	1·3	37	0·65	18
13+14	1·1	22	0·55	11
>14	<1·0	19	<0·50	9

5.2. *Angular Distribution*

As indicated with reference to the angle of collection (§ 4.2) the instrument defines the angle of emergence of any particle to about ± 1°, and for detailed behaviour in subsequent experiments this angle may be used. The general geometry of experiments will be determined by the angular distribution covering all possible counter channels which contribute to the momentum category required. This distribution has already been summarized (Owen and Wilson 1949, Figure 2), and shows that the maximum spread of particles of a single category is ± 8°. For most purposes this spread is of little importance.

5.3. *Spatial Distribution*

The spatial distribution of particles emerging from the bottom counter tray of the spectrograph is summarized in Table 5 for typical momentum categories. It is apparent from the Table that in every category a substantial fraction of all particles can be selected emerging from about eight counters, say from an area $30 \times 15\,\text{cm}^2$.

Table 5. Spatial Distribution of Particles Emerging from Spectrograph

Momentum Category	0	+4	+8	+12
Mean momentum at full excitation (10^9 ev/c.)	26	4	2	1·4
*n**	Relative number of particles emerging from *n*th counter of bottom measuring row.			
1	2·0			
2	3·0			
3	4·5	1·0		
4	5·5	2·0		
5	6·0	3·2	0·5	
6	6·0	4·5	1·6	
7	6·0	5·5	2·6	
8	6·0	6·0	3·2	0·5
9	6·0	6·0	3·8	0·9
10	6·0	6·0	5·0	2·7
11	6·0	6·0	5·0	3·0
12	6·0	6·0	5·0	3·2
13	5·5	6·0	5·0	3·8
14	4·5	6·0	5·0	4·0
15	3·0	5·8	5·0	4·0
16	2·0	5·0	6·0	5·0

* *n* is the serial number of counter of emergence (axis of symmetry, between counters 8 and 9).

ACKNOWLEDGMENTS

The construction of this apparatus was made possible by a grant from the Treasury Fund of the Royal Society.

The authors wish to thank Professor P. M. S. Blackett for his support throughout the work and for his continued interest and advice, the staff of the Research Department, Metropolitan Vickers Electrical Co. (in particular Messrs. P. P. Starling, W. E. Edgar, A. Armour and G. W. G. Cogle) for their helpfulness at all stages of the project, and the technical staff of the Physical Laboratories, Manchester University (in particular Mr. R. E. Bradford) for their share in the construction of the apparatus.

Three of us (B. D. H., M. G. M. and B. G. O.) are indebted to the Department of Scientific and Industrial Research for maintenance grants during some part of the work.

REFERENCES

ALIKHANIAN, A., ALIKHANOV, A., and WEISSENBERG, A., 1947 a, *J. Phys. USSR*, **11**, 97; 1947 b, *Ibid.*, **11**, 199; 1948 a, *J. Exp. Theor. Phys.*, **18**, 301.

ALIKHANIAN, A., ALIKHANOV, A., MOROZOV, V., MUSKHELISHVILI, G., and KHRIMIAN, A., 1948 b, *J. Exp. Theor. Phys.*, **18**, 673.

BLACKETT, P. M. S., 1936, *Proc. Roy. Soc.* A, **154**, 564.

JÁNOSSY, L., 1948, *Cosmic Rays* (Oxford: Clarendon Press).

OWEN, B. G., 1950, *Proc. Phys. Soc.* A, **63**, 1074.

OWEN, B. G., and WILSON, J. G., 1949, *Proc. Phys. Soc.* A, **62**, 601.

ROSSI, B., 1948, *Rev. Mod. Phys.*, **20**, 538.

ROSSI, B., and GREISEN, K., 1941, *Rev. Mod. Phys.*, **13**, 240.

WILLIAMS, E. J., 1939, *Proc. Roy. Soc.* A, **169**, 531.

A Magnetic Cosmic-Ray Spectrograph with Counter Recording—II: The Electronic and Recording System

BY B. G. OWEN
Physical Laboratories, University of Manchester

Communicated by P. M. S. Blackett; MS. received 28th March 1950

ABSTRACT. The paper describes the electronic selection and recording systems of the spectrograph and the performance and overall serviceability of the equipment as shown in continuous operation over about one year.

§ 1. INTRODUCTION

A GENERAL description is given in the preceding paper (Hyams, Mylroi, Owen and Wilson 1950, referred to here as I) of the main features of performance and operation of the spectrograph. The present paper deals, in detail, with the discriminating and recording sections of the instrument. In the design of these sections serviceability and stability have been essential considerations since the apparatus is required to run unattended for long periods. It is found, in addition, that a high resolution is necessary in order that the casual coincidence rate between the various sections of the instrument, which might give rise to spurious records, shall be at a low level. The performance which has been obtained is satisfactory in all these respects.

§ 2. REQUIREMENTS OF THE RECORDING SECTION

It has been shown in I that the 'accepted event', which is interpreted as the record of a fast particle traversing the apparatus, requires a five-fold counter coincidence between one counter, and one only, from each of the three 'measuring trays', and at least one counter of each of the two 'defining groups' located in the field gap of the two deflecting magnets. To simplify the design and increase reliability it is found convenient to record all five-fold coincidences between three 'measuring trays' and two 'defining groups' irrespective of the number of counters which are actually discharged in the measuring trays and give rise to the five-fold coincidence. Since it is in any case necessary to have a means of identifying any counter which is discharged in a recorded event, this selection clearly includes all 'accepted events' in a recognizable way: the additional records, in which more than one counter in one or more of the measuring trays is discharged, are valuable since they give a continuous record of the most important disturbing factors which can on occasion simulate the passage of a single particle. For example, it is possible for the particles in an extensive air shower to discharge the selection of counters which we have described as the 'accepted event' and so give rise to a spurious record. Such events, however, bear a readily determined relation to similar events in which more than one counter is discharged in any tray, and records of the latter events are therefore a continuous check on the actual level of shower recording at any time. In addition, internal faults arising from interaction between the various counter channels, leading, perhaps, to records in which certain counters are shown to have discharged when in fact they have not done so, are much more easily detected and corrected if the more extended records are taken.

It has already been pointed out (I) that a primary purpose of the apparatus is to supply a beam of particles of measured momentum for experimental purposes. It is therefore necessary for the recording system to have capacity either for interconnection with the recording system of any apparatus using the output, or for receiving the whole record of such apparatus. Whenever possible the second alternative has clear advantages.

Throughout the design emphasis has further been given to economy, both in initial assembly and in maintenance, and to the achievement of a high level of serviceability over long periods. The circuits used have therefore been based on a minimum of components and valve types. Test equipment has been developed so that failure at any stage of the circuits can be quickly located.

§ 3. SUMMARY OF CIRCUIT SEQUENCE

In the previous paper (I) it has been shown that a 'resolving' time of 3 microseconds or less is desirable. With the sequence adopted here, this fixes the length of pulse from the various counters between which coincidence must be established. Unless these pulses are limited to about 3 microseconds an unacceptable increase in the level of spurious operation is to be expected; this figure was accordingly adopted for the purposes of design.

Counter pulses must be transmitted to a central mixing and coincidence unit over distances up to 10 metres. An initial electronic unit (suppressor and shaping unit) is therefore introduced close to each counter and a cathode follower used to transmit the 3-microsecond pulse to the later sections down a screened cable. It is found valuable, also, to incorporate at this stage a 'flip-flop' or monostable multivibrator, which rapidly suppresses each counter discharge, thus adding significantly to the useful life of the counters.

The master coincidence event is a five-fold coincidence of the shaped pulses from the three measuring counter trays and from the two defining counter groups. Such an event leads to the formation of a master coincidence pulse. It is now necessary to indicate the precise counters which have been discharged in each of the measuring counter trays.

For this purpose the pulses from the suppressor and shaping units 'triggered' by the appropriate counter discharges giving rise to the coincidence are mixed individually with the master pulse so that counter discharge is indicated by the striking of the corresponding neon lamp at a display board. This is viewed by an unshuttered camera and recorded on film. The master pulse with suitable delay causes a white light to flash momentarily, photographing the instruments on the display board—the magnet current meter, sequence number etc. After this illumination, the camera is caused to turn one frame and the apparatus is reset (see Figure 1).

When operating secondary apparatus using the output of the spectrograph, exactly comparable mixing circuits are used with similar suppressor and shaping units in conjunction with the auxiliary counters, and the operation of this equipment is indicated by the striking of further neon lamps at the display unit.

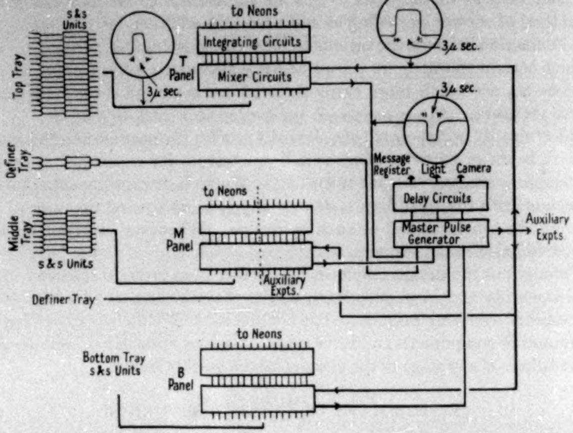
s&s Units
Top Tray
to Neons
Integrating Circuits
T Panel
Mixer Circuits
3μ sec.
3μ sec.
3μ sec.
Definer Tray
Message Register
Light
Camera
Delay Circuits
Master Pulse Generator
Auxiliary Expts
to Neons
Middle Tray
M Panel
s&s Units
Auxiliary Expts.
Definer Tray
to Neons
Bottom Tray s&s Units
B Panel

Figure 1.

The various elements of the recording circuits will be considered in the next Section in greater detail.

§ 4. DESCRIPTION OF RECORDING CIRCUITS

4.1. *Suppressor and Shaping Unit*

This unit, which receives the discharge pulses of a single counter, provides as output a low impedance 2–3 microsecond 60 volt positive pulse, the rising edge of which corresponds to the beginning of the counter discharge. A schematic diagram and circuit are shown in Figures 2 (*a*) and 2 (*b*). The suppression of the counter is provided from a monostable multivibrator which effectively lowers the voltage on the counter (normally operating 40 volts above starting potential) by 200 volts for 2 milliseconds.

A suppressor and shaping unit is connected to each counter, 44 in all (16, top measuring layer, 2, upper magnet gap defining counters, 8, middle measuring layer, 2, lower magnet gap defining counters, 16, bottom measuring layer), and the outputs from all of these are carried in screened cables to the coincidence and mixing units.

4.2. *Mixing Panels*

When a master coincidence event takes place (see below) it is necessary to illuminate neon lamps at the display panel corresponding to the particular counters discharged in the three measuring layers, and to identify in a similar way counter combinations of equipment using the spectrograph output. The necessary mixing circuits are carried on three panels each controlling 16 neon lamps (one panel each for top and bottom measuring layers, one panel for the middle measuring layer together with eight lamps to carry auxiliary information).

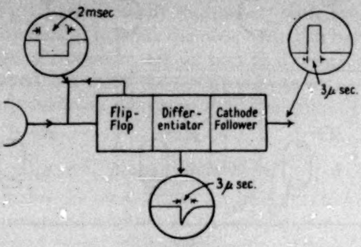

Figure 2 (*a*).

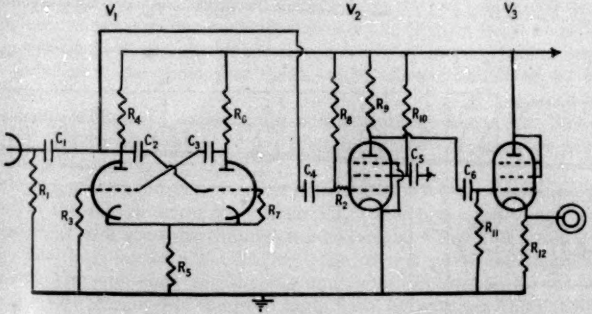

Figure 2 (*b*).

R_1, R_{11} 1 MΩ
R_3, R_7 ¼ MΩ
R_4 22 kΩ
R_6 39 kΩ
R_8 270 kΩ
R_9 20 kΩ
R_{10} 33 kΩ
R_2 500 Ω
C_1 0·1 μF.
C_2, C_3 0·002 μF.
C_4 25 pF.
C_5, C_6 0·1 μF.
V_1 6SN7
V_2, V_3 EF50.

The basis of the operation of these panels may be explained by considering the four channels shown in Figure 3. All the input valves (V_{1a},V_{2a},V_{3a},...) in a panel are biased off on G_1, the screen grids are interconnected and fed through R_4, and the suppressors are joined together and biased off at -100 volts through R_5.

The discharge of any counter (or counters) in any tray 'turns on' the screen current of the appropriate input valve for 3 microseconds and at the same instant a negative pulse appears across the common screen resistance of that panel. The simultaneous discharge of five or more counters (at least one per tray and one per defining counter group) generates a master pulse which is used to open the suppressor gate of all input valves by removing the negative bias for rather less than

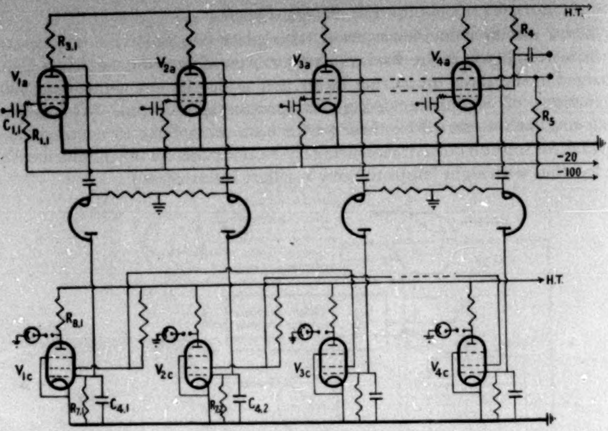
H.T.
R3,1
V1a
V2a
V3a
V4a
R4
R5
C1,1
R1,1
-20
-100
H.T.
R8,1
V1c
V2c
V3c
V4c
R7,1
C4,1
R7,2
C4,2

Figure 3.

$C_{1\cdot1}$ 0·1 μF.
$C_{4\cdot1}$ 0·01 μF.
R_{11} 1 MΩ

$R_{3\cdot1}$ 33 kΩ
$R_{7\cdot1}$ 5 MΩ
R_4 3 kΩ

R_5 1 MΩ
$R_{8\cdot1}$ 68 kΩ
V_{1a}, V_{1c}, V_{2a}, V_{2c}, etc. EF50.

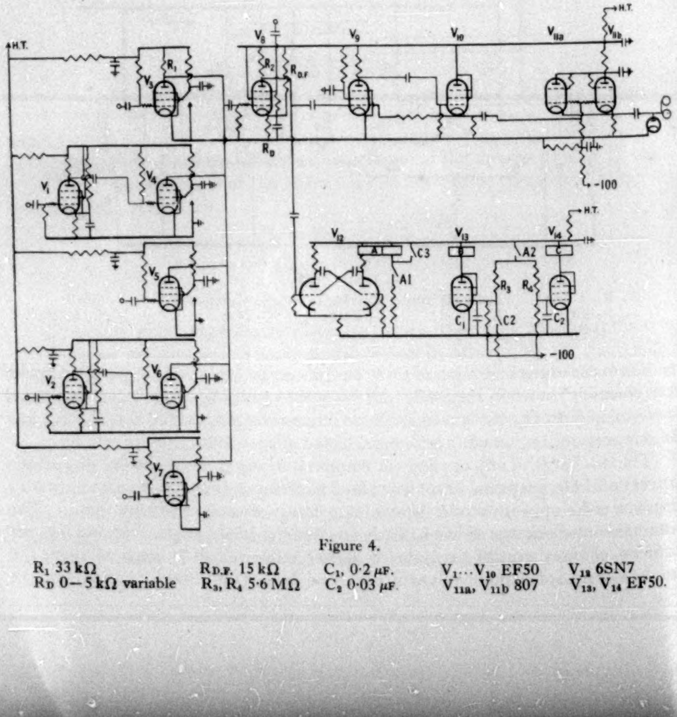
H.T.
V8
V9
V10
V11a
V11b
H.T.
R1
R2
RD.F
RD
V3
V1
V4
V5
V2
V6
V7
-100
H.T.
V12
V13
V14
A
B
C
C3
A1
A2
R3
R4
C1
C2
C2
-100

Figure 4.

R_1 33 kΩ
R_D 0–5 kΩ variable

$R_{D.F.}$ 15 kΩ
R_3, R_4 5·6 MΩ

C_1, 0·2 μF.
C_2 0·03 μF.

$V_1 \ldots V_{10}$ EF50
V_{11a}, V_{11b} 807

V_{12} 6SN7
V_{13}, V_{14} EF50.

3 microseconds. The valves receiving auxiliary data are similar in all respects except that the common screen resistor is not connected to the master unit. The time delay between the arrival of the pulse at the input valves and generation of the master pulse by the necessary five-fold coincidence is of the order of ¼ microsecond. The coincidence between a pulse on G_1 and a master pulse on G_3 provides a negative pulse at the anode of the appropriate valve of the row (V_{1a}, V_{2a},..). This pulse is, in turn, integrated by the condenser C_{4n} the resistance R_{7n} and the appropriate diode ($n=1$ to 16 for a given panel) and reduced in amplitude but increased in duration to about ¼ second.

The valves (V_{1c},V_{2c}...) are normally 'bottomed' with anode voltage of about +20 volts, which is insufficient to strike the neon lamp tied between the anode and earth. The discharge of a counter, taking part in a coincidence, causes one of these valves to be cut off; on these the anode voltage rises until the neon lamp strikes, and the lamp remains in discharge until the grid of the valve returns to earth potential.

4.3. *Master Pulse Panel*

This unit, which makes the master selection of events to be recorded, receives pulses from the five groups of counters in the spectrograph, coincidence among which forms the 'accepted event' of the instrument. The pulses reaching it from the measuring trays are taken from the corresponding common screens in the mixing units and are negative; those received directly from the two groups of 'defining counters' are positive and are reversed in valves V_1,V_2 (Figure 4). Valves V_3–V_7 form a conventional Rossi coincidence circuit receiving in every case a negative pulse. Switches at the screens of these valves allow channels to be tested individually.

A coincidence leads to a positive pulse at the common resistor R_1. Assuming a total stray capacity per valve of 20 pF., the time constant of the anode circuit is about 2 microseconds.

The output of the coincidence circuit is fed to the valve V_8 which is normally biased off by the voltage across the resistor R_D. This bias is set to a minimum value consistent with good discrimination between the 4-fold and 5-fold coincidences. The delay between the leading edge of this pulse and that coming initially from the suppressor and shaping units is of importance, for too long a delay reduces the duration of the neon lamp flash by reducing the pulse to be integrated at V_{nc} in the mixing panels. In our apparatus this delay can be reduced to ¼ microsecond. The output pulse across R_2 is then fed to two channels: (*a*) the relay channel leading to the operation of the recording equipment, and (*b*) the master pulse shaper channel from which the master pulse is returned to the mixing panels.

(*a*) The pulse across R_2 triggers the monostable multivibrator at V_{12} which is of sufficiently long time constant to close relay A which holds itself closed through contacts A1.

Closure of contact A2 charges C_1 and C_2 through R_3 and R_4 respectively. The time constants are adjusted so that relay B closes first, causing the display panel to be momentarily illuminated, titling the film, numbering the neon lamps and recording the instantaneous reading of a clock and of an ammeter in spectrograph magnet coils. About 1 second after the closure of A1, relay C closes, cancelling relay A and causing the film in the recording camera to move through one frame.

(*b*) In the second channel the pulse from R_2 is shaped at V_9, V_{10} giving a 100 volt positive pulse of duration 3 microseconds which then passes to the cathode follower stage V_{11a}, V_{11b}. The final pulse raises the suppressor voltage of all input valves in the mixing units to earth potential.

§ 5. PERFORMANCE OF THE RECORDING CIRCUITS

(*a*) *Valves.* The majority of the valves used are of EF50 type and the failure rate during this period has been approximately 3% occurring almost entirely in circuit positions where the valves are continuously conducting and not in positions where the valves are switched on for short pulses of duration of 3 microseconds.

If the emission of a valve in the integrating position decreases, the associated neon lamp occasionally remains in discharge for periods longer than ¼ second, leading to an exceptionally dense record : the valve can thus be replaced before complete failure of the particular channel occurs.

(*b*) *Counters.* The counters are operated at 40 volts above the threshold and in about 1 year only one failure has occurred.

(*c*) *Test procedure.* The daily check consists in switching the several trays singly into the coincidence circuit and examining the neon lamps flashing at the display board. The performance is examined of any counter channel for which the neon lamp is not flashing at the expected rate of a single counter. If the fault persists after the counter voltage has been checked, the whole channel is checked systematically by feeding in appropriate test pulses at various stages and examining the response on an oscilloscope. Test equipment has been developed for this specific purpose and enables faults to be located rapidly; it has contributed notably to the high level of serviceability obtained.

After the first month of operation, in which faults were located and eliminated the apparatus has operated continuously for about a year, during which more than 80,000 traversals have been recorded. The total time the equipment has been inoperative due to failure and testing has been less than 5% of the total time.

REFERENCE

Hyams, B. D., Mylroi, M. G., Owen, B. G., and Wilson, J. G., 1950, *Proc. Phys. Soc.* A, **63**, 1053.

Observations on Cosmic-Ray Penetrating Showers at High Altitude, Sea Level and Below Ground

By E. P. GEORGE and A. C. JASON
Birkbeck College, University of London

MS. received 1st *February* 1950

ABSTRACT. Penetrating showers have been investigated, using Geiger counters, at a depth of 30 m. below ground, at sea level and at an altitude of 3,457 m. The influence of the geometry of the absorbers was studied. The transition curves for local showers, corrected for this geometric effect, give the following collision lengths of the generating particles : Pb, 180 ± 40; Al, 85 ± 15; Paraffin ∼80 gm/cm². These values correspond to a collision cross section close to the geometric cross section of the nuclei. From the results obtained for extensive penetrating showers, it is concluded that most of the penetrating particles in these showers appear to be generated in the atmosphere. In 40 days, no penetrating showers were recorded below ground. Using photographic plates, the density distribution of shower tracks associated with nuclear disintegrations was found to be similar at sea level and 3,457 m.

§ 1. INTRODUCTION

During the past 2½ years, an investigation has been made of penetrating cosmic-ray showers, using apparatus similar to that described by Broadbent and Jánossy (1947). Observations were carried out first at a depth of 30 metres below ground at Holborn Station, in London ; secondly at the Scientific Station, Jungfraujoch, Switzerland (altitude 3,457 m.), and finally on the roof of the Senate House, University of London.

The purpose of the investigation was to study the absorption of the primary radiation responsible for the showers in air and other substances. Observations are reported on the transition curves obtained for various materials and on the barometer effect.

The effect of the geometry of the top absorber on the frequency of the showers has been studied, and in this way the penetrating shower transition curves have been corrected for the effects of absorber geometry. The corrected transition curves for the local showers appear to be inverse-exponential in form, the range of the primary radiation being near to that corresponding to the geometric cross section of the atomic nuclei of the absorbing materials.

The frequency of extensive penetrating showers is shown to depend very little on the arrangement of the absorbers, and it is argued that in the majority of cases the penetrating particles are more likely to originate from the air than from the local absorbers.

The same apparatus was used to study secondary, knock-on showers, and the results are recorded in an appendix. A second appendix contains the results of a comparison of the mean particle density in penetrating-shower type events observed in photographic plates exposed at sea level and at the Jungfraujoch. The particle distribution is found to be very similar at both altitudes.

§ 2. EXPERIMENTAL ARRANGEMENT

The apparatus used is indicated in Figure 1. It consisted of a penetrating shower set P, containing three trays of Geiger counters (t, m, b) separated by lead absorbers 15 cm. thick. In addition to the set P, an unscreened tray of counters E was placed nearby to indicate the presence of air showers.

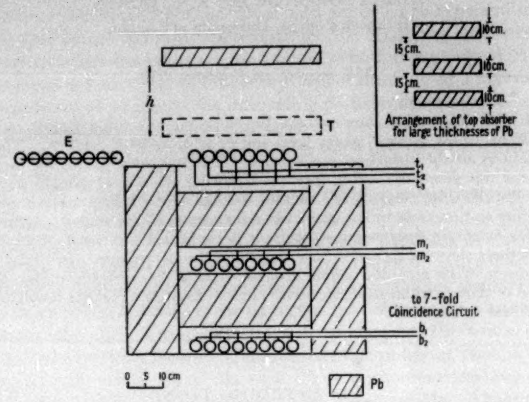
10cm.
15cm.
10cm.
15cm.
10cm.
Arrangement of top absorber for large thicknesses of Pb
h
T
E
t₁
t₂
t₃
m₁
m₂
to 7-fold Coincidence Circuit
b₁
b₂
0 5 10 cm
Pb

Figure 1. General arrangement of apparatus.

Each of the trays in P consisted of eight counters of effective area 40 × 3 cm. The top tray t was subdivided into three groups (t_1, t_2, t_3) as shown, the remaining two trays m and b were divided into groups m_1, m_2, and b_1, b_2.

The air-shower tray E consisted of eight counters in parallel. Each counter had an effective surface of $60 \times 3{\cdot}8$ cm^2, making a total area of 1,824 cm^2.

Sevenfold coincidences, P, consisting of the simultaneous discharge of at least one counter in each group of P were recorded and, in addition, coincidences P accompanied by a discharge in the air-shower tray, E, were recorded separately (P, E). The anticoincidences (P, − E) will be referred to as local penetrating showers, while the coincidences (P, E) will be referred to as extensive penetrating showers in conformity with the nomenclature established by other workers (Broadbent and Jánossy 1947).

Absorbers, T, of paraffin wax, aluminium and lead were placed above the top of tray t. The absorbers were 45 cm. square and their lower surfaces 4½ cm. above the top of counters t, shown by the dotted outline in Figure 1. For some observations to be described later, the absorber T was raised a distance *h* above its normal position as indicated in Figure 1.

§ 3. UNDERGROUND OBSERVATIONS

During a period of 1,065 hours, no sevenfold coincidences were recorded at Holborn Station. Frequent tests of the satisfactory performance of the apparatus were made both by recording coincidences of a lower order than seven, and by using test pulses from a dry cell.

The possibility that sevenfold coincidences might be caused by a single meson passing through the apparatus and producing a secondary electron near each counter tray has been pointed out by Jánossy. The frequency of sevenfold coincidences arising from this mechanism was estimated by observing the frequency of the knock-on showers in the various trays. We calculate that during the period of the experiment, we should have recorded between two and three sevenfold coincidences due to knock-on electrons. The fact that none was recorded may be attributed to statistical fluctuations. The details are given in Appendix I.

§ 4. OBSERVATIONS AT SEA LEVEL

Investigations were carried out at sea level on (*a*) the dependence of the rate of penetrating showers on the thickness of material T in Figure 1 (the transition effect), and (*b*) the dependence of the penetrating shower rate on the distance, *h*, between the absorber T and the penetrating shower set P, Figure 1 (the geometric effect). The contribution from knock-on showers was also recorded.

(a) *The Transition Effect at Sea Level*

Measurements at sea level on the transition effect have already been published by other workers with similar apparatus (Jánossy and Rochester 1944 a, Broadbent and Jánossy 1947), and our object in repeating them was simply to standardize our apparatus.

The results are given in Table 1, and are drawn out in Figures 2 (*a*) and (*b*) for the local and the extensive penetrating showers respectively. These results are substantially in agreement with the sea-level measurements of Broadbent and Jánossy (1947). A marked transition effect is recorded for the local showers, showing signs of a saturation in the vicinity of 100 to 200 gm/cm ^{2} of lead. The points for paraffin and lead appear to fall on the same curve. The extensive showers show a small maximum in the vicinity of 2 cm. of lead, decreasing again up to 100 gm/cm^2 lead, after which the rate of extensive showers varies only slowly with the thickness of absorber T.

Table 1. Dependence of Penetrating Showers on the Thickness of Absorber T at Sea Level.

Material T (gm/cm²)	Time *t* (hrs.)	Local showers (P, –E) *N*	*N*/*t*	Extensive showers (P, E) *N*	*N*/*t*
0	580	57	0·098±0·013	53	0·092±0·012
Paraffin					
11·3	1420	226	0·16 ±0·011	128	0·09 ±0·008
22·6	943	224	0·24 ±0·016	96	0·102±0·010
Lead					
22·6	538	102	0·19 ±0·019	77	0·143±0·016
56·5	674	207	0·307±0·021	79	0·118±0·013
113	570	208	0·365±0·025	63	0·110±0·014
226	615	209	0·34 ±0·023	70	0·114±0·014

For the larger thicknesses of lead at T, the absorber layers were spaced out as shown in the inset of Figure 1. It was hoped in this way to reduce the influence of the large difference in density of the lead, aluminium and paraffin wax absorbers.

(*b*) *The Geometric Effect*

It is clear that penetrating showers arising in various parts of the transition material T are not all recorded with the same efficiency. It would be expected that those arising in the top layers of T would be recorded with a lower average efficiency than those arising in the lower layers. This change of efficiency might be attributable to: (i) the change in the solid angle that the P set subtends at the point of origin of the shower, or (ii) absorption of the shower particles in the transition material T.

The measurements of Jánossy (1942) on the absorption of the penetrating-shower particles in lead show that even with the maximum thickness of absorber used at T (30 cm. Pb) this self-absorption (ii) will be small.

The effect of changes in geometry (i) was investigated by keeping the thickness of the absorber T fixed at 5 cm. of lead, and placing it at various heights *h* above the shower set P (Figure 1.)

The results are shown in Table 2, and are plotted in Figures 3 (*a*) and (*b*).

Table 2. Penetrating Showers as a Function of the Height, *h*, of the Absorber T.

Height *h* (cm.)	Time *t* (hrs.)	Local showers (P, –E)		Extensive showers (P, E)	
		N	*N*/*t*	*N*	*N*/*t*
0	674	207	0·307±0·021	79	0·118±0·013
4·5	304	75	0·246±0·028	39	0·128±0·020
9·5	334·5	77	0·230±0·026	43	0·128±0·019
14	394·5	62	0·161±0·020	60	0·152±0·020
25	146	20	0·137±0·031	15	0·103±0·026
48	277·5	33	0·119±0·021	40	0·144±0·023
68·5	220	22	0·100±0·021	25	0·114±0·023

The local showers are seen to show a strong dependence on the height, *h*, of the absorber T, while the extensive showers appear to be independent of *h*, within the limits of accuracy of the experiment. The curve in Figure 3 (*a*) may now be used to eliminate the influence of the absorber geometry on the transition curve for local penetrating showers. The details of this procedure will be left until we have discussed the observations made at the Jungfraujoch.

(*c*) *Knock-on Showers*

The observations are recorded in Appendix I. The calculated frequency of sevenfold coincidences due to knock-on showers is 0·01/hour, small compared with the penetrating-shower frequency.

§ 5. OBSERVATIONS AT THE JUNGFRAUJOCH

At the Jungfraujoch, observations were made on (*a*) the transition effect, and (*b*) the dependence of the shower frequency on the barometric pressure.

(*a*) *The Transition Effect at the Jungfraujoch*

The shower transition curves were measured at the Jungfraujoch in paraffin, aluminium and lead. The results are given in Table 3.

Figure 4 (*a*) shows the transition curve for local penetrating showers (P, –E) at the Jungfraujoch. It is seen that the points appear to lie about a common curve

Table 3. Dependence of Penetrating Showers on the Thickness of Absorber, T, at the Jungfraujoch

Paraffin						Aluminium						Lead					
Thickness (gm/cm²)	*t* (hrs.)	Local Showers		Extensive Showers		Thickness (gm/cm²)	*t* (hrs.)	Local Showers		Extensive Showers		Thickness (gm/cm²)	*t* (hrs.)	Local Showers		Extensive Showers	
		N	*N/t*	*N*	*N/t*			*N*	*N/t*	*N*	*N/t*			*N*	*N/t*	*N*	*N/t*
0	167·7	349	2·08 ±0·11	230	1·38 ±0·1	0	167·7	349	2·08 ±0·11	230	1·38 ±0·1	0	167·7	349	2·08 ±0·11	230	1·38 ±0·1
11·3	72·1	226	3·15 ±0·21	114	1·58 ±0·15	10	78·2	276	3·52 ±0·21	128	1·63 ±0·14	11·3	120	511	4·26 ±0·19	172	1·4 ±0·11
22·6	70·7	256	3·65 ±0·23	129	1·82 ±0·16	20	112·1	489	4·35 ±0·20	137	1·23 ±0·1	22·6	137	696	5·09 ±0·19	221	1·62 ±0·11
						30	54·2	317	5·83 ±0·33	83	1·53 ±0·17	33·9	86·3	470	5·43 ±0·25	88	1·01 ±0·11
						40	80·1	448	5·6 ±0·26	141	1·76 ±0·15	45·2	89	455	5·11 ±0·24	91	1·02 ±0·11
						60	69	511	7·42 ±0·33	132	1·94 ±0·17	56·5	34·4	200	5·81 ±0·41	36	1·04 ±0·17
						100	137	1152	8·4 ±0·25	272	1·98 ±0·12	113	44·9	315	7·02 ±0·39	50	1·1 ±0·16
						150	71·5	597	8·38 ±0·34	116	1·62 ±0·15	169	60·2	398	6·61 ±0·33	60	1·0 ±0·13
						200	69	570	8·25 ±0·34	113	1·63 ±0·15	226	48·1	319	6·61 ±0·37	52	1·1 ±0·15
												282	30·1	157	5·21 ±0·41	40	1·30 ±0·21

for thicknesses of material up to 50 gm/cm^2, after which the curves for aluminium and lead diverge. The curve for lead rises to a peak at about 150 gm/cm^2, after which it declines again. The aluminium was only taken up to a thickness of 200 gm/cm^2, but here too the recorded rate of local penetrating showers appears to reach a peak at about 150 gm/cm^2.

The transition curves for the extensive showers (P, E) are drawn out in Figure 4 (*b*). The curves for lead and aluminium are of typical cascade form, showing maxima at approximately 22·6 and 100 gm/cm^2 respectively. There appears to be a small transition effect in paraffin also.

From the curves of Figures 4 (*a*) and 2 (*a*) we obtain the ratios:

$$\frac{\text{Local penetrating showers at Jungfraujoch}}{\text{Local penetrating showers at sea level}} = 23 \pm 2, \qquad \ldots\ldots(1)$$

and for $T=0$

$$\frac{\text{Extensive penetrating showers at Jungfraujoch}}{\text{Extensive penetrating showers at sea level}} = 15 \pm 2. \qquad \ldots\ldots(2)$$

(*b*) *The Barometer Coefficient of Penetrating Showers at the Jungfraujoch*

The observations at the Jungfraujoch reported in the previous section were obtained over a period of four months. The barometer pressures were also noted over this same period, and it has been possible to derive a value at the Jungfraujoch for the barometer coefficient of the local penetrating showers for those thicknesses of the local absorber T for which the barometer changes were appreciable. The barometer coefficient has been determined at sea level by Jánossy and Rochester (1944 b) who obtained a value of $B = -11{\cdot}7 \pm 2{\cdot}7\%$ per cm. Hg. The value we find at the Jungfraujoch is $B = -13{\cdot}7 \pm 4{\cdot}5\%$ per cm. Hg, in reasonable agreement with the sea-level value. The values obtained for various thicknesses of the absorber T are given in Table 4.

Table 4

Absorber (gm/cm^2)	Time (hrs.)	Count	B (% per cm. Hg)	Standard error $\delta B/B$
11·3 Al, Pb or Paraffin	266	999	−7·5	1·2
22·6 Al, Pb or Paraffin	320	1426	−15·8	0·4
40 Al	80	448	−3·5	3·9
100 Al	137	1152	−13·6	0·8

Weighted average : $B = -(13{\cdot}7 \pm 4{\cdot}5)\%$ per cm. Hg.

§ 6. THE TRANSITION CURVES OF PENETRATING SHOWERS AFTER ELIMINATION OF THE EFFECTS OF ABSORBER GEOMETRY

From Figures 3 (*a*) and (*b*) it is seen that the geometry of the top absorber does not affect the rate of recording of extensive penetrating showers to any marked extent, and hence it is not worth while introducing a correction into the extensive shower transition curve to allow for the finite height of the top absorber. For the local showers on the other hand, the situation is quite different. Here there is a strong dependence of the rate of recording of local showers on the position from which they originate. We have used the curve of Figure 3 (*a*) in order to correct the transition curves 2 (*a*) and 4 (*a*) for local showers observed at both sea level and the Jungfraujoch.

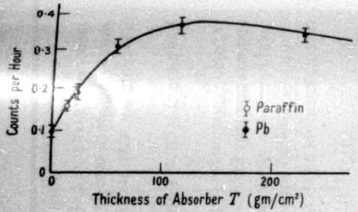

Figure 2(*a*). Transition curve for local showers at sea level.

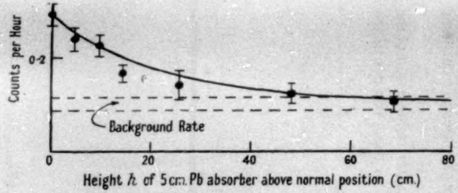

Figure 3 (*a*). Geometric effect for local showers.

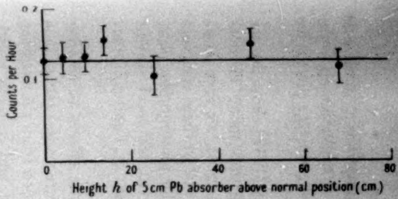

Figure 3 (*b*). Geometric effect for extensive showers.

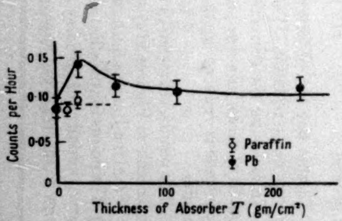

Figure 2 (*b*). Transition curves for extensive showers at sea level.

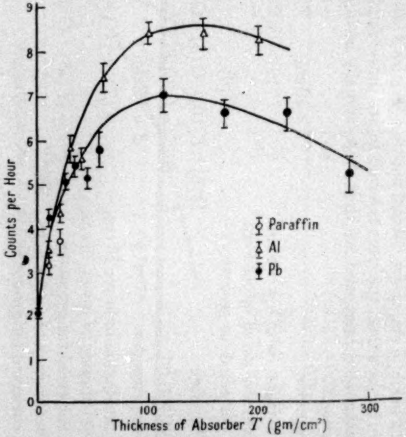

Figure 4 (*a*). Transition curves for local showers at the Jungfraujoch.

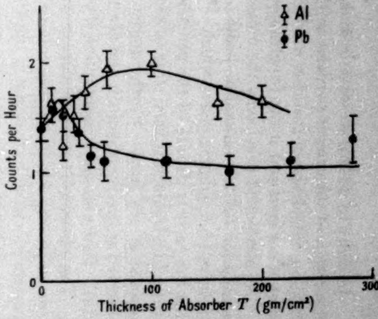

Figure 4 (*b*). Transition curves for extensive showers at the Jungfraujoch.

In order to do this we have to make the following assumptions: (*a*) the self-absorption of the shower particles in the top absorber T is negligible up to the maximum thickness of absorber used (300 gm/cm^2); (*b*) the geometry effect is the same at sea level and at the Jungfraujoch.

As mentioned previously the measurements of Jánossy (1942) show that the assumption (*a*) is reasonably justified. In an investigation using electron-sensitive photographic plates which is reported in Appendix II, we have shown that the particle density of the penetrating showers observed in these emulsions at the Jungfraujoch is very close to that observed in similar photographic plates exposed at sea level. Furthermore, the transition curves for local showers observed at the Jungfraujoch and sea level are very similar: cf. Figures 2 (*a*) and 4 (*a*). Hence we think assumption (*b*) is justified also.

The observed transition curves were corrected for the effects of absorber geometry using Figure 3 (*a*) as follows: Let $I'(T)$ be the recorded rate of local showers produced by material of thickness T cm., as obtained from the transition curves, $I(T)$ the above rate after correction for geometry, and $G(h)$ the experimentally recorded rate of local showers produced by a layer of material 5 cm. thick at a height h cm. above normal position (Figure 3 (*a*)).

In the above, the rates referred to are those obtained after subtraction of the background rates, and are thus those actually attributed to the presence of the material.

Consider $T = 10$ cm.

Contribution of lower 5 cm. $= I'(10) - G(5)$.

Contribution of upper 5 cm. corrected for geometry $= G(0)$.

Therefore $$I(10) = I'(10) - G(5) + G(0). \qquad \ldots\ldots(3)$$

Further, let $B(T) = I(T)/I'(T)$.

Now, consider $T = 15$ cm.

Contribution of lower 10 cm. $= I'(15) - G(10)$.

Contribution of lower 10 cm. corrected for geometry $= \{I'(15) - G(10)\}\, B(10)$.

Contribution of upper 5 cm. corrected for geometry $= G(0)$.

Therefore $$I(15) = \{I'(15) - G(10)\}B(10) + G(0). \qquad \ldots\ldots(4)$$

In general $$I(T) = \{I'(T) - G(T-5)\}B(T-5) + G(0). \qquad \ldots\ldots(5)$$

In this way the observed transition curves were corrected empirically, step by step, using equation (5) without invoking any theory of the geometric effect.

In assessing the corrections for aluminium, we have made the assumption that $G(h)$ varies in a way similar to that found for lead, except that the absolute magnitude is reduced in the ratio $I(5)_{\mathrm{Al}}/I(5)_{\mathrm{Pb}}$. Similar arguments apply for paraffin.

The results, corrected in this manner, are given in Table 5, and are plotted on a linear scale in Figures 5 (*a*) and (*b*).

From the Jungfraujoch results, for which we have the most data, we may note: (i) The points for paraffin, aluminium and lead no longer appear to lie on the same curve, initially (cf. Jánossy and Rochester 1944 a). (ii) The curves no longer show an inversion but appear to be inverse exponential in form.

Table 5. **Transition Curve Results corrected for Absorber Geometry.**

Material	T gm/cm²	Correction factor C	Corrected rate of showers (per hour)
JUNGFRAUJOCH			
Pb	56·5	1·0	5·81 ± 0·41
	113	1·21	8·49 ± 0·47
	169·5	1·59	10·67 ± 0·52
	226	2·19	14·47 ± 0·81
	282·5	2·66	13·82 ± 1·10
Al	10	1·0	3·53 ± 0·21
	20	1·1	4·84 ± 0·22
	30	1·21	7·04 ± 0·40
	40	1·31	7·31 ± 0·33
	60	1·47	10·38 ± 0·48
	100	1·60	13·41 ± 0·40
	150	1·78	14·76 ± 0·60
	200	1·94	15·98 ± 0·66
Paraffin	11·3	1·21	3·81 ± 0·25
	22·6	1·47	5·40 ± 0·33
SEA LEVEL			
Pb	0	1·0	0·098 ± 0·013
	22·6	1·0	0·190 ± 0·020
	56·5	1·0	0·307 ± 0·021
	113·0	1·18	0·432 ± 0·029
	226·0	1·69	0·580 ± 0·039
Paraffin	11·3	1·18	0·190 ± 0·013
	22·6	1·41	0·338 ± 0·022

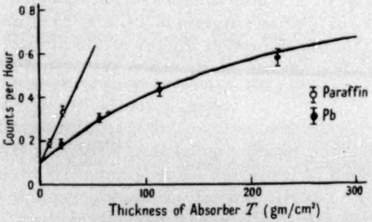

Figure 5 (*a*). Sea level.

Transition curves for local showers corrected for effect of absorber geometry.

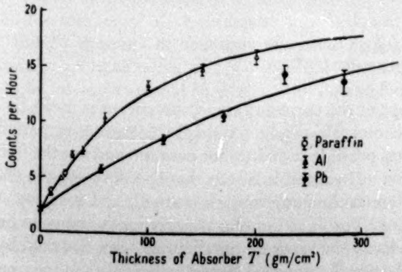

Figure 5 (*b*). Jungfraujoch.

Transition curve for local showers corrected for effect of absorber geometry.

It was therefore assumed tentatively that the points of Figures 5 (*a*) and (*b*) could be represented by curves of the form $a+b(1-e^{-T/R})$, where a, the background rate is the same for all materials. The quantity R would then be interpreted as giving the collision length of the penetrating shower primaries in a given material, and the quantity b the frequency of showers recorded for large thicknesses of the top absorber when corrected for the showers lost for geometric reasons. The term b would be expected to be given by the product of the frequency of the shower primaries, N, multiplied by a factor expressing the efficiency of recording the showers produced in the top absorber, ϵ, which factor might depend on the nature of the top absorber :

$$b = \mathrm{N}\epsilon. \qquad \ldots\ldots(6)$$

In order to obtain the best values of b and R for given set of points, the following procedure was adopted. The background rate, i.e. $I(0) \equiv a$, was first subtracted, and assuming certain values of b and R, the values $C(T)$ of $b(1-e^{-T/R})$ calculated for each of the thicknesses T used. The value of χ^2 was then evaluated for the set of points :

$$\chi^2 = \sum_T \frac{[I(T)-C(T)]^2}{C(T)}. \qquad \ldots\ldots(7)$$

For a fixed value of R, b was varied and χ^2 obtained as a function of b. χ^2 passed through a minimum at a certain value of b, the optimum for the assumed value of R. This was then repeated for other values of R giving a family of curves of χ^2 against b, with R as parameter. In this way the *optimum optimorum* was determined. The range in air, 114 ± 10 gm/cm^2, was determined from the observed ratio of 23 for the local showers at the Jungfraujoch and sea level (cf. Wataghin 1947, Tinlot 1948). The results obtained in this way are given in Table 6. For comparison, we have included in this table the absorption lengths of the primary particles of stars obtained using nuclear emulsions (cf. Bernadini 1949, George and Jason 1949).

Table 6

Material	R (gm/cm^2)	b (per hour)	Initial slope $=b/R$	R (star primaries) (gm/cm^2)
JUNGFRAUJOCH				
Pb	240 ± 50	17·7	0·074	310 ± 15
Al	95 ± 15	16·4	0·170	180
Paraffin	~ 90		0·17	160 ± 13
Air	114 ± 10			150 ± 7
SEA LEVEL				
Pb	160 ± 50	0·68	0·0042	
Paraffin	~ 70		0·01	

The inital slope of the corrected transition curves is given by b/R and since it was only possible to obtain results for small thicknesses of paraffin, it is only the ratio b/R that it was possible to deduce for paraffin, and not the individual values of b and R separately. However, it is seen that the difference in the values of b for lead and aluminium at the Jungfraujoch is small, and we have assumed that the mean value of b is applicable to paraffin also, giving the range indicated in Table 6. Similarly, at sea level, the range in paraffin has been deduced by comparing the initial slopes of the paraffin and lead curves.

§7. DISCUSSION OF RESULTS FOR EXTENSIVE PENETRATING SHOWERS

The following features of our observations on the extensive penetrating showers will be commented on :

(i) the frequency of these showers,
(ii) the smallness of the transition effect (Figures 2 (*b*) and 4 (*b*)),
(iii) the absence of any pronounced effect due to the height of the top absorber (Figure 3 (*b*)).

There is considerable interest in the place of origin of the penetrating particles recorded in extensive showers. Several authors, e.g. Salvini and Tagliaferri (1948), Broadbent and Jánossy (1948), and Auger, Daudin, Fréon and Maze (1948), have suggested that the penetrating particles are mainly produced locally in the absorbers.

This view has been questioned by Cocconi, Tongiorgi and Greisen (1948, 1949), and by Alekseev, Zatsepin and Morozov (1948), who have concluded that the penetrating particles mainly originate in the air above the apparatus. This latter view, which now seems the more likely one, was based principally on observations in which coincidences were recorded between trays of counters with separations of several metres, one or more of the trays being heavily shielded with absorbers. On the other hand, the production of penetrating particles in lead plates in a cloud chamber investigation of extensive showers has been observed by Brown and McKay (1949) and by Ise and Fretter (1949), although these authors agreed that this process is much less frequent than the passage of single penetrating particles through the cloud chamber. Hence, the possibility remained that a close-packed system of screened counter trays, as used by us and by Broadbent and Jánossy, might introduce a bias in favour of the locally produced groups of penetrating particles sufficient to make their contribution to the measured frequency of extensive penetrating showers appreciable. However, we think that even in the events recorded by our apparatus, the penetrating particles originate mainly in the air also, for the following reasons.

We will first form an estimate of the frequency with which the known spectrum of extensive showers containing penetrating particles would be expected to discharge the counter set P (Figure 1) in the absence of an upper absorber ($T=0$). Using three trays of screened counters, Ise and Fretter find that the frequency $F(x)$ of extensive showers in which the penetrating particle density is greater than x is given by an expression similar to that established for the totality of particles in the showers $F(x)=Kx^{-\gamma}$ with $\gamma=1{\cdot}65$.

Let $C_n(S)$ be the frequency of coincidences in n screened counter trays of area S, and S_1 and S_2 the area of counter trays used by Ise and Fretter and ourselves respectively. Then the frequency of twofold coincidences between the two lower trays b_1, b_2, of our set would be given by (cf. Ise and Fretter 1949)

$$C_2(S_2)=1{\cdot}28C_3(S_1)\left(\frac{S_2}{S_1}\right)^{\gamma}\frac{(2^{\gamma}-2)}{(3.2^{\gamma}-3^{\gamma}-3)} \qquad \ldots\ldots(8)$$

the factor 1·28 expressing the effect of the difference in height of the two observations. This gives $C_2(S_2)=1{\cdot}75$ counts per hour at the Jungfraujoch.

The cloud chamber observations of Brown and McKay (1949) have shown that the penetrating particles in the extensive showers are mostly concentrated near the vertical, and given that the separation between the middle and bottom trays of the counter set (Figure 1) was 22 cm., a rough calculation based on the angular distribution found by them gives the result that 0·75 of the penetrating particles crossing the bottom tray would cross the middle one also, and thus the estimated frequency of fourfold coincidences in our trays (m_1, m_2, b_1, b_2,) is $0{\cdot}75 \times 1{\cdot}75 = 1{\cdot}3$ per hour.

It is now necessary to estimate in how many of these fourfold coincidences the unscreened counter trays would be discharged also. Bearing in mind that the mean density of electrons in the showers is of the order 50 times that of the penetrating particles, and that two penetrating particles must arrive within an area of 0·1 m^2 to be recorded, it is clear that the mean density of the electrons accompanying the particular penetrating showers considered will be high, of the order of 1,000 per m^2, and that the probability that the unscreened trays will also be discharged will be close to unity. A detailed calculation gives 0·9 for this probability, and hence the figure for the expected rate of recording extensive penetrating showers with an apparatus at the Jungfraujoch, produced by the known spectra of hard and soft particles, is $0{\cdot}9 \times 1{\cdot}3 = 1{\cdot}2$ per hour. A similar calculation gives for the expected sea-level figure 0·13 per hour (cf. Cocconi, Tongiorgi and Greisen 1949). The observed frequencies were 1·4 and 0·09 per hour respectively, and it is seen that there is no difficulty in understanding the observed shower frequencies under the assumption that the particles are mainly produced in the air, with the density-spectrum as given by the authors quoted above.

The above view is further supported by the very small transition maxima observed with $T = 2$ cm. Pb. This result can be readily understood in the light of the high electron density already existing in the recorded showers. The increase in particle density brought about by such an absorber would be hardly expected to increase much the probability of discharge of all the unshielded trays, since this probability is already approximately 0·9. For comparison we might mention that the threefold coincidences (t_1, t_2, t_3) in the top tray alone increased by a factor of 7 for $T = 2$ cm. Pb, as expected for the more frequent, lower density showers. Again, the absence of any observed effect produced by the height of the top absorber (Figure 3 (*b*)), is consistent with the suggested origin of the coincidences observed. If the penetrating particles were generated locally in the top absorber, then since, if they are to be recorded by the lower trays they must diverge sufficiently, a height effect similar to that observed for the local showers would be expected. The statistical accuracy of the results in Figure 3 (*b*) is rather limited, and the possibility of a local production of penetrating particles in 10 to 15% of the events recorded could not be eliminated, but it would be rather difficult to maintain that a very significant contribution to the recorded coincidences is produced by such locally produced particles.

§ 8. DISCUSSION OF RESULTS FOR LOCAL PENETRATING SHOWERS

The influence of the absorber geometry raises a difficulty in the interpretation of all counter experiments on penetrating showers, where absorbers sufficiently thick to eliminate electron cascade showers are necessarily used. Furthermore, the range of the initiating particles is about 100 to 200 gm/cm^2, which means that the showers will only be produced with reasonable efficiency in further thick layers of material; this introduces more complication into the geometrical factors. Two more features of the local showers revealed by cloud chamber studies, which must be borne in mind when discussing the results of counter experiments, are the frequent occurrence of electrons at all depths in addition to penetrating particles, and the occurrence of the successive production of penetrating particles.

It would appear that a counter system such as we have used, when responding to local penetrating showers, is in general discharged by the electrons produced near the top tray at the initial encounter of the primary, and near the lower trays by the successive nuclear encounters of the penetrating particles in the shower. The penetrating particles play the rôle of carrying the electronic radiation through thick layers of lead or other absorber, but are not necessarily responsible themselves for the counter discharges observed, cf. Birger *et al.* (1949).

The reduction in counting rate on raising the top absorber would then follow from two causes: the loss of penetrating particles carrying electron cascades through the lower block of absorbers, and the reduction of the electrons through the top tray. Since the electron accompaniment is usually rather dense, it is likely that the former would have the greater effect. This would account for the qualitative difference in the dependence of the local and the extensive showers on the height of the top absorber, though it is nevertheless likely that the two types of shower are very similar, the only difference lying in the point of origin of the shower: the top absorber or the air respectively.

The transition curve for local showers can be understood along the following lines. Initially, with no absorber over the top tray, ($T=0$) shower primary particles are incident on the apparatus and generate penetrating showers in the lower lead absorbers, causing fourfold coincidences in the middle and bottom trays. It is known that the secondary particles are frequently scattered in the backward direction, and these will sometimes discharge the top tray giving the observed background rate, as suggested by J. G. Wilson (cf. Broadbent and Jánossy 1947). With the increase of the thickness, T, of the top absorber, the primaries will make their first encounter above the top tray, which will be discharged mainly by the ensuing electrons. The same primary or its penetrating but strongly interacting progeny will proceed and cause further showers in the lower fixed lead absorbers, discharging the middle and bottom counter trays. Butler *et al.* (1949) have recently reported that about half of the ionizing penetrating particles of showers formed in lead are likely to be protons. The transition curves, Figure 4, would be principally explained by the increasing probability of discharge of the top tray by the electron accompaniment, the subsequent fall at about 200 gm/cm^2 by the loss of penetrating carriers from the lower absorber. A similar explanation of the later decline of the transition curve has been advanced by Meyer *et al.* (1949), though no attempt was made by them to allow for this loss. Our method of doing so has been outlined in §6, and we will now discuss the results obtained. The approximate equality of the height b of the corrected transition curves for Pb and Al would have the trivial explanation that the density of electron accompaniment is sufficient to saturate the top tray independently of the nature of the transition material. This precludes drawing conclusions concerning the multiplicity of meson production from the shape of the transition curves.

The ranges for the occurrence of a collision in lead are found to be different at the two altitudes, although the accuracy is not high. Cocconi (1949) has found the collision length to be the same at sea level and at Echo Lake, and we will take the mean of our two results as giving the most probable value of the collision length in lead, viz. 200 ± 40 gm. This, and the values for aluminium and paraffin must then be reduced by a further 10% due to the absorption of the background rate, a, in the presence of the top absorbers. Our final figures for the collision lengths in local absorbers are: Pb, 180 ± 40 gm/cm^2; Al, 85 ± 15 gm/cm^2; Paraffin ~ 80 gm/cm^2.

These figures are all close to the range given by the geometric cross section, and are all smaller than the absorption lengths found for the star primaries by us and by Bernadini (1949), also tabulated in Figure 6. Collision lengths of the local shower primaries have been reported as follows: Tinlot (1948) 300 gm/cm^2 Pb; Cocconi (1949) 160 gm/cm^2 Pb, 100 gm/cm^2 C; Fretter (1949) ~ 170 gm/cm^2 Pb. It is likely that Tinlot's figure would be too large, due to loss of events in the counter system for the geometric reasons discussed above. The above figures, and ours, seem to be in agreement that the collision length is roughly given by the geometric cross section.

More recently, Walker (1950) has shown that the range is a function of the energy of the shower (selected on a basis of multiplicity). High energy showers were found by him to correspond to a primary range of 150 gm/cm^2 Pb, lower energy local showers having a longer primary range. Our results appear consistent with this, in that we were selecting penetrating showers of high energy.

Rossi (1948) has indicated the importance of distinguishing between the collision length L_c and the absorption length L_A of events in cosmic rays ascribed to nucleons (i.e. penetrating showers and stars). Jánossy and Heitler have shown on theoretical grounds that L_c should be given by the geometric cross section, and that L_A is expected to be about $2L_c$.

The collision lengths reported here are in agreement with this view, as also are the absorption lengths of the star primaries. It is also further supported by the absorption length in air which appears to be nearly equal to $2L_c$.

Concerning the absence of penetrating showers below ground, we can of course only set an upper limit to the reduction in frequency, from the sea-level value, of about 300 : 1. This is derived from the fact that with $T = 5$ cm. Pb, as used below ground, then in the 40 days of observation about 300 local showers would have been observed at sea level. Recently, the production of small groups of penetrating particles in the same underground laboratory has been reported by George and Trent (1949). However, the primary particles of these events are hardly likely to be nucleons, and the absence of nucleon cascades would reduce considerably the efficiency of our counter system for recording these penetrating groups compared with the type of shower recorded above ground. The occurrence of penetrating secondaries was found to be less frequent than that of knock-on electrons, and hence these apparent penetrating showers would not have been recorded in our apparatus during its sensitive time. A further attempt is being made to detect penetrating showers below ground using a counter system of lower multiplicity, which it is hoped will have considerably greater chances of recording sparse groups of mesons.

§ 9. CONCLUSIONS

The results of this investigation, taken in conjunction with those of other investigators, lead to the following conclusions concerning penetrating showers:

(i) The cross section for the production of penetrating showers is close to the geometric nuclear cross section, while the cross section for the absorption of the radiation producing the showers is about one half of this value.

(ii) The disposition of the absorbers has a marked effect on the transition curves of the local showers.

(iii) The reduction in frequency of the showers recorded by our apparatus below ground is large: more than 300 times smaller than the sea-level frequency.

(iv) The penetrating particles in the extensive showers are not produced locally in the absorbers to any marked extent.

ACKNOWLEDGMENTS

We would like to express our thanks to Professor Bernal for his continuous support of the investigations, and to Professor Blackett and Dr. Wilson for much helpful criticism in the preparation of this paper. We are greatly indebted to Professors Jánossy and Heitler for discussions concerning collisions in nuclear matter, and to Professors C. F. Powell and K. Greisen for communicating to us unpublished results. The investigation was made possible by a grant from the Department of Scientific and Industrial Research.

We would like to thank Professor von Muralt for enabling us to carry out the investigations at the Jungfraujoch, and we are particularly indebted to Herr Wiederkehr for much assistance there. The sea-level and underground observations were made with the kind co-operation of the University of London authorities and the London Transport Executive respectively.

APPENDIX I.

KNOCK-ON SHOWERS

The expected number of sevenfold coincidences in P, due to knock-on showers, was evaluated by observing coincidences in various tray combinations. The results are collected in Tables 7 (*a*) and 7 (*b*) :

Table 7 (*a*) Knock-on Showers Underground. $T=5$ cm. Pb

Description	Symbol	Rate/hour	Knock-on probability %
$(t_1+t_2+t_3, b_1+b_2)$	R_1	400	
$(t_1+t_2+t_3, m_1+m_2)$	R_2	960	
$(t_1+t_2+t_3, b_1, b_2)$	R_3	15	$\alpha_b=3{\cdot}7$
$(t_1+t_2+t_3, m_1, m_2)$	R_4	55	$\alpha_m=5{\cdot}7$
$(t_1+t_2+t_3, m_1, m_2, b_1, b_2)$	R_5	0·64	$\alpha_{mb}=0{\cdot}16$
(t_1, t_2, t_3, m_1+m_2)	R_6	7·1	$\alpha_t=0{\cdot}74$
(t_1, t_2, t_3, b_1+b_2)	R_7	2	$\alpha_t=0{\cdot}5$

Table 7 (*b*) Knock-on Showers at Sea Level. $T=5$ cm. Pb

Description	Symbol	Rate/hour	Knock-on probability %
$(t_1+t_2+t_3, b_1+b_2)$	R_1	6000	
$(t_1+t_2+t_3, m_1+m_2)$	R_2	12300	
$(t_1+t_2+t_3, b_1, b_2)$	R_3	148	$\alpha_b=2{\cdot}5$
$(t_1+t_2+t_3, m_1, m_2)$	R_4	396	$\alpha_m=3{\cdot}1$
$(t_1+t_2+t_3, m_1, m_2, b_1, b_2)$	R_5	2·75	$\alpha_{mb}=0{\cdot}046$
(t_1, t_2, t_3, m_1+m_2)	R_6	46	$\alpha_t=0{\cdot}37$
(t_1, t_2, t_3, b_1+b_2)	R_7	18	$\alpha_t=0{\cdot}3$

In the above tables, $(t_1+t_2+t_3, b_1+b_2)$ means twofold coincidences between the top bank made up of t_1, t_2 and t_3 in parallel and the bottom bank consisting of b_1 and b_2 in parallel. Similarly (t_1, t_2, t_3, b_1+b_2) means fourfold coincidences between t_1, t_2, t_3, and b_1+b_2 in parallel. Then, $\alpha_b = R_3/R_1$, gives the probability per meson of producing a knock-on electron near the bottom tray and is found to be 3·7% underground and 2·5% at sea level. Similarly, the knock-on probabilities for the middle tray, $\alpha_m = R_4/R_2$ are 5·7 and 3·1% respectively. The knock-on probabilities are expected to be greater below ground due to hardening of the meson beam (Bhabha 1938). With the top counters in parallel, a meson can produce a secondary electron near the middle and bottom trays, giving rise to a fivefold coincidence R_5. The calculated probability for this event is α_b^2 which agrees reasonably well in each case with the observed value α_{mb}.

The expected triple knock-on rates, which would give sevenfold coincidences not caused by genuine penetrating showers is given by $R_1 \times \alpha_b^2 \times \alpha_t$, which has the value $2{\cdot}7 \times 10^{-3}$ per hour underground and 0·01 per hour at sea level.

APPENDIX II

THE DENSITY OF SHOWER PARTICLES

In § 6, the assumption was made that the distribution of particles in the local penetrating showers was the same at the Jungfraujoch and at sea level. This was checked in the following manner.

Nuclear research photographic plates*, sensitive to particles at minimum ionization were exposed to the cosmic radiation at these two places. In these plates, nuclear disintegrations are sometimes found to be accompanied by showers of thin tracks (Brown *et al.* 1949 a, b). These events have been assumed by these authors, and by Heitler and Jánossy, to be examples of the production of penetrating showers, and we will make the same assumption.

Table 8. Particle Density in Penetrating Showers observed in Photographic Plates

θ (degrees)	25	37	45	53	60	66
ρ (Jungfraujoch)	3·0 ±0·7	2·5 ±0·45	2·05 ±0·33	1·8 ±0·25	1·6 ±0·24	1·4 ±0·2
ρ (sea level)	2·4 ±0·8	2·1 ±0·56	1·9 ±0·4	1·5 ±0·3	1·4 ±0·3	1·25 ±0·25

The following measurements were performed on a series of stars associated with three or more tracks with ionization less than 1·5 times minimum, selected at random from the two batches of plates. The direction in space of all the shower particles associated with a given star was determined, and a unit vector ascribed to each shower particle. The resultant of all these unit vectors was determined, giving the centre of gravity on the axis of the shower. The angular distribution of the shower particles referred to the shower axis was determined. This was repeated for all the showers, and the results averaged to give the mean particle distribution round the shower axis. The mean density per shower of the particles within a cone of semi-angle θ from the axis was then determined. The results are tabulated in Table 8, in which it is seen that the mean density of the shower particles at sea level does not differ significantly from that at the Jungfraujoch. The small difference observed may easily be due to statistical fluctuations, but in any case, if it is real, it is sufficiently small to have a negligible effect on the correction for absorber geometry discussed in §6.

---

* Ilford type G5 and Kodak type NT4.

ρ is the density of particles per steradian within a cone of semi-angle θ round the shower axis. The errors express the standard deviations of the number of particles recorded within the direction θ.

The dependence of ρ on θ appears to agree reasonably well with the results reported by Brown *et al.* (1949 b) although we are not able to compare the absolute values of ρ. The absolute values are similar to those determined from cloud chamber observations of penetrating showers (cf. Fretter 1949, Butler *et al.* 1950).

REFERENCES

Alekseev, D. M., Zatsepin, G. T., and Morozov, I. G., 1948, *Dokl. Akad. Nauk., USSR.*, **63,** 375.

Auger, P., Daudin, J., Fréon, A., and Maze, R., 1948, *C. R. Acad. Sci., Paris*, **226,** 169.

Bernadini, G., 1949, *Cosmic Radiation* (London: Butterworth Scientific Publications).

Bhabha, H. J., 1938, *Proc. Roy. Soc.* A, **164,** 357.

Birger, N. G., Veksler, V. I., Dobrotin, G. T., Zatsepin, G. T., Kurnasova, L. V., Ljubimov, A. L., Rozental, I. L., and Eidus, L. K., 1949, *J. Exp. Theor. Phys.*, **19,** 826.

Broadbent, D., and Jánossy, L., 1947, *Proc. Roy. Soc.* A, **190,** 497; 1948, *Ibid.*, **192,** 364.

Brown, R. H., Camerini, U., Fowler, P. H., Muirhead, H., Powell, C. F., and Ritson, D. M., 1949 a, *Nature, Lond.*, **163,** 47.

Brown, R. H., Camerini, U., Fowler, P. H., Heitler, H., King, D. T., and Powell, C.F., 1949 b, *Phil. Mag.*, **40,** 862.

Brown, W. W., and McKay, A. S., 1949, *Phys. Rev.*, **76,** 1034.

Butler, C. C., Rosser, W. V. G., and Barker, K. H., 1950, *Proc. Phys. Soc.* A, **63,** 145.

Cocconi, G., 1949, *Phys. Rev.*, **76,** 984.

Cocconi, G., and Greisen, K., 1948, *Phys. Rev.*, **74,** 62.

Cocconi, G., Tongiorgi, V., Greisen, K., 1949 a, *Phys. Rev.*, **75,** 1063; 1949 b, *Ibid.*, **76,** 1020.

Fretter, W. B., 1948, *Phys. Rev.*, **73,** 41; 1949, *Ibid.*, **76,** 511.

George, E. P., and Jason, A. C., 1949, *Cosmic Radiation* (London: Butterworth Scientific Publications).

George, E. P., and Trent, P. T., 1949, *Nature, Lond.*, **164,** 838.

Heitler, W., and Jánossy, L., 1949, *Proc. Phys. Soc.* A, **62,** 374.

Ise, J., and Fretter, W. B., 1949, *Phys. Rev.*, **76,** 933.

Jánossy, L., 1942, *Proc. Roy. Soc.* A, **179,** 361.

Jánossy, L., and Rochester, G. D., 1944 a, *Proc. Roy. Soc.* A, **183,** 181; 1944 b, *Ibid.*, **183,** 186.

Meyer, H. A., Schwachheim, G., Wataghin, A., and Wataghin, G., 1949, *Phys. Rev.*, **76,** 598.

Rossi, B., 1948, *Rev. Mod. Phys.*, **20,** 537.

Salvini, G., and Tagliaferri, G., 1948, *Phys. Rev.*, **73,** 261.

Tinlot, J., 1948, *Phys. Rev.*, **73,** 1476.

Tinlot, J., and Gregory, B., 1949, *Phys. Rev.*, **75,** 519.

Walker, W. D., 1950, *Phys. Rev.*, **77,** 686.

Wataghin, G., 1947, *Phys. Rev.*, **71,** 453.

Slow Mesons in the Backward Flux of the Cosmic Radiation

By D. M. RITSON
Dublin Institute for Advanced Studies

Communicated by L. Jánossy; MS. received 25th May 1950

ABSTRACT. Using the method of 'delayed coincidences' measurements have been made at sea level on the flux of slow mesons travelling backwards from the ground.

---

§1. INTRODUCTION

Extensive observations have been made on the flux of slow mesons in the cosmic radiation with both counter and photographic plate technique (cf. for instance Kraushaar 1949, Camerini *et al.* 1948). One feature of the measurements with the photographic plate has been the presence of an appreciable flux of mesons arising from the ground beneath the plates. As this has not hitherto been confirmed by counter measurements, we have made measurements on this backward flux using conventional delayed coincidence methods.

§2. EXPERIMENTAL ARRANGEMENT

The experimental arrangement is shown in the Figure, and is similar in type to that described by Rossi *et al.* (1947). The set consisted of four trays of counters A, B, C, D. Trays A and B both consisted of five counters, each of active area $3\cdot4\times25$ cm. Trays C and D consisted of nine and ten counters respectively of active area $3\cdot4\times50$ cm. The absorber S_3 consisted of 50 gm/cm^2 of lead. The absorber S_2 was 5 gm/cm^2 of paraffin wax, and the absorber S_1 consisted of lead and could be varied from 0–50 gm/cm^2 of lead.

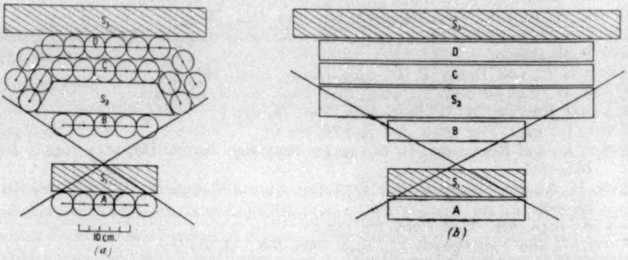

Delayed coincidence apparatus used for measuring the backward flux of slow mesons.

The apparatus recorded coincidences $[AB-(C+D)]$, $CD_{\rm del}$; i.e. prompt coincidence between trays A and B unaccompanied by a prompt coincidence in either trays C or D, and followed by a delayed coincidence CD. The resolving times were as follows: The resolving time of each of the channels AB and CD was 2 μsec., the anticoincidence channel was operative from 2 μsec. before to 12 μsec. after AB coincidence, and the delayed channel recorded coincidences from 1·5–6·5 μsec. after AB coincidences.

§3. RESULTS

The results of the experiments are summarized in the Table. Column (3) gives the observed rates $[\mathrm{AB}-(\mathrm{C}+\mathrm{D})]$, $\mathrm{CD}_{\mathrm{del}}$. Column (4) gives the delayed coincidence rates corrected for the random rate. The random rate is obtained quite simply from the $[\mathrm{AB}-(\mathrm{C}+\mathrm{D})]$ rate and the CD rate, and is given by the resolving time $\mathrm{T}\times[\mathrm{AB}-(\mathrm{C}+\mathrm{D})]\times\mathrm{CD}$. The correction due to spurious delays in counter trays C and D was negligible. Column (5) gives values of twice the ratio of the backward to forward flux.

The AB and CD and $[\mathrm{AB}-(\mathrm{C}+\mathrm{D})]$ rates were measured throughout the experiment at daily intervals, the AB and CD rates being 140 per min. and 950 per min. respectively.

(1)	(2)	(3)	(4)	(5)
Downward flux				
0 cm.	12	2·55 ±0·2	2·50 ±0·2	—
Backward flux				
0 cm.	7·5	0·155±0·22	0·117±0·022	0·094±0·018
2·5 cm.	4·9	0·073±0·016	0·050±0·016	0·040±0·012
5 cm.	4·7	0·052±0·013	0·030±0·013	0·024±0·010

(1) Thickness of S_1 (cm. lead); (2) $\mathrm{AB}-(\mathrm{C}+\mathrm{D})$ rate (per min.); (3) $[\mathrm{AB}-(\mathrm{C}+\mathrm{D})]$, $\mathrm{CD}_{\mathrm{del}}$ uncorrected rate (per hr.); (4) $[\mathrm{AB}-(\mathrm{C}+\mathrm{D})]$, $\mathrm{CD}_{\mathrm{del}}$ corrected for casual rate (per hr.); (5) twice ratio of the backward to forward flux.

Note. The values have been corrected for the failure of one counter in tray C during the course of the experiment.

§4. DISCUSSION AND COMPARISON WITH OTHER EXPERIMENTS

The genuine coincidences $[\mathrm{AB}-(\mathrm{C}+\mathrm{D})]$, $\mathrm{CD}_{\mathrm{del}}$ can be due to: (*a*) a meson traversing trays AB, stopping in the absorber S_2 and emitting a 'delayed' particle; (*b*) a penetrating shower event formed in S_2 by a neutral primary and giving rise to a meson stopping in S_2; (*c*) a penetrating shower formed in absorber S_1 by a neutral primary and giving rise to a meson in the backward direction.

The use of a very thin absorber made events of type (*b*) unlikely. Events of type (*c*) are likely to be a small fraction of the events of the same type due to showers in the ground under the apparatus. We therefore believe that the majority of genuine delayed coincidences were in fact due to mesons travelling away from the ground

The results given in the Table show that the backward mesons must on the whole have comparatively low energies, the majority being cut out by an absorber thickness S_1 of 5 cm. of lead. This is consistent with their origin in 'nuclear' showers in the ground, for high energy mesons can only be emitted at small angles to the direction of the primary nucleon, whereas low energy mesons can be emitted at large angles and thus constitute a backward flux.

Comparison of the results can be made with those obtained in photographic plate measurements at 12,000 ft. (Camerini **et al.** 1948). The photographic plate results lead to values of the backward flux of the order of $0\cdot25\pm0\cdot05$ of the downward flux. These measurements also indicate that the backward flux consists predominantly of π-mesons whereas the downward flux is composed of μ-mesons. μ-mesons both positive and negative will decay when stopped in a paraffin absorber. On the other hand only positive π-mesons will eventually be able to give rise to decay electrons, negative π-mesons suffering nuclear capture. We thus consider the true ratios of the intensity of backward or forward mesons to be given approximately by twice our observed ratios.

Our result for this true ratio $0{\cdot}09 \pm 0{\cdot}02$, determined in the absence of absorber S_1 has increased to about $0{\cdot}25 \pm 0{\cdot}05$ at a height of 12,000 ft. as determined by the photographic plate. The downward flux increases by a factor of 4 (Rossi 1948, Sands 1950) between these altitudes and thus the backward flux must increase by a factor of 10 ± 2. An increase in the intensity of this magnitude corresponds to a mean free path of 160 ± 20 gm/cm^2 of the primaries.

This is of course similar to the mean free path of 140 gm/cm^2 for the component producing the ' stars ' in the photographic plate. The predominance of π-mesons in the backward component (Camerini *et al.* 1948), the rapid increase of intensity with height, and the low energies of the mesons, all strongly indicate their origin in local nuclear interactions.

As a check on the correct functioning of our apparatus we calculated the absolute downward flux of mesons taking into account the geometry and the efficiency of our apparatus. The calculated value, with estimated error due to the uncertainties inherent in the correction factor is $3{\cdot}5 \pm 0{\cdot}5 \times 10^{-6}$ gm^{-1} sterad^{-1} sec^{-1} under 10 gm/cm^2 of absorber (roof). The value obtained from extrapolation of higher energy values is $4{\cdot}5 \times 10^{-6}$ gm^{-1} sterad^{-1} sec^{-1} (Rossi 1948, and further discussed by Kraushaar 1949 and Sands 1950). The agreement is reasonably satisfactory for this type of measurement.

The framework of the apparatus was mounted so that it could be turned round a horizontal axis through 180°; thus the apparatus could be turned upside down for reading the downward flux of slow mesons.

Assuming, on the basis of our results, that the average range of the backward mesons corresponds to 25 gm/cm^2 of lead, we obtain a ratio of the total backward to forward flux of the order of 2×10^{-4} at sea level.

ACKNOWLEDGMENTS

The author is grateful to the Dublin Institute for Advanced Studies for the provision of a research scholarship, to Professor Jánossy for discussion throughout the course of the work, to Professor McCusker and Mr. Millar for help in the running of the apparatus, and to Mr. Daly for his work in the construction of the apparatus.

REFERENCES

Camerini, U., Muirhead, H., Powell, C. F., and Ritson, D. M., 1948, *Nature, Lond.*, **162,** 433.

Kraushaar, W. L., 1949, *Phys. Rev.*, **76,** 1045.

Rossi, B., 1948, *Rev. Mod. Phys.*, **20,** 537.

Rossi, B., Sands, M., and Sard, R. D., 1947, *Phys. Rev.*, **72,** 120.

Sands, M., 1950, *Phys. Rev.*, **77,** 180.

Fluctuations of the Electron-Photon Cascade—Moments of the Distribution

By L. JÁNOSSY and H. MESSEL
Dublin Institute for Advanced Studies

MS. received 31*st March* 1950

ABSTRACT. The second moments of the electron-photon cascades are evaluated. It is found that the mean square fluctuation at the cascade maximum is that expected for a Poisson distribution or less; before and after the maximum the fluctuation exceeds greatly that expected for a Poisson distribution. The correlation coefficient between electrons and photons is zero for small thicknesses or near the cascade maximum. For other regions the correlation coefficient is positive. Both mean square fluctuation and correlation between electrons and photons can be understood qualitatively in terms of fluctuation of effective depth.

---

§ 1. INTRODUCTION

In a previous paper (Jánossy 1950) it was shown that a cascade can be represented by the following set of equations :

$$G^{(i)}(\epsilon, u_1, u_2, \zeta) = \sum_{n_1, n_2=0}^{\infty} \phi^{(i)}(\epsilon, n_1, n_2, \zeta) u_1^{n_1} u_2^{n_2}, \qquad \ldots\ldots(1)$$

where $\phi^{(i)}(\epsilon, n_1, n_2, \zeta)$ is the probability that at a depth ζ a primary of energy E_0 has given rise to n_1 electrons and n_2 photons with energies above $E = \epsilon E_0$ and also to an arbitrary number of electrons and photons with energies less than E. The index i refers to the nature of the primary: $i=1$ to an electron primary and $i=2$ to a photon primary.

Considering the 'approximation A' the $G^{(i)}$'s satisfy the following set of equations:

$$\frac{G^{(i)}(\epsilon, \zeta)}{\partial \zeta} = \int_0^1 \left\{ G^{(i)}\left(\frac{\epsilon}{1-\epsilon'}, \zeta\right) G^{(3-i)}\left(\frac{\epsilon}{\epsilon'}, \zeta\right) - G^{(i)}(\epsilon, \zeta) \right\} w^{(i)}(\epsilon')\, d\epsilon'. \qquad \ldots\ldots(2)$$

$$i = 1, 2.$$

The variables u_1 and u_2 were omitted for simplicity. The initial condition imposed on the $G^{(i)}$'s can be written

$$G^{(i)}(\epsilon, \zeta=0) = \left\{ \begin{array}{ll} u_i & \epsilon \leqslant 1, \\ 1 & \epsilon > 1. \end{array} \right\} \qquad \ldots\ldots(3)$$

Inserting (3) into (2) we find immediately

$$\left. \begin{array}{llll} G^{(i)}(\epsilon, \zeta) = 1 & \text{for} & \epsilon > 1, & \text{any } u_1, u_2, \\ G^{(i)}(\epsilon, \zeta) = 1 & \text{for} & \epsilon \leqslant 1, & u_1 = u_2 = 1. \end{array} \right\} \qquad \ldots\ldots(4)$$

Except for the trivial solutions (4) the equation (2) does not admit of simple solutions. As equation (2) is essentially non-linear the usual methods employed to solve diffusion equations of the cascade theory fail. However, there exist certain linear equations which can be derived from (2) and in the present paper we investigate such equations.

§ 2. MOMENTS

The first order moments of the cascade distribution can be defined as

$$S^{(i,k)}(\epsilon,\zeta)=\left(\frac{\partial G^{(i)}(\epsilon,\zeta)}{\partial u_k}\right)_{u_1=u_2=1} \qquad \ldots\ldots(5)$$

$$i,k=1,2.$$

The four functions $S^{(i,k)}$ represent average numbers in the following manner:

Table 1

	$\bar{n}$	$\bar{m}$
Primary electron	$S^{(1,1)}$	$S^{(1,2)}$
Primary photon	$S^{(2,1)}$	$S^{(2,2)}$

$\bar{n}$ is the average number of electrons, and
$\bar{m}$ the average number of photons.

Similarly second order moments can be defined as follows :

$$T^{(i,k,l)}(\epsilon,\zeta)=\left(\frac{\partial G^{(i)}(\epsilon,\zeta)}{\partial u_k \partial u_l}\right)_{u_1=u_2=1} \qquad \ldots\ldots(6)$$

$$i,k,l=1,2.$$

It follows from (6) that $T^{(i,k,l)}=T^{(i,l,k)}$, thus only six of the eight moments are different. These six moments represent the mean square numbers of photons and electrons and also the correlation coefficient between electrons and photons. We can tabulate the meanings of the T's as follows :

Table 2

	$\overline{n(n-1)}$	$\overline{n\,m}$	$\overline{m(m-1)}$
Primary electron	$T^{(1,1,1)}$	$T^{(1,1,2)}$	$T^{(1,2,2)}$
Primary photon	$T^{(2,1,1)}$	$T^{(2,1,2)}$	$T^{(2,2,2)}$

Physically we are not so much interested in the second moments themselves but in deviations from the average. We introduce therefore apart from the T's the following quantities :

$$\sigma^{(i,k,l)}=T^{(i,k,l)}-S^{(i,k)}S^{(i,l)}. \qquad \ldots\ldots(6\,a)$$

As is well known the σ's have the following significance :

Table 3

	$\overline{\delta n^2}-\bar{n}$	$\overline{\delta n\,\delta m}$	$\overline{\delta m^2}-\bar{m}$
Primary electron	$\sigma^{(1,1,1)}$	$\sigma^{(1,1,2)}$	$\sigma^{(1,2,2)}$
Primary photon	$\sigma^{(2,2,1)}$	$\sigma^{(2,1,2)}$	$\sigma^{(2,2,2)}$

with $\delta n=n-\bar{n}$, $\delta m=m-\bar{m}$. The σ's in the first and third column represent deviations from the Poisson distribution.

For the consideration of higher moments a notation somewhat different from (5) and (6) is of advantage. We may write

$$\overline{n^{\alpha}m^{\beta}}=S^{(i;\ \alpha\beta)}(\epsilon,\zeta)=\left(\frac{\partial^{\alpha+\beta}G^{(i)}(\epsilon,\zeta)}{(\partial \log u_1)^{\alpha}\,(\log u_2)^{\beta}}\right)_{u_1=u_2=1}. \qquad \ldots\ldots(6\,b)$$

§3. DIFFUSION EQUATIONS FOR FIRST ORDER MOMENTS

Differentiating (2) with respect to u_k, $k=1$ or 2, and putting afterwards $u_1=u_2=1$ we find with help of (4) and (5)

$$\frac{\partial S^{(i,k)}(\epsilon,\zeta)}{\partial\zeta}=\int_0^1\left\{S^{(1,k)}\left(\frac{\epsilon}{1-\epsilon'},\zeta\right)+S^{(3-i,k)}\left(\frac{\epsilon}{\epsilon'},\zeta\right)-S^{(i,k)}(\epsilon)\right\}w^{(i)}(\epsilon')\,d\epsilon'. \qquad \ldots\ldots(7)$$

Equation (7) is somewhat similar to the diffusion equation which usually is taken as starting point of the cascade theory; it differs however in the following points from the usual equations :

(i) Equation (7) refers to integral spectra and not to differential spectra.

(ii) In equation (7) $S^{(1,k)}$ and $S^{(2,k)}$ for fixed k obey a set of simultaneous equations, while in the older treatment simultaneous equations for $S^{(i,1)}$ and $S^{(i,2)}$ are given.

In spite of the above differences the solutions of (7) are, as they must be, identical with the well-known solutions of the old treatment. So as to get the solution of (7), following Landau and Rumer (1938), we take the Mellin transform of (7). Introducing

$$\int_0^1 \epsilon^{s-1}S^{(i,k)}(\epsilon,\zeta)d\epsilon=P^{(i,k)}(s,\zeta) \qquad \ldots\ldots(8)$$

we find

$$\frac{\partial P^{(i,k)}(s,\zeta)}{\partial\zeta}=\sum_l A_{il}(s)P^{(l,k)}(s,\zeta) \qquad \ldots\ldots(9)$$

with

$$\left.\begin{aligned}
A_{11}(s)&=-\int_0^1[1-(1-\epsilon)^s]w^{(1)}(\epsilon)\,d\epsilon=-A(s+1),\\
A_{12}(s)&=\int_0^1\epsilon^s w^{(1)}(\epsilon)d\epsilon=C(s+1),\\
A_{21}(s)&=2\int_0^1\epsilon^s w^{(2)}(\epsilon)\,d\epsilon=B(s+1),\\
A_{22}(s)&=-\int_0^1 w^{(2)}(\epsilon)\,d\epsilon=-D.
\end{aligned}\right\} \qquad \ldots\ldots(10)$$

The expressions on the very right of (10) are those used in the old version; thus (10) shows the connection between our coefficients A_{ik} and the well-known quantities A, B, C, D.

The solutions of (9) can be written as

$$P^{(i,k)}(s,\zeta)=\sum_{\nu=1}^{2}M_\nu^{(i,k)}(s)\exp\{-\lambda_\nu(s)\zeta\}/s \qquad \ldots\ldots(11)$$

the coefficients $M_\nu^{(i,k)}(s)$ have to be chosen suitably and $\lambda_1(s)$ and $\lambda_2(s)$ are the characteristic exponents of (9); thus they are the roots of the following equation for λ :

$$|A_{ik}+\lambda\delta_{ik}|=0. \qquad \ldots\ldots(12)$$

As usual we postulate $\lambda_1\leqslant\lambda_2$ for $s>0$. From (4) and (5) we get as our initial condition

$$S^{(i,k)}(\epsilon,0)=\delta_{ik}. \qquad \ldots\ldots(13)$$

Thus

$$P^{(i,k)}(s,0)=\delta_{ik}/s. \qquad \ldots\ldots(14)$$

Inserting (11) into (9) we find with help of (14)

$$M_\nu^{(i,k)}(s)=(A^*_{ik}+\delta_{ik}\lambda_\nu)/(\lambda_1-\lambda_2) \qquad \ldots\ldots(15)$$

with

$$A^*_{ik}=(-)^{i+k}A_{3-k,\,3-i}.$$

As an example, we have with help of (10)

$$M_1^{(1,1)}(s)=-\frac{A_{22}+\lambda_1}{\lambda_2-\lambda_1}=\left(\frac{D-a_1}{a_2-a_1}\right)_{s+1}.$$

Thus the M's are the usual coefficients. Taking the inverse transform of (11) we have finally

$$S^{(i,k)}(\epsilon,\zeta)=\frac{1}{2\pi i}\sum_\nu\int_{s_0-i\infty}^{s_0+i\infty}\epsilon^{-s}M_\nu^{(i,k)}(s)\exp\{-\lambda_\nu(s)\zeta\}ds/s. \qquad \ldots\ldots(16)$$

§ 4. EVALUATION OF THE SECOND MOMENTS

Differentiating (2) with respect to u_k and u_l and putting $u_1=u_2=1$ after differentiations, we find with help of (4), (5) and (6)

$$\frac{\partial T^{(i,k,l)}(\epsilon,\zeta)}{\partial\zeta}=\int_0^1\left\{T^{(i,k,l)}\left(\frac{\epsilon}{1-\epsilon'},\zeta\right)+T^{(3-i,k,l)}\left(\frac{\epsilon}{\epsilon'},\zeta\right)\right.$$
$$\left.-T^{(i,k,l)}(\epsilon,\zeta)\right\}w^{(i)}(\epsilon')\,d\epsilon'+f^{(i,k,l)}(\epsilon,\zeta), \qquad \ldots\ldots(17)$$

where

$$f^{(i,k,l)}(\epsilon,\zeta)=\sum_{(k,l)}\int_0^1 S^{(1,k)}\left(\frac{\epsilon}{1-\epsilon'},\zeta\right)S^{(3-i,l)}\left(\frac{\epsilon}{\epsilon'},\zeta\right)w^{(i)}(\epsilon')\,d\epsilon'. \qquad \ldots\ldots(18)$$

$\sum_{(k,l)}$ shall signify a summation over the permutations of k and l, e.g.

$$\sum_{(k,l)}A_{kl}=A_{kl}+A_{lk}.$$

The above equations are equivalent to equations obtained by Scott and Uhlenbeck (1942) except that the full Bethe–Heitler cross sections have been used by us. Bhabha and Ramakrishnan have found equations equivalent to (17) and (18) by a method different from that given here†.

We introduce

$$\left.\begin{aligned}\int_0^1\epsilon^{s-1}T^{(i,k,l)}(\epsilon,\zeta)\,d\epsilon&=Q^{(i,k,l)}(s,\zeta),\\ \int_0^1\epsilon^{s-1}f^{(i,k,l)}(\epsilon,\zeta)\,d\epsilon&=F^{(i,k,l)}(s,\zeta).\end{aligned}\right\} \qquad \ldots\ldots(19)$$

The Mellin transform of (17) can thus be written (cf. (9))

$$\frac{\partial Q^{(i,k,l)}(s,\zeta)}{\partial\zeta}=\sum_m A_{im}Q^{(m,k,l)}(s,\zeta)+F^{(i,k,l)}(s,\zeta). \qquad \ldots\ldots(20)$$

Equation (20) is the inhomogeneous counterpart to (9). The solutions of (20) can thus be expressed in terms of the solutions of (9). From (3), (6) and (19) we obtain the initial condition

$$Q^{(i,k,l)}(s,\zeta=0)=0, \qquad \ldots\ldots(21)$$

---

† We are greatly indebted to Mr. Ramakrishnan for communicating unpublished results.

and the corresponding solution of (20) can be written as

$$Q^{(i,k,l)}(s,\zeta)=\sum_m \int_0^\zeta sP^{(i,m)}(s,\zeta-z)F^{(m,k,l)}(s,z)\,dz. \qquad \ldots\ldots(22)$$

Inserting (22) into (20) it is easily verified that (22) is indeed the correct solution.

§5. EXPLICIT EXPRESSION FOR THE SECOND MOMENTS

Taking the reverse transform of (22) we find

$$T^{(i,k,l)}(\epsilon,\zeta)=\frac{1}{2\pi i}\int_{s_0-i\infty}^{s_0+i\infty} s\epsilon^{-s}\,ds\int_0^\zeta P^{(i,m)}(s,\zeta-z)F^{(m,k,l)}(s,z)\,dz. \qquad \ldots\ldots(23)$$

We express $P^{(i,m)}$ and $F^{(m,k,l)}$ in terms of the moments $S^{(i,k)}$. With help of (8), (18) and (19) we find

$$T^{(i,k,l)}(\epsilon,\zeta)=\frac{1}{2\pi i}\sum_m\sum_{(k,l)}\int_{s_0-i\infty}^{s_0+i\infty} s\epsilon^{-s}\,ds\int_0^\zeta dz\int_0^1 \eta^{s-1}S^{(i,m)}(\eta,\zeta-z)\,d\eta\int_0^1 \eta'^{s-1}d\eta'$$
$$\times\int_0^1 S^{(1,k)}\left(\frac{\eta'}{1-\epsilon'},z\right)S^{(3-m,l)}\left(\frac{\epsilon'}{\eta'},z\right)w^{(m)}(\epsilon')\,d\epsilon'. \qquad \ldots\ldots(24)$$

We note that

$$\int_0^1 s\eta^{s-1}S^{(i,m)}(\eta,\zeta)\,d\eta=-\int_0^1 \eta^s\frac{\partial S^{(i,m)}(\eta,\zeta)}{\partial\eta}\,d\eta$$

for real $s>1$. Introducing this into (24) we can carry out the integration into s. Collecting all the factors containing s we have

$$\frac{1}{2\pi i}\int_{s_0-i\infty}^{s_0+i\infty}\left(\frac{\epsilon}{\eta\eta'}\right)^{-s}ds=\delta\left(1-\frac{\epsilon}{\eta'\eta}\right).$$

Further, integrating over η, we find after introducing $\epsilon''=\epsilon/\eta'$ as a new variable

$$T^{(i,k,l)}(\epsilon,\zeta)=-\sum_m\sum_{(k,l)}\int_0^1\int_0^\zeta\frac{\partial S^{(i,m)}(\epsilon'',\zeta-z)}{\partial\epsilon''}\int_0^1 S^{(1,k)}\left(\frac{\epsilon}{\epsilon''(1-\epsilon')},z\right)$$
$$\times S^{(3-m,l)}\left(\frac{\epsilon}{\epsilon''\epsilon'},z\right)w^{(m)}(\epsilon')\,d\epsilon'\,d\epsilon''\,dz. \qquad \ldots\ldots(25)$$

The equation (25) shows that the second moments can be expressed as integrals over the first moments. This is an interesting property of the moments. Actually (25) can be generalized for higher moments. Using the notation (6 *a*) the following equation can be shown to hold:

$$S^{(i,\alpha,\beta)}(\epsilon,\zeta)=\sum_m\int_0^1\int_0^\zeta\frac{\partial S^{(i,m)}(\epsilon'',\zeta-z)}{\partial\epsilon''}\,d\epsilon''\,dz\sum_{\alpha'=1}^{\alpha-1}\sum_{\beta'=1}^{\beta-1}\binom{\alpha}{\alpha'}\binom{\beta}{\beta'}\int_0^1 S^{(1,\alpha',\beta')}$$
$$\times\left(\frac{\epsilon}{\epsilon''(1-\epsilon')},z\right)S^{(3-m;\alpha-\alpha',\beta-\beta')}\left(\frac{\epsilon}{\epsilon''}\right)w^{(m)}(\epsilon')\,d\epsilon'. \qquad \ldots\ldots(25\,a)$$

Equation (25) is not suitable for the numerical evaluation of the moments as its application requires threefold integration. Also the numerical value of (25) depends critically on values of $S(\epsilon,\zeta)$ $\epsilon\simeq 1$; the usual approximations for

$S(\epsilon, \zeta)$ are inaccurate in this region. In order to obtain more suitable expressions we introduce the values for the S's from (16) into (25). The integrations into z can be carried out and we have

$$T^{(i,k,l)}(\epsilon,\zeta) = +\frac{1}{(2\pi i)^3} \sum_{\substack{m,\nu_1\\ \nu_2,\nu_3}} \sum_{(k,l)} \int_{s_0-i\infty}^{s_0+i\infty} ds \int_{r_0-i\infty}^{r_0+i\infty} \frac{dr}{r}\epsilon^{-r}$$

$$\times \int_{t_0-i\infty}^{t_0+i\infty} \frac{dt}{t}\epsilon^{-t} M_{\nu_1}{}^{(i,m)}(s) M_{\nu_2}{}^{(1,k)}(r) M_{\nu_3}{}^{(3-m,l)}(t) W^{(m)}(r,t)$$

$$\times \frac{\exp\{-\lambda_{\nu_1}(s)\zeta\} - \exp\{-[\lambda_{\nu_2}(r)+\lambda_{\nu_3}(t)]\zeta\}}{\lambda_{\nu_2}(r)+\lambda_{\nu_3}(t)-\lambda_{\nu_1}(s)} \int_0^1 \epsilon''^{-s+r+t+1}\, d\epsilon'',$$

where
$$W^{(m)}(r,t) = \int_0^1 \epsilon^r (1-\epsilon)^t w^{(m)}(\epsilon)\, d\epsilon.$$

We carry out the integrations into ϵ'' and s. These two integrations have the effect of replacing s by $r+t$. Thus

$$T^{(i,k,l)}(\epsilon,\zeta) = \frac{1}{(2\pi i)^2} \int_{r_0-i\infty}^{r_0+i\infty} \int_{t_0-i\infty}^{t_0+i\infty} \epsilon^{-r-t} H^{(i,k,l)}(r,t)\, dr\, dt,$$

$$H^{(i\,k,l)}(r,t) = \sum_{\substack{m,\nu_1\\ \nu_2,\nu_3}} \sum_{(k,l)} M_{\nu_1}{}^{(i,m)}(r+t) M_{\nu_2}{}^{(1,k)}(r) M_{\nu_3}{}^{(3-m,l)}(t) W^{(m)}(r,t)$$

$$\times \frac{\exp\{-\lambda_{\nu_1}(r+t)\zeta\} - \exp\{-[\lambda_{\nu_2}(r)+\lambda_{\nu_3}(t)]\zeta\}}{\lambda_{\nu_2}(r)+\lambda_{\nu_3}(t)-\lambda_{\nu_1}(r+t)} \frac{1}{rt}. \qquad \ldots\ldots(26)$$

An expression equivalent to (26) for $i=k=l=1$ was given by Scott and Uhlenbeck (1942).

§ 6. NUMERICAL EVALUATION OF THE MOMENTS

(i) *Double Saddle Point Integration*

The integral (26) can be evaluated approximately by the saddle point method. Note that on account of the summations we have

$$H^{(i,k,l)}(t,r) = H^{(i,k,l)}(r,t). \qquad \ldots\ldots(27)$$

Further for $r=t \to 0$, $H(r,t)$ tends to infinity. Thus for $\epsilon \geqslant 1$ the integrand taken along the line $r=t$ tends towards infinity both for $r \to 0$ or $r \to \infty$. As the integrand is positive in this region it must have at least one minimum along this line. On account of (27) a minimum for $r=t$ is simultaneously an extremum in both variables r and t. Actually one finds that there is one such extremum only and that it is a minimum.

So as to apply the saddle point method we may put $r_0 = t_0$ and require

$$\log \epsilon = \left(\frac{\partial \log H(t,r)}{\partial r}\right)_{t=r=r_0}, \qquad \ldots\ldots(28)$$

we drop for simplicity the index (i,k,l) where it is unimportant. Equation (28), which is the saddle-point condition, can also be used to give the value of ϵ for which the saddle point is situated at an arbitrarily given point $r=t=r_0$.

The saddle point integration can be carried out in the usual way ; neglecting terms of the third order in the expansion of H around the saddle point we find

$$T^{(i,k,l)}(\epsilon,\zeta)=\frac{H^{(i,k,l)}(r_0,r_0)}{2\pi(ac-b^2)^{1/2}} \qquad \ldots\ldots(29)$$

with

$$\left.\begin{aligned} a=\frac{\partial^2 \log H^{(i,k,l)}(r,t)}{\partial r^2}, \qquad b=\frac{\partial^2 \log H^{(i,k,l)}(r,t)}{\partial r\,\partial t}, \\ c=\frac{\partial^2 \log H^{(i,k,l)}(r,t)}{\partial t^2}, \end{aligned}\right\} \ldots\ldots(30)$$

all derivatives to be taken for $r=t=r_0$; on account of the symmetry we have $a=c$; (29) is only valid if $ac>b^2$ as otherwise the extremum of $H(r,t)$ is not a minimum. This condition is however always fulfilled in the cases under consideration. The values of the derivatives (30) can be found by numerical differentiation. In this way (28), (29) and (30) give a parametric representation of $T^{(i,k,l)}(\epsilon,\zeta)$.

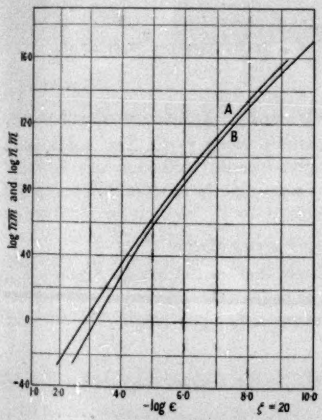

Figure 1. The logarithm of the mixed moment $\overline{nm}$ and the logarithm of the product of the first moments $\bar{m}$ and $\bar{n}$ for a depth $\zeta=20$ cascade units. A : log $\overline{nm}$. B : log $\bar{n}\,\bar{m}$.

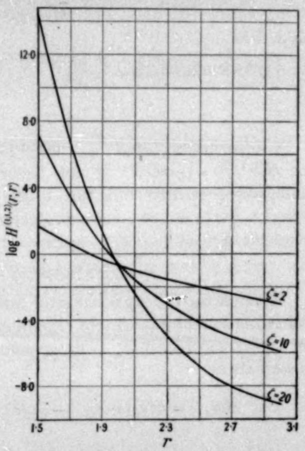

Figure 2. A plot of the logarithm of $H^{(1,1,2)}$ (r,r) as defined by equation (26) for depths $\zeta=2$, 10, and 20 cascade units.

We have carried out the rather lengthy computation for the mixed moment $T^{(1,1,2)}(\epsilon,\zeta)=\overline{nm}$ for various values of ζ ; the result of the computation for $\zeta=20$ is shown in Figure 1. We have also plotted in Figure 1 for the sake of comparison the values of $S^{(1,1)}(\epsilon,\zeta)\,S^{(1,2)}(\epsilon,\zeta)=\bar{n}\bar{m}$. The latter are taken from tables computed recently.* In Figure 2 log $H^{(1,1,2)}(r,r)$ is plotted as a function of r for $\zeta=2, 10, 20$.

From Figure 1 we see that the difference $\sigma=\overline{nm}-\bar{n}\,\bar{m}$ is not large. We cannot, however, infer with safety the actual value of σ, as the errors of both $\bar{n}\,\bar{m}$ and $\overline{nm}$ arising from the saddle point integrations are of the same order of magnitude as their difference. In order to evaluate the physically important σ's directly, instead of computing first approximations for $\overline{nm}$ and $\bar{n}\,\bar{m}$ a new procedure had to be employed.

---

* L. Jánossy and H. Messel ; circulated by the Dublin Institute for Advanced Studies (1949).

Note that $\bar{n}\,\bar{m}$ can be represented as a double complex integral not unlike $\overline{nm}$, namely

$$\left.\begin{aligned} \bar{n}\,\bar{m} &= S^{(1,1)}(\epsilon,\zeta)S^{(1,2)}(\epsilon,\zeta) \\ &= \frac{1}{(2\pi i)^2}\int_{r_0-i\infty}^{r_0+i\infty}\int_{t_0-i\infty}^{t_0+i\infty} \epsilon^{-r-t}h(r,t)\,dr\,dt \end{aligned}\right\} \qquad \ldots\ldots(31)$$

with

$$h(r,t) = \sum_{\nu_1,\nu_2} M_{\nu_1}{}^{(1,1)}(r)M_{\nu_2}{}^{(1,2)}(t)\exp\{-[\lambda_{\nu_1}(r)+\lambda_{\nu_2}(t)]\zeta\}\,\frac{1}{rt}. \qquad \ldots\ldots(32)$$

We may replace $h(r,t)$ by the symmetrical function

$$\bar{h}(r,t) = \tfrac{1}{2}\{h(r,t)+h(t,r)\}$$

and find

$$\sigma^{(1,1,2)} = \overline{nm} - \bar{n}\,\bar{m} = \frac{1}{(2\pi i)^2}\int_{r_0-i\infty}^{r_0+i\infty}\int_{t_0-i\infty}^{t_0+i\infty} \epsilon^{-r-t}(H^{(1,1,2)}(r,t)-\bar{h}(r,t))\,dr\,dt. \qquad \ldots\ldots(33)$$

The integral (33) can be evaluated precisely as (27). A difficulty arises however, as $H^{(1,1,2)}(r,t)-\bar{h}(r,t)$ is not positive definite along $r=t$. The saddle-point integration is therefore not quite straightforward. Although this difficulty can be overcome we have preferred to use a slightly modified procedure for evaluating (33).

(ii) *Method of Slowly Varying Factor*

Evaluating $H(r,t)$ it is found immediately that for not too small values of ζ, all terms containing λ_2 in the exponent can be neglected. This reduces the number of terms considerably. The remaining terms are of two types. We can write schematically

$$H(r,t) = A(r,t)\exp\{-(\lambda_1(r)+\lambda_1(t))\zeta\} + B(r,t)\exp\{-\lambda_1(r+t)\zeta\}. \qquad \ldots\ldots(34)$$

The exponentials determine, as a rule, which of the two terms is the predominant one. Inspecting the numerical values it is found that

$$2\lambda_1(r) = \lambda_1(2r) \quad \text{for} \quad r = r_1 \sim 2{\cdot}6.$$

For $r<r_1$ the first term predominates while for $r>r_1$ the second predominates; this suggests that there is a qualitative change in the behaviour of the second moment with increasing r, the change setting in while r passes r_1. To see what kind of change is involved, we note that the minimum of $H(r,t)$ is largely determined by the variation of $\epsilon^{-(r+t)}$ and that of the exponentials; $A(r,t)$ and $B(r,t)$ are only slowly varying factors. Therefore for the purpose of qualitative considerations we may modify those factors without greatly changing the general behaviour of the integral. Now if we were to replace

$$\left.\begin{aligned} A(r,t) &\to M^{(i,k)}(r)M^{(i,l)}(r)/rt, \\ B(r,t) &\to M^{(i,k)}(r+t)/rt, \end{aligned}\right\} \qquad \ldots\ldots(35)$$

the integral could be evaluated immediately and we should find that the process (35) leads to the following replacement:

$$T^{(i,k,l)}(\epsilon,\zeta)\rightarrow S^{(i,k)}(\epsilon,\zeta)S^{(i,l)}(\epsilon,\zeta)+S^{(i,k)}(\epsilon,\zeta). \qquad \ldots\ldots(36)$$

The above equation sheds light in the behaviour of the second moments in a qualitative manner. *The order of magnitude of the second moment is comparable either with the square or with the first power of the first moment according to which power has the larger value.*

As $\bar{h}(r,t)$ contains terms of the same type as $H(r,t)$ the above conclusion is valid not only for the T's but also for the σ's. For the purpose of quantitative evaluation we write (cf. (11))

$$\begin{aligned}T^{(i,k,l)}(\epsilon,\zeta)=\frac{1}{(2\pi i)^2}\int_{r_0-i\infty}^{r_0+i\infty}\int_{t_0-i\infty}^{t_0+i\infty}&\Big\{\tfrac{1}{2}\sum_{(k,l)}P^{(i,k)}(r,\zeta)P^{(i,l)}(t,\zeta)\\&+\frac{r+t}{rt}P^{(i,k)}(r+t,\zeta)\Big\}K^{(i,k,l)}(r,t)\epsilon^{-r-t}dr\,dt \quad \ldots\ldots(37)\end{aligned}$$

with

$$K^{(i,k,l)}(r,t)=H^{(i,k,l)}(r,t)\Big/\Big\{\tfrac{1}{2}\sum_{(k,l)}P^{(i,k)}(r,\zeta)P^{(i,l)}(t,\zeta)+\left(\frac{r+t}{rt}\right)P^{(i,k)}(r+t,\zeta)\Big\}. \qquad \ldots\ldots(38)$$

The function $K^{(i,k,l)}(r,t)$ is stripped of all fast moving components and thus it is a *slowly varying function*. Thus evaluating the integral (37) one obtains a good approximation by taking $K^{(i,k,l)}(r,t)=K^{(i,k,l)}(r_0,r_0)$ where the saddle point is determined by the fast moving factor in the curly brackets. Thus the saddle point condition becomes

$$\log\epsilon=\tfrac{1}{2}\frac{d}{dr}\left(\log\{P^{(i,k)}(r,\zeta)P^{(i,l)}(r,\zeta)+\frac{2}{r}P^{(i,k)}(2r,\zeta)\zeta\}\right)_{r=r_0} \qquad \ldots\ldots(39)$$

and we have approximately

$$T^{(i,k,l)}(\epsilon,\zeta)=S^{(i,k)}(\epsilon,\zeta)\{1+S^{(i,l)}(\epsilon,\zeta)\}K^{(i,k,l)}(r_0,r_0). \qquad \ldots\ldots(40)$$

Equations (39) and (40) give a parametric representation of $T^{(i,k,l)}(\epsilon,\zeta)$. Similarly we can get a representation for $\sigma^{(i,k,l)}(\epsilon,\zeta)$ defined in equation (6*a*): introduce

$$\overline{H}^{(i,k,l)}(r,t)=H^{(i,k,l)}(r,t)-\tfrac{1}{2}\sum_{(k,l)}P^{(i,k)}(r,\zeta)P^{(i,l)}(t,\zeta) \qquad \ldots\ldots(41)$$

and

$$\overline{K}^{(i,k,l)}(r,t)=K^{(i,k,l)}(r,t)\overline{H}^{(i,k,l)}(r,t)/H^{(i,k,l)}(r,t).$$

We find thus

$$\sigma^{(i,k,l)}(\epsilon,\zeta)=S^{(i,k)}(\epsilon,\zeta)\{1+S^{(i,l)}(\epsilon,\zeta)\}\overline{K}^{(i,k,l)}(r_0,r_0). \qquad \ldots\ldots(42)$$

Equations (39) and (42) provide a parametric representation for the σ's.

A few numerical values of some of the functions appearing above are collected in Tables 4–8 for convenience.

Table 4. Log $H^{(1,1,2)}(r,t)$; $r=t$

r	$\zeta=2$	$\zeta=4$	$\zeta=6$	$\zeta=8$	$\zeta=10$	$\zeta=15$	$\zeta=20$
1·5	1·63472	3·05542	4·46642	5·87704	7·28765	10·81417	14·34069
1·6	1·00201	2·01834	3·01848	4·01749	5·01642	7·51373	10·01103
1·7	0·48058	1·18015	1·85631	2·52983	3·20305	4·88599	6·56893
1·8	0·03661	0·48074	0·89455	1·30329	1·71113	2·73029	3·74943
1·9	−0·35078	−0·11708	0·08079	0·27026	0·45764	0·92454	1·39122
2·0	−0·69545	−0·63788	−0·61945	−0·61320	−0·61104	−0·60997	−0·60989
2·1	−1·00709	−1·09870	−1·23006	−1·37710	−1·53091	−1·92531	−2·32318
2·2	−1·29277	−1·51184	−1·76838	−2·04292	−2·32696	−3·05546	−3·79337
2·3	−1·55781	−1·88645	−2·24749	−2·62679	−3·01737	−4·02109	−5·04404
2·4	−1·80627	−2·22945	−2·67751	−3·14148	−3·61643	−4·83475	−6·08014
2·5	−2·04125	−2·54620	−3·06650	−3·59760	−4·13669	−5·50869	−6·90364
2·6	−2·26512	−2.84089	−3·42093	−4·00421	−4·58997	−6·06188	−7·54056
2·7	−2·47978	−3·11688	−3·74616	−4·36924	−4·98756	−6·51957	−8·04075
2·8	−2·68655	−3·37678	−4·04649	−4·69942	−5·33965	−6·90656	−8·45108
2·9	−2·88651	−3·62273	−4·32552	−5·00051	−5·65508	−7·24261	−8·80270
3·0	−3·08044	−3·85647	−4·58626	−5·27731	−5·94109	−7·54159	−9·11391

Table 5. Log $H^{(1,1,2)}(r,t)$; $t=r-0{\cdot}2$

r	$\zeta=2$	$\zeta=4$	$\zeta=6$	$\zeta=8$	$\zeta=10$	$\zeta=15$	$\zeta=20$
1·8	0·52028	1·24746	1·95327	2·65683	3·36015	5·11837	6·87659
1·9	0·06614	0·52993	0·96531	1·39615	1·82622	2·90106	3·97586
2·0	−0·32797	−0·07971	0·13433	0·34062	0·54505	1·05480	1·56437
2·1	−0·67732	−0·60860	−0·57781	−0·55851	−0·54297	−0·50795	−0·47378
2·2	−0·99235	−1·07519	−1·19697	−1·33383	−1·47706	−1·84418	−2·21434
2·3	−1·28055	−1·49256	−1·74164	−2·00827	−2·28405	−2·99079	−3·70610
2·4	−1·54751	−1·87035	−2·22555	−2·59883	−2·98315	−3·97029	−4·97556
2·5	−1·79743	−2·21579	−2·65929	−3·11878	−3·58924	−4.79607	−6·02943
2·6	−2·03355	−2·53445	−3·05120	−3·57907	−4·11516	−5·48028	−6·86901
2·7	−2·25834	−2·83067	−3·40797	−3·98901	−4·57292	−6·04146	−7·51796
2·8	−2·47367	−3·10786	−3·73503	−4·35663	−4·97395	−6·50474	−8·02557
2·9	−2·68100	−3·36875	−4·03686	−4·68888	−5·32867	−6·89545	−8·44017

Table 6. Log $H^{(1,1,2)}(r,t)$; $t=r-0{\cdot}4$

r	$\zeta=2$	$\zeta=4$	$\zeta=6$	$\zeta=8$	$\zeta=10$	$\zeta=15$	$\zeta=20$
1·9	0·64609	1·46150	2·26157	3·06034	3·85899	5·85558	7·85218
2·0	0·15843	0·68426	1·18738	1·68737	2·18690	3·43557	4·68422
2·1	−0·25736	0·03644	0·30093	0·55945	0·81670	1·45905	2·10130
2·2	−0·62156	−0·51824	−0·44900	−0·38931	−0·33249	−0·19303	−0·05407
2·3	−0·94721	−1·00298	−1·09506	−1·20041	−1·31101	−1·59433	−1·87969
2·4	−1·24327	−1·43357	−1·65952	−1·90167	−2·15187	−2·79156	−3·43762
2·5	−1·51615	−1·82123	−2·15838	−2·51392	−2·87776	−3·81323	−4·76364
2·6	−1·77061	−2·17422	−2·60364	−3·04913	−3·50546	−4·67580	−5·87179
2·7	−2·01023	−2·49876	−3·00454	−3·52228	−4·04881	−5·39156	−6·75931
2.8	−2·23773	−2·79963	−3·36844	−3·94243	−4·52040	−5·97762	−7·44629
2·9	−2·45520	−3·08055	−3·70120	−4·31811	−4·93215	−6·45862	−7·97796
3·0	−2·66420	−3·34447	−4·00762	−4·65672	−5·29503	−6·86113	−8·40634

Table 7. $\overline{K}^{(1,1,1)}(r,r)$

r	$\zeta=2$	$\zeta=4$
1·5	0·08173	0·10919
1·6	0·03666	0·07506
1·7	−0·00393	0·04246
1·8	−0·03909	0·01186
1·9	−0·06899	−0·01592
2·0	−0·09434	−0·03983
2·1	−0·11588	−0·05890
2·2	−0·13414	−0·07250
2·3	−0·14944	−0·08056
2·4	−0·16189	−0·08357
2·5	−0·17149	−0·08245
2·6	−0·17824	−0·07835
2·7	−0·18220	−0·07239
2·8	−0·18351	−0·06551
2·9	−0·18239	−0·05842
3·0	−0·17914	−0·05161

Table 8. $\overline{K}^{(1,1,2)}(r,r)$

r	$\zeta=2$	$\zeta=4$
1·5	0·08036	0·10914
1·6	0·03046	0·07465
1·7	−0·01781	0·04086
1·8	−0·06276	0·00752
1·9	−0·10353	−0·02525
2·0	−0·14003	−0·05691
2·1	−0·17257	−0·08656
2·2	−0·20156	−0·11317
2·3	−0·22735	−0·13583
2·4	−0·25018	−0·15393
2·5	−0·27016	−0·16726
2·6	−0·28732	−0·17599
2·7	−0·30169	−0·18062
2·8	−0·31326	−0·18172
2·9	−0·32208	−0·18000
3·0	−0·32826	−0·17612

The table shows that we are justified in treating the K's as slowly varying functions. In Figures 3, 4, 5, 6 we have plotted $\sigma^{(1,1,1)}/\overline{n}(\overline{n}+1)$, and $\sigma^{(1,1,2)}/\overline{m}(\overline{n}+1)$ for various values of ϵ and ζ.

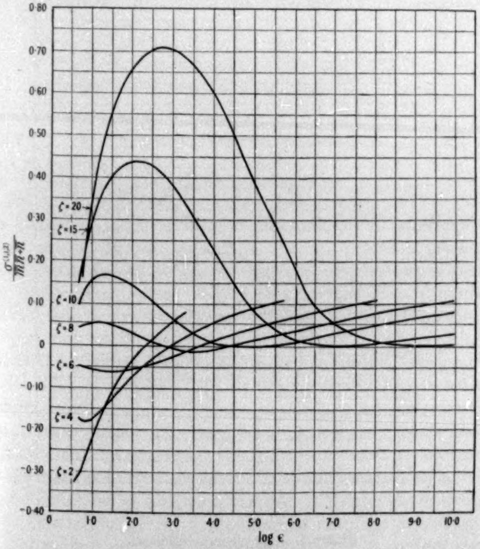

Figure 3. Standard deviation.

The plot of the coefficient $\sigma^{(1,1,2)}/(\overline{m}\,\overline{n}+\overline{n})$ for depths $\zeta=2$, 4, 6, 8, 10, 15 and 20 cascade units. The value of ζ is attached to each curve.

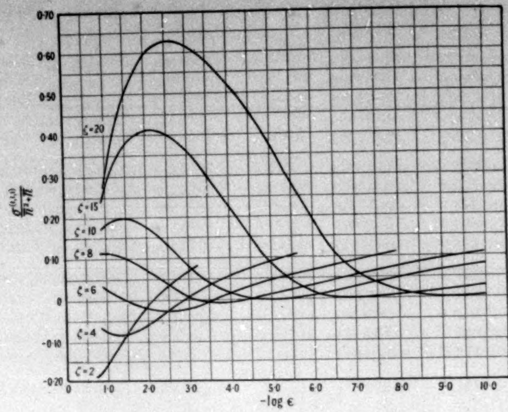

Figure 4. Standard deviation.

The plot of the coefficient $\sigma^{(1,1,1)}/(\bar{n}^2+\bar{n})$ for depths $\zeta=2, 4, 6, 8, 10, 15$ and 20 cascade units. The value of ζ is attached to each curve.

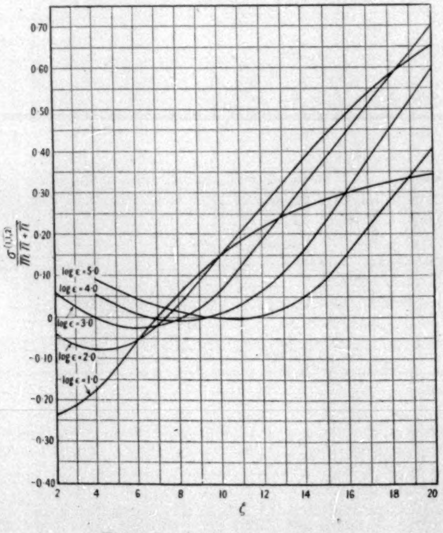

Figure 5. Correlation coefficient.

Plot of the coefficient $\sigma^{(1,1,2)}/(\bar{n}\bar{m}+\bar{n})$ for fixed energies; $-\log\epsilon=1, 2, 3, 4$ and 5. ζ is the depth in cascade units.

§ 7. DISCUSSION OF THE RESULTS

(i) *Medium Depth*

Examining Figures 5 and 6 we see that both $\sigma^{(1,1,1)}$ and $\sigma^{(1,1,2)}$ for constant ϵ show a minimum for a certain depth. The position of this minimum coincides with the cascade maximum. The minimum is not caused by the maximum of the denominator alone, as the values become slightly negative in that region. The actual dependence of the moments on the depths ζ can be easily understood in the following manner.

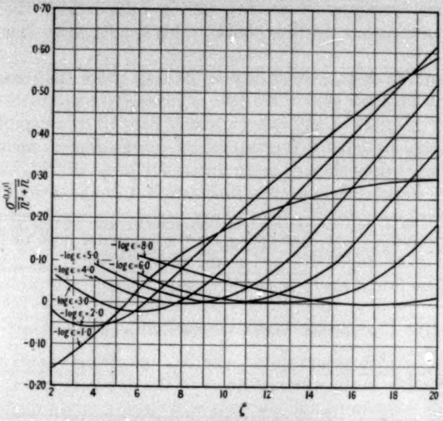

Figure 6. Standard deviation.

The plot of the coefficient $\sigma^{(1,1,1)}/(\bar{n}^2+\bar{n})$ for fixed energies; $-\log\epsilon = 1, 2, 3, 4, 5, 6$ and 8. ζ is the depth in cascade units.

The fluctuation of the total number of electrons as expressed by $\sigma^{(1,1,1)}$ is about *normal* at the cascade maximum (i.e. in accordance with a Poisson distribution); both before and after the cascade maximum the fluctuation exceeds the random fluctuation. This behaviour was already noticed by Scott and Uhlenbeck, and it can be accounted for as follows. The most important source of fluctuation is the uncertainty as to when the first few collisions will take place. If the primary happens to traverse a considerable layer of material before it suffers its first collision, then the delay will be shared by all descendants, thus the whole shower will be displaced in depth. Similarly the first collision may take place immediately after the primary enters and thus the shower may be shifted towards small thicknesses. We have therefore fluctuations which may be termed *fluctuations in effective depth*. The fluctuation of effective depth will cause a large fluctuation in numbers wherever the slope of the average curve is pronounced. Therefore we get fluctuations of numbers exceeding the normal fluctuation before and after the maximum. At the maximum itself only the intrinsic fluctuations remain and this fluctuation is about normal.

(ii) *Great Depth*

It is a remarkable feature of the cascade process that for large depth, where $\bar{n} \ll 1$, $\overline{\delta n^2}$ is of the order of $\bar{n}$ and not of the order of $\bar{n}^2$. This means that the probability of finding two particles at a great depth (and presumably that of finding several) is of the same order of magnitude as the probability of finding one particle there. This feature of the showers again demonstrates the importance of the fluctuation in effective depth. The large value of $\overline{\delta n^2}$ could not be understood if one were to regard particles at great depth as 'stragglers' of low energy left behind by chance when most of the shower had died down. Consider, for instance, two such 'stragglers': as their fate is independent, the probability of their both arriving at a great depth is considerably smaller than that of one of them arriving there.

The comparatively high probability of finding more than one particle at a great depth shows that the tail of showers is caused not so much by low energy stragglers but by particles of any energy which happen to escape from the main body of the shower by chance fluctuation of energy loss; such particles will break up into a secondary shower at an unusually large depth. In the extreme case the primary itself suffers such a fluctuation and the whole of the shower may thus be shifted to a depth where under usual circumstances no particles at all are to be expected. Note that owing to this unusual type of fluctuation the identification at great depth of the condition $\bar{n} \ll 1$ with the probability that one particle will be found there is not justified.

(iii) *Correlation between Electrons and Photons*

The sign of $\sigma^{(1,1,2)}$ determines whether electrons and photons show fluctuations preferably in the same sense or in the opposite sense. For such ϵ, ζ for which $\sigma^{(1,1,2)} > 0$ electrons and photons will show a tendency to deviate from the average in the same sense. σ is greater than zero for not too small thicknesses both before and after the maximum. At the cascade maximum itself and at very small thicknesses $\sigma^{(1,1,2)}$ is zero or negative. The positive correlation of electrons and photons both for ascent to the maximum and descent after the maximum is easily understood in terms of fluctuation of the effective depth, as explained above. At the maximum where effective depth fluctuation is of minor importance there is either no correlation between δn and δm or a slight negative correlation.

The comparatively strong correlation between electrons and photons at great depths is not surprising in view of what was said in § 7 (ii) concerning the fluctuation of electrons at great depths. At such depths the probability of the presence of two electrons is of the same order as that of one electron only; we see now that the probability of the presence of a photon is relatively high whenever there is one electron present. This further confirms the view that particles (electrons or photons) at great depths are largely caused by particles of any energies escaping out of the main body of the shower and breaking up later than usual.

The correlation is negative between electrons and photons for small depths and especially for high values of ϵ. This can be understood immediately. Consider first the extreme case of $\epsilon > \frac{1}{2}$. On account of the conservation law we cannot have an electron and photon both with energies greater than $\frac{1}{2}E_0$. Thus there is an absolute exclusion and therefore negative correlation. Apart from this extreme case it is plausible that for not too small values of ϵ an increased number of electrons should mainly arise on account of a deficiency of photons and vice versa ; a negative correlation is thus to be expected. The fact that at most depths the correlation is in fact positive is probably caused by the strong positive correlation arising from the fluctuation of effective depth, this fluctuation being parallel for electrons and photons.

The above discussion shows that a great deal of information can be derived as to the fluctuation processes from the consideration of first and second moments only. We hope to complete these considerations in a later publication where we intend to deal with the general solutions of equation (2).

REFERENCES

Jánossy, L., 1950, *Proc. Phys. Soc.* A, **63**, 241.
Landau, L., and Rumer, G., 1938, *Proc. Roy. Soc.* A, **166**, 213.
Scott, W. T., and Uhlenbeck, G. E., 1942, *Phys. Rev.*, **62**, 497.

The Effect of Nuclear Structure on the Elastic Scattering of Fast Electrons

By L. R. B. ELTON
University College, London

Communicated by H. S. W. Massey; *MS. received 8th March* 1950

ABSTRACT. The cross section for the scattering of electrons by atomic nuclei is investigated at energies for which the nuclei can no longer be treated as point charges. Two simple nuclear models are used. A general expression is obtained using Born's approximation, and an exact numerical calculation is carried through for 20 Mev. electrons scattered by gold nuclei. It is concluded that at this energy considerable deviations from the formulae which treat the nucleus as a point charge should be expected, and that these should furnish some information about the charge distribution within the nucleus.

§ 1. INTRODUCTION

The elastic scattering of fast electrons by atomic nuclei has been investigated theoretically by Mott (1929, 1932), and calculations by Bartlett and Watson (1940) and McKinley and Feshbach (1948) based on Mott's formulae agree well with the experimental results of Van de Graaff *et al.* (1946, 1947) and Sigrist (1943). In these calculations the scattering nucleus was taken to be a point charge, and the agreement with the experimental results shows that at the energies considered (up to 3 Mev.) this approximation was justified. At higher energies, however, the electron wavelength becomes comparable with and even smaller than the diameter of the nucleus, and scattering experiments at such energies should give information about the charge distribution within the nucleus. The present investigation is concerned with (*a*) estimating by means of Born's approximation at what energies effects due to the finite extent of the nucleus would first become measurable and (*b*) carrying through a numerical calculation at one energy for gold. Three nuclear models were used:

A. Point charge.
B. Uniform spherical charge distribution of radius R.
C. Uniform spherical shell charge distribution of radius R.

These will hereafter be referred to as cases A, B and C respectively. These letters will also appear as affixes to distinguish corresponding quantities for the three cases. The nuclear radius is taken, as given by Wheeler (1949), to be

$$R=\frac{\mathbf{e}^2}{2\mathbf{m}\mathbf{c}^2}A^{1/3},$$

where $\mathbf{m}$ and $\mathbf{e}$ are the mass and charge of the electron, $\mathbf{c}$ the velocity of light and A the mass number of the nucleus.*

§ 2. DIFFERENTIAL CROSS SECTION BY BORN'S APPROXIMATION

The differential cross section for a Dirac particle in the Born approximation is given by Mott and Massey (1949 b) as

$$I(\theta)=\frac{1-\beta^2\sin^2\theta/2}{1-\beta^2}|f(\theta)|^2,$$

where

$$f(\theta)=-\frac{2\mathbf{m}}{\hbar^2}\int_0^\infty \frac{\sin Kr}{Kr}V(r)r^2\,dr.$$

Here

$$K=2k\sin\theta/2,\quad k^2=\frac{W^2-\mathbf{m}^2\mathbf{c}^4}{\hbar^2\mathbf{c}^2}=\frac{\mathbf{m}^2v^2}{\hbar^2(1-\beta^2)},\qquad \beta=\frac{v}{\mathbf{c}},$$

and W, v and m are the total energy, the velocity and the rest mass of the particle respectively. This formula is now applied to the three types of nuclei under consideration. The integrals which occur are not convergent, because of the slow falling-off of the Coulomb field, but if each integrand is multiplied by $\exp(-\mu r)$, the limit as $\mu\to 0$ exists and is taken to be the value of the integral.

Similar formulae have already been given by Rose (1948).

Case A.

$$V(r)=-\frac{Z\mathbf{e}^2}{r}.$$

Therefore

$$f_{\mathrm{A}}(\theta)=\frac{Z\mathbf{e}^2(1-\beta^2)}{2mv^2}\operatorname{cosec}^2\frac{\theta}{2}.$$

Case B.

$$V(r)=\begin{cases}-\dfrac{Z\mathbf{e}^2}{R}\left(\dfrac{3}{2}-\dfrac{r^2}{2R^2}\right), & r<R.\\[2ex] -\dfrac{Z\mathbf{e}^2}{r}\qquad\qquad, & r\geqslant R.\end{cases}$$

Therefore

$$f_{\mathrm{B}}(\theta)=\frac{2\mathbf{m}Z\mathbf{e}^2}{K\hbar^2}\left\{\int_0^R\frac{1}{R}\left(\frac{3}{2}-\frac{r^2}{2R^2}\right)r\sin Kr\,dr+\int_R^\infty \sin Kr\,dr\right\}$$

$$=\frac{3}{K^3R^3}(\sin KR-KR\cos KR)f_{\mathrm{A}}(\theta).$$

---

* Since these calculations were completed, Lu (1950) has advocated a radius of $r_0A^{1/3}$, where $r_0=1{\cdot}47\times10^{-13}$ cm. for case B and $r_0=1{\cdot}34\times10^{-13}$ cm. for case C, as against the value $r_0=\mathbf{e}^2/2\mathbf{m}\mathbf{c}^2=1{\cdot}41\times10^{-13}$ cm. which has been used for both cases in the present calculation. Clearly, if his values are used, any effects due to the finite extent of the nucleus will be slightly increased in case B and slightly decreased in case C.

Case C.
$$V(r)=\begin{cases} -\dfrac{Ze^2}{R}, & r<R. \\ -\dfrac{Ze^2}{r}, & r\geqslant R. \end{cases}$$

Therefore

$$f_{\mathrm{C}}(\theta)=\frac{2mZe^2}{K\hbar^2}\left\{\int_0^R \frac{r}{R}\sin Kr\,dr+\int_R^\infty \sin Kr\,dr\right\}$$
$$=\frac{\sin KR}{KR}f_{\mathrm{A}}(\theta).$$

That the Born approximation is invalid for any but the lightest nuclei ($Z\lesssim 15$) can be seen from the calculations of McKinley and Feshbach (1948). Nevertheless, it gives a useful indication as to the magnitude of the effects to be expected even for heavy nuclei, though it will underestimate them. From Table 1 it is clear that observable effects can hardly be expected for energies below 20 Mev. for heavy nuclei and for energies below 40 Mev. for light nuclei, particularly since scattering at large angles is difficult to measure because of the small intensity at these angles.

Table 1. $I_{\mathrm{B,\,C}}(\theta)/I_{\mathrm{A}}(\theta)$

Ratio of the differential cross sections for the two cases of the extended nucleus to that for the case of the point nucleus, for electrons of energy Wmc^2 being scattered by aluminium and gold nuclei, using Born's approximation.

	Aluminium : $Z=13$, $A=27$				Gold : $Z=79$, $A=197$			
θ	30°		150°		30°		150°	
	B	C	B	C	B	C	B	C
$W/mc^2=$ 5	1·00	1·00	1·00	1·00	1·00	1·00	1·00	0·99
10	1·00	1·00	1·00	0·99	1·00	1·00	0·97	0·95
20	1·00	1·00	0·96	0·94	1·00	0·98	0·87	0·79
40	1·00	0·98	0·86	0·78	0·96	0·94	0·57	0·37
80	0·96	0·94	0·55	0·35				

§ 3. EXACT CALCULATION OF THE DIFFERENTIAL CROSS SECTION

This calculation will be carried out for gold nuclei and electrons of energy $40mc^2$ ($\simeq 20$ Mev.). For gold, $Z=79$ and $R=8{\cdot}196\times10^{-13}$ cm. The theory of the scattering of electrons by a centre of force can be found in Mott and Massey (1949 a) and their notation will be largely followed here.

(i) *The Differential Cross Section*

The differential cross section is

$$I(\theta)=|f(\theta)|^2+|g(\theta)|^2, \qquad \ldots\ldots(1)$$

where

$$\left.\begin{aligned} f(\theta)&=\frac{1}{2ik}\Sigma\{(n+1)(\exp[2i\eta_n]-1)+n(\exp[2i\eta_{-n-1}]-1)\}P_n(\cos\theta),\\ g(\theta)&=\frac{1}{2ik}\Sigma\{-\exp[2i\eta_n]+\exp[2i\eta_{-n-1}]\}P_n{}'(\cos\theta), \end{aligned}\right\}\qquad \ldots\ldots(2)$$

and η_n, η_{-n-1} are the phases. Now it will be shown below that the phases for the cases of the extended nucleus and of the point nucleus differ significantly only for $n=0$ and $n=-2$. Hence the differential cross section for case B can be written

$$I_{\mathrm{B}}(\theta)=|f_{\mathrm{B}}(\theta)|^2+|g_{\mathrm{B}}(\theta)|^2, \qquad \ldots\ldots(3)$$

where

$$\left.\begin{aligned}
f_{\mathrm{B}}(\theta)&=f_{\mathrm{A}}(\theta)+\frac{1}{2ik}\{(\exp[2i\eta_0^{\mathrm{B}}]-\exp[2i\eta_0^{\mathrm{A}}])P_0(\cos\theta)\\
&\qquad+(\exp[2i\eta_{-2}^{\mathrm{B}}]-\exp[2i\eta_{-2}^{\mathrm{A}}])P_1(\cos\theta)\},\\
g_{\mathrm{B}}(\theta)&=g_{\mathrm{A}}(\theta)+\frac{1}{2ik}(\exp[2i\eta_{-2}^{\mathrm{B}}]-\exp[2i\eta_{-2}^{\mathrm{A}}])P_1'(\cos\theta),\\
f_{\mathrm{A}}(\theta)&=\frac{1}{2ik}\Sigma\{(n+1)(\exp[2i\eta_n^{\mathrm{A}}]-1)+n(\exp[2i\eta_{-n-1}^{\mathrm{A}}]-1)\}P_n(\cos\theta),\\
g_{\mathrm{A}}(\theta)&=\frac{1}{2ik}\Sigma(-\exp[2i\eta_n^{\mathrm{A}}]+\exp[2i\eta_{-n-1}^{\mathrm{A}}])P_n'(\cos\theta),
\end{aligned}\right\} \qquad \ldots\ldots(4)$$

and similarly for C. f_{A} and g_{A} are calculated from the formulae

$$\left.\begin{aligned}
kf_{\mathrm{A}}=i\gamma'F+G, \qquad kg_{\mathrm{A}}&=\{i\gamma'(1+\cos\theta)F+(1-\cos\theta)G\}\operatorname{cosec}\theta,\\
\gamma'&=\frac{Ze^2}{\hbar v}\sqrt{(1-\beta^2)},
\end{aligned}\right\} \qquad \ldots\ldots(5)$$

where F and G are found by extrapolation to the higher energy from the tables of Bartlett and Watson (1940). These have actually been calculated for the case of Hg, but there will be no significant difference for the case of Au.

(ii) *Method of Calculation of the Phase Shifts*

To find the phase shifts we have to fit the regular solutions of the two radial equations inside the nucleus to the regular and irregular solutions of the radial equations outside the nucleus. This is equivalent to the condition of continuity of charge and current.

The radial equations are

$$\left.\begin{aligned}
\frac{1}{\hbar}\left(\frac{W}{\mathbf{c}}-\frac{V}{\mathbf{c}}+m\mathbf{c}\right)R_n+\frac{dS_n}{dr}-\frac{n}{r}S_n&=0,\\
-\frac{1}{\hbar}\left(\frac{W}{\mathbf{c}}-\frac{V}{\mathbf{c}}-m\mathbf{c}\right)S_n+\frac{dR_n}{dr}+\frac{n+2}{r}R_n&=0,
\end{aligned}\right\} \qquad \ldots\ldots(6)$$

where W is the energy of the electron. By elimination of R_n we have

$$\frac{d^2S_n}{dr^2}+\left(\frac{2}{r}-\frac{\alpha'}{\alpha}\right)\frac{dS_n}{dr}+\left\{k^2-\frac{2WV}{\hbar^2\mathbf{c}^2}+\frac{V^2}{\hbar^2\mathbf{c}^2}-\frac{n(n+1)}{r^2}+\frac{n}{r}\frac{\alpha'}{\alpha}\right\}S_n=0, \qquad \ldots\ldots(7)$$

where $\alpha=\frac{1}{\hbar}\left(\frac{W}{\mathbf{c}}-\frac{V}{\mathbf{c}}+m\mathbf{c}\right), \qquad k^2=\frac{W^2-m^2\mathbf{c}^4}{\hbar^2\mathbf{c}^2},$

or, putting
$$S_n = r^{-1}\alpha^{1/2}\mathscr{S}_n,$$
$$\frac{d^2\mathscr{S}_n}{dr^2} - f_n(r)\mathscr{S}_n = 0, \qquad \ldots\ldots(8)$$
where
$$f_n(r) = -k^2 + \frac{n(n+1)}{r^2} + \frac{2WV}{\hbar^2\mathbf{c}^2} - \frac{V^2}{\hbar^2\mathbf{c}^2} - \frac{n+1}{r}\frac{\alpha'}{\alpha} + \frac{3}{4}\frac{\alpha'^2}{\alpha^2} - \frac{1}{2}\frac{\alpha''}{\alpha}.$$
Similarly for $\mathscr{R}_n = r\alpha^{-1/2}R_n$.

Corresponding to $\mathscr{R}_n$ and $\mathscr{S}_n$ let the regular solutions inside the nucleus be $\mathscr{D}_n$ and $\mathscr{K}_n$, the regular solutions outside the nucleus $\mathscr{F}_n$ and $\mathscr{G}_n$, and the irregular solutions outside the nucleus $\mathscr{E}_n$ and $\mathscr{H}_n$ respectively. Similarly D_n, K_n, F_n, G_n, E_n, H_n correspond to R_n, S_n. Then for $r = R$,
$$\left.\begin{aligned}\mathscr{K}_n &= A_n\mathscr{G}_n + B_n\mathscr{H}_n,\\ \mathscr{D}_n &= A_n\mathscr{F}_n + B_n\,\mathscr{E}_n.\end{aligned}\right\} \qquad \ldots\ldots(9)$$

Now asymptotically, in the usual notation,
$$\left.\begin{aligned}\mathscr{G}_{n,-n-1} &\sim \mu^{-1/2}\sin(kr + \gamma\ln 2kr - \tfrac{1}{2}n\pi + \eta_{n,-n-1}),\\ \mathscr{H}_{n,-n-1} &\sim \mu^{-1/2}\sin(kr + \gamma\ln 2kr - \tfrac{1}{2}n\pi + \eta_{n,-n-1} + \theta_{n,-n-1}),\end{aligned}\right\} \qquad \ldots\ldots(10)$$
where $\mu = (W + \boldsymbol{m}\mathbf{c}^2)/\hbar\mathbf{c}$, $\gamma = Z\mathbf{e}^2/\hbar v$, and the phase $\theta_{n,-n-1}$ depends on the particular irregular solution used. The required phase shift $\zeta_{n,-n-1}$ is then given by
$$A_{n,-n-1}\mathscr{G}_{n,-n-1} + B_{n,-n-1}\mathscr{H}_{n,-n-1}$$
$$\sim C_{n,-n-1}\sin(kr + \gamma\ln 2kr - \tfrac{1}{2}n\pi + \eta_{n,-n-1} + \zeta_{n,-n-1}). \qquad \ldots\ldots(11)$$
From (10) and (11),
$$\zeta_n = \tan^{-1}\frac{B_n\sin\theta_n}{A_n + B_n\cos\theta_n}. \qquad \ldots\ldots(12)$$

(iii) *Solution outside the Nucleus*

If $V = -Z\mathbf{e}^2/r$ in (3), then, for positive and negative n, the regular solution is given by Mott and Massey (1949 a) as
$$\mathscr{G}_n = \alpha^{-1/2}N_n(2kr)^{\rho_{n+1}}e^{-ikr}\{(n+1+i\gamma')F(i\gamma + \rho_{n+1} + 1, 2\rho_{n+1} + 1, 2ikr)$$
$$+ (\rho_{n+1} - i\gamma)F(\rho_{n+1} + i\gamma, 2\rho_{n+1} + 1, 2ikr)\}, \qquad \ldots\ldots(13)$$
where
$$N_n = \frac{1}{2}\frac{|\Gamma(\rho_{n+1} + 1 + i\gamma)|}{\Gamma(2\rho_{n+1} + 1)}\mathrm{e}^{\frac{1}{2}\pi\gamma}\{(i\gamma' + n + 1)(\rho_{n+1} - i\gamma)\}^{-1/2},$$
and
$$\rho_n = \sqrt{(n^2 - \lambda^2)}, \qquad \lambda = Z\mathbf{e}^2/\hbar\mathbf{c}.$$
The corresponding phase is given by
$$\left.\begin{aligned}\exp(2i\eta_n) &= \frac{n+1+i\gamma'}{\rho_{n+1} - i\gamma}\frac{\Gamma(\rho_{n+1} + 1 - i\gamma)}{\Gamma(\rho_{n+1} + 1 + i\gamma)}\exp\{-\pi i(\rho_{n+1} - n - 1)\}, \qquad n \geqslant 0.\\ \exp(2i\eta_{-n-1}) &= \frac{n - i\gamma'}{\rho_n - i\gamma}\frac{\Gamma(\rho_n + 1 - i\gamma)}{\Gamma(\rho_n + 1 + i\gamma)}\exp\{-\pi i(\rho_n - n)\}, \qquad n > 0.\end{aligned}\right\} \qquad \ldots\ldots(14)$$

Thus if
$$\mathscr{G}_n = \alpha^{-1/2} r^{\varrho_{n+1}} (a_{n0} + a_{n1} r + \ldots), \qquad \ldots\ldots(15)$$
then
$$a_{n0} = N_n (2k)^{\varrho_{n+1}} \{n + 1 + \rho_{n+1} + i(\gamma' - \gamma)\}. \qquad \ldots\ldots(16)$$
As ρ_{n+1} is not an integer, we obtain an independent irregular solution $\mathscr{H}_n$ by replacing ρ_{n+1} by $-\rho_{n+1}$ throughout. Hence
$$\mathscr{H}_n = \alpha^{-1/2} r^{-\varrho_{n+1}} (b_{n0} + b_{n1} r + \ldots), \qquad \ldots\ldots(17)$$
where
$$b_{n0} = M_n (2k)^{-\varrho_{n+1}} \{n + 1 - \rho_{n+1} + i(\gamma' - \gamma)\}, \qquad \ldots\ldots(18)$$
and M_n is obtained from N_n by replacing ρ_{n+1} by $-\rho_{n+1}$. Also
$$\exp 2i(\eta_n + \theta_n) = \frac{n + 1 + i\gamma'}{-\rho_{n+1} - i\gamma} \frac{\Gamma(-\rho_{n+1} + 1 - i\gamma)}{\Gamma(-\rho_{n+1} + 1 + i\gamma)} \exp\{-\pi i(-\rho_{n+1} - n - 1)\}, \quad n \geqslant 0,$$
and hence
$$\exp 2i\theta_n = \frac{\rho_{n+1} - i\gamma}{-\rho_{n+1} - i\gamma} \frac{\Gamma(-\rho_{n+1} + 1 - i\gamma)}{\Gamma(-\rho_{n+1} + 1 + i\gamma)} \frac{\Gamma(\rho_{n+1} + 1 + i\gamma)}{\Gamma(\rho_{n+1} + 1 - i\gamma)} \exp 2\pi i \rho_{n+1}. \qquad \ldots\ldots(19)$$
This is clearly true for negative as well as positive n.

The analytical expressions for $\mathscr{G}_n$ and $\mathscr{H}_n$ are very unsuitable for numerical calculation. Hence equation (7) was solved directly by a numerical method (Mott and Massey 1949 c). Putting $V = -Z\mathbf{e}^2/r$, (7) can be written
$$\left(\mu + \frac{\lambda}{r}\right) \frac{d^2 S_n}{dr^2} + \left(\frac{2\mu}{r} + \frac{3\lambda}{r^2}\right) \frac{dS_n}{dr} + \left\{\mu^2 \nu + \frac{\lambda\mu(\mu + 2\nu)}{r} + \frac{\lambda^2(2\mu + \nu) - n(n+1)\mu}{r^2} + \frac{\lambda^3 - n(n+2)\lambda}{r^3}\right\} S_n = 0, \qquad \ldots\ldots(20)$$
where $\mu = (W + \mathbf{mc}^2)/\hbar\mathbf{c}$, $\nu = (W - \mathbf{mc}^2)/\hbar\mathbf{c}$. The initial integration by the method of Frobenius gives
$$G_n = r^{-1+\varrho_{n+1}} \sum_{m=0}^{\infty} a_{nm} r^m, \qquad H_n = r^{-1-\varrho_{n+1}} \sum_{m=0}^{\infty} b_{nm} r^m, \qquad \ldots\ldots(21)$$
where the coefficients satisfy the recurrence relation
$$\mu^2 \nu a_{nm} + \lambda\mu(\mu + 2\nu) a_{n,m+1} + \{\lambda^2(\mu + \nu) + \mu(3 + 3\rho_{n+1} + n) + \mu(3 + 2\rho_{n+1})m + \mu m^2\} a_{n,m+2} + \lambda\{9 + 6\rho_{n+1} + (6 + 2\rho_{n+1})m + m^2\} a_{n,m+3} = 0. \qquad \ldots\ldots(22)$$

A similar relation holds for b_{nm}, if ρ_{n+1} is replaced by $-\rho_{n+1}$. The forward integration is then carried out on equation (8). This method checks itself very satisfactorily.

In calculating a_{n0} and b_{n0} the common factor $2^{-1/2} \exp(\frac{1}{2}\pi\gamma)$ can be omitted since (12) only contains the ratio A_n/B_n. Thus
$$a_{n0} = \frac{|\Gamma(\rho_{n+1} + 1 + i\gamma)|}{\sqrt{2}\,\Gamma(2\rho_{n+1} + 1)} (2k)^{\varrho_{n+1}} \frac{n + 1 + \rho_{n+1} + i(\gamma' - \gamma)}{\{(n + 1 + i\gamma')(\rho_{n+1} - i\gamma)\}^{1/2}}$$
$$= \frac{|\Gamma(\rho_{n+1} + 1 + i\gamma)|}{\Gamma(2\rho_{n+1} + 1)} (2k)^{\varrho_{n+1}} \left\{1 + \frac{(n+1)\rho_{n+1} - \gamma\gamma'}{\rho_{n+1}^2 + \gamma^2}\right\}^{1/2}, \qquad \ldots\ldots(23)$$
if numerator and denominator are multiplied by $n + 1 + \rho_{n+1} - i(\gamma' - \gamma)$, and similarly for b_{n0}.

Lastly, from (14) and (19),

$$\left.\begin{aligned} \eta_n &= \frac{\pi}{2}(n+1-\rho_{n+1})+\tfrac{1}{2}\arg(\rho_{n+1}+i\gamma)-\arg\Gamma(\rho_{n+1}+1+i\gamma) \\ &\qquad +\tfrac{1}{2}\arg(n+1+i\gamma'), \qquad n\geqslant 0, \\ \eta_{-n-1} &= \frac{\pi}{2}(n-\rho_n)+\tfrac{1}{2}\arg(\rho_n+i\gamma)-\arg\Gamma(\rho_n+1+i\gamma) \\ &\qquad -\tfrac{1}{2}\arg(n+i\gamma'), \qquad n>0, \end{aligned}\right\} \qquad \ldots\ldots(24)$$

$$\theta_n=\pi(\rho_{n+1}+\tfrac{1}{2})-\arg(\rho_{n+1}+i\gamma)+\arg\Gamma(\rho_{n+1}+1+i\gamma)-\arg\Gamma(-\rho_{n+1}+1+i\gamma). \qquad \ldots\ldots(25)$$

(iv) *Solution inside the Nucleus*

For the solutions inside the nucleus the different expressions for the potential for cases B and C must be substituted in (7).

Case B. $$V=-\frac{Ze^2}{R}\left(\frac{3}{2}-\frac{r^2}{2R^2}\right).$$

If the variable is changed to $\sigma=r^2/R^2$, equation (7) can be written

$$2(A\sigma^2-\lambda\sigma^3)\frac{d^2S_n}{d\sigma^2}+(3A\sigma-\lambda\sigma^2)\frac{dS_n}{d\sigma} + \{-\tfrac{1}{2}An(n+1)+[\tfrac{1}{2}\lambda n(n-1)+B]\sigma+C\sigma^2+D\sigma^3+E\sigma^4\}S_n=0, \qquad \ldots\ldots(26)$$

where

$$\begin{aligned} A&=2\mu R+3\lambda, \\ B&=\tfrac{1}{8}A\{4\mu\nu R^2+6\lambda R(\mu+\nu)+9\lambda^2\}, \\ C&=-\tfrac{1}{4}A\lambda\{R(\mu+\nu)+3\lambda\}-\tfrac{1}{8}\lambda\{4\mu\nu R^2+6\lambda R(\mu+\nu)+9\lambda^2\}, \\ D&=\tfrac{1}{8}A\lambda^2+\tfrac{1}{4}\lambda^2\{R(\mu+\nu)+3\lambda\}, \\ E&=-\tfrac{1}{8}\lambda^3. \end{aligned}$$

The initial integration gives for the regular solution

$$K_n^{\mathrm{B}}=\sigma^{n/2}\sum_{m=0}^{\infty}c_{nm}\sigma^m, \quad n\geqslant 0, \qquad K_n^{\mathrm{B}}=\sigma^{-(n+1)/2}\sum_{m=0}^{\infty}c_{nm}\sigma^m, \quad n<0, \qquad \ldots\ldots(27)$$

where

$$\left.\begin{aligned} &Am(2m+2n+1)c_{nm}+[B-\lambda(m-1)(2m+2n-3)]c_{n,m-1}+Cc_{n,m-2}+Dc_{n,m-3} \\ &\qquad +Ec_{n,m-4}=0, \qquad n\geqslant 0, \\ &Am(2m-2n-1)c_{nm}+[B-\lambda(m-2)(2m-2n-3)]c_{n,m-1}+Cc_{n,m-2}+Dc_{n,m-3} \\ &\qquad +Ec_{n,m-4}=0, \qquad n<0. \end{aligned}\right\} \qquad \ldots\ldots(28)$$

It is found that for the energy considered the series are sufficiently rapidly convergent for a forward integration to be unnecessary. Thus for $\sigma=1$,

$$\left.\begin{aligned}
\mathscr{K}_n^{\mathrm{B}} &= R\left(\frac{R}{\mu R+\lambda}\right)^{1/2} K_n^{\mathrm{B}},\\
\frac{d\mathscr{K}_n^{\mathrm{B}}}{dr} &= \left(\frac{R}{\mu R+\lambda}\right)^{1/2}\left\{\left[1+\frac{\lambda}{2(\mu R+\lambda)}\right]K_n^{\mathrm{B}}+2\frac{dK_n^{\mathrm{B}}}{d\sigma}\right\},\\
\frac{d^2\mathscr{K}_n^{\mathrm{B}}}{dr^2} &= \frac{1}{R}\left(\frac{R}{\mu R+\lambda}\right)^{1/2}\\
&\quad\times\left\{\left[\frac{3\lambda}{2(\mu R+\lambda)}+\frac{3\lambda^2}{4(\mu R+\lambda)^2}\right]K_n+\left(6+\frac{2\lambda}{\mu R+\lambda}\right)\frac{dK_n}{d\sigma}+4\frac{d^2K_n}{d\sigma^2}\right\}.
\end{aligned}\right\} \quad \ldots\ldots(29)$$

A check was carried out by substitution in equation (8).

Case C. $$V=-\frac{Ze^2}{R}.$$

Equation (7) becomes

$$\frac{d^2S_n}{dr^2}+\frac{2}{r}\frac{dS_n}{dr}+\left\{\kappa^2-\frac{n(n+1)}{r^2}\right\}S_n=0, \quad \ldots\ldots(30)$$

where $\kappa^2=(\mu+\lambda/R)(\nu+\lambda/R)$. The regular solution of the equation is

$$K_n^{\mathrm{C}}=\left(\frac{\pi}{2\kappa r}\right)^{1/2}J_{n+\frac{1}{2}}(\kappa r),\quad n\geqslant 0;\qquad K_n^{\mathrm{C}}=\left(\frac{\pi}{2\kappa r}\right)^{1/2}J_{-n-\frac{1}{2}}(\kappa r),\quad n<0. \quad \ldots\ldots(31)$$

Neglecting a constant factor,

$$\mathscr{K}_n^{\mathrm{C}}=rK_n^{\mathrm{C}}. \quad \ldots\ldots(32)$$

(v) *The Second Radial Equation*

From equation (6), $$\alpha R_n=\frac{n}{r}S_n-\frac{dS_n}{dr}.$$

Therefore $$\mathscr{R}_n=r\alpha^{-1/2}R_n=\frac{1}{\alpha}\left(\frac{n+1}{r}\mathscr{S}_n-\frac{1}{2}\frac{\alpha'}{\alpha}\mathscr{S}_n-\frac{d\mathscr{S}_n}{dr}\right).$$

Thus for $r=R$,

$$R\alpha\mathscr{F}_n=\left\{n+1+\frac{\lambda}{2(\mu R+\lambda)}\right\}\mathscr{G}_n-R\frac{d\mathscr{G}_n}{dr}. \quad \ldots\ldots(33)$$

The same relation holds for $\mathscr{E}_n$, $\mathscr{H}_n$ and for $\mathscr{D}_n^{\mathrm{B}}$, $\mathscr{K}_n^{\mathrm{B}}$ respectively. However, in case C,

$$R\alpha\mathscr{D}_n^{\mathrm{C}}=(n+1)\mathscr{K}_n^{\mathrm{C}}-R\frac{d\mathscr{K}_n^{\mathrm{C}}}{dr}. \quad \ldots\ldots(33')$$

(vi) *Numerical Results*

The phase shifts ζ_n were calculated for $n=0, -2, 1, -3$, and it was found that, at the energy considered, only the first two phase shifts were significant. The differential cross sections were then calculated using (3) and (4). The results of the calculations are summarized in Tables 2 and 3 and also in the Figure, where $I_B(\theta)/I_A(\theta)$ and $I_C(\theta)/I_A(\theta)$ are plotted against θ.

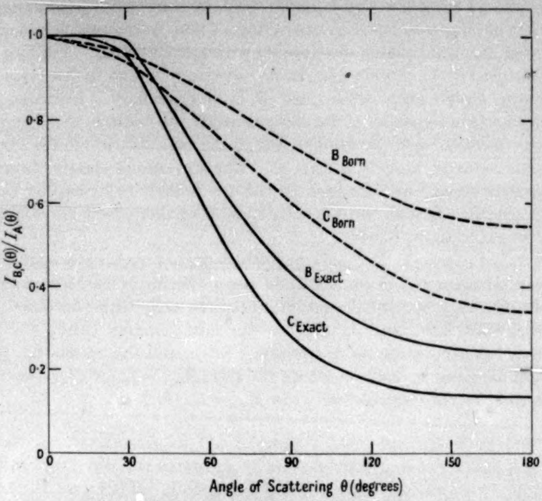

Angular distribution of the ratio of the differential cross sections for the two cases of the extended nucleus to that for the case of the point nucleus, for electrons of energy 40 $\boldsymbol{mc}^2$ being scattered by gold nuclei.

(Full line —— exact calculation, dotted line - - - Born approximation.)

Table 2

Phases η_n^A for the case of the point nucleus, and phase shifts $\zeta_n^{B,C}$ for the difference in phase between the case of the point and that of the extended nucleus, for electrons of energy 40 $\boldsymbol{mc}^2$ being scattered by gold nuclei.

n	η_n^A	$\zeta_n^B = \eta_n^B - \eta_n^A$	$\zeta = \eta_n^C - \eta_n^A$
0	0·415	−0·196	−0·271
−2	0·400	−0·195	−0·268
1	−0·234	−0·002	−0·004
−3	−0·242	−0·001	−0·004

Table 3

Differential cross sections for the case of the point nucleus and the two cases of the extended nucleus, for electrons of energy 40 $\boldsymbol{mc}^2$ being scattered by gold nuclei.

θ (deg.)	30	45	60	90	120	150	180
$k^2 I_A(\theta)$	25·608	6·489	2·543	0·638	0·186	0·0377	0·00015
$k^2 I_B(\theta)$	25·268	5·463	1·735	0·277	0·056	0·0096	0·00005
$k^2 I_C(\theta)$	24·707	5·019	1·450	0·178	0·031	0·0052	0·000018

§4. CONCLUSION

The investigation has shown that, if 20 Mev. electrons are scattered elastically by gold nuclei, considerable deviations from calculations based on the Mott formulae should occur for angles greater than about 45°, showing up most clearly in the ratio of large to small angle scattering. These deviations should give some information about the charge distribution within the nucleus. For that purpose the models used in the present calculation have been chosen so that cases A and C are extreme possibilities, while case B is intermediary. However, because of the electrostatic repulsion of the charges inside the nucleus, the charge density is likely to increase with the radius, and so the true distribution is likely to be somewhere between models B and C. The deviations should therefore not be larger than those found for case C, and are unlikely to be smaller than those found for case B. Similar but probably slightly smaller effects are to be expected for light nuclei at about 40 Mev.

Note added in proof. Recently published preliminary experimental results by Lyman, Hanson and Scott (1950) on the scattering of 16·5 Mev. electrons by Be, C, Al, Cu, Ag, Au nuclei agree quite satisfactorily with the above calculations, when these have been adjusted to the lower energy (Elton 1950). The adjustment has been made more accurately since, and the results for gold and aluminium are given in Table 4, where the ratio $R_{\mathrm{B,C}} = I_{\mathrm{B,C}}(\theta)/I_{\mathrm{A}}(\theta)$ is compared with the most recent experimental ratio $R_{\mathrm{exp}} = I_{\mathrm{exp}}(\theta)/I_{\mathrm{A}}(\theta)$.

Table 4

θ (degrees)		30			90			150		
	Z	R_{B}	R_{C}	R_{exp}	R_{B}	R_{C}	R_{exp}	R_{B}	R_{C}	R_{exp}
Al	13	1·00	0·99	0·91	0·97	0·95	0·89	0·89	0·84	1·06
Au	79	0·99	0·97	0·87	0·52	0·35	0·59	0·41	0·32	0·43

ACKNOWLEDGMENTS

The author wishes to express his sincere thanks to Professor H. S. W. Massey for his suggestion of this problem and general guidance of the work.

REFERENCES

Bartlett, J. H., and Watson, R. E., 1940, *Proc. Amer. Acad. Arts Sci.*, **74**, 53.

Elton, L. R. B., 1950, *Phys. Rev.*, **79**, 412.

Lu, H., 1950, *Phys. Rev.*, **77**, 416.

Lyman, M., Hanson, A. O., Scott, M. B., 1950, *Bull. Amer. Phys. Soc.*, **25**, 3, and private communication.

McKinley, W. A., Jr., and Feshbach, H., 1948, *Phys. Rev.*, **74**, 1759.

Mott, N. F., 1929, *Proc. Roy. Soc.* A, **124**, 426; 1932, *Ibid.*, **135**, 429.

Mott, N. F., and Massey, H. S. W., 1949, *The Theory of Atomic Collisions*, 2nd edition (Oxford: University Press), (*a*) Chapter IV, § 4; (*b*) Chapter VII, § 3, (*c*) Chapter VII, § 6.

Rose, M. E., 1948, *Phys. Rev.*, **73**, 279.

Sigrist, W., 1943, *Helv. Phys. Acta*, **16**, 471.

Van de Graaff, R. J., *et al.*, 1946, *Phys. Rev.*, **69**, 452; 1947, *Ibid.*, **72**, 678.

Wheeler, J. A., 1949, *Rev. Mod. Phys.*, **21**, 133.

Non-physical Solutions in Classical Finite Electron Theory

By J. IRVING

Department of Natural Philosophy, The University, Glasgow

Communicated by R. E. Peierls; MS. received 1st *February* 1950

ABSTRACT. An approximate linear form of the Peierls–McManus equations of motion for an electron is shown to yield runaway solutions for a particular influence function, which otherwise satisfies all the conditions imposed by the theory. The general problem is to discuss the existence of complex roots of a transcendental equation for an arbitrary form of the influence function. It is shown that this equation always has roots. These, however, may be such that the corresponding motion of the free electron is of a damped nature. It has not been found possible to construct a function which avoids runaway solutions or to prove whether or not such a function exists when all conditions are satisfied.

§ 1. INTRODUCTION

An unsatisfactory feature of the Lorentz–Dirac equations of motion for a point electron is the existence of non-physical runaway solutions (Dirac 1938, Eliezer 1943). Bohm and Weinstein (1948), however, have found distribution functions in a non-relativistic rigid electron theory, which do not lead to runaway solutions. The theory yields the result that self-oscillating motions of finite amplitude are possible for a free electron. In a relativistic theory of the McManus type, the latter kinds of motion could not occur. Since the amplitude determining the emission of real light waves is the same as for a point electron and, therefore, could not vanish, radiation would be emitted in such a motion.

The investigation in the present paper, in which an approximate form of the relativistically invariant equations of motion of Peierls and McManus (McManus 1948) is used, shows that the conditions imposed on the influence function $H(\mathbf{R}^2)$ in the development of this form of finite electron theory are not stringent enough. An explicit form of $H(\mathbf{R}^2)$ is considered, which satisfies all the conditions necessary for the derivation of the equations of motion but yields an infinite number of runaway as well as damped motions for a free electron. The function chosen results in the electromagnetic mass of the electron being positive and much smaller, if desired, than the mechanical mass. For all forms of $H(\mathbf{R}^2)$, however, self-oscillating motions of finite amplitude never arise.

The problem of the existence of non-physical solutions of the equations of motion reduces to the investigation of the complex roots of a transcendental equation, (2.2) below. The latter equation is transformed into a simple equation, (4.3), for investigation. It is then shown that the latter equation always admits solutions, but these may be such that the electron has only a damped motion, either exponential or oscillatory. We have not been able to construct a function which avoids increasing solutions or to prove whether or not such a function exists.

§2. DERIVATION OF THE GENERAL FORM OF THE TRANSCENDENTAL EQUATION AND RESTRICTIONS ON $H(\mathbf{R}^2)$

For the rectilinear motion of an electron of small velocity, $\dot{\zeta} \ll c = 1$, but whose acceleration and higher derivations of velocity may be large, the Peierls–McManus equations of motion reduce to (Irving 1949)

$$m\ddot{\zeta} - (2e^2/3)\dddot{\zeta} = 2e^2 \int_{-\infty}^{+\infty} [(\zeta - \zeta') - \dot{\zeta}'(t-t')] h\{(t-t')^2\}\, dt' + X(t), \quad \ldots\ldots (2.1)$$

where $h\{(t-t')^2\} = dH(\mathbf{R}^2)/d\mathbf{R}^2$ and $X(t)$ is the force due to the 'averaged' external field; m is the mechanical mass of the electron; $\zeta' \equiv \zeta(t')$. Thus for a free electron $X(t) = 0$ and equation (2.1) becomes a homogeneous linear integro-differential equation with the obvious solutions $\zeta = \text{constant}$ and $\dot{\zeta} = \text{constant}$. Any other solutions may be considered to be of the form $C \exp(-i\omega t)$ where ω is real or complex.

Equation (2.1) then assumes the form

$$az^2 + ibz^3 = 2 \int_{-\infty}^{+\infty} h(v^2)\{(1 + izv)\exp(izv) - 1\}\, dv. \quad \ldots\ldots (2.2)$$

We have used here dimensionless variables choosing as our unit of length the electron radius r_0, i.e. the distance over which the functions H and h are appreciable; $H(\mathbf{R}^2)$ is, in fact, a function of $\mathbf{R}^2/r_0^2$. Then the variables entering in (2.2) are, in terms of ordinary units:

$$a = mr_0/e^2, \qquad z = \omega r_0, \qquad b = 2/3, \qquad v = (t-t')/r_0, \qquad h(v^2) \equiv dH(v^2)/dv^2.$$

The 'influence' function $H(\mathbf{R}^2)$ must, in the theory of McManus, satisfy the following conditions:

(i) The four-dimensional transform of $H(\mathbf{R}^2)$ must be of the form $-16\pi^3 g^2(\mathbf{K}^2)/\mathbf{K}^2$, where g is the Fourier transform of the form function $F(\mathbf{R}^2)$. This means that the transform of $\Box H(\mathbf{R}^2)$ is of the form $16\pi^3 g^2(\mathbf{K}^2)$, and, in particular, must be positive. McManus has shown that if $H(\mathbf{R}^2)$ is the same in both the light and space cones, that is, is an even function of $\mathbf{R}^2$, then $g(\mathbf{K}^2)$ is replaced by $g(|\mathbf{K}^2|)$ in the transform of $H(\mathbf{R}^2)$. Also, since $g(0) = (2\pi)^{-2}$, we must have $\int_{-\infty}^{+\infty} H(\mathbf{R}^2)\, d\mathbf{R}^2 = 1$, and if H is even, $\int_0^{\infty} H(\mathbf{R}^2)\, d\mathbf{R}^2 = 1/2$.

(ii) For convergence of the integrals in (2.2), when z is purely imaginary or complex, $h(v^2)$ must fall off more rapidly than $\exp(zv)$ for any z. If the integral in (2.2) diverges, it is no longer justified to replace the general equation of motion by its linearized form (2.1).*

The method adopted for finding the number of roots and the regions in which they lie involves the principle of the 'argument theorem' (Phillips 1940). The change in the argument of $w = f(z)$ is found from the contour described in the w-plane, corresponding to the boundary of the region of the z-plane, within which the existence of roots of the equation $f(z) = 0$ is being considered.

---

* The more precise form of the equation of motion, as given by McManus, is less likely to diverge because there is a limit to the velocity and this will mean that the influence function can bring down the integrand sufficiently rapidly for convergence. For a value of z which is not purely imaginary the integrand of (2.2) is of an oscillatory character, and it is reasonable to assume that the more exact equations of motion may lead to the same result as working out the integral (2.2) for values of z for which it converges and then using analytic continuation.

From equation (2.2), since $h(v^2)$ is always a real function, so that the integral is real for real z, it follows that $z=0$ is the only possible real root of the equation. Thus, self-oscillating motions of finite amplitude are never possible for any real $H(\mathbf{R}^2)$.

§ 3. EXAMPLE: DISCUSSION OF A PARTICULAR INFLUENCE FUNCTION

In this section a particular form of $H(\mathbf{R}^2)$, which satisfies all the conditions of §2, is considered. This function, namely

$$H(\mathbf{R}^2)=(1/2r_0^4)\int_{|\mathbf{R}^2/r_0^2|}^{\infty}\exp(-y)/y\,dy,$$

corresponds to

$$H(v^2)=A\int_{v^2}^{\infty}\exp(-u)/u\,du. \qquad \ldots\ldots(3.1)$$

Then

$$h(v^2)=-A\exp(-v^2)/v^2. \qquad \ldots\ldots(3.1\,a)$$

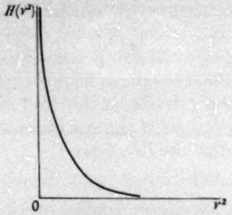

Figure 1. The influence function $H(v^2)$ (qualitative).

Since we may assume $H(v^2)=H(-v^2)$, we then have, for normalization, $2\int_0^{\infty}H(v^2)\,dv^2=1$, using units in which $r_0=1$, and

$$H(v^2)=-\int_{v^2}^{\infty}h(v'^2)\,dv'^2.$$

Hence

$$2\int_0^{\infty}H(v^2)\,dv^2=-8\int_0^{\infty}h(v'^2)v'\,dv'\int_0^{v'}v\,dv=-4\int_0^{\infty}v'^3h(v'^2)\,dv'=1. \qquad \ldots\ldots(3.2)$$

Substitution of expression (3.1*a*) gives $A=1/2$.

The electromagnetic mass $m_e=(e^2/r_0)\int_0^{\infty}H(v^2)\,dv$. (McManus 1948).

Hence

$$m_e=-(2e^2/r_0)\int_0^{\infty}v'^2h(v'^2)\,dv'. \qquad \ldots\ldots(3.3)$$

Therefore, using (3.1 *a*), $m_e=\sqrt{\pi}e^2/2r_0$. Equation (2.2) takes the form

$$az^2+ibz^3=-\int_{-\infty}^{+\infty}[(1+izv)\exp(-izv)-1]\exp(-v^2)\,dv=-Y(z),\ \text{say}.$$

Now

$$dY(z)/dz=\int_{-\infty}^{+\infty}z\exp(-v^2-izv)\,dv=\sqrt{\pi}z\exp(-z^2/4),$$

hence

$$Y(z)=2\sqrt{\pi}\{1-\exp(-z^2/4)\}.$$

The transcendental equation is then

$$\exp(-z^2/4) = 1 + a'z^2 + ib'z^3, \qquad \ldots\ldots(3.4)$$

where

$$a' = a/2\sqrt{\pi}, \qquad b' = b/2\sqrt{\pi}.$$

Since $\exp(-z^2/4)$ undergoes very rapid changes when $|z|$ is large, it is convenient to consider the roots of the equation equivalent to (3.4), namely,

$$w = z^2/4 + \log(1 + a'z^2 + ib'z^3) + 2n\pi i = 0, \qquad \ldots\ldots(3.5)$$

where $n = 0, \pm 1, \pm 2, \pm 3, \ldots.$ and the principal value of the logarithm is taken.

When $n = 0$, the resulting equation can be shown to have no roots, apart from $z = 0$, if $4a'^3 \geqslant 27b'^2$, this being the condition for purely imaginary roots of the equation $1 + a'z^2 + ib'z^3 = 0$. The latter condition is equivalent to

$$m \geqslant \{2(3)^{1/3}/(\pi)^{1/2}\} m_e. \qquad \ldots\ldots(3.6)$$

However, this means that for any other value of n equation (3.5) will have roots both in the upper and lower half of the z-plane. The inequality (3.6) allows an electromagnetic mass to be taken much smaller than the mechanical mass, but this does not alter the number of non-physical solutions.

It is shown in the Appendix that the 'influence' function under consideration has the correct four-dimensional transform, so that all the conditions of the Peierls-McManus theory are satisfied. It follows then that more stringent conditions are necessary if non-physical solutions of the equations of motion are to be avoided.

It is of interest to find that the functions

(i) $H(v^2) = A\exp(-v^2)$,

(ii) $H(v^2)$ of square wave-form, leading to a δ-form for $h(v^2)$,

also lead to non-physical solutions.

§ 4. SIMPLIFIED GENERAL FORM OF THE TRANSCENDENTAL EQUATION

The general choice of 'influence' functions is more easily discussed if equation (2.2) is transformed.

Let

$$p(z) = \int_{-\infty}^{+\infty} h(v^2)\{\exp(-izv) - 1\}\,dv. \qquad \ldots\ldots(4.1)$$

Equation (2.2) then becomes

$$az^2 + ibz^3 = 2\{p - z\,dp/dz\} = -2z^2\,d\{p/z\}/dz,$$

or, writing

$$q(z) = -d\{p/z\}/dz, \qquad \ldots\ldots(4.2)$$

the equation is

$$2q(z) = a + ibz. \qquad \ldots\ldots(4.3)$$

Formulae for $H(v^2)$, the normalization condition, and the electromagnetic mass in terms of $q(z)$ are now derived.

From the relation (4.1),

$$d^3p/dz^3 = i\int_{-\infty}^{+\infty} v^3 h(v^2)\exp(-izv)\,dv,$$

so that

$$h(v^2) = -(i/2\pi v^3)\int_{-\infty}^{+\infty} p'''\exp(izv)\,dz$$

$$= (1/\pi v^3)\int_0^{\infty} p'''\sin zv\,dz. \qquad \ldots\ldots(4.4)$$

Hence $H(v^2)$ may be calculated.

From equation (3.2) the normalization condition becomes

$$-\frac{4}{\pi}\int_0^\infty dv\int_0^\infty p''' \sin zv\,dz=\frac{4}{\pi}\int_0^\infty \frac{\partial}{\partial v}\left[\int_0^\infty \frac{p'''\cos zv}{z}\,dz\right]dv.$$

Thus

$$\int_0^\infty (p'''/z)\,dz=-\pi/4. \qquad \ldots\ldots(4.5)$$

Since p is even in z, relation (4.3) gives

$$p=-z\int_0^\infty q(z')\,dz'. \qquad \ldots\ldots(4.6)$$

Hence, from (4.5) and (4.6) the normalization condition is

$$\int_0^\infty (q'/z)\,dz=\pi/12, \qquad \ldots\ldots(4.7)$$

since q' may be assumed to vanish at $z=0$ and $z=\infty$.

From relations (3.3) and (4.4) the electromagnetic mass is obtained, namely

$$m_e=-(2e^2/\pi r_0)\int_0^\infty dv'/v'\int_0^\infty p''' \sin zv'\,dz=-(e^2/r_0)\int_0^\infty p'''\,dz.$$

Using (4.6) it may be deduced that

$$m_e=-2e^2q(0)/r_0, \qquad \ldots\ldots(4.8)$$

since $q'(\infty)=q(\infty)=0$.

Thus, when $q(z)$ is known, all other quantities may be calculated.

§ 5. DISCUSSION OF POSSIBLE FUNCTIONS $q(z)$

Consider the equation

$$f(z)=2q(z)-a-ibz=0, \qquad \ldots\ldots(5.1)$$

$q(z)$ being even in z.

If $z=0$ is a root of equation (5.1), then $2q(0)=a$. Now $a=mr_0/e^2$ so that the mechanical mass is given by $m=2e^2q(0)/r_0$. The total mass is $M=m+m_e$. Hence, using (4.8),

$$M=2e^2q(0)/r_0-2e^2q(0)/r_0=0.$$

Thus for physically sensible solutions, $z=0$ cannot be a root of equation (5.1). It is now shown that equation (5.1) must have at least one solution for any form of $q(z)$. This root, of course, may lie in either the upper or lower half of the z-plane.

Consider $1/f(z)$. Since $q(z)$ is even in z, it cannot contain a term $+ibz$, so that $1/f(z)\to 0$ as $z\to\infty$. Now if $f(z)$ has no zero, then $1/f(z)$ has no poles or essential singularities. Hence, if $q(z)$ is uniform, by Liouville's theorem, $1/f(z)$ is a constant. Thus $f(z)$ must have at least one zero. If $q(z)$ is not single-valued, for example, $q(z)=A/(c^2+z^2)^{1/2}$, then, by considering the branches of the function separately with suitable cross-cuts in the z-plane, the problem reduces to the previous case.

From the above calculation a function $q(z)$ can exist such that equation (5.1) has roots only in the lower half-plane, these roots corresponding to damped motions of the electron. However, it may well be that such a function will not satisfy the conditions imposed by the theory.

It should be noted that the term ibz in equation (5.1) corresponds to radiation damping. If this term is neglected, the above argument is no longer valid and functions $q(z)$ will then exist, such that the transcendental equation has no roots. This is the Bohm–Weinstein case. It has not been found possible to derive explicitly a suitable function $q(z)$, satisfying all the necessary conditions. Indeed, even if a function q, which gives no unwanted roots, can be found, the condition of positiveness of the Fourier transform of $\Box H$ would still have to be satisfied.

ACKNOWLEDGMENTS

The author wishes to thank Professor Peierls for many valuable discussions, and the Nuffield Foundation for the award of a Fellowship, during the tenure of which part of the work was carried out.

APPENDIX

§ A. The general method of deriving the four-dimensional transform of the influence function $H(|\mathbf{R}^2|)$ is now given. The function $G(|\mathbf{R}^2|)$, whose four-dimensional transform is $-4\pi g(|\mathbf{K}^2|)/\mathbf{K}^2$ can be expressed in the form (McManus 1948)

$$G(R^2)=(8/R^2)\int_0^\infty\int_0^\infty g(uv)\cos v\sin(nu)(du/u)\,dv, \qquad \ldots\ldots(a)$$

where $g(uv)$ is obtained by replacing aK^2 by uv, with

$$K=|\mathbf{K}|, \qquad R=|\mathbf{R}|, \qquad n=R^2/4a.$$

Now $$H(|\mathbf{R}^2|)=(2\pi)^{-2}\int 16\pi^3\{-g^2(|\mathbf{K}^2|)/\mathbf{K}^2\}\exp(-i\mathbf{K}.\mathbf{R})\,d\mathbf{K}^{(4)}.$$

Therefore $$\Box H(R^2)=(2\pi)^{-2}\int 16\pi^3 g^2(K^2)\exp(-i\mathbf{K}.\mathbf{R})\,d\mathbf{K}^{(4)},$$

so that $$16\pi^3 g^2(K^2)=(2\pi)^{-2}\int \Box H(R^2)\exp(i\mathbf{K}.\mathbf{R})\,d\mathbf{R}^{(4)}.$$

Now $$\Box H(R^2)=(4/\mathbf{R}^2)\frac{\partial}{\partial R^2}R^4\frac{\partial H}{\partial R^2}.$$

Thus $\Box H(R^2)$ is an odd function of $\mathbf{R}^2$, so that that a relation similar to (a) can be obtained, namely,

$$16\pi^3 g^2(K^2)=(8/4\pi K^2)\int_0^\infty\int_0^\infty \mathscr{H}(uv)\cos v\sin mu(du/u)\,dv, \qquad \ldots\ldots(b)$$

where $m=K^2/4a$ and $\mathscr{H}(uv)$ corresponds to $\Box H(R^2)$.

§ B. The 'influence' function used in § 3 may be written in the form

$$H(V^2)=(1/2)\int_{V^2}^\infty \exp(-u)/u\,du,$$

where $\mathbf{V}$ is the four-vector whose time constant is v, $V=|\mathbf{V}|$, and units in which $r_0=1=c$ are used.

Hence $$\Box H(V^2)=-\{2(1-V^2)/\mathbf{V}^2\}\exp(-V^2).$$

Then

$$g^2(K^2)=\{(2\pi)^{-4}/m\}\int_0^\infty\int_0^\infty (1-uv)\cos v\sin mu\exp(-uv)(du/u)\,dv. \qquad \ldots\ldots(c)$$

Carrying out the integration gives

$$g^2(K^2)=\{(2\pi)^{-4}/m\}\{I-m\,dI/dm\},$$

where $I=\int_0^\infty \{\sin mu/(1+u^2)\}\,du$ and $m=K^2/4$.

I may be transformed to $m\mathrm{P}\int_0^\infty \exp(-y)/(m^2-y^2)\,dy$, where P denotes the principal value of the integral.

Hence
$$\begin{aligned}I&=(1/2)\mathrm{P}\left[\int_0^\infty \exp(-y)\{1/(m-y)+1/(m+y)\}\right]dy\\&=J_1\sinh m+J_2\exp(-m),\end{aligned}$$

where $J_1=\int_m^\infty \exp(-y)/y\,dy=-\mathrm{Ei}(-m),$

and $J_2=\int_0^m \sinh y/y\,dy=\{\overline{\mathrm{Ei}(m)}-\mathrm{Ei}(-m)\}/2.$

Hence

$$g^2(K^2)=\{(2\pi)^{-4}/m\}[(\sinh m-m\cosh m)J_1+(1+m)\exp(-m)J_2].$$

For m very large, $g^2(K^2)\sim 2(2\pi)^{-4}/m^2.$

For m very small, $g^2(K^2)\sim(2\pi)^{-4}(1+m/2),$

so that $g^2(0)=(2\pi)^{-4}$. For intermediate values of m, $g^2(K^2)$ may be obtained from tables (Jahnke and Emde 1943). It is then found that $g^2(K^2)$ has the correct behaviour (Figure 2).

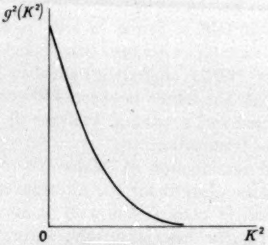

Figure 2. The form function $g^2(K^2)$ resulting from the influence function shown in Figure 1 (qualitative).

REFERENCES

Bohm, D., and Weinstein, M., 1948, *Phys. Rev.*, **74,** 1789.
Dirac, P. M., 1938, *Proc. Roy. Soc.* A, **167,** 156.
Eliezer, C. J., 1943, *Proc. Camb. Phil. Soc.*, **39,** 173.
Irving, J., 1949, *Proc. Phys. Soc.* A, **62,** 780.
Jahnke, E., and Emde, F., 1943, *Tables of Functions* (New York : Dover Publications).
McManus, H., 1948, *Proc. Roy. Soc.* A, **195,** 323.
Phillips, E. G., 1940, *Functions of a Complex Variable* (London : Oliver and Boyd)

The Band-Spectrum of Barium Oxide

By A. LAGERQVIST, E. LIND and R. F. BARROW

Physics Department, University of Stockholm, and Physical Chemistry Laboratory,
University of Oxford

MS. received 30th January 1950

ABSTRACT. The band-spectrum of BaO between 5000 and 7000 A., which consists of a single $^1\Sigma-^1\Sigma$ system, has been the subject of a new rotational analysis in which the following bands have been examined: 5,0, 4,0, 3,0, 3,1, 2,0, 2,1, 1,1, 1,2, 0,2, 0,3 and 0,4. The constants derived are:

$$B_v''=0{\cdot}3124_9-0{\cdot}0013_0(v''+\tfrac{1}{2})-0{\cdot}0000_2(v''+\tfrac{1}{2})^2 \qquad B_v'=0{\cdot}2584-0{\cdot}0011_1(v'+\tfrac{1}{2})$$

$$D''=26{\cdot}5\times10^{-8} \qquad D'=28\times10^{-8}$$

$$r_e''=1{\cdot}940\times10^{-8}\text{ cm.} \qquad r_e'=2{\cdot}133\times10^{-8}\text{ cm.}$$

$$\omega_e''=669{\cdot}8_1, \quad x_e''\omega_e''=2{\cdot}05_4 \qquad \omega_e'\sim500, \quad x'\omega_e'=1{\cdot}_6$$

$$\nu_{e,0}=16722{\cdot}2_5\text{ cm}^{-1}.$$

In the upper state some 16 perturbations have been found. They appear to arise from interactions with at least four electronic states or substates. Fairly complete information about one of the perturbing levels has been obtained. The constants of this state are:

$$B_v=0{\cdot}2254-0{\cdot}0013_5(v+\tfrac{1}{2}),$$
$$G_v=450{\cdot}_4(v+\tfrac{1}{2})-2{\cdot}_9(v+\tfrac{1}{2})^2,$$
$$\nu_{0,0}=17476{\cdot}_7\text{ cm}^{-1}.$$

The band-constants of the other perturbing states are very similar to those given above.

§1. INTRODUCTION

THE addition of barium salts to flames or arcs leads, in presence of oxygen, to the production of a characteristic band-spectrum attributed to BaO. Mecke and Guillery (1928) arranged the band-heads in a vibrational scheme. Mahanti (1934) showed that the bands between 4300 and 8000 A. form a single system, and gave vibrational and rotational analyses of this system, which was shown to arise from a $^1\Sigma-^1\Sigma$ transition.

Although a superficial examination of Mahanti's rotational analysis reveals no inconsistencies, the value derived for the internuclear distance in the lower state is unexpectedly small in comparison with analogous molecules, and, on checking the published figures more carefully, several discrepancies become apparent. Thus, some of the plots of $2\nu_0$ against J^2,

$$(2\nu_0\simeq \mathrm{R}(J-1)+\mathrm{P}(J)-2(B'-B'')J^2)$$

show anomalous changes of slope, some of the combination differences agree rather poorly, and the graphical method for the determination of B—by plotting $\Delta_2F(J)/(J+\frac{1}{2})$ against $(J+\frac{1}{2})^2$—gives for B_2' a value other than that quoted by Mahanti. These facts were disclosed by James (1947), who, from an examination of some relatively low-dispersion plates, also discovered the existence of at least one perturbation, and was able to suggest an alternative rotational analysis, with $B_0''\sim0{\cdot}31\text{ cm}^{-1}$, $B_0'\sim0{\cdot}26\text{ cm}^{-1}$.

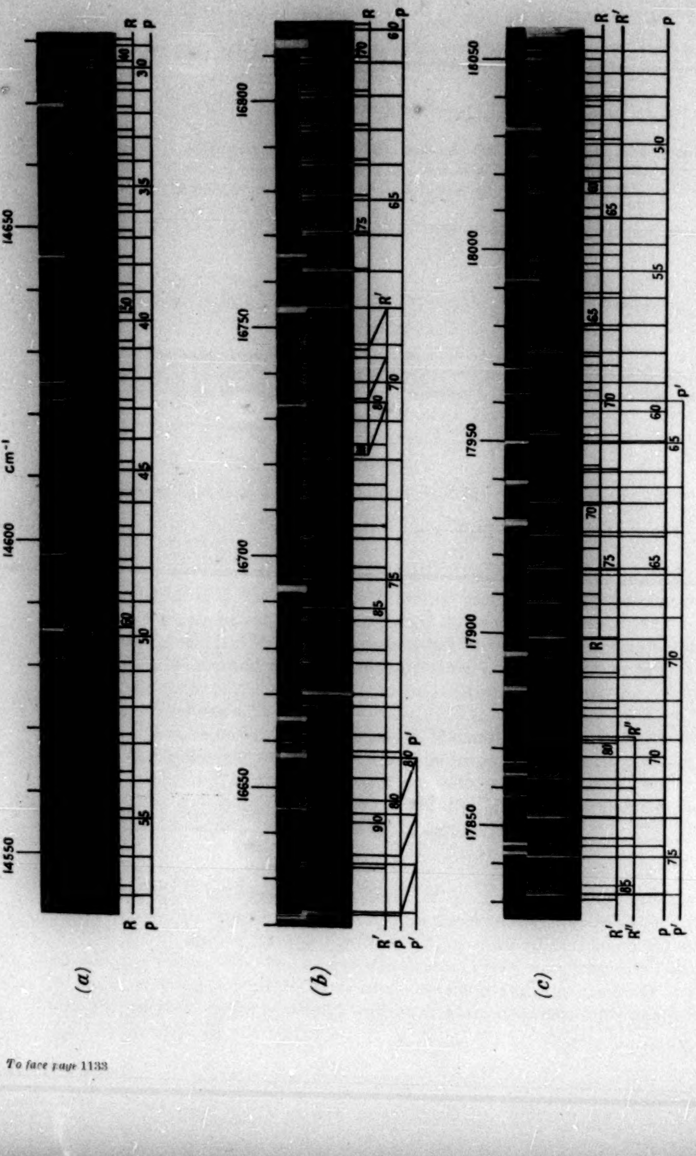

Figure 1. The ¹Σ*–¹Σ system of BaO: parts of (a) 0,3, (b) 2,1, (c) 3,0 bands.

It was evident that a new fine-structure analysis was desirable, especially as it was possible for us to use an instrument of greater dispersion and resolving power than that used by Mahanti (1·2 A/mm. as against Mahanti's 1·8 A/mm.).

Mahanti's vibrational scheme is confirmed by the present work, but his rotational analysis is incorrect. His constants are $B_e''=0{\cdot}36440$, $B_e'=0{\cdot}30995$, $r_e''=1{\cdot}787\times10^{-8}$ cm. The new values are $B_e''=0{\cdot}3124_9$, $B_e'=0{\cdot}2584$, $r_e''=1{\cdot}940$. We have also found a number of perturbations in the upper vibrational levels, some of which are very apparent (Figure 1 (*b*), (*c*), Plate).

§ 2. EXPERIMENTAL

The spectrograms were taken in a first order of a 21-ft. Wood concave grating (165,000 lines) having a dispersion of about 1·2 A/mm.

As source we used an acetylene–air flame running at about 4 atmospheres pressure of air fed with an aqueous solution of $BaCl_2$. This gave a much cleaner spectrum than that obtained with a carbon arc. In the arc atomic lines of Ba appear very strongly, and the background also contains a number of interfering lines. With the flame little trouble arose from atomic lines (Figure 1). The exposure time was about 15 hours. Eastman ID, IIE and IN plates were used.

The band-lines were measured by two of us independently from about 5000 to 7000 A. against Fe arc lines whose wavelengths were taken from the M.I.T. tables (1939). It is considered that the errors do not in general exceed ±0·03 cm^{-1}.

§ 3. STRUCTURE OF THE BANDS

The appearance of the structure in some typical regions is shown in the spectrograms reproduced in Figure 1. Only two branches were found in each band, and we conclude that the system arises from a $^1\Sigma$–$^1\Sigma$ transition. The structure is very open as the bands lie on a wide Condon parabola; thus the heads are formed by lines of low *J* values, commonly R(3) to R(6).

Table 1. Deslandres Scheme of Band-Origins

5	19172·64								
	485·01								
4	18687·63								
	486·97								
3	18200·66	665·71	17534·95						
	488·40		488·41						
2	17712·26	665·72	17046·54						
			495·03						
1			16551·51	661·54	15889·97				
					495·00				
0					15394·97	657·51	14737·46	653·38	14084·08
v' / v''	0		1		2		3		4

Eleven bands have been analysed: the positions of their origins are set out in the Deslandres scheme in Table 1. Perturbations have been found in all the upper state vibrational levels from $v'=1$ to $v'=5$. As is shown in Table 1, these perturbations displace the positions of some of the origins so that $\Delta G'_{v',v'+1}$ alters irregularly with v'.

The wave-numbers of the band-lines are given in Tables 2–6, where overlapped lines are indicated with an asterisk. In all the bands in which perturbations have been found, two columns for both R and P lines are given, one for each of the interacting levels. It will be seen that for many of the perturbations, the companion-lines have been found for several *J* values (see also Figure 1).

Barium has seven isotopes, but of these ^{138}Ba is by far the most abundant (71·7%), the next most common being ^{137}Ba (11·3%). We have made no effort to measure lines other than those ascribed to ^{138}BaO: the plates do, however, show weak lines which may well arise from other isotopic molecules.

Table 2. Wave-numbers of the 0,2, 0,3, and 0,4 Bands

	0,2		0,3		0,4	
J	R(*J*)	P(*J*)	R(*J*)	P(*J*)	R(*J*)	P(*J*)
0						
1		15394·35*				
2		93·65*				14082·78
3	15396·53*	92·80*		14735·23		81·99
4	96·53*	91·90*	14739·00*	34·43	14085·67*	80·96
5	96·53*	90·86*	39·00*	33·29	85·67*	80·05
6	96·53*	89·74*	39·00*	32·23	85·67*	78·91
7	96·18	88·53*	—	31·00	85·67*	77·76
8	95·88	87·17*	38·53	29·73	85·30	76·51
9	95·47	85·70*	38·11	28·30	84·90	75·08
10	94·98	84·18*	37·61	26·85	84·40	73·60
11	94·35*	82·54*	37·03	25·20	83·78	72·10
12	93·65*	80·82*	36·38	23·49	83·24	70·35
13	92·80*	78·96*	35·57	21·64	82·49	68·60
14	91·90*	77·00*	34·73	19·78	81·65	66·71
15	90·86*	74·95*	33·68	17·78	80·74	64·75
16	89·74*	72·80*	32·66	15·58	79·68	62·67
17	88·53*	70·54*	31·42	13·40	78·58	60·52
18	87·17*	68·20*	30·17	11·13	77·32	58·23
19	85·70*	65·71*	28·79	08·72	75·98	55·87
20	84·18*	63·14*	27·32	06·23	74·59	53·44
21	82·54*	60·49*	25·75	03·60	73·05	50·90
22	80·82*	57·68*	24·10	00·92	71·43	48·23
23	78·96*	54·83*	22·26	698·10	69·73	45·52
24	77·00*	51·86*	20·39	95·20	67·90	42·68
25	74·95*	48·78*	18·42	92·22	66·00	39·75
26	72·80*	45·58*	16·33	89·10	64·00	36·73
27	70·54*	42·33*	14·15	85·84	61·88	33·56
28	68·20*	38·92*	11·88	82·56	59·69	30·34
29	65·71*	35·44*	09·51	79·17	57·38	27·00
30	63·14*	31·83*	07·06	75·66	54·98	23·59
31	60·49*	28·13*	04·46	72·09	52·49	20·08
32	57·68*	24·36*	01·77	68·34	49·89	16·47
33	54·83*	20·44*	698·98	64·55	47·23	12·79
34	51·86*	16·43*	96·10	60·66	44·45	08·98
35	48·78*	12·35*	93·18	56·64	41·58	05·07
36	45·58*	08·12*	90·07	52·53	38·60	01·06
37	42·33*	03·81*	86·89	48·32	35·51	13996·98
38	38·92*	299·42*	83·60	44·03	32·33	92·78
39	35·44*	94·88*	80·24	39·63	29·07	88·50

Table 2 (*cont.*).

	0,2		0,3		0,4	
J	R(*J*)	P(*J*)	R(*J*)	P(*J*)	R(*J*)	P(*J*)
40	15331·83*	15290·27*	14676·75	14635·17	14025·71	13984·13
41	28·13*	85·55*	73·17	30·54	22·23	79·65
42	24·36*	80·71*	69·49	25·83	18·68	75·04
43	20·44*	75·79*	65·72	21·03	15·05	70·33
44	16·43*	70·75*	61·81	16·15	11·29	65·52
45	12·35*	65·60*	57·83	11·16	07·44	60·65
46	08·12*	60·39*	53·74	06·05	03·49	55·70
47	03·81*	55·05*	49·58	00·85	13999·45	50·64
48	299·42*	49·59*	45·30	595·55	95·31	45·44
49	94·88*	44·06*	40·94	90·14	91·03	40·21
50	90·27*	38·42*	36·45	84·65	86·71	34·86
51	85·55*	32·66*	31·84	79·04	82·30	29·40
52	80·71*	26·81*	27·17	73·34	77·75	23·86
53	75·79*	20·96	22·36	67·55	73·09	18·17
54	70·75*	14·89	17·49	61·68	68·36	12·46
55	65·60*	08·71	12·52	55·67	63·47	06·63
56	60·39*	02·52	07·44	49·59	58·54	00·71
57	55·05*	196·13	02·26	43·37	53·54	894·68
58	49·59*	89·68	596·98	37·09	48·43	88·53
59	44·06*	83·11	91·58	30·70	43·20	82·32
60	38·42*	76·45	86·07	24·17	37·92	76·00
61	32·66*	69·70	80·49	17·55	32·48	69·57
62	26·81*	62·84	74·81	10·85	26·98	63·04
63	20·77	55·86	69·05	04·04	21·35	56·44
64	14·69	48·80	63·14	497·20	15·64	49·75
65	08·51	41·59	57·17	90·19	09·84	42·91
66	02·22	34·35	51·06	83·07	03·98	36·03
67	195·84	26·94	44·90	75·98	897·94	29·03
68	89·34	19·47	38·58	68·60	91·86	21·94
69	82·78	11·87	32·18	61·18	85·65	14·71
70	76·10	04·19	25·65	53·71	79·37	07·45
71	69·32	096·40	19·06	46·14	72·98	00·05
72	62·43	88·52	12·34	38·47	66·49	792·59
73	55·45	80·48	05·58	30·67	59·91	85·02
74	48·35	72·39	498·69	22·73	53·21	77·38
75	41·16		91·69	14·84	46·45	69·62
76	33·82		84·57	06·76	39·58	61·73
77	26·38		77·36	398·55	32·60	53·76
78	18·85		70·05	90·25	25·51	45·66
79	11·26		62·65	81·86	18·34	37·50
80	03·50		55·17	73·38	11·08	29·23
81	095·69		47·58	64·75	03·72	20·92
82	87·76		39·87	56·11	796·24	12·48
83	79·70		32·11	47·33	88·70	03·89
84	71·55		24·16	38·41	81·03	695·28
85			16·23	29·45	73·30	86·68
86			08·11	20·37	65·44	77·70
87			399·91	11·19	57·49	68·74
88			91·62	01·90	49·42	59·73
89			83·18	292·51	41·28	50·59

Table 2 (*cont.*)

	0,2		0,3		0,4	
J	R(*J*)	P(*J*)	R(*J*)	P(*J*)	R(*J*)	P(*J*)
90			14374·71	14282·95	13733·00	13641·36
91			66·10	73·39	24·68	32·03
92			57·35	63·71	16·24	22·61
93			48·51	53·90	07·71	
94			39·62	44·02	699·03	
95			30·63	34·06	90·31	
96			21·51	23·96	81·48	
97			12·30	13·82	72·50	
98			02·97	03·50	63·50	
99			293·54	193·13	54·36	
100			83·99	82·62	45·12	
101			74·34	72·07	35·78	
102			64·56	61·33	26·29	
103			54·82	50·62		
104			44·89	39·66		
105			34·85	28·67		
106			24·73	17·59		
107			14·53	06·52*		
108			04·16	095·13*		
109			193·72			
110			83·21			
111			72·49			
112			61·79			
113			50·93			
114			39·97			
115			28·94			
116			17·80			
117			06·52*			
118			095·13*			

Table 3. Wave-numbers for the 1,1 and 1,2 Bands

	1,1		1,2	
J	R(*J*)	P(*J*)	R(*J*)	P(*J*)
3	16552·90*	16549·33	15891·38*	
4	52·90*	48·41	—	
5	52·90*	47·31	—	15885·86
6	52·90*	46·20	91·38*	84·77
7	52·61	44·89	—	83·49
8	52·27	43·49	90·71	82·09
9	51·76	42·00	90·39	80·61
10	51·18	40·36	89·90	79·01
11	50·50	38·72	89·22	77·33
12	49·72	36·82	88·51	75·54
13	48·86	34·99	87·59	73·67
14	47·85	32·98	86·66	71·81
15	46·73	30·83	85·60	69·57
16	45·49	28·60	84·39	67·35
17	44·18	26·30	83·04	65·05
18	42·71	23·79	81·70	62·62
19	41·20	21·20	80·19	60·10

Table 3 (*cont.*)

	1,1				1,2			
J	R(*J*)		P(*J*)		R(*J*)		P(*J*)	
20	16539·56		16518·55		15878·58		15857·54	
21	37·78		15·78		76·83		54·79	
22	35·92		12·87		75·08		51·95	
23	33·95		09·90		73·18		49·04	
24	31·92		06·80		71·12		45·95	
25	29·67		03·59		69·03		42·85	
26	27·42		00·27		66·77		39·64	
27	24·96		496·87		64·41		36·25	
28	22·45		93·29		61·99		32·82	
29	19·85		89·65		59·52		29·23	
30	17·10		85·86		56·79		25·55	
31	14·25		82·04		54·04		21·78	
32	11·30		78·00		51·14		17·90	
33	08·22		73·99		48·21		13·93	
34	05·10		69·78		45·15		09·82	
35	01·79		65·53		41·96		05·64	
36	498·41		61·11		38·69		01·32	
37	94·94		56·63		35·26		796·90	
38	91·31		51·97		31·78		92·42	
39	87·58		47·22		28·01		87·79	
40	83·80		42·35		24·45		83·04	
41	79·83		37·42		20·60		78·24	
42	75·79		32·36		16·66		73·32	
43	71·62		27·19		12·64		68·25	
44	67·05	16467·92	21·94		08·16	15809·03	63·12	
45		63·04	16·50			04·41	57·82	
46		58·56	10·71	16411·56		00·00	52·15	15752·98
47		53·95		05·51		795·50		47·10
48		49·25		399·80		90·90		41·49
49		44·34		93·94		86·23		35·79
50		39·48		87·99		81·43		30·00
51		34·42		81·96		76·51		24·08
52		29·23		75·78		71·48		18·09
53		23·95		69·54		66·37		11·97
54		18·49		63·12		61·11		05·68
55		12·97		56·65		55·71		699·38
56		07·24		49·88		50·20		92·86
57		01·40		43·30		44·51		86·27
58	02·28	395·14		36·21	15745·42	38·39		79·53
59	393·59	88·36		29·12	37·00	31·66		72·56
60	85·97	80·16	328·74	21·76	29·50	23·65	672·29	65·28
61	79·13		18·87	13·65	22·83		62·65	57·34
62	72·55		10·10	04·24	16·49		53·93	48·11
63	66·05		02·07		10·10		46·09	
64	59·49		294·31		03·70		38·48	
65	52·84		86·52		697·25		30·93	
66	46·15		78·73		90·62		23·31	
67	39·13		70·81		83·93		15·61	
68	32·08		62·83		77·12		07·81	
69	24·98		54·73		70·22		599·95	
70	17·77		46·60		63·16		91·92	
71	10·46		38·26		56·01		83·80	
72	02·99		29·77		48·75		75·57	
73	295·44		21·21		41·35		67·24	
74	87·68		12·52		33·85		58·71*	
75	79·78				26·16		50·11	
76	71·77				18·34		41·40	
77	62·83				10·37		32·52	
78	55·19				02·29		23·50	
79	46·60				593·99		14·37	

Table 3 (*cont.*)

	1,1		1,2			
J	R(*J*)	P(*J*)	R(*J*)		P(*J*)	
80	16237·98		15585·54		15505·09	
81	29·11		76·84		495·60	
82	19·98		67·98		85·96	
83	10·54		58·71*		76·09	
84			49·27	15593·07	66·01	
85			39·43	80·52	55·65	
86			29·22	67·98	44·98	15488·74
87			18·48	55·82	33·96	75·05
88			07·28	43·84	22·53	61·38
89			495·27	32·03	10·65	47·99
90			83·11	20·52	398·29	34·90
91			70·22	09·35	85·20	21·85
92				498·37	71·66	09·17
93				87·51	57·67	396·76*
94				76·75		84·55
95				66·01		72·46
96				55·23		60·49*
97				44·22		48·59
98				32·99		
99				21·44		
100				09·44		
101				396·76*		

Table 4. Wave-numbers for the 2,0 and 2,1 Bands

	2,0		2,1	
J	R(*J*)	P(*J*)	R(*J*)	P(*J*)
1	17713·16*	17711·64*		
2	13·49*	10·89*		
3	13·49*	10·08*	17047·91*	
4	13·64*	09·10*	47·91*	17043·30
5	13·64*	08·00*	47·91*	42·35
6	13·49*	06·84*	47·91*	41·16
7	13·16*	05·61*	47·53	39·87
8	12·71	04·13*	47·19	38·50
9	12·23	02·63*	46·71	37·01
10	11·64*	00·98*	46·14	35·41
11	10·89*	699·26*	45·49	33·73
12	10·08*	97·39*	44·53	31·84
13	09·10*	95·45*	43·79	29·95
14	08·00*	93·23	42·71	27·92
15	06·84*	91·15*	41·59	25·70
16	05·61*	88·75	40·31	23·48
17	04·13*	86·45*	38·96	21·11
18	02·63*	83·93*	37·52	18·60
19	00·98*	81·10	35·93	16·03
20	699·26*	78·43	34·28	13·33
21	97·39*	75·55	32·45	10·55
22	95·45*	72·52	30·57	07·62
23	93·37	69·55*	28·53	04·64
24	91·15*	66·26	26·42	01·46
25	88·91	62·97	24·19	16998·19
26	86·45*	59·43	21·84	94·81
27	83·93*	55·94	19·37	91·31
28	81·29	52·17	16·84	87·78
29	78·50	48·49	14·15	84·06
30	75·69	44·63	11·33	80·30
31	72·69	40·60	08·50	76·42
32	69·55*	36·53	05·49	72·31

Table 4 (*cont.*)

	2,0				2,1			
J	R(*J*)		P(*J*)		R(*J*)		P(*J*)	
33	17666·34		17632·34		17002·36		16968·23	
34	63·16		27·89		16999·16		64·00	
35	59·64		23·46		95·80		59·61	
36	56·12		18·90		92·38		55·12	
37	52·40		14·23		88·80		50·61	
38	48·67		09·44		85·12		45·89	
39	44·80		04·55		81·34		41·11	
40	40·77		599·55		77·44		36·20	
41	36·79		94·44		73·53		31·20	
42	32·39		89·31*		69·30		26·04	
43		17628·28	83·90*			16965·28	20·84	
44		23·72	78·31			60·86	15·43	
45		19·13		17572·95*		56·41		16910·17
46		14·44		67·21*		51·86		04·52
47		09·64		61·38*		47·17		898·84
48		04·76		55·46*		42·39		93·07
49		599·73		49·44*		37·51		87·17
50		94·61		43·29*		32·55		81·16
51		89·31*		37·07*		27·38		75·04
52		83·90*		30·70*		22·14		68·82
53		78·50		24·15*		16·84		62·46
54		72·95*		17·58*		11·38		56·04
55		67·21*		10·83*		05·89		49·49
56		61·38*		04·04*		00·24		42·88
57		55·46*		497·09*		894·49		36·07
58		49·44*		90·01*		88·58		29·21
59		43·29*		82·91		82·61		22·21
60		37·07*		75·71		76·50		15·13
61		30·70*		68·30		70·29		07·92
62		24·15*		60·78		63·95		00·60
63		17·58*		53·19		57·47		793·29
64		10·83*		45·46		50·93		85·62
65		04·04*		37·61		44·26		77·99
66		497·09*		29·65		37·51		70·21
67		90·01*		21·58		30·62		62·34
68		82·69		13·42		23·60		54·33*
69		75·23		05·17		16·46		46·23
70		67·94		396·73		09·25		38·02
71		60·37		88·19		01·88		29·67
72		52·68		79·56		794·38		21·26
73		44·85		70·74		86·73		12·69
74		36·88		61·86		78·97		04·00
75		28·70		52·84		71·05		695·18
76		20·36		43·66		62·87		86·17
77		11·59		34·24		54·33*		77·04
78	411·50	02·03		24·62	754·33	45·02		67·66
79	00·16	391·31		14·66	43·42	34·42		57·89
80	390·25	78·94	313·30	03·90	33·65	22·33	656·68	47·42
81	80·95		00·88	291·97	24·53		44·57	35·60
82	71·77		289·60	78·40	15·64		33·62	22·33
83	62·67		79·06		06·75		23·33	
84	53·56		68·82		697·88		13·22	
85	44·30		58·55		88·91		03·18	
86	35·01		48·21		79·86		593·07	
87	25·63		37·77		70·69		82·96	
88	16·10		27·28		61·43		72·69	
89	06·43		16·69		52·03		62·30	
90	296·65		05·96		42·52			
91	86·68		195·09		32·86			
92	76·45							

Table 5. Wave-numbers for the 3,0 and 3,1 Bands

	3,0				3,1			
J	R(*J*)		P(*J*)		R(*J*)		P(*J*)	
3	18202·00*						17532·79*	
4	02·00*						31·86*	
5	02·00*						30·70*	
6	01·79		18195·25				29·57*	
7	01·56		93·93		17535·89		28·23*	
8	01·10		92·44		35·47		26·84	
9	00·57		90·94*		35·00		25·27	
10	199·97		89·18*		34·39		23·72	
11	99·18		87·41*		33·63		21·93	
12	98·31		85·53		32·79*		20·09	
13	97·30		83·52		31·86*		18·16	
14	96·20		81·42		30·81*		16·07	
15	94·92		79·19		29·57*		13·88	
16	93·50		76·83		28·23*		11·50	
17	91·88		74·35		26·73		09·11	
18	89·71	18190·94*	71·59		24·71	17525·87	06·48	
19		89·18*	68·67*			24·06	03·69	
20		87·35*	65·36	18166·71		22·16	00·64	17501·67
21		85·38		63·55		20·22		498·62*
22		83·32		60·46		18·26		95·50*
23		81·18		57·28		16·21		92·40*
24		78·89		54·00		14·02		89·19*
25		76·48		50·62		11·77		85·88*
26		73·99		47·12		09·41		82·44*
27		71·39		43·56		06·76		78·85*
28		68·67*		39·80		04·04		75·23*
29		65·81		35·96		01·41		71·43*
30		62·88		32·00		498·51		67·52*
31		59·79		27·91		95·50*		63·50*
32		56·59		23·71		92·40*		59·40*
33		53·29		19·39		89·19*		55·16*
34		49·84		14·90		85·88*		50·82*
35		46·40		10·39		82·44*		46·34*
36		42·78		05·73		78·85*		41·78*
37		38·95		00·96		75·23*		37·18
38		35·07		096·04		71·43*		32·41
39		31·07		91·03		67·52*		27·51
40		26·97		85·91		63·50*		22·48
41		22·71		80·67		59·40*		17·38
42		18·33		75·31		55·16*		12·09
43		13·97		69·82		50·82*		06·75
44		09·25		64·22		46·34*		01·26
45		04·53		58·49		41·78*		395·70
46		099·66		52·69		36·88		89·97
47		94·73		46·73		32·12		84·15
48		89·63		40·65		27·18		78·25
49		84·40		34·43		22·08		72·16
50		79·07		28·13		16·91		65·98
51		73·61		21·68		11·59		59·67
52		67·99		15·10		06·16		53·26
53		62·26		08·42		00·56		46·68
54		56·43		01·58		394·87		40·03
55		50·45		17994·64		89·03		33·23
56		44·30		87·56		83·06		26·27
57		38·01		80·33		76·94		19·26
58		31·56		72·91		70·74		12·07
59		24·98		65·45		64·23		04·71
60		118·20		957·79		357·62		297·21
61	049·18	11·22		49·95		50·77		89·60
62	39·49	04·00		41·97		43·66		81·70
63	29·31	17996·58	17971·71	33·74	369·16	36·49		73·66
64	19·08	88·85*	60·84	25·28*	59·17	28·94		65·43

Table 5 (*cont.*)

	3,0				3.1			
J	R(*J*)		P(*J*)		R(*J*)		P(*J*)	
65	18008·88	17980·71	17949·42	17916·66*	17349·14	17320·99	17289·69	17256·97
66	17998·94	72·25	37·97	07·69*	39·30	12·70	78·40	48·21
67	88·85*	63·26	26·60	898·40	29·48	03·90	67·28	39·04
68	79·23	53·78	15·26	88·71	20·07	294·59	56·05	29·51
69	69·87	43·79	04·18	78·52	10·86	84·85	45·18	19·60
70	60·68	33·22	893·36	67·82	01·85	74·44	34·54	09·13
71	51·74	22·19	82·64	56·62	293·04	63·64	24·02	197·97
72	42·74	10·63	72·25	44·72	84·40		13·86	86·37
73	33·95	898·83*	62·01*	32·46	75·78		03·80	74·42
74	25·28*		51·95	19·83	67·28		193·93	
75	16·49*		41·95*	06·68	57·74		84·16	
76	07·69*		32·02		50·16		74·43	
77	898·83*		22·01		41·53		64·66	
78	89·86		12·04		32·75		54·92	
79	80·77		01·92		23·96		45·03	
80	71·51		791·72		14·83		34·97	
81	62·01*		81·43		05·56		25·07	
82	52·26	73·14	70·83		196·00		14·82	
83	41·95*	59·63	60·34		85·98		04·49	
84	30·97	46·73	49·27	770·08			093·71	
85	18·89	34·54	37·78	55·59			82·45	
86	05·70	23·01	25·50	41·33				
87	91·72	12·27	12·23	28·01				
88		01·80	697·93	15·34				
89		791·42	82·78	03·30				
90		81·01		691·60				
91		70·98		80·05				
92		60·54		68·55				
93		50·05		57·07				
94		39·52		45·52				
95		28·98		33·94				
96		18·27		22·24				
97				10·47				

Table 6. Wave-numbers for the 4,0 and 5,0 Bands

	4,0		5,0	
J	R(*J*)	P(*J*)	R(*J*)	P(*J*)
2			19173·91*	
3	18688·81*		73·91*	19170·41
4	88·81*		73·91*	69·50
5	88·81		73·91*	68·34
6	—	18682·12	—	67·08
7	—	80·80	—	65·79
8	87·92	79·32	72·88	64·34
9	87·38	77·79	72·31	62·73
10	86·67	76·09	71·64	61·01
11	85·93	74·26	70·94	59·20
12	85·06	72·33	69·87	57·28
13	84·03	70·31	68·89	55·27
14	82·91	68·16	67·71	53·09
15	81·59	65·92	66·40	50·76
16	80·23	63·55	64·99	48·36
17	78·76	61·05	63·52	45·82
18	77·14	58·43	61·85	43·16
19	75·43	55·67	60·08	40·42
20	73·64*	52·85	58·21	37·54
21	71·60	49·87	56·22	34·54
22	69·51	46·74	54·10	31·38
23	67·31	43·53	51·85	28·16
24	64·99	40·22	49·48	24·84
25	62·62*	36·80	47·02	21·30

Table 6 (*cont.*)

	4,0				5,0			
J	R(*J*)		P(*J*)		R(*J*)		P(*J*)	
26	18660·03		18633·23		19144·38		19117·70	
27	57·32		29·55		41·65		13·99	
28	54·64		25·76		38·83		10·12	
29	51·58*		21·83		35·87		06·17	
30	48·57		17·69		32·76		02·02	
31	45·44		13·61		29·52		097·85	
32	42·12		09·33		26·20		93·54	
33	38·73		04·94		22·67		89·01	
34	35·21		00·44		19·00		84·49	
35	31·57		595·78		15·15		79·72	
36	27·82		91·03		11·00	19116·47	74·88	
37	23·89		86·11		06·29	20·80	69·76*	
38	19·89		81·14		00·92*	05·62	64·40	19069·76*
39	15·77		76·01		094·63	00·92*	58·38	62·81
40	11·47		70·76			096·38	51·80	56·46
41	07·05		65·36			91·87	44·25	50·58
42	02·52		59·84			87·27		44·75
43	597·88		54·19			82·62		39·01
44	93·03		48·46			77·80		33·18
45	88·07		42·49			72·94		27·25
46	82·93		36·45			67·82		21·23
47	77·70		30·24			62·81		15·08
48	72·20		23·91			57·57		08·87
49	66·51		17·39			52·25		02·48
50	60·58		10·65			46·74		18996·03
51	54·30	18577·71	03·80			41·17		89·48
52	47·98	59·62	496·68			35·48		82·77
53	41·14	61·50	89·25	18512·51		29·65		75·95
54	33·85	53·49	81·57	03·20		23·67		69·03
55	26·09	45·67	73·45	493·84		17·61		61·99
56	17·86	38·06	64·97	84·62		11·42		54·81
57	09·05	30·64	55·97	75·57		05·12		47·53
58	499·94	23·36	46·52	66·70		18998·71		40·10
59		16·15	36·46	58·09		92·14		32·57
60		09·03	26·03	49·56		85·49		24·92
61		01·83		41·14		78·68		17·20
62		494·65		32·75	18975·95	71·72		09·29
63		87·45		24·37	65·59	64·00		01·24
64		80·14		15·99	57·91	53·03	18897·27	893·04
65		72·76		07·53	50·55		85·72	84·05
66		65·31		399·07*	43·14		76·76	71·96
67		57·64		90·42	35·65		68·21	
68		50·03		81·72	28·04		59·59	
69		42·16		72·91	20·30		50·89	
70		34·12		63·98	12·43		42·02	
71		26·00		54·94	04·47		33·08	
72		17·52		45·72	896·37		24·00	
73	21·79	08·68		36·34	88·16		14·83	
74	10·03	399·07*		26·68	79·81		05·52	
75	399·07*	88·50	329·70	16·66	71·36		796·09	
76	89·07	76·65	16·72	05·87	62·75		86·53	
77	79·65		04·65	294·05	54·04		76·92	
78	70·48		293·39	80·95	45·24		67·07	
79	61·37		82·76		36·33		57·17	
80	52·24		72·38		27·26		47·13	
81	43·06		62·05		18·06		37·00	
82	33·80		51·73		08·78		26·74	
83	24·45		41·32		799·35		16·37	
84	15·07		30·89		89·81		05·88	
85	05·48		20·33		80·15		695·26	
86	295·79		09·68		70·33		84·45	

Table 6 (*cont.*)

	4,0			5,0			
J	R(J)		P(J)	R(J)		P(J)	
87	18286·05		18198·98	18760·38		18673·58*	
88	76·17		88·09		18750·92	62·58*	
89	66·17		77·10		40·34	51·54*	
90	56·06		65·97		30·02		18640·85
91	45·83		54·80		19·62		29·10
92	35·46				09·10		17·69
93	25·02				698·44		06·00
94	14·45				87·64		594·24
95	03·76				76·68		82·38
96	192·90				65·50		70·42
97		18182·39			54·14		
98		171·05					
99		159·79					
100		148·60					

§4. DETERMINATION OF ROTATIONAL CONSTANTS

The rotational energy of a $^1\Sigma$ state is often represented rather closely by a two-constant expression,

$$F(J) = BJ(J+1) - DJ^2(J+1)^2$$

The values of these constants are generally derived by treatment of the quantity $\Delta_2F(J)$, where

$$\frac{\Delta_2F(J)}{J+\frac{1}{2}} = 4B - 8D(J+\tfrac{1}{2})^2$$

and $\Delta_2F'(J) = \mathrm{R}(J) - \mathrm{P}(J)$; $\Delta_2F''(J) = \mathrm{R}(J-1) - \mathrm{P}(J+1)$.

A common procedure is to plot the graph of $\Delta_2F(J)/(J+\frac{1}{2})$ against $(J+\frac{1}{2})^2$ and then to determine B from the intercept and D from the slope. It is, however, sometimes difficult to decide the correct location of the line. The very tedious least-squares method or the centre-of-gravity method may then be used. (In the latter method the points are divided into two groups each containing the same number, and, after taking the centres of gravity of these groups, two points are obtained which give the line.) Neither method, unless some weighting of the points is made, takes account of variation in accuracy of the values of $\Delta_2F(J)/(J+\frac{1}{2})$ with J. The centre-of-gravity method can, however, be modified quite simply so as to include this effect. The error in $\Delta_2F(J)$ is roughly constant for all lines of a band, so long as differences involving only unblended lines are used; the error in $\Delta_2F(J)/(J+\frac{1}{2})$ is thus proportional to $1/(J+\frac{1}{2})$ and each point should on this account be given a weight of $(J+\frac{1}{2})^2$. This procedure is of course only applicable when $F(J)$ is satisfactorily represented by a two-constant expression, as the points at high J values make a large contribution to the final result.

For perturbed levels, other methods of determining the rotational constants must be used. Where the perturbation does not occur until moderately large J values, accurate values of ΔB may be obtained from the expression

$$\mathrm{R}(J-1) + \mathrm{P}(J) \simeq 2\nu_0 + 2(B' - B'')J^2.$$

Then if one of the B values is known, the other can be derived.

Alternatively, the methods introduced by Gerö (1935) may be used. For bands with only P and R branches and in which the perturbations are in the upper state,

$$\frac{\mathrm{R}(J-2)-\mathrm{R}(J-1)+\mathrm{P}(J)-\mathrm{P}(J+1)}{4J}=B''-B'+6D''-2J^2(D''-D').$$

If the left-hand side of this expression is plotted against J^2, ΔB is obtained as the intercept at $J=0$. In unperturbed regions, the points lie on a straight line which is almost horizontal if $D'' \sim D'$. The last two methods are also, of course, useful for unperturbed bands, especially the former, which gives not only ΔB but also ν_0.

For the v'' levels and for $v'=0$, we examined all the above methods, except that of least squares, and obtained for the v'' levels results which were in close agreement. For $v'=0$, the agreement was somewhat less satisfactory. For all these levels, the mean values of all determinations have been taken as the best values (Table 7): the values obtained with the weighted centre-of-gravity methods lie close to these mean values, and it seems to us to be the most reliable single method where $F(J)$ can be represented with only two constants. We estimate the errors in the B'' values to be about $\pm 0{\cdot}00005$; for B_0' the error is about $\pm 0{\cdot}0001$ cm^{-1}.

The constants for the other v' levels were determined by using the ΔB methods described above. As will be seen from Table 7, the B values vary somewhat irregularly with v': this arises from the fact that in some of these vibrational states none of the rotational levels is entirely unperturbed.

Table 7. Rotational Constants for the $^1\Sigma$ and $^1\Sigma^*$ States

v	B''_{obs}	B''_{calc}	B'_{obs}	B'_{calc}
0	$0{\cdot}3118_4$	$0{\cdot}3118_4$	0·2578	0·2578
1	$0{\cdot}3104_8$	$0{\cdot}3104_9$	0·2564	0·2567
2	$0{\cdot}3091_2$	$0{\cdot}3091_1$	0·2556	0·2556
3	$0{\cdot}3076_7$	$0{\cdot}3076_9$	0·2541	0·2545
4	$0{\cdot}3062_4$	$0{\cdot}3062_3$	0·2532	0·2532
5			0·2523	0·2523
	$D''=26{\cdot}_5\times10^{-8}$		$D'=28\times10^{-8}$	

The calculated values are from the expressions

$$B_v''=0{\cdot}3124_9-0{\cdot}0013_0(v''+\tfrac{1}{2})-0{\cdot}0000_2(v''+\tfrac{1}{2})^2.$$
$$B_v'=0{\cdot}2584-0{\cdot}0011_1(v'+\tfrac{1}{2}).$$

With the values of ω_e'' and ω_e' given in § 6, we obtain, from Kratzer's relation, $(D=4B^3/\omega^2)$, $D''=27{\cdot}2\times10^{-8}$, $D'=27{\cdot}6\times10^{-8}$ cm^{-1} in satisfactory agreement with the experimental values.

§ 5. PERTURBATIONS

(i) *Treatment of the Perturbations*

In all, we have found some sixteen perturbations in the upper-state levels, $v'=1$ to $v'=5$: none has been detected in the lower state or in $v'=0$ up to $J=120$. From their appearance, the B values of the perturbing states are always less than B': and in many of the perturbations companion lines are found. An example of a large perturbation will be seen in the spectrogram reproduced in Figure 1 (*c*): it is also illustrated in Figure 2, where the deviations of the levels in

$v'=3$ from the unperturbed positions are plotted against J. It will be noted that the perturbation at $J=69$ is so strong that it influences all the levels at lower J values.

The weaker perturbations have been detected by the method of Gerö (1935). We have, as before,

$$\frac{\mathrm{R}(J-2)-\mathrm{R}(J-1)+\mathrm{P}(J)-\mathrm{P}(J+1)}{4J}=T/4J=B''-B'+6D''+2(D'-D'')J^2.$$

If $T/4J$ is plotted against J, for unperturbed regions a straight line parallel to the axis of J is obtained, if the effect of the D term is small. The plots for all the bands investigated are given in Figures 3–5. The error in $T/4J$ of course increases as J decreases, so that the scatter of the points becomes considerable at low J values.

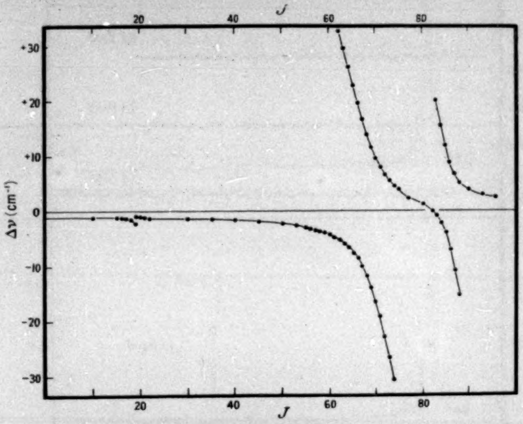

Figure 2. Perturbations in $v'=3$: deviations of the rotational levels from their 'unperturbed' positions.

The theoretical treatment of singlet–singlet interactions has been developed by Kovács (1937). The fundamental point of this treatment is that the mean value of the perturbed and perturbing energy levels is everywhere unperturbed. In Figure 6 is illustrated the course of the vibrational–electronic energy levels in a graph of energy against $J(J+1)$. The lower level is Σ, and the upper level Σ^* is perturbed by a state P. The levels of the unperturbed Σ^* state, W_{unp}, approximate at low J values to W_2, and at high values, after the perturbation, to W_1. If a range of values of both W_1 and W_2 is known, the plot of $T/4J$ against J will take the form shown in Figure 7. Theoretical expressions, f_1 and f_2, for the two branches, which arise from W_1 and W_2 in Figure 6, have been given by Kovács. The ordinate at the intersection is

$$\frac{B_{\mathrm{p}}+B_{\Sigma^*}}{2}-B_{\Sigma};$$

it is moreover equal to the mean value of the ordinates of the two branches at any value of J. The J value at the intersection, J^*, is related simply to the J value at which the perturbation culminates, J_0, by $J_0 \sim J^* - \frac{1}{2}$. It is also possible to determine the separation of the levels $J = 0$ in P and Σ^*, marked C in Figure 6: if P is a $^1\Sigma$ state, we have

$$C_{\Sigma\Sigma} = -2(\nu_0 - B_\Sigma) + \tfrac{1}{4}[\{P_1(J) + R_1(J-2) + P_2(J) + R_2(J-2)\}(J+1) \\ - \{P_1(J+1) + R_1(J-1) + P_2(J+1) + R_2(J+1)\}(J-1)],$$

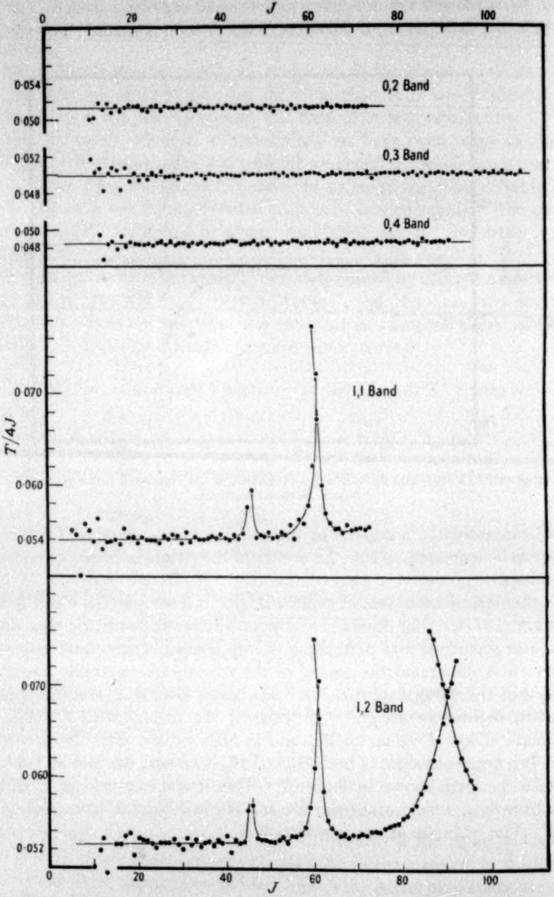

Figure 3. $[R(J-2) - R(J-1) + P(J) - P(J+1)]/4J = T/4J$ plotted against J for the 0,2, 0,3, 0,4, 1,1 and 1,2 bands.

where the suffixes 1 and 2 indicate lines from W_1 and W_2. If P is a $^1\Pi$ state

$$C_{\Pi\Sigma} = C_{\Sigma\Sigma} + B_{\Pi} \simeq C_{\Sigma\Sigma}.$$

The importance of this method is that it enables the B and C values of the perturbing states to be determined without a knowledge of the displacements of the levels from their unperturbed positions.

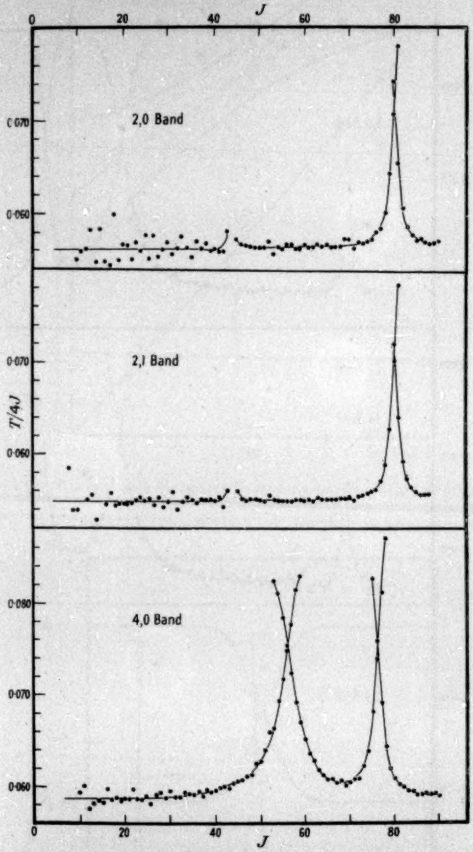

Figure 4. $T/4J$ plotted against J for the 2,0, 2,1 and 4,0 bands.

It is possible to distinguish between $^1\Sigma^1\Sigma$ and $^1\Pi^1\Sigma$ interactions if the magnitudes of the displacements and of the separation of the unperturbed levels (ϵ and δ_0 in Figure 6) are known over a range of J values. Then, simply,

$\epsilon(\epsilon+\delta_0)=|H|^2$, where $|H|$ is the perturbing matrix element. For ${}^1\Sigma{}^1\Sigma$ perturbations, $|H|$ is independent of J: in the ${}^1\Pi{}^1\Sigma$ case it varies with J according to $H=\{2\alpha^2 J(J+1)\}^{1/2}$, where $2\alpha^2$ is a constant. ϵ and δ_0 may be determined as follows:

$$\mathrm{R}_1(J-1)-\mathrm{R}_2(J-1)=\mathrm{P}_1(J+1)-\mathrm{P}_2(J+1)=(2\epsilon+\delta_0)_J$$

and

$$\delta_0=[J(J+1)-J_0(J_0+1)](B_{\Sigma^*}-B_{\mathrm{p}}).$$

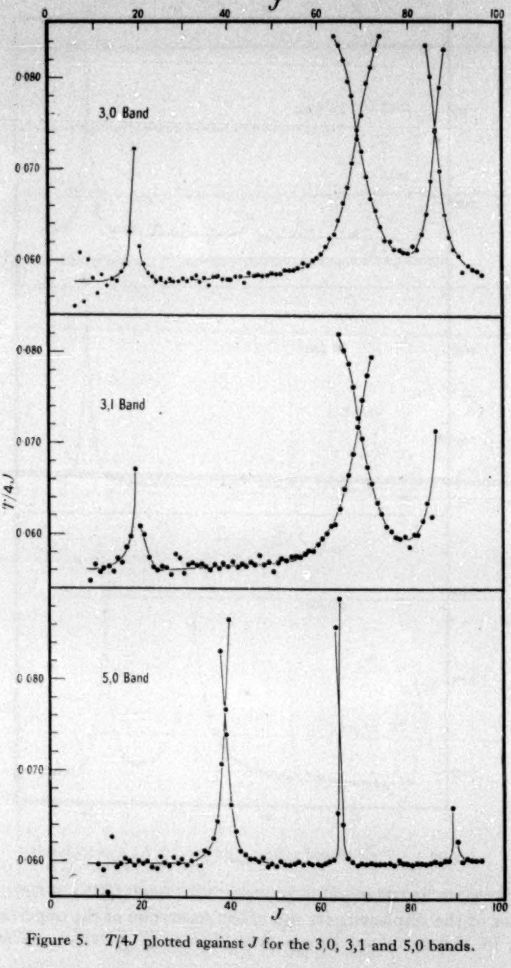

Figure 5. *T*/4*J* plotted against *J* for the 3,0, 3,1 and 5,0 bands.

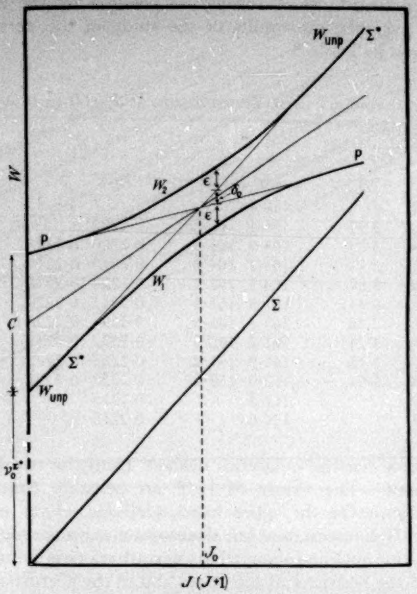
W_{unp}
Σ^*
W_2
ϵ
δ_0
P
P
ϵ
W_1
Σ
W
C
Σ^*
W_{unp}
$\nu_0^{\Sigma^*}$
J_0
$J(J+1)$

Figure 6. The course of the energy levels for a singlet–singlet perturbation.

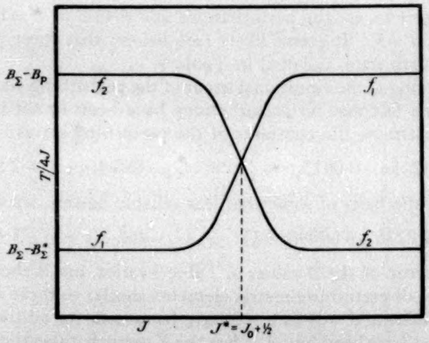
$B_\Sigma - B_P$
f_2
f_1
$T/4J$
f_1
f_2
$B_\Sigma - B_\Sigma^*$
J
$J^* = J_0 + \frac{1}{2}$

Figure 7. The variation of $T/4J$ with J for an interaction between two singlet states.

Plots of $T/4J$ have been given in Figures 3–5. The perturbations revealed there have been treated as completely as possible by the methods described above. As an example, the results of the study of the perturbation at $J=69$ in $v'=3$ are given in Table 8.

Table 8. The Perturbation at $J=69$ in $v'=3$

J	$\frac{\lvert H\rvert^2}{J(J+1)}\times 10^2$		$\lvert H\rvert^2$		B_p		$C_{\Sigma\Sigma}$	
	3,0	3,1	3,0	3,1	3,0	3,1	3,0	3,1
63	4·18		168·4					
64	4·00	3·99	166·4	165·8	0·2225		156·4	
65	3·84	3·83	164·9	164·3	0·2220	0·2223	158·8	157·7
66	3·71	3·71	164·2	164·2	0·2219	0·2219	159·5	159·4
67	3·59	3·57	164·5	162·7	0·2224	0·2218	156·7	160·0
68	3·45	3·44	161·8	161·3	0·2213	0·2220	162·2	158·8
69	3·36	3·35	162·1	161·6	0·2224	0·2226	156·7	156·3
70	3·24	3·24	161·2	160·9	0·2222	0·2218	157·8	160·1
71	3·17	3·15	161·9	161·2	0·2215	0·2222	161·1	159·6
72	3·08	3·04	162·0	159·6	0·2222	0·2221	158·0	159·1
73	2·99		161·2		0·2215		161·6	
74	2·82		156·6		0·2218		159·6	

It will be seen that the quantities derived from the two bands are in satisfactory agreement. The values of $|H|^2$ are sensibly constant, indicating a $^1\Sigma{}^1\Sigma$ perturbation. On the other hand, $|H|^2/J(J+1)$ is not constant, as it should be for a $^1\Pi{}^1\Sigma$ interaction, but decreases monotonously with increasing J.

The information obtained about all the perturbations is summarized in Table 9, and in Figure 8 the positions of the states and of the perturbations are indicated in a plot of energy against $J(J+1)$. In the diagram, circles indicate the positions where the perturbations culminate: the straight lines are drawn with slopes equal to the appropriate values of B. It will be seen that most of the perturbations can be explained as arising from interactions with three states, X, Y and Z. The three exceptions are the perturbations at $J=43{\cdot}5$ in $v'=1$, at 97·5 in $v'=4$ and at 88·9 in $v'=5$. It seems likely (see below) that these perturbations are caused by a fourth state, called Q in Table 9.

The numbering of the vibrational levels of the perturbing states, v_p in Table 9, follows from the fact that no perturbations have been found in $v'=0$. We are thus able to determine the constants of the perturbing states: for state Y,

$$B_v=0{\cdot}2254-0{\cdot}0013_5(v+\tfrac{1}{2});\qquad G_v=450{\cdot}4(v+\tfrac{1}{2})-2{\cdot}9(v+\tfrac{1}{2})^2;$$

for state X, on the basis of somewhat less reliable figures, we obtain

$$B_v=0{\cdot}2236-0{\cdot}0009(v+\tfrac{1}{2});\qquad G_v=462{\cdot}7(v+\tfrac{1}{2})-5{\cdot}4(v+\tfrac{1}{2})^2.$$

The probable error of the B values in Table 9 varies, but is about $\pm 0{\cdot}0005$ cm^{-1}.

Calculations of perturbing matrix elements similar to those already illustrated for the perturbation at $J=69$ in $v'=3$ have been made for all the perturbations in which extra lines have been found. For the Y perturbations the matrix element is everywhere independent of J: for the X and Z perturbations the results are less definite, but for both these interactions the matrix elements seem to depend on J.

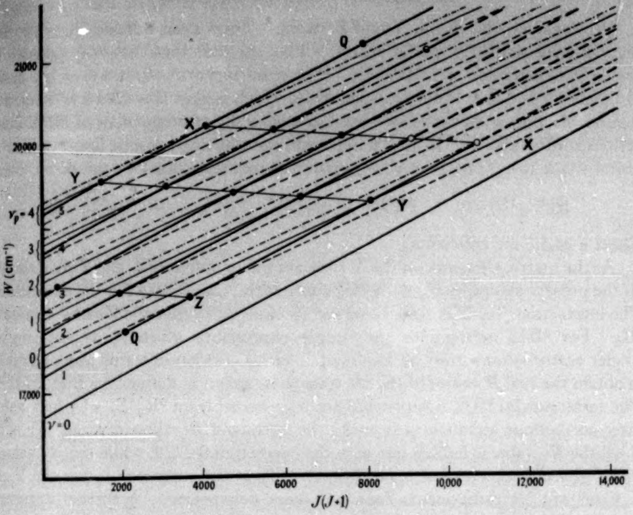

Figure 8. Perturbations in BaO: term values plotted against $J(J+1)$.

Σ: thick continuous lines for the analysed parts; broken lines for the extrapolated regions. Perturbing states: thin lines.

Full circles indicate analysed perturbations: the half filled circle a perturbation analysed in R-branch only; open circles, perturbations noticed in R-branch before culmination.

Table 9. Summary of the Perturbations

$v'(\Sigma^*)$	J^*	B_p	$C+\nu_v^{\Sigma^*}$	Perturbing state	v_p	$\|H\|^2$ (approx.)
1	45·6	—	—	Q	—	—
1	60·8	0·2252	17332	Z	0	—
1	90·1	0·2248	17476·5	Y	0	330
1	104·5	—	—	X	0	—
2	44·0	—	17777	Z	1	—
2	80·2	0·2231	17919·$_9$	Y	1	19
2	96·$_5$	—	—	X	1	—
3	19·3	—	18213	Z	2	—
3	69·2	0·2220	18359·$_4$	Y	2	163
3	86·2	0·2215	18454	X	2	—
4	56·1	0·2206	18792·1	Y	3	96
4	76·2	0·2202	18885	X	3	—
4	98·0	—	—	Q	—	—
5	38·8	0·219	19222·$_2$	Y	4	5
5	64·4	0·220	19308	X	4	—
5	89·4	—	—	Q	—	—

(ii) *Nature of the Perturbing States*

We consider first the X, Y and Z states. Their most notable feature is that they all have similar B and ω values. This suggests that they may perhaps be the three components of a $^3\Pi$ state. The splittings at $J=0$, however, are found to be about 94 and 146 cm^{-1} respectively, which makes this idea less attractive. Before rejecting it, however, we must consider the consequences of $^3\Pi^1\Sigma$ interactions a little further. If they are present, the splitting must be large, indicating Hund's case (*a*). The perturbing matrix elements in this case are of the form:

$$H(^3\Pi_2{}^1\Sigma)=0, \qquad H(^3\Pi_1{}^1\Sigma)=\eta\{J(J+1)\}^{1/2}, \qquad H(^3\Pi_0{}^1\Sigma)=2\xi,$$

where η and ξ are constants.

As the matrix elements for the Y state are independent of J, the Y state should, on the present assumption, be the $^3\Pi_0$ component, the X state the $^3\Pi_1$ component. The interaction $^3\Pi_2{}^1\Sigma$ is zero, however, in case (*a*), so that the Z state cannot be $^3\Pi_2$. For $^3\Pi^1\Sigma$ interactions the simple expressions given above for singlet-singlet perturbations must be modified. Small correction terms must be added to obtain the real B values of the $^3\Pi$ state (here taken as defined by Budó (1935)). The correction for $^3\Pi^1\Sigma$ is very small but is appreciable for $^3\Pi_0{}^1\Sigma$. Unfortunately these corrections are such as to make the corrected B values diverge. Thus for $v'=3$ the B_Y value is 0·2220 but with the correction 0·2229, while the B_X value is 0·2215 (here the correction is negligible). Thus the supposition that the Y and X states are $^3\Pi$ components does not seem convincing. A further argument against this assumption is as follows: for higher J values the matrix elements will alter somewhat, as Hund's coupling case (*a*) is fulfilled only when $A/B_{^3\Pi} \gg J$ (here A is of order 100), and will approach expressions for coupling intermediate between (*a*) and (*b*). This means that $H(^3\Pi_2{}^1\Sigma)\neq 0$ at high J values, and we should expect another set of perturbations. We have not been able to find them.

The possibility is also raised that we have Y as $^3\Pi_0$ and Z as $^3\Pi_1$ in an inverted $^3\Pi$ state. It is hardly fruitful to discuss this in detail, as we have so little information about the Z state: moreover it will be seen below that Z can be explained plausibly as belonging to a $^3\Sigma^-$ state.

The other two perturbing states Z and Q may be the components $^3\Sigma_{J+1}$ and $^3\Sigma_{J-1}$ respectively of a $^3\Sigma^-$ state. Perturbations between $^1\Sigma^+$ and $^3\Sigma^-$ states have been treated by Budó and Kovács (1938–39). Unfortunately we know rather little about the constants of the Z and Q states. We have been able to determine only one B value and the J^* value for six perturbations. It is nevertheless possible to make rough calculations even with these data. Thus the true $B_{^3\Sigma}$ value is equal to the observed value, 0·2252, divided by $(1+J^{-1})$: also the C values must be corrected by adding $\pm(B_{^3\Sigma}J)$. Using the expressions for $B_v=B_0-\alpha\,.\,v$ and for the rotational energy, $B_{^3\Sigma}(J+1)(J+2)$ and $B_{^3\Sigma}(J-1)J$, together with the ordinary vibrational expression $\omega_e(v+\frac{1}{2})-x_e\omega_e(v+\frac{1}{2})^2$ we obtain, using the data of Table 9,

$$B_v=0{\cdot}2233-0{\cdot}0016_5(v+3),$$

$$T_e+G(v+\tfrac{1}{2})=17094+448{\cdot}4(v+\tfrac{1}{2})-(v+\tfrac{1}{2})^2.$$

The assumption of a perturbing $^3\Sigma$ state requires, however, $^3\Sigma^-_{J-1}{}^1\Sigma$ interactions also at about $J=32$ in $v'=2$, and at $J=10$ in $v'=3$. That the first one has not been discovered may be the result of an unusually small matrix element (it is composed of two terms of opposite signs), while the latter would be extremely difficult to discover at such a low J value.

We reach then the following tentative conclusions about the perturbing states. The Y state is probably $^1\Sigma$, and X is probably $^1\Pi$. The Z and Q states may be two components of a $^3\Sigma^-$ state. These are, however, only tentative conclusions, and it seems to us not quite impossible that the X and Y states are sub-states of a $^3\Pi$ state.* This would fit well with the fact that a $^3\Pi$ state, likewise a $^3\Sigma^-$ state, is expected to arise from the ground-state atomic combination $\mathrm{Ba}(^1S)+\mathrm{O}(^3P)$.

§6. DETERMINATION OF VIBRATIONAL CONSTANTS

The Deslandres scheme of band-origins has been given in Table 1. The lower-state intervals vary linearly with v, and the expression

$$G_v'' = 669{\cdot}8_1(v+\tfrac{1}{2}) - 2{\cdot}05_4(v+\tfrac{1}{2})^2$$

represents the observed levels very closely.

There is, however, no such regular variation for the upper-state levels. It is probable that some of this irregularity arises from the effects of the strong Y perturbations. We have accordingly calculated these effects, using the approximate values of the perturbing matrix elements given in Table 9. The results are shown in Table 10. It will be seen that the 'corrected' values of $\Delta G'_{v,v+1}$ do indeed vary more smoothly with v than do the original values, but there are still irregularities which are considerably greater than the experimental error. These doubtless arise from other perturbations which we are unable to treat quantitatively. However, rough values for the vibrational constants of the 'unperturbed' upper state may be derived from these corrected values of $\Delta G'$: we obtain

$$G_v' = 499{\cdot}_7(v+\tfrac{1}{2}) - 1{\cdot}6_4(v+\tfrac{1}{2})^2.$$

Using these figures, and with $\nu_{0,0} = 16722{\cdot}2_5$, we find $\nu_e = 16812{\cdot}_2\,\mathrm{cm}^{-1}$.

Table 10

$v', v'+1$	$\Delta G'_{v,v+1}$ observed	Effect of Y perturbations at $J=0$		$\Delta G'_{v,v+1}$ corrected
		$v'=0$	0·00	
0,1	494·99			496·37
		1	+1·28	
1,2	95·01			93·83
		2	+0·10	
2,3	88·41			89·36
		3	+1·05	
3,4	86·97			86·85
		4	+0·93	
4,5	85·01			83·18
		5	+0·10	

---

* *Note added in proof.* An investigation of the effect of one perturbation on another (Kovács and Lagerqvist, *Ark. Fys.*, 1950, **2**) supports the view that the X and Y states are sub-states of a $^3\Pi$ state.

§7. DISCUSSION AND COMPARISON OF BaO WITH THE OTHER ALKALINE EARTH OXIDES

The results of the present work are summarized in Table 11. The lower $^1\Sigma$ state is probably the ground state of BaO, for the $^1\Sigma^*$–$^1\Sigma$ system is known to be emitted quite strongly by relatively low-temperature flames. It is also probable that both are $^1\Sigma^+$ states, for there are few electron configurations which can give rise to $^1\Sigma^-$ states in this molecule. It is, however, difficult to correlate these, and the perturbing states, with the atomic states of Ba and O because so little is known about their energies of dissociation. By a very long Birge–Sponer extrapolation, $D_0'' = 6{\cdot}_7$ ev., but the error in this value may well amount to some electron volts. For the heat of formation of BaO in its ground state from *ground-state* atoms, there are at least two values. Huldt (1948) has calculated this quantity from measurements of the concentration of Ba atoms in an acetylene–oxygen flame fed with a dilute solution of $BaCl_2$: his result is $5{\cdot}_5$ ev. The second value comes from thermochemical data. The standard heat of formation of BaO_c is -134 kcal. (Bichowski and Rossini 1936): then using the heat of formation of O from $\frac{1}{2}O_2$, 58·6 kcal., the heat of sublimation of Ba (Rudberg and Lempert 1935), 41 kcal., and the heat of sublimation of BaO (Blewett, Liebhafsky and Hennelly 1939), 88 kcal., and, neglecting small effects arising from temperature differences between these measurements, the heat of formation of BaO_g from $Ba(^1S_0) + O(^3P)$ is $(-134 + 88 - 41 - 59) = -146$ kcal. or 6·3 ev. In this cycle, the value known with least certainty appears to be the heat of sublimation of BaO. Earlier measurements of this quantity by Herrmann (1937) gave the much higher value -119 kcal., which leads to -115 kcal. or 5·0 ev. for the heat of formation of BaO_g. However, Herrmann's work is criticized by Blewett, Liebhafsky and Hennelly, and, if their criticisms are valid, the thermochemical result must be taken to be 6·3 ev. We take the mean of this and of Huldt's value, $5{\cdot}9 \pm 0{\cdot}4$ ev. Now, it has been concluded that the lower $^1\Sigma$ state is probably the ground state: further, unless it is really case (*c*), $\Omega = 0$—and there is no evidence for this—it cannot be formed from the ground-state atoms, the lowest states from which it could be formed being $Ba(^3D) + O(^3P)$, $Ba(^3P) + O(^3P)$ and $Ba(^1S) + O(^1D)$ with atomic excitation energies of 1·2, 1·6 and 2·0 ev. respectively. It seems rather unlikely that D_0'' is greater than 6·7 ev., so that the only dissociation products compatible with the present value of the heat of formation seem to be $Ba(^3D) + O(^3P)$.

Table 11. Summary of Constants for BaO

State	$\nu_{0,0}$	ω_e	$x_e\omega_e$	B_e	α_e	D	$r_e \times 10^8$ cm.
$(^1\Sigma^{**}?)$	17477	450	2·9	0·2254	$0{\cdot}0013_5$	—	2·284
$^1\Sigma^*$	16722·3	500	$1{\cdot}6_4$	0·2584	$0{\cdot}0011_1$	$2{\cdot}8 \times 10^{-7}$	2·133
$^1\Sigma$	0	$669{\cdot}8_1$	$2{\cdot}05_4$	$0{\cdot}3124_9$	$0{\cdot}0013_0$*	$2{\cdot}6_5 \times 10^{-7}$	1·940

$* -0{\cdot}0000_2(v+\frac{1}{2})^2$

Finally, it is of some interest to compare the data for $^1\Sigma$ of BaO with the lowest $^1\Sigma$ states of the other alkaline earth oxides. The force constants and internuclear distances are given in Table 12.

The most striking feature of this table is the unexpected way in which the force constants vary in going from BeO to BaO. The trend is unlike that found for the ground states of any other group of oxides, where there is always a monotonic decrease in k_e'' from the lightest to the heaviest member. This irregularity does not appear to be characteristic of this group of metals, for the fluorides, chlorides and hydrides behave quite normally in this respect. Thus we are led to suggest—as the simplest explanation—that some at least of these states may not be the ground states. It may be recalled here that the complex ultra-violet bands attributed to MgO have been observed in absorption at high temperatures (Barrow and Crawford 1945), and it may prove that the lower state of these bands is the ground state of MgO, but they have not yet been analysed. So far as is known this is the only observation on the absorption spectra of these molecules

Table 12. Force Constants and Internuclear Distances for the lowest States of the Alkaline Earth Oxides

	k_e'' (dynes/cm.)	r_e'' (cm.)	Reference
BeO	$7 \cdot 52 \times 10^5$	$1 \cdot 33 \times 10^{-8}$	Lagerqvist and Westöö (1945)
MgO	$3 \cdot 46$	$1 \cdot 75$	Lagerqvist and Uhler (1949)
CaO	$3 \cdot 61$	$1 \cdot 75$	Lagerqvist and Hultin (1950)
SrO	$3 \cdot 40$	$1 \cdot 92$	Almkvist and Lagerqvist (1949)
BaO	$3 \cdot 79$	$1 \cdot 94$	

ACKNOWLEDGMENTS

We are glad to acknowledge our debt to Professor I. Kovács, on whose theoretical work, both published and unpublished, and advice we have drawn heavily, and to Professor E. Hulthén for his keen interest.

REFERENCES

ALMKVIST, G., and LAGERQVIST, A., 1949, *Ark. Fys.*, **1,** 477.
BARROW, R. F., and CRAWFORD, D. V., 1945, *Proc. Phys. Soc.*, **57,** 12.
BICHOWSKI, F. R., and ROSSINI, F. D., 1936, *Thermochemistry of Chemical Substances* (New York : Reinhold).
BLEWETT, J. P., LIEBHAFSKY, H. A., and HENNELLY, E. F., 1939, *J. Chem. Phys.*, **7,** 478.
BUDÓ, A., 1935, *Z. Phys.*, **96,** 219.
BUDÓ, A., and KOVÁCS, I., 1938–39, *Z. Phys.*, **111,** 633.
GERÖ, L., 1935, *Z. Phys.*, **93,** 669.
HERRMANN, G., 1937, *Z. phys. Chem.*, **35B,** 298.
HULDT, L., 1948, *Diss. Stockholm* (Uppsala : Almkvist a. Wiksell).
JAMES, J. A., 1947, *B.A. Thesis*, Oxford.
KOVÁCS, I., 1937, *Z. Phys.*, **106,** 431.
LAGERQVIST, A., and HULTIN, M., 1950, *Ark. Fys.*, **2,** in the press.
LAGERQVIST, A., and UHLER, U., 1949, *Ark. Fys.*, **1,** 459.
LAGERQVIST, A., and WESTÖÖ, R., 1945, *Ark. Mat. Astr. Fys.*, **32A,** No. 10.
MAHANTI, P. C., 1934, *Proc. Phys. Soc.*, **46,** 51.
MECKE, R., and GUILLERY, M., 1928, *Phys. Z.*, **28,** 514.
M.I.T. Wavelength Tables, 1939 (London : Chapman and Hall).
RUDBERG, E., and LEMPERT, J., 1935, *J. Chem. Phys.*, **3,** 628.

Band-Spectrum of ZrO

By M. AFAF
Imperial College, London

Communicated by R. W. B. Pearse; MS. received 9th February 1950

ABSTRACT. The spectrum of ZrO has been photographed in the ultra-violet, the visible and the infra-red, from arcs running under special conditions. This has made possible the identification of three new systems in the ultra-violet, as well as two less conspicuous ones in the infra-red. It has also made it possible to extend the blue system α of ZrO.

---

§ 1. INTRODUCTION

Compounds of titanium and zirconium have special importance in astrophysics. The oxides TiO and ZrO have for long been known to exist in the atmospheres of 'Late Type Stars'. While the former predominates in Class M stars, the latter causes extensive absorption in S type stars. Merrill (1922) was the first to identify the bands of ZrO in stars, and the first to distinguish the two classes M and S separately. After the classification of the M and S stars had been completed King (1924), using an electric furnace for vaporizing and exciting TiO and ZrO in the laboratory, showed that S type stars had a slightly greater temperature than the corresponding M type stars. Richardson (1939), using Saha's 'equation of dissociative equilibrium', attacked the same problem from a theoretical angle, and concluded that though the temperature of S type stars was not different from that of M type stars, the former definitely had a denser atmosphere. Later Bobrovnikoff (see ZrO in Class M stars) established the existence of absorption in ZrO bands in M type stars, the corresponding TiO bands being already known to exist in S type stars. He therefore concluded that the chief distinction between M and S stars perhaps lay in the relative abundance of the two elements in their stellar atmospheres.

On the laboratory side of the work on the ZrO molecule, the most comprehensive contribution is that from Lowater (1932). Three conspicuous triplet systems were identified in the blue, yellow and red by Miss Lowater. It was shown that the lower $^3\Pi$ state was the final state in all the three systems. The systems were termed α, β and γ respectively, and the vibrational constants evaluated. Later, Lowater (1931) studied the rotational structure of the (0, 0), (1, 0) and (0, 1) bands of system α, and derived the rotational constants in both the states of this system. Rotational constants of the states in system γ were determined by Tanaka and Horie (1941) by their analysis of the (0, 0) and (1, 1) bands. The transitions responsible for the systems α, β and γ were supposed to be $C^3\Pi \rightarrow X^3\Pi$, $B^3\Sigma\,? \rightarrow X^3\Pi$, and $A^3\Sigma \rightarrow X^3\Pi$ respectively. The molecular constants thus determined for these states are presented below.

Levels	$\nu_{0,0}$	Multiplet separations	ω_e	$x_e\omega_e$	B_e	α_e
$X^3\Pi$	0	292·1, 313·4	937·20	3·35	0·6189	0·0045
$A^3\Sigma$	16048·4	0·0, 0·0	856·97	3·37	0·5658	0·0077
$B^3\Sigma$?	17483·5	44·9, 36·7	846·28	3·41	—	—
$C^3\Pi$	21599·5	304·4, 397·3	820·58	3·31	0·5333	0·0123

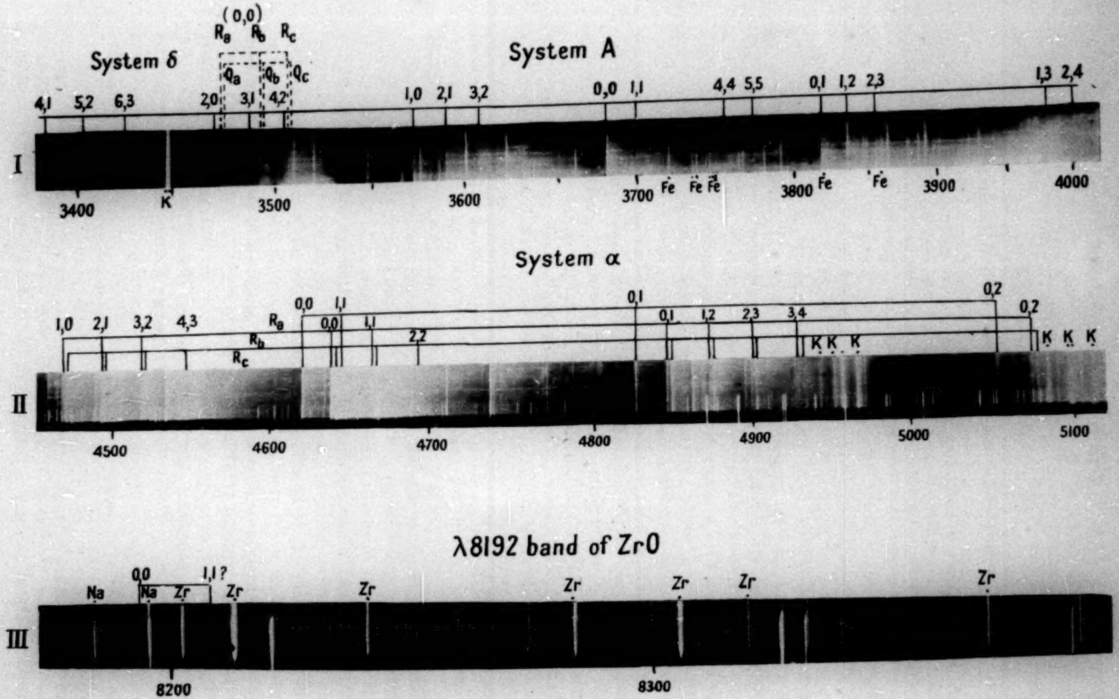

Systems δ, A, α, and λ8192 bands of ZrO.

Johnson (1932) also photographed the ZrO bands in the visible and the infra-red, and confirmed the above analysis.

Meggers and Kiess (1932) have further reported a group of complex bands of ZrO in the region λλ9500–9300. However, they have not offered an analysis of these bands. Many conspicuous and strong bands of ZrO in the visible region also remain unclassified.

Further, there have been doubts about the nature of the ground state of TiO and ZrO. The spectrum of TiO was analysed before that of ZrO, and one singlet and three triplet systems have so far been established for this molecule. Assuming an analogy between TiO and Ca, Lowater (1929) postulated that the ground state of TiO should be $^1\Sigma$ like the ^1S ground state of Ca, and consequently she adopted a $^1\Pi \rightarrow {}^1\Sigma$ transition for the yellow system β of TiO. Miss Lowater could however establish only three triplet systems for ZrO, with a common final level $x^3\Pi$, and so refrained from commenting on the nature of the ground state of ZrO. Quite recently, however, Herbig (1949), after studying the rotational structure in the λ3682 band of ZrO, postulated that this band was the (0, 0) band of a $^1\Sigma - {}^1\Sigma$ system, and raised the same doubts whether $^1\Sigma$ or the $x^3\Pi$ was the ground state of ZrO.

§ 2. EXPERIMENTAL DETAILS

Apart from the electric furnace used by King (1924) to vaporize and excite TiO and ZrO, it appears that the only sources of the spectra of these molecules so far employed have been ordinary low voltage arcs in air. Lowater (1932) used an arc in air with iron or copper poles, on the lower of which was placed ZrO_2 or some other compound of zirconium. The chief disadvantage of this source was the appearance of strong atomic lines due to Zr and the pole material, making the identification of weaker band heads extremely difficult. Different kinds of arcs used by the author are described below.

ZrO_2 arc. Copper electrodes were used. The upper was rather thick (diameter 0·5 in.) and flat at the bottom in order to facilitate rapid conduction of heat along its length. The lower electrode was also of copper, shaped at the upper end into a cylindrical cup of extremely thin walls ($\leqslant$0·01 in.) of about $\frac{1}{4}$ in. diameter and about $\frac{3}{8}$ in. deep. The base of this cylindrical cup was also very thin and separated from the main electrode, except for a wire of about 1 mm. diameter about 1 cm. long. This cylindrical cup at the top of the electrode (henceforth referred to as the anode cup) was filled tightly with zirconium oxide powder. Current was drawn from the 220-volt D.C. mains. As soon as the arc was struck the anode cup became red hot, and the thin copper walls of the anode cup vaporized leaving a hot bead of zirconium oxide on the wire. Finally the arc was maintained between this hot zirconium oxide bead and the thick upper electrode of copper, the arc gap being of the order of 2–3 cm. This gave the strongest source of ZrO bands. The band spectrum of ZrO was very strong even in the central region of the arc, but Zr lines developed with considerable intensity though the spectrum of the electrode material was entirely eliminated (see Plate, III).

ZrF_4 arc. This arc was used often as it yielded very good results. The upper electrode was similar to that mentioned already, and the lower one was also similar in general features, but the walls of the anode cup were quite thick, about 1–1·2 mm. The anode cup was filled with ZrF_4, which contained some KF and water of hydration. Starting with low currents, K and H_2O are the first to vaporize;

the current is then increased until ZrF_4 melts in the cup, and vapours of ZrF_4 begin to rise above the anode cup. This ZrF_4 arc was steady. It appears that under these conditions the temperature of the anode cup is only sufficient to melt ZrF_4 and allow ZrF_4 vapour to rise slowly without rapid oxidization, but this on its journey upward is slowly oxidized. This is supported by the fact that bands of ZrF appear only in the region of the central arc just above the anode cup, whereas bands of ZrO in this region are relatively weak, though the atomic spectrum of Zr is very strong. However, just below the cathode the best excitation conditions are reached, and the atomic spectrum of Zr becomes very weak and the bands of ZrO appear conspicuously. This region was photographed for ZrO bands in the ultra-violet (Plate, I).

If the current is increased slightly at this stage, the steady condition of the arc undergoes sudden change. The temperature in the anode cup rises, and the sudden oxidization sets in within the anode cup, resulting in further heating of the anode cup and vaporizing of the oxidized ZrF_4. The spectral features are about the same throughout the arc which is in the shape of a cylindrical beam of incandescent vapour. The atomic spectra of zirconium and copper become extremely weak, and the bands of ZrO become very strong. However, an unidentified continuum extending from λ2960 to λ4300 develops with sufficient intensity to make this source useless for photographing bands in the ultra-violet (Plate, II).

Zirconium Arc in Moist Hydrogen. This is by far the best source of the ZrO spectrum, though the high price of metallic zirconium makes wide use of this source uneconomical. The electrodes are of the same type as used in the ZrF_4 arc. The anode cup is filled with powered zirconium, and the arc is struck in an atmosphere of hydrogen at atmospheric pressure, in a vacuum jacket cooled from outside by immersing it in water. A few drops of water are left inside the jacket to make the hydrogen sufficiently moist. The two electrodes are kept close together, the arc gap being of the order of a few millimetres. However, when the temperature of the anode cup has risen sufficiently, moisture attacks the zirconium suddenly, and yellow coloured flames shoot out horizontally from the anode cup, showing the purest spectrum of ZrO obtained so far.

Using these arcs the spectrum of ZrO was photographed from λ2560 to λ9000 on various spectrographs. For ultra-violet photography a Hilger E1 quartz spectrograph, and a ten-foot grating in the second order were used. For the visible region, photographs were obtained both on a ten-foot grating and a large glass Littrow spectrograph. The infra-red spectrum of ZrO was photographed on a ten-foot grating. The spectrum of ZrO in the region λ3500 to λ3800 was also photographed in the second order of a twenty-foot grating with 30,000 lines per inch.

§ 3. OBSERVATIONAL DATA

The observed data are recorded in Table 1. The dispersion of the spectrograms which were used for measurements generally ranged from 2·8 A/mm. to 7·6 A/mm. The definition of the spectrograms was very good, and with few exceptions, the records of band heads presented here relate to features, which by one method or the other have been proved by the author to be band heads of ZrO. Doubtful band heads have been neglected, and in the infra-red where the weakness and the complex nature of the spectrum makes the identity of band heads doubtful, the author's opinion has been expressed in column (6). In this column too, the wavelengths of the same band heads, if measured by any other author have been given for comparison. These data have chiefly been quoted from the records published by Lowater (1932). A point of interest here is the wavelength of twelve band heads in the ultra-violet which Miss Lowater mentions: Of these twelve bands only five agree with those measured by the author, and the remaining seven appear to be spurious ; some of them can be identified with the edges of the weak atomic lines, which appear on the spectrograms prepared by the author. The identification of these lines has not been possible, as it appears that they have not been included in Harrison's *Wavelength Tables*, and have also been ignored by other workers due to their extremely low intensity.

It also appears that the group of bands in the infra-red recorded by Meggers and Kiess (1932) belong to the same system as the group of bands observed by the author in the region λλ9000–8600, and consequently data for these ZrO bands from Meggers and Kiess (1932) have been included in the present Table.

In the Table, wavelengths, intensities and wave-numbers of the band heads are given in columns (1), (2) and (3). The analysis of these bands suggested by the author is given in column (4), while column (5) shows the deviation of the observed wave-number of the band head from that calculated from the equation relating the band heads of the system.

Table 1

Data of ZrO Band Heads Degrading towards Longer Wavelength

(1) air	(2) *I*	(3) vac	(4) Classification	(5) (O–C)	(6) Remarks
2940·9	1	33993·7	ϕ (0, 0) R_a		
2950·0	1	33888·4	ϕ (0, 0) R_b		
2967·8	1	33685·2	ϕ (0, 0) R_c		
3023·8	0	33061·4	ϕ (0, 1) R_a		
3033·5	0	32955·7	ϕ (0, 1) R_b		
3052·4	0	32752·2	ϕ (0, 1) R_c		
3110·9	0	32135·7	ϕ (0, 2) R_a		
3121·0	0	32031·8	ϕ (0, 2) R_b		
3390·05	1	29489·7	A (4, 1)	0·8	
3407·89	0	29335·3	A (5, 2)	−1·0	
3425·92	0	29180·9	A (6, 3)	−2·9	
3468·90	1	28819·4	A (2, 0)	0·6	
3472·39	3	28790·5	δ (0, 0) R_a		3472·43†
3473·62	1	28780·3	δ (0, 0) Q_a		
3486·71	2	28672·2	A (3, 1)	0·5	
3491·80	3	28630·4	δ (0, 0) R_b		3491·84*
3493·06	1	28620·1	δ (0, 0) Q_b		
3504·22	1	28528·9	A (4, 2)	2·8	
3506·30	3	28512·0	δ (0, 0) R_c		3506·22*
3507·56	1	28501·7	δ (0, 0) Q_c		
3571·96	8	27987·9	A (1, 0)	−0·1	
3589·87	6	27848·3	A (2, 1)	0·1	3589·81*
3607·61	1	27711·4	A (3, 2)	1·6	
3682·07	10	27151·0	A (0, 0)	0·0	3682·43*
3700·11	2	27018·6	A (1, 1)	0·1	
3754·72	1	26625·6	A (4, 4)	−0·5	
3772·9 ?	0	26497·4	A (5, 5)	—	
3791·6	0	26366·7	A (6, 6)	—	

Table 1 (*cont.*)

(1) air	(2) *I*	(3) vac	(4) Classification	(5) (O–C)	(6) Remarks
3818·32	4	26182·2	A (0, 1)	−0·1	
3836·38	1	26059·0	A (1, 2)	0·9	
3854·18	0	25938·5	A (2, 3)	2·9	
3981·45	3	25109·4	A (1, 3)	1·8	
4000·72	0	24988·4	A (2, 4)	−3·3	
4195·80	0	23826·8	α (4, 1) R_c		4195·81†
4217·0	0	23706·9	α (5, 2) R_b		
4218·98	0	23695·7	α (5, 2) R_c		
4267 ?	0	23429·1	α (7, 4) R_c		
4292·88	1	23287·9			
4313·30	1	23177·6	α (2, 0) R_b		4313·32*
4315·57	1	23165·4	α (2, 0) R_c		
4337·46	1	23048·5	α (3, 1) R_b		4337·55*
4339·66	1	23036·9	α (3, 1) R_c		4340·18*
4358·25	1	22938·6			
4361·96	0	22919·1	α (4, 2) R_b		4361·95*
4364·26	1	22907·0	α (4, 2) R_c		4364·38*
4368·05	1	22887·1			4368·16*
4368·90	0	22882·7			
4386·80	0	22789·3	α (5, 3) R_b		
4389·10	0	22777·3	α (5, 3) R_c		
4452·17	0	22454·7	α (1, 0) R_a		4452·21*
4460·34	2	22413·6			4460·39*
4469·36	3	22368·4	α (1, 0) R_b		4469·38*
4471·45	3	22357·9	α (1, 0) R_c		4471·53*
4493·76	3	22246·9	α (2, 1) R_b		4493·79*
4496·20	3	22234·8	α (2, 1) R_c		4496·26*
4519·07	0	22122·2	α (3, 2) R_b		4519·26*
4521·12	0	22112·3	α (3, 2) R_c		4521·26*
4619·72	8	21640·3	α (0, 0) R_a		4619·82*
4637·70	10	21556·4	α (0, 0) R_b		4637·79*
4640·43	10	21543·7	α (0, 0) R_c		4640·56*
4644·70	0	21524·0	α (1, 1) R_a		4644·68*
4662·70	0	21439·8	α (1, 1) R_b		4663·17†
4665·68	1	21427·1	α (1, 1) R_c		4665·27†
4692·01	0	21306·9	α (2, 2) R_c		
4736·91	6	21105·0			4736·90*
4769·40	2	20961·2			4769·35*
4826·55	1	20713·0	α (0, 1) R_a	isotope ^{94}Zr ^{16}O	4827·38*
4827·45	3	20709·1	α (0, 1) R_a		4827·59*
4846·39	1	20628·2	α (0, 1) R_b	isotope ^{94}Zr ^{16}O	
4847·10	4	20625·2	α (0, 1) R_b		4847·19*
4849·96	4	20613·0	α (0, 1) R_c		4849·72*
4873·74	2	20512·7	α (1, 2) R_b		4873·03*
4875·96	2	20503·1	α (1, 2) R_c		4876·12*
4899·60	1	20404·2	α (2, 3) R_b		4899·76*
4902·36	1	20392·7	α (2, 3) R_c		4902·47*
4926·00	0	20294·8	α (3, 4) R_b		
4929·03	0	20282·4	α (3, 4) R_c		
4996·28	2	20009·3			
5022·95	1	19902·9			
5052·79	1	19785·6	α (0, 2) R_a		5052·91†
5073·94	1	19703·1	α (0, 2) R_b		5073·96†
5077·60	1	19688·9	α (0, 2) R_c		

Table 1 (*cont.*)

(1) air	(2) *I*	(3) vac	(4) Classification	(5) (O–C)	(6) Remarks
8178·76	2	12223·4			spurious
8185·39	1	12213·5			spurious
8192·36	10	12203·2			
8460·25	1	11816·7			violet degrad.
8519·07	2	11735·2			violet degrad.
8525·15	2	11726·8			violet degrad.
8558·48	1	11681·1			A line ?
8574·02	1	11659·9			
8597·38	2	11628·1			
8684·58	2	11511·4			violet degrad.
8695·23	3	11497·1	I (2, 1) a		
8709·3	3	11478·8	I (2, 1) b		
8721·3	3	11463·0	I (2, 1) c		
8734·0	2	11446·4	I (2, 1) d		
8744·10	2	11433·1	I (2, 1) e		
8769·19	2	11400·4	I (3, 2) a		
8784·5	1	11380·6	I (3, 2) b		
8815·0	1	11343·8			spurious
8813·0	1	11341·2			spurious
8820·41	2	11334·2	I (3, 2) e		
8822·32	2	11331·8			
8825·09	1	11328·2			
8852·43	2	11293·2			
8857·50	2	11286·8	I (4, 3) b		
8867·45	1	11274·4			
8868·99	1	11272·2	I (4, 3) c		
8881·23	2	11256·6	I (4, 3) d		
8882·67	2	11254·8			
8892·37	2	11242·5	I (4, 3) e		
8917·12	1	11211·3			
8945·31	1	11176·0			violet degrad.
8950·34	2	11169·7			violet degrad.
8965·51	1	11150·8			violet degrad.

* Bands reported by Lowater (1932). † Bands reported by Johnson (1932).

Band Heads of ZrO (as given by Meggers and Kiess (1932))

(1)	(2)	(3)	(4)	(5)	(6)
9299·56	5	10750·25	I (0, 0) a		
9315·87	5	10731·43	I (0, 0) b		
9329·93	5	10715·26	I (0, 0) c		
9343·19	4	10700·05	I (0, 0) d		
9356·12	3	10685·36	I (0, 0) e		
9358·33	1	10682·74			
9360·34	3	10680·45			
9370·74	3	10668·59	I (1, 1) a		
9387·26	2	10649·82	I (1, 1) b		
9397·21	2	10638·54			
9401·04	2	10634·15	I (1, 1) c		
9402·84	2	10632·17			

(1)	(2)	(3)	(4)	(5)	(6)
9408·92	1	10625·30			
9412·03	2	10621·79	I (1, 1) d		
9413·75	2	10599·58	I (1, 1) e		
9438·24	1	10592·29			
9443·92	1	10585·91	I (2, 2) a		
9453·55	1	10575·14			
9476·65	1	10549·36	I (2, 2) c		
9483·55	2	10541·69			

§ 4. CLASSIFICATION AND ANALYSIS

The bands of ZrO in the ultra-violet have been classified into three systems by the author, the one to the shortest wavelength side being termed ϕ, the next δ and the last A. The conspicuous bands in the visible region have already been classified by Lowater (1932), and the chief contribution of the author lies in remeasuring the bands of ZrO under better conditions, and recording band heads not so far reported. It has thus been possible to fill the gaps in the Deslandres Table of system α, for which several more band heads have been recorded. A headless band structure of ZrO has been observed in the region $\lambda\lambda$7900–7600, but the band lines have not been measured. A band head of ZrO at λ8192 has been recorded and is considered by the author to belong to the (0, 0) band of a new system. Another new system ‘ I ’ of ZrO in the region $\lambda\lambda$9500–8600 has been established and a tentative analysis offered. The group of band heads measured by Meggers and Kiess (1932) forms the main part of system ‘ I ’.

A brief description and discussion on these systems follows.

(i) *System* ϕ, 3121–2940 A.

This system is very weak, lying some distance from the rest of ZrO bands. Of the eight bands discovered for this system, only three at λ2940·9, λ2950·0 and λ2967·8 have any appreciable intensity, the rest being very weak. The first three appear to be the three R heads of the (0, 0) band of the system, the next three of the (0, 1) and the last two, which are extremely faint, belong to (0, 2) band of the system. The vibrational differences $\Delta''\ (v'+\frac{1}{2})$ agree with those in systems α, β and γ, which shows that the lower level of system ϕ is $X^3\Pi$.

Band heads	(0, 0)	$\Delta''1/2$	(0, 1)	$\Delta''3/2$	(0, 2)
R_a	33993·7	*932·3*	33061·4	*925·7*	32135·7
R_b	33888·4	*932·7*	32955·7	*923·9*	32031·8
R_c	33685·2	*932·9*	32752·2	—	—

Since only R heads have been observed in this system, the upper state of system ϕ should be of the same type as $X^3\Pi$, the final level. The upper level of this system should therefore be a $^3\Pi$ state and has been termed $E^3\Pi$. Since no bands have been recorded except from the $v=0$ level of $E^3\Pi$ state, the vibrational constants in the $E^3\Pi$ state cannot be determined. Since $R_a-R_b=105{\cdot}3$ and $R_b-R_c=203{\cdot}3$ cm^{-1} and the multiplet separations $X^3\Pi_1-X^3\Pi_0=292{\cdot}1$, and $X^3\Pi_2-X^3\Pi_1=313{\cdot}4$ cm^{-1} in the lower $X^3\Pi$ state, those in the upper $E^3\Pi$ state could either be $E^3\Pi_1-E^3\Pi_0=186{\cdot}8$ cm^{-1} $(292{\cdot}1-105{\cdot}3)$ or $495{\cdot}4$ cm^{-1} $(292{\cdot}1+203{\cdot}3)$ and $E^3\Pi_2-E^3\Pi_1=110{\cdot}1$ cm^{-1} $(313{\cdot}4-203{\cdot}3)$ or $418{\cdot}7$ cm^{-1} $(313{\cdot}4+105{\cdot}3)$. In the view of the author the smaller multiplet separations of 186·8 and 110·1 cm^{-1} are more probable and have been adopted. The three $\mathrm{E}^3\Pi$ states are therefore supposed to be 33,993·7, 34,180·5 and 34,290·6 cm^{-1} above the $\mathrm{X}^3\Pi_0$ ground state of ZrO.

(ii) *System* δ, 3508–3472 A.

This is another triplet system of ZrO, which, though quite weak compared with the triplet systems α, β and γ in the visible, is several times stronger than the triplet system φ already described. Only six heads have been observed, and all appear to belong to the (0, 0) band. There are three sharp and strong heads of about the same intensity at irregular intervals, and displaced by about 10 cm^{-1} from these on the longer wavelength side are weaker and diffuse heads. The former appear to be three R heads and the latter three Q heads. The analysis is as follows :—

3472·39	(3)	28790·5	(0, 0) R_a	3493·06	(1)	28620·1	(0, 0) Q_b
3473·62	(1)	28780·3	(0, 0) Q_a	3506·30	(3)	28512·0	(0, 0) R_b
3491·80	(3)	28630·4	(0, 0) R_b	3507·56	(1)	28501·7	(0, 0) Q_c

The bands in the singlet system β of TiO, supposed to arise from a $^1\Pi - {}^1\Sigma$ transition, are somewhat similar, for there are four similar double band heads (R and Q heads). Since the bands of the system β of TiO have been designated (0, 0), (1, 1), (2, 2) and (3, 3), i.e. the bands have been supposed to lie in a sequence, one is apt to suppose that the same is the case with the three double headed bands of system δ of ZrO, and that they belong to (0, 0), (1, 1) and (2, 2) bands of a singlet system. This analogy is quite superficial, for whereas in system β of TiO the intensity falls regularly from the (0, 0) to the (3, 3) band, the intensity in the three double-headed bands of system δ is about the same. Nevertheless, if it is supposed that system δ does arise from singlet levels, one has to accept that either the upper or the final level of system δ will be the same as one of those giving rise to singlet system A (to be mentioned later). If the final level is common between system δ and A, the magnitude of $x_e' \omega_e'$ in the supposed upper state of system δ will be $-5{\cdot}80$ cm^{-1}. If on the other hand the initial level is common to both the values of ω_e'' and $x_e'' \omega_e''$ in the supposed final level of system δ should be 1,045·5 and 24·0 cm^{-1} respectively. Evidently both of these conditions are impossible. System δ, therefore, does not appear to arise from singlet levels. The only possibility left is to accept that the system arises from triplet levels and accept the analysis offered. It is difficult to assign these triplet levels, since only band heads of the (0, 0) band are known. If one assumes that system δ shares the initial $\mathrm{E}^3\Pi$ state with system φ, the question at once arises as to why system δ is so much stronger than system φ, even though its final level lies well above the ground state $\mathrm{X}^3\Pi$ of ZrO. The only other possibility is to assume that the final level of system δ is the $\mathrm{X}^3\Pi$ ground state of ZrO. There is no objection to this assumption. If such is the case it may explain why the weaker (0, 1) band heads of this system δ were not observed, for these weak bands would lie on the strong (2, 1) and (3, 2) bands of system A.

The upper state of system δ should either be a Δ or a Σ state, for transition between a Π state and $\mathrm{X}^3\Pi$ state would not give strong Q branches. Since $R_a - R_b = 160{\cdot}1$ cm^{-1} and $R_b - R_c = 118{\cdot}4$ cm^{-1}, the multiplet separations in the upper state of system δ would either be 132·0 and 195·0 cm^{-1} or 410·8 and 473·6 cm^{-1}.

Since Σ states cannot possess such large separations, the upper state is likely to be the D$^3\Delta$ state of ZrO with probably the multiplet separations of 132·0 and 195·0 cm^{-1} lying at 28,780·3, 28,912·3 and 29,107·3 cm^{-1} above the X$^2\Pi_0$ ground state of ZrO. The smaller splittings in the $^3\Delta$ state are more likely than the larger 410·8 and 473·6 cm^{-1} as they are in accordance with other spectra. The larger ones, however, were assumed to be the multiplet separations by the author (1949) when he first reported this system.

(iii) *Singlet System* 'A', 4000–3390 A.

Although this system is only about one third as strong as the triplet systems α, β and γ of ZrO, the singlet nature of the levels responsible for this system A, is beyond doubt. Of the nineteen bands measured by the author, nine are quite conspicuous; the rest are weak. Two bands of this system at λ3682 and λ3590 have been reported by Lowater (1932). The rotational structure of the λ3682 band was studied by Herbig (1949), who measured about 130 lines in the band, and found that they consisted of only two branches, evidently P and R branches. The Deslandres table of system A (given in Table 2) is evidence of the correctness of the classification. However it is observed that $\Delta'(v'+\frac{1}{2})$ and $\Delta''(v''+\frac{1}{2})$ decrease and increase regularly with increase in v'' and v' respectively. This at once suggests that θ has an appreciable magnitude. By usual calculations, it is found that θ has widely different values for different sets of bands. Nevertheless, an average value of $\theta = -0{\cdot}90$ cm^{-1} is found most suitable. The following constants were determined for system A:

$$\begin{array}{lll}
\omega_e' = 843{\cdot}75 \text{ cm}^{-1} & \omega_e'' = 978{\cdot}07 \text{ cm}^{-1} & \nu_e = 27{,}217{\cdot}92 \text{ cm}^{-1} \\
x_e'\omega_e' = 3{\cdot}15 \text{ cm}^{-1} & x_e''\omega_e'' = 5{\cdot}04 \text{ cm}^{-1} & \theta = -0{\cdot}90 \text{ cm}^{-1} \\
y_e'\omega_e' = 0{\cdot}00 \text{ cm}^{-1} & y_e''\omega_e'' = 0{\cdot}072 \text{ cm}^{-1} &
\end{array}$$

Here the values of ω_e and $x_e\omega_e$ are only approximate since they have been determined for the band heads and not the band origins. The formula representing the nineteen band heads is

$$\begin{aligned}
\nu_h^{v',v''} = 27{,}217{\cdot}92 &+ \{843{\cdot}75(v'+\tfrac{1}{2}) - 3{\cdot}15(v'+\tfrac{1}{2})^2\} \\
&- \{978{\cdot}07(v''+\tfrac{1}{2}) - 5{\cdot}04(v''+\tfrac{1}{2})^2 + 0{\cdot}072(v''+\tfrac{1}{2})^3\} \\
&- 0{\cdot}90(v'+\tfrac{1}{2})(v''+\tfrac{1}{2}).
\end{aligned}$$

Only weak bands badly superimposed by other structure have any considerable deviation from this formula (Plate, I).

It is difficult to say what is the nature of the levels involved in this system. Herbig (1949) studied the rotational structure in the λ3682, (0, 0) band, on a spectrogram taken on 20-foot grating in the first order with a dispersion of 3·7 A/mm. The spectrogram published by him is very weak, and the lines cannot be traced to the origin or the head. Nevertheless the identity of the two P and R branches has been established beyond doubt.

Herbig, however, goes on to conclude that a Q branch is definitely absent, which in the author's opinion is not certain. The author obtained a large dispersion spectrum of the λ3682 band on the twenty-one-foot grating with 30,000 lines/inch in the second order giving a dispersion of 0·59 A/mm., and though the spectrum as a whole was much stronger and the definition better than in the one published by Herbig, the P and R branches could not be traced to their origin. In a $^1\Pi_1 \rightarrow {}^1\Pi_1$ transition the relative intensity of the Q branch to P and R branches should be the same as in a $^3\Pi_1 \rightarrow {}^3\Pi_1$ transition. Nevertheless, Lowater (1935) failed to detect any Q branch for the $^3\Pi_1 \rightarrow {}^3\Pi_1$ bands in system α when she studied the rotational structure in the (0, 0), (1, 0), and (0, 1) bands of that system, even though her spectrograms were several times more intense than those prepared by the author or by Herbig. If a Q branch has been overlooked in the λ3682 band, the system A may arise from a $^1\Pi - {}^1\Pi$ transition. But until this is proved to be the case, it may be assumed as more probable that the transition involved is $b^1\Sigma \rightarrow a^1\Sigma$.

Herbig (1949) also established the indentity of the λ3682 band in the spectra of late type stars, and therefore expressed doubts as to which of the two states, $a^1\Sigma$ or $x^3\Pi$, the lower states of singlet and triplet systems respectively, is the ground state of ZrO. In the author's opinion there can be little doubt that the $a^1\Sigma$ state of system A is a low excited state of ZrO, lying somewhere about 1,300 cm^{-1} above the $x^3\Pi_0$ ground state. The reason for this supposition will be presented later while discussing the energy levels of ZrO.

Table 2. Deslandres Table of System ' A '

v' / v''	0	Δ"1/2	1	Δ"3/2	2	Δ"5/2	3	Δ"7/2	4	5	6
0	27151·0	*968·8*	26182·2								
Δ'1/2	*836·9*		*836·4*								
1	27987·9	*969·3*	27018·6	*959·6*	26059·0	*949·6*	25109·4				
Δ'3/2	*831·5*		*829·7*				*829·1*				
2	28819·4	*971·1*	27848·3				25938·5	*950·1*	24988·4		
Δ'5/2			*823·9*								
3			28672·2	*960·8*	27711·4						
Δ'7/2			*817·5*		*817·5*						
4			29489·7	*960·8*	28528·9				26625·6		
Δ'9/2					*806·3*						
5					29335·3					26497·4	
Δ'11/2											
6							29180·9				26366·7

Herbig (1949) has further mentioned an absorption band at λ3571 in the spectra of stars, where the λ3682 band of ZrO has been observed. The absorption band at λ3571 was identified with the OH$^+$ band of the same wavelength by Herbig. This absorption band can now be identified with the λ3571·9 band of ZrO which is the (1, 0) band of system A. There is evidence of the presence of an absorption band at λ3590, (2, 1) in the spectrum of R. Andromedae, examined by the author, but other bands of system A cannot be identified with the same certainty. However, this proves the existence of absorption in the stellar atmospheres of Late Type Stars of bands of system A. If the lower $a^1\Sigma$ state of system A is really a low excited state of ZrO, it will provide an interesting method of determining the difference in the temperature of the various Late Type Stars, for any difference in the above parameter should affect the relative intensity of absorption in the singlet system A compared with that of the triplet system α, β, γ, by altering the relative concentration of ZrO molecules in the low excited $a^1\Sigma$ state.

§ 5. EXTENSION OF SYSTEM α

Since many bands of system α, hitherto unobserved have been recorded by the author, and since these remove serious discontinuities in the Deslandres table of system α, the latter has been reproduced in Table 3 without altering the classification. However band heads designated (8, 8) R_a, R_b and R_c by Lowater (1932) have been identified with $^{94}Zr^{16}O$ (0, 1) R_a, R_b and R_c and it appears that bands designated (0, 4) do not really belong to system α (see Plate, II).

Table 3. Deslandres Table of System A

v' \ v''		0	Δ″1/2	1	Δ″3/2	2	Δ″5/2	3	Δ″7/2	4
0	a	21640·3	*931·2*	20709·1	*923·5*	19785·6	*916·7*	18868·9		
	b	21556·4	*931·4*	20625·0	*921·9*	19703·1	*918·5*	18784·6		
	c	21543·7	*930·9*	20612·8	*922·9*	19688·9	—	—		
Δ′1/2		*814·2*		*814·9*		—				
		813·1		*814·5*		*809·6*				
		814·2		*814·3*		*814·2*				
1	a	22454·7	*930·7*	21524·0	—	—	—	—		
	b	22369·5	*930·0*	21439·5	*926·8*	20512·7	—	—		
	c	22357·9	*930·8*	21427·7	*924·0*	20503·1	(*915·5*)	19587·6		
Δ′3/2		*803·4*		—		—		—		
		808·1		*807·4*		—		—		
		807·5		*807·7*		*803·7*		*805·1*		
2	a	23258·1	—		—	—	—	—	—	—
	b	33177·6	*930·7*	22246·9	—	—	—	20404·7	*912·4*	19492·3
	c	23165·4	*930·6*	22234·8	*927·9*	21306·8	*914·1*	20392·7	*911·3*	19481·4
Δ′5/2		—		—		—		—		—
		802·9		*801·6*		—		—		*801·5*
		—		*802·1*		*805·4*		*801·9*		*801·0*
3	a	—	—	—	—	—	—	—	—	—
	b	23980·5	*932·0*	23048·5	*926·3*	22122·2	—	—	—	20294·8
	c	—	—	23036·9	*926·6*	22112·3	*917·7*	21194·6	*912·2*	20282·4
Δ′7/2				—		—		—		
				—		*796·9*		—		
				789·9		*794·7*		*794·2*		
4	a			—	—	—	—	—		
	b			—	—	22919·1	*918·2*	22000·9		
	c			23826·8	*919·8*	22907·0	*918·2*	21988·8		
Δ′9/2						—		—		
						787·8		*788·4*		
						788·7		*788·6*		
5	a					—	—	—		
	b					23706·9	*917·6*	22789·3		
	c					23695·7	*918·3*	22777·4		

§ 6. ZrO BANDS IN THE REGION λλ7900–7600

The spectrum of ZrO in the region 7900-7600 A. was photographed in the first order of a 10-foot grating with a dispersion of 5·5 A/mm., with the ZrO_2 arc as source. The bands of ZrO in this region are fairly strong, and fairly well resolved; it appears that many headless bands are superposed on each other. The branches can easily be followed at a distance from the origin, though due to superposition of bands, it becomes impossible to locate the origin. C. C. Kiess (1948), who very kindly sent a private communication to the author, mentions several band heads of

ZrO in this region, which cannot be found on the spectrograms obtained by the author, though some of the band heads mentioned by him can be identified with blendings of the rotational lines of the bands. Further study of these bands is required before any conclusions can be drawn.

§7. λ8192 BAND OF ZrO

In complete isolation free from the confusion shown by neighbouring bands, there is a strong band of ZrO in the λ8200 region, forming a conspicuous, though somewhat weak head at λ8192 (see Plate, III). At this dispersion the fine structure of the band is fairly well resolved away from the head. The band is degraded to longer wavelength but the branches remain unresolved at the head. It appears that a P and R branch are fairly well superposed on each other, but as the branch proceeds away from the head the branches diffuse out on the shorter wavelength side, until two weaker components emerge at about λ8350 from beneath the main branch lines. These might be the isotopic lines due to $^{94}\mathrm{Zr}\,^{16}\mathrm{O}$ and $^{92}\mathrm{Zr}\,^{16}\mathrm{O}$. That this isotopic displacement is not observed near the head may be due to the fact that the band is the (0, 0) band of a new system. If it is supposed that the band belongs to triplet levels, if, for instance, a transition $^3\Sigma - {}^3\Sigma$ were responsible, then intercombination of these levels with $\mathrm{X}^3\Pi$, $\mathrm{A}^3\Sigma$ and $\mathrm{C}^3\Pi$ would be expected. It appears that the $\mathrm{A}^3\Sigma$ level of ZrO is not involved in this system, or otherwise a double band head either at 13,845 or 28,251 cm^{-1} should be expected due to the combination between $\mathrm{X}^3\Pi$ and the other $^3\Sigma$ state of λ8192 system. Since no double-headed band can be found in the region mentioned, it is certain that $\mathrm{A}^3\Sigma$ state is not involved. The possibility of $^3\Pi$ states being involved is more remote, for in that case one would expect other band heads of the multiplet in the neighbourhood. One would, therefore, expect that the levels involved in the λ8192 band are singlets. The absence of a Q branch indicates that the transition involved is of $^1\Sigma - {}^1\Sigma$. The λ8192 band may be the (0, 0) band of the system, the weaker and less conspicuous band of ZrO at λ8210 may be the (1, 1) band.

§8. INFRA-RED SYSTEM 'I'

Attention was first drawn to the bands of ZrO in the infra-red by Meggers and Kiess's (1932) publication of the wavelength of the heads of a group of bands in the region λλ9200–9500. The bands have a very complicated structure and are quite weak. Later the author discovered a similar structure between λλ8500–8950 (also very weak), on spectrograms obtained in the first order of a 10-foot grating with the $\mathrm{ZrO_2}$ arc. Further, there appeared to be bands in this region which degrade to shorter wavelength. Assuming that the λλ9200–9500 group of ZrO bands form the (0, 0) sequence of a system of which the λλ8500–8900 group of bands might form the (1, 0) sequence, the author tried to discover some kind of relationship between various band heads; it is hard to claim, however, that a successful analysis of this system has been made. Doubts are increased by the fact that many bands in the λλ8500–8900 group and as well in the λλ9200–9500 are unclassified, but the general similarity of structure between the two groups of bands supports the view that they belong to the same system. The following constants were determined, but should be accepted with reservation:

$\omega_e' = 862{\cdot}9\,\mathrm{cm}^{-1}$, $x_e'\omega_e' = 8{\cdot}8\,\mathrm{cm}^{-1}$, $\omega_e'' = 945{\cdot}4\,\mathrm{cm}^{-1}$ and $x_e''\omega_e'' = 8{\cdot}6\,\mathrm{cm}^{-1}$, The formula representing the system 'I' is

$$\nu_h^{v',v''} = \left\{\begin{matrix} 10790{\cdot}8 \\ 10771{\cdot}9 \\ 10756{\cdot}8 \\ 10742{\cdot}6 \\ 10727{\cdot}8 \end{matrix}\right\} + \{862{\cdot}9(v'+\tfrac{1}{2}) - 8{\cdot}8(v'+\tfrac{1}{2})^2\} - \{945{\cdot}4(v''+\tfrac{1}{2}) - 8{\cdot}6(v''+\tfrac{1}{2})^2\}.$$

The ω_e'' in the final level of this system has about the same magnitude as that in the $x^3\Pi$ ground state of ZrO, but it would be misleading to conclude that this $x^3\Pi$ level is really involved in the system 'I', while it will be quite premature to assume that because five heads have been recognized for each band the levels involved are really quintets, since several triplet systems are known which show five heads. Table 4 gives the Deslandres table of the system 'I'.

§ 9. ENERGY LEVELS OF ZrO

Having described the various systems of bands of the ZrO molecule, it is desirable to discuss certain energy levels already known for this molecule. The first to arouse interest is the ground state, since much confusion had persisted about it. It has very recently been suggested by Herbig (1949) that perhaps the $a^1\Sigma$ state of system A instead of $x^3\Pi$ state might be the ground state of ZrO. A similar suggestion had previously been made for the TiO molecule by Miss Lowater. One fact however stands out for our guidance, viz. that absorption in the stellar atmospheres by the ZrO molecule takes place from both $a^1\Sigma$ and $x^3\Pi$ states. This shows that these states lie very close to each other. Since the absorption from the $x^3\Pi$ state is much stronger than from the $a^1\Sigma$, it appears that it is the latter which is a low excited state. This is supported by the following consideration: A Zr atom in the $^3F_2$ ground state and an oxygen atom in its ground state $^3P_0$ in combination are expected to give rise to singlet, triplet and quintet levels. Since only $a^1\Sigma$ and $x^3\Pi$ occur as lower states of the systems known, these two may be expected to originate from a combination of the zirconium and oxygen atoms in their ground states. If so, the energy of dissociation in the two states should provide a clue as to which is the excited state; denoting the energy of dissociation in the two states by $D(x^3\Pi)$ and $D(a^1\Sigma)$, we find

$$D(x^3\Pi) \simeq 62200\,\mathrm{cm}^{-1}; \quad D(a^1\Sigma) \simeq 47400\,\mathrm{cm}^{-1}$$

from Birge–Sponer extrapolation.

From this it would appear that the $a^1\Sigma$ state lies about 15,000 cm^{-1} (62,200–47,400) above the ground state. This, although showing that the $a^1\Sigma$ state is an excited state, cannot be considered to be an accurate value, since $x_e\omega_e$ is not accurately known for $a^1\Sigma$ where $y_e\omega_e$ is also appreciable.

However, if we picture the ZrO molecule as Lowater (1929) had pictured the molecule of TiO, that is, in the molecule two of the least strongly held electrons of the Zr atom are influenced in such a manner as effectively to complete the oxygen shell, the only contribution towards the momenta will come from such a depleted Zr atom. The electronic configuration of the latter will be the same as Zr^{++}. The nature of the low-lying states of the molecule of ZrO will be analogous to the low-lying states of Zr^{++}. The ground state of the latter is a triplet state, and the singlet states of the doubly ionized Zr atom lie a little above the triplet ground state. It would appear, therefore, that in the ZrO molecule also the triplet state lies deeper than the corresponding singlet state. Therefore one would expect

$x^3\Pi$ as the ground state and $a^1\Sigma$ as a low excited state of ZrO. This should also be the case with TiO. If the correspondence between Zr^{++} and ZrO holds quantitatively for these excited states, one would expect the $a^1\Sigma$ state to lie between

Table 4. Deslandres Table of System 'I'

v' \\ v''		0	$\Delta''1/2$	1	$\Delta''3/2$	2	$\Delta''5/2$	3
0	a	10750·3						
	b	10731·4						
	c	10715·3						
	d	10700·1						
	e	10685·3						
$\Delta'1/2$		—						
		—						
		—						
		—						
		—						
1	a			10668·6				
	b			10649·5				
	c			10632·2				
	d			10621·8				
	e			10599·6				
$\Delta'3/2$				*828·8*				
				829·0				
				830·8				
				834·6				
				833·5				
2	a			11497·4	*911·5*	10585·9		
	b			11478·8	—	—		
	c			11463·0	*913·6*	10549·4		
	d			11446·4	—	—		
	e			11433·1	—	—		
$\Delta'5/2$						*814·6*		
						—		
						—		
						—		
						—		
3	a					11400·5		
	b					11380·0		
	c					—		
	d					—		
	e					11334·2		
$\Delta'7/2$						—		
						—		
						—		
						—		
						—		
4	a							—
	b							11286·8
	c							11272·2
	d							11256·6
	e							11242·5

$2{,}534/2{\cdot}57 = 986\ \mathrm{cm}^{-1}$ and $3{,}835/2{\cdot}34 = 1{,}639\ \mathrm{cm}^{-1}$ above the ground state, where 2·57 and 2·34 are the factors by which multiplet separations are reduced in the $x^3\Pi$ state of ZrO compared with the ^3F ground state of Zr^{++}. At an average, therefore, the $a^1\Sigma$ state should lie about $\frac{1}{2}(986 + 1{,}639) = 1{,}300\ \mathrm{cm}^{-1}$ above the

$x^3\Pi_0$ ground state. The $b^1\Sigma$ state should therefore lie roughly at (27,151·0 + 1,300) = 28,451 cm^{-1} above the $x^3\Pi_0$ ground state of ZrO. It is evident that absorption is possible from such a low excited state as $a^1\Sigma$ in the stellar atmospheres, where sufficient molecules may be maintained in that state at the temperature prevailing.

There is also some doubt concerning the upper state of system β. The multiplet separations in this state are 44·9 and 36·7 cm^{-1}; Lowater (1932) assumed that this state was the $B^3\Sigma$ state, but furnished no explanation as to why multiplet splittings were so high in an $A^3\Sigma$ state. Furthermore, Johnson (1932) has reported many weaker band heads to each main band of system B, which might well have formed in unusually strengthened satellite branches. This would support the hypothesis that the state of system β is $B^3\Delta$ with multiplet separations of 44·9 and 36·7 cm^{-1}. The smaller magnitude of multiplet separations in a $^3\Delta$ state compared with an $a^3\Pi$ state would further be in keeping with the general rules. A summary of the constants in the various levels of ZrO is given in Table 5.

Table 5

State	$\nu_0^{0,0}$	ω_e	$x_e\omega_e$	B_e	α_e	$-D_e$
$x^3\Pi$	0	937·20	3·35	0·6189	0·0045	$1{\cdot}413 \times 10^{-7}$
$a^1\Sigma$	*130·0*	978·07	5·04	—	—	—
$A^3\Sigma$	16048·4	856·97	3·37	0·5658	0·0077	$1{\cdot}477 \times 10^{-7}$
$B^3\Delta$	17483·5	846·28	3·41	—	—	—
$C^3\Pi$	21599·5	820·58	3·31	0·5333	0·0123	$1{\cdot}521 \times 10^{-7}$
$b^1\Sigma$	*2845·1*	843·75	3·15	—	—	—
$D^3\Delta$	28922·5	—	—	—	—	—
$E^3\Pi$	33993·7	—	—	—	—	—

A point to be noted is that the ω_e and B_e values for the TiO molecule in its ground state are 1,008·1 and 0·5352 cm^{-1}. This is surprising as it appears that whereas ω_e decreases from TiO to ZrO, B_e actually increases. This is perhaps the only example known of its kind.

ACKNOWLEDGMENTS

The author expresses his deep sense of obligation and gratitude to Dr. R. W. B. Pearse, under whose guidance the preceding work had been pursued, for many helpful discussions. The author further expresses his gratitude to the Sunni Central Board of Waqfs, Lucknow (India), who financed and made possible the present work by awarding a scholarship to the author.

REFERENCES

Afaf, M., 1949, *Nature, Lond.*, **164**, 752.

Bobrovnikoff, N. T., 1933, *ZrO in Class M Stars, Perkins Obs. Misc. Sc. Papers*, Reprint No. 23.

Herbig, G. H., 1949, *Astrophys. J.*, **109**, 109.

Johnson, L. W., 1932, *Phil. Mag.*, Ser. 7, **14**, 286.

Kiess, C. C., 1948, *Publ. Astr. Soc. Pacif.*, **60**, 252.

King, A. S., 1924, *Publ. Astr. Soc., Pacif.*, **36**, 140.

Lowater, F., 1929, *Proc. Phys. Soc.*, **41**, 557; 1932, *Ibid.*, **44**, 51; 1935, *Proc. Roy. Soc.* A, **234**, 355.

Meggers, W. F., and Kiess, C. C., 1932, *J. Res. Nat. Bur. Stand., Wash.*, **9**, 325.

Merrill, P. W., 1922, *Astrophys., J.*, **56**, 457.

Richardson, R. S., 1939, *Astrophys. J.*, **48**, 354.

Tanaka, T., and Horie, T., 1941, *Proc. Phys.-Math. Soc., Japan*, **23**, 464.

LETTERS TO THE EDITOR

The Photo-Disintegration of Oxygen into Four Alpha-Particles

Observation of $^{16}O \rightarrow 4\,^4He$ photo-disintegration stars in nuclear emulsions irradiated by 23 MeV. bremsstrahlung was reported recently by Goward, Titterton and Wilkins (1949). Over a hundred of these stars have now been identified, using 23 and 25 MeV. bremsstrahlung, and give some information concerning the mechanism of the disintegration.

The processed plates (Ilford E1) were searched twice, and every star was measured and its apparent momentum unbalance $|\Delta|$ calculated, following the techniques described by Goward and Wilkins (1950). Detailed measurement of every star avoids misinterpretation of four-particle stars with one small or obscured prong; only after considerable experience thus gained was it considered permissible to pick out oxygen stars by inspection (some 15 in the present experiments). The accuracy of measurement obtained is shown in Figure 1 (*a*); only stars with $|\Delta| < 1{\cdot}0$ were accepted for further analysis.

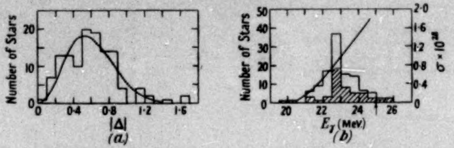

Figure 1 (*a*). Apparent momentum unbalance, $|\Delta|$, for all suspected $^{16}O \rightarrow 4\,^4He$ stars, in units of (mass number × particle energy in MeV.)$^{1/2}$.
The fitted curve is of the form $(K\,|\Delta|)^2 \exp-(K\,|\Delta|)^2$.

Figure 1 (*b*). Histogram showing the gamma-quantum energy E_γ for all stars with $|\Delta| < 1{\cdot}0$ 25 MeV. is the approximate spectral limit for the highest energy irradiation; stars not involving an ^8Be ground state nucleus are shown shaded. A curve of absolute cross section, σ, is added.

The gamma-quantum energy E_γ appropriate to a star is $E_T + 14{\cdot}5$ MeV., where E_T is the total energy of the alpha-particles of the star. Figure 1 (*b*) shows an E_γ histogram for all accepted stars, and the superposed cross section curve is probably accurate to about ±50%. Several possible modes of disintegration may be considered, e.g.

$$^{16}O + h\nu \rightarrow {}^{12}C^* + {}^4He, \qquad {}^{12}C^* \rightarrow {}^8Be + {}^4He, \qquad \ldots\ldots (1)$$

$$^{16}O + h\nu \rightarrow {}^8Be + {}^8Be^*, \qquad \ldots\ldots (2)$$

$$^{16}O + h\nu \rightarrow {}^{12}C^* + {}^4He, \qquad {}^{12}C^* \rightarrow {}^8Be^* + {}^4He, \qquad \ldots\ldots (3)$$

$$^{16}O + h\nu \rightarrow {}^8Be^* + {}^8Be^*, \qquad \ldots\ldots (4)$$

where an asterisk denotes an excited level. Following the methods given by Goward, Telegdi and Wilkins (1950), the disintegration energies, Q_B, of any intermediate ^8Be nuclei may be calculated. Six Q_B values are obtained for each star, of which no more than two can be significant.

Figure 2 (*a*) shows part of the Q_B histogram obtained. Most of the 66 stars which give a Q_B value less than 0·25 MeV. clearly involve a ground-state ^8Be nucleus and are instances of reactions (1) or (2); the 12 additional stars giving a Q_B value less than 0·4 MeV. are doubtful. No star gave more than one Q_B value less than 0·4 MeV.

To distinguish reaction (2) stars, a Q_B histogram is plotted (Figure 2 (*b*)) corresponding to the tracks opposite to those giving $0 < Q_B < 0{\cdot}25$ MeV. in Figure 2 (*a*). The characteristic level structure of ^8Be should be obtained, obscured only by a continuum from reaction (1) stars. No significant structure is obtained, and reaction (2) therefore accounts for few, if any, stars.

Figure 2 (*c*) shows a Q_B histogram for the 49 stars which give no Q_B values less than 0·25 MeV. Although no significant ^8Be level structure appears, any such structure would here be obscured by a continuum of twice the area for reaction (4) stars and five times the area for reaction (3) stars. The present statistics are hardly adequate to support or eliminate reaction (3), involving, for instance, a 3 Mev. level ^{8}Be nucleus, but they are adequate to eliminate a reaction (4) involving two such nuclei.

Ignoring the unlikely possibility of direct splitting into four alpha-particles, the likely reactions are, therefore, (1) and (3), both passing through ^{12}C. These may be further investigated by plotting a histogram for the function

$$Q_C = E_T - (4E_A/3) - (M_\gamma^2/12) + \tfrac{1}{3}M_\gamma \cos\theta_A \,.\, E_A^{1/2}, \qquad \ldots\ldots (5)$$

where E_A (Mev.) is the energy of an alpha-particle whose track makes an angle θ_A with the incident gamma-quantum, and $M_\gamma = 0{\cdot}023E_\gamma$. Q_C is significant only when E_A refers to the first alpha-particle emitted, and is then the total disintegration energy of the intermediate ^{12}C nucleus. For the 66 possible reaction (1) stars, only two Q_C values need be plotted, one of which is significant. As shown by the theoretical curve, Figure 3 (*a*) is consistent with disintegration via a 9·7 Mev. ^{12}C level (e.g. Gibson 1949) of total observed width approximately 1·8 Mev. and true width approximately 1·3 Mev. For the 49 possible reaction (3) stars, four Q_C values (one significant) per star are plotted in Figure 3 (*b*). The present statistics are inconclusive, except that any ^{12}C level concerned is certainly above 9·7 Mev. A level around 11 Mev. would be consistent both with Figure 3 (*b*) and the slightly higher effective threshold energy of these stars indicated by Figure 1 (*b*).

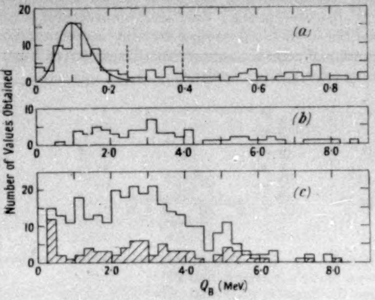

Figure 2.

(*a*) Low energy Q_B values for all possible intermediate reactions ^{8}Be (or ^{8}Be*)→2 ^{4}He+Q_B. Allowing for the errors shown in Figure 1 (*a*), the fitted curve shows the expected histogram shape if 66 stars involve ground state ^{8}Be nuclei, with $Q_B = 0{\cdot}1$ Mev. and negligible width.

(*b*) Q_B values for excited ^{8}Be nuclei occurring in an assumed reaction ^{16}O→^{8}Be+^{8}Be*.

(*c*) Complete Q_B histogram for stars having no Q_B value $<0{\cdot}25$ Mev. Values for stars with a Q_B value between 0·25 and 0·4 Mev. are shaded.

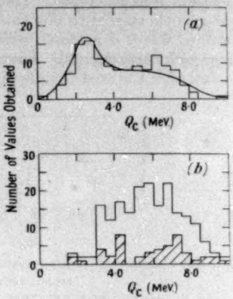

Figure 3.

(*a*) Q_C values for possible intermediate reactions ^{12}C*→3 ^{4}He+Q_C, proceeding via an ^{8}Be ground state nucleus. The fitted curve assumes a 9·7 Mev. ^{12}C level ($Q_C = 2{\cdot}4$ Mev.), width 1·3 Mev.

(*b*) Q_C values for stars not involving ^{8}Be ground state nuclei. Shaded values are for stars also shown shaded in Figure 2 (*c*).

To sum up the above analysis, some 50 to 55% of the stars observed were formed by reaction (1) via the ^{12}C 9·7 Mev. level and the ^{8}Be ground level. The remainder were probably formed by reaction (3) via levels as yet undetermined.

Atomic Energy Research Establishment,
Harwell, Didcot, Berks.
26th June 1950.

F. K. Goward.
J. J. Wilkins.

Gibson, W. M., 1949, *Proc. Phys. Soc.* A, **62**, 586.
Goward, F. K., Telegdi, V., and Wilkins, J. J., 1950, *Proc. Phys. Soc.* A, **63**, 402.
Goward, F. K., Titterton, E. W., and Wilkins, J. J., 1949, *Proc. Phys. Soc.* A, **62**, 460.
Goward, F. K., and Wilkins, J. J., 1950, *Proc. Phys. Soc.* A, **63**, 662.

Ground State ^{8}Be Nuclei in Photo-Disintegration Stars

Recent studies of photo-disintegration stars, formed in nuclear emulsions by irradiation with 23–25 MeV. bremsstrahlung, have shown that ground state ^{8}Be nuclei occur frequently in the disintegrations $^{12}C \rightarrow 3\ ^{4}He$ (Goward, Telegdi and Wilkins 1950) and $^{16}O \rightarrow 4\ ^{4}He$ (Goward and Wilkins 1950 b). The characteristic appearance of such stars is illustrated by Figures 1 and 2, the tracks of the ground state ^{8}Be alpha-particles appearing as a distinctive, not necessarily symmetrical, 'V'. Two further similar disintegrations have now been observed in a boron-loaded emulsion, and may almost certainly be identified as $^{11}B \rightarrow {}^{3}H + {}^{8}Be$ with the aid of momentum balance analysis (Goward and Wilkins 1950 a, Goward, Titterton and Wilkins 1950). As shown in Figure 3, the characteristic 'V' is again in evidence.

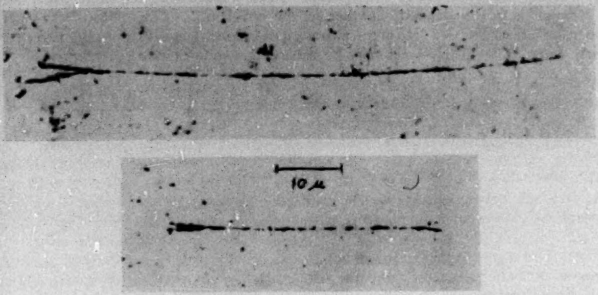

Figure 1. Photo-disintegrations $^{12}C \rightarrow {}^{4}He + {}^{8}Be$.
Observers: Mrs. A. M. Brown and Miss W. Ruck.

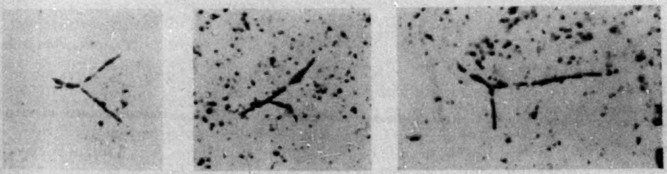

(*a*) (*b*) (*c*)

Figure 2. Photo-disintegrations $^{16}O \rightarrow 2\,{}^{4}He + {}^{8}Be$.
Observers: Mrs. J. M. Taylor and Miss W. Ruck.

The accuracy with which the disintegration energy of ^{8}Be can be deduced from measurement of the 'V' has been shown by Goward, Telegdi and Wilkins (1950) for $^{12}C \rightarrow 3\ ^{4}He$ stars and by Goward and Wilkins (1950 b) for $^{16}O \rightarrow 4\ ^{4}He$ stars. The former stars tend to give less accurate results since the star centres are generally not so well defined.

Some confusion appears to be common regarding the expected appearance of stars such as those mentioned above. It is often assumed that the ^{8}Be (ground state) nucleus will produce a single thick track (Hänni, Telegdi and Zünti 1948, Millar and Cameron 1950). On the contrary, the lifetime of ^{8}Be is too short, according to Wheeler (1941), for it to form an appreciable track before disintegration, and its disintegration energy ($\sim 0{\cdot}1$ MeV.) is sufficient to ensure an observable angle between the two alpha-particle tracks in the majority of stars. Scattering by other atoms in the emulsion significantly assists resolution of the tracks. Difficulties of observation do arise, however, as discussed below, particularly when one track is very short. An observable angle may be obtained even when the ^{8}Be nucleus is emitted with considerable energy, for example 20 Mev., as in the photo-fission event reported by Goward, Titterton and Wilkins (1949); scattering ensures some resolution of the tracks at such energies.

Figure 2 (*c*) illustrates the difficulties of distinguishing the presence of ^{8}Be nuclei with certainty in some stars. Although the ^{8}Be nucleus is emitted with about 3 Mev. kinetic energy in this case, the angle between the resulting tracks happens to be small; one track is consequently short and easily overlooked. Such a track is much more easily overlooked when formed vertically beneath another in the emulsion. Thus some $^{16}\mathrm{O} \rightarrow 4\,{}^4\mathrm{He}$ stars may be mistaken for $^{12}\mathrm{C} \rightarrow 3\,{}^4\mathrm{He}$ stars, although momentum analysis usually reveals the error. Similarly some $^{12}\mathrm{C} \rightarrow 3\,{}^4\mathrm{He}$ stars may be recorded as one or two particle tracks.

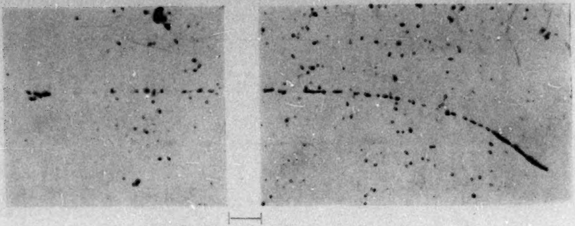

60 microns not shown

Figure 3. Photo-disintegration $^{11}\mathrm{B} \rightarrow {}^3\mathrm{H} + {}^8\mathrm{Be}$.
Observer: Mrs. A. M. Brown.

Note: All figures are reproduced to the same scale.
Photomicrographs: N. F. Shammon.

The search for the reaction $^{14}\mathrm{N} \rightarrow {}^6\mathrm{Li} + 2\,{}^4\mathrm{He}$ (Wilkins and Goward 1950) is essentially an extreme case of the same difficulty. Although a balance of evidence was obtained favouring assignation of a few stars to this reaction, no certain differentiation was possible from $^{16}\mathrm{O} \rightarrow 4\,{}^4\mathrm{He}$ stars with one very short (unobservable) alpha-particle track from ^{8}Be. More recent experiments using slightly higher gamma-ray energies, which might be expected to produce a greater proportion of stars identifiable as nitrogen, have, so far, failed to do so. The upper limit to the cross section must certainly, therefore, be reduced by a factor of four from the original estimate.

Atomic Energy Research Establishment,
Harwell, Didcot, Berks.
26th June 1950.

J. J. Wilkins.
F. K. Goward.

Goward, F. K., Telegdi, V. L., and Wilkins, J. J., 1950, *Proc. Phys. Soc.* A, **63**, 402.
Goward, F. K., Titterton, E. W., and Wilkins, J. J., 1949, *Nature, Lond.*, **164**, 661; 1950, *Proc. Phys. Soc.* A, **63**, 172.
Goward, F. K., and Wilkins, J. J., 1950 a, *Proc. Phys. Soc.* A, **63**, 662; 1950 b, *Ibid.*, **63**, 1171.
Hänni, H., Telegdi, V. L., and Zünti, W., 1948, *Helv. Phys. Acta*, **21**, 203.
Millar, C. H., and Cameron, A. C. W., 1950, *Phys. Rev.*, **78**, 78.
Wheeler, J. A., 1941, *Phys. Rev.*, **59**, 27.
Wilkins, J. J., and Goward, F. K., 1950, *Proc. Phys. Soc.* A, **63**, 663.

Pile Neutron Absorption Cross Sections of some of the Elements

Measurements have been made using a pile oscillator in the Graphite Low Energy Experimental Pile at Harwell of the absorption cross sections of a number of elements.

The pile oscillator was used in the following way. A sample of the element to be measured was taken rapidly from the edge to the centre of the pile, left at the centre for twenty seconds, and then rapidly removed from the pile. The sample was then left out of the pile for twenty seconds, and the whole cycle repeated many times. This periodic motion of the sample produced a periodic change in the reproduction constant of the pile, which in turn caused a modulation of the pile power.

It may be shown that, under these circumstances, the fractional depth of modulation (the actual depth of modulation divided by the mean power level) is proportional to the total absorption cross section of the sample (Weinberg and Schweinler 1948).

The absorption cross sections of the samples measured were compared with the absorption cross section of boron, and for the latter we took the value of 710 barns at 2,200 m/sec. given by Ross and Story (1949). If f_s and f_B are the fractional depths of modulation produced per atom of the sample and per atom of boron respectively, the pile neutron absorption cross section of the sample is given by $\sigma_S=\sigma_B f_S/f_B$, where $\sigma_B=710$ barns is the absorption cross section of boron.

Since boron follows a $1/v$ cross-section law, if the element being measured follows a $1/v$ law also, the pile neutron cross section will be the value of the thermal neutron cross section at 2,200 m/sec. In any case, since the graphite pile neutron flux is predominantly thermal, the pile absorption cross sections will be very nearly equal to the thermal absorption cross sections unless the elements have absorption resonances at energies only slightly above thermal energy.

There were three possible sources of error to be considered in making these measurements:

(*a*) That the change in reproduction constant produced by the sample was not entirely due to absorption of neutrons. For samples with a very small absorption cross section the effects of slowing down and scattering of neutrons are also important. These effects were investigated separately, and it was found that for all the elements listed in the table below these effects were negligible.

(*b*) That there was appreciable self-screening in the sample. If the sample has a large nuclear cross section contained in a small volume, then the neutron flux throughout the sample will not be constant. Thus it would be incorrect to compare one sample having self-screening with another which has none.

Self-screening may be avoided by uniformly dispersing the sample through a large volume. This may be done either by mixing the sample with powdered graphite or by dissolving a salt of the element in heavy water, since both graphite and heavy water have small absorption cross sections. Some of the elements of large cross section were measured by dissolving one of their compounds in heavy water, and thus there was no self-screening effect. In other cases this was not done, and corrections had to be applied for the self screening. This was done by empirically determining the self-screening effect, using different volumes of powdered graphite all containing the same weight of cobalt chloride (a compound with a large cross section).

(*c*) That the chemical sample used was contaminated with small quantities of other elements of large cross section. This meant that chemical analysis had to be carried out for very many of the samples used. (To illustrate the accuracy required in the chemical analysis, it should be noted that, in the case of phosphorus, for example, one part per million of boron contamination will change the absorption cross section by 1%.)

In the Table below we list the cross sections measured. The standard errors quoted are a combination of the errors in the pile measurements and uncertainties in the self-screening corrections.

The cross sections are classified into three categories, A, B and C.

Category A: Those elements for which there was no self-screening correction, and either a complete chemical analysis was made on the sample or the element was specially prepared in a pure state.

Element	Absorption cross section (units of 10^{-24} cm^2)	Classification	Element	Absorption cross section (units of 10^{-24} cm^2)	Classification
Aluminium	0·212 ±0·005	A	Magnesium	0·057 ±0·006	B
Antimony	7·6 ±0·5	C	Manganese	12·8 ±0·8	C
Argon	0·62 ±0·04	A	Molybdenum	2·95 ±0·15	C
Arsenic	4·9 ±0·25	C	Nickel	4·8 ±0·3	C
Barium	1·25 ±0·04	B	Nitrogen	1·76 ±0·05	A
Bismuth	0·0205 ±0·0015*	—	Palladium	10·0 ±0·7	C
Boron	710	A	Phosphorus	0·193 ±0·007	A
Bromine	8·7 ±0·6	C	Platinum	15·0 ±1·0	C
Calcium	0·40 ±0·02	A	Potassium	1·89 ±0·06	B
Cerium	<0·92†	—	Selenium	11·4 ±0·5	B
Chlorine	31·3 ±0·8	B	Silicon	0·16 ±0·01	B
Chromium	3·1 ±0·2	C	Sodium	0·50 ±0·015	A
Cobalt	38·2 ±3·0	B	Strontium	1·35 ±0·05	B
Columbium	1·26 ±0·13	B	Sulphur	0·49 ±0·02	B
Copper	3·6 ±0·25	C	Tantalum	21·2 ±1·5	C
Gadolinium	37600 ±1500	A	Tin	0·70 ±0·04	B
Hafnium	110 ±20	C	Titanium	5·0 ±0·3	C
Iodine	7·4 ±0·35	C	Tungsten	20·5 ±1·5	C
Iron	2·4 ±0·2	C	Vanadium	4·4 ±0·3	C
Lead	0·28 ±0·01	B	Zinc	1·09 ±0·05	B
Lithium	65·5 ±2·0	A	Zirconium	0·250 ±0·025	A

* This measurement was made by irradiating bismuth in a known thermal neutron flux and subsequently measuring the alpha activity of the polonium produced.

† This sample was very impure, and only a partial chemical analysis was made.

Category B: Those elements for which there was no self-screening correction, but no chemical analysis was made on the sample.

Category C: Those elements for which a self-screening correction was applied and no chemical analysis was made on the sample.

All the chemicals used in categories B and C were the purest we could obtain, but it is still possible that they may have contained impurities of large cross section. This means that the quoted cross-section figures may be subject to a systematic error.

We have not attempted to compare our values with the large number of values already appearing in the published literature, since a very comprehensive account of the published data is given by Ross and Story (1949).

We would like to express our thanks to the members of the Chemical Inspectorate branches of the Ministry of Supply at Chatham and Woolwich for the many chemical analyses made during the course of these measurements, and to the Director of the Atomic Energy Research Establishment for permission to publish this Letter.

Atomic Energy Research Establishment,
Harwell, Didcot, Berks.
15th June 1950.

F. C. W. Colmer.
D. J. Littler.

Ross, M., and Story, J. S., 1949, *Rep. Prog. Phys.*, **12** (London: Physical Society), p. 291.
Weinberg, A. M., and Schweinler, H. C., 1948, *Phys. Rev.*, **74**, 851.

The Effect of Screening of the Cross Section for Pair Production by Electrons

In photographic plates exposed to cosmic-rays there have been observed events interpreted as pair production by high energy electrons colliding with nuclei.* It is of interest to estimate the effect on the cross section for this process of the screening of the field of the nucleus by the atomic electrons, since screening reduces considerably the cross section for pair production by high energy photons (Bethe and Heitler 1934).

The cross section for pair production by an electron in the (unscreened) Coulomb field of a nucleus has been calculated by Racah (1937); for a 1,000 MEV. incident electron the value given is $64{\cdot}6\,Z^2r_0^2/(137)^2$. ($Z$ is the atomic number of the nucleus and $r_0(=e^2/mc^2)$ is the classical electron radius.)

In this letter the effect of screening (as given by the Thomas–Fermi model) is estimated using the Weiszäcker–Williams method (Williams 1935). (The *ratio* of screened to unscreened cross sections is found.) This is done in two ways : (*a*) the field of the incident electron is decomposed into that of a distribution of ' photons '; for the cross sections for pair production by photons in Coulomb and screened nuclear fields the values of Bethe and Heitler (1934) are used; (*b*) the effective photon distribution of a screened nuclear field is found (see, for example, Heitler and Peng 1943) and Borsellino's values (Borsellino 1947) for the cross section for pair production by a photon in the field of an electron are used. In Borsellino's work recoil of the initially stationary electron is taken into account, but the effect of exchange between this electron and the electron of the pair is neglected. This should have only a small effect on the total cross section.

It is found that for $Z=40$ the cross section is decreased by 5·6 or 6·2% according to (*a*) or (*b*) respectively.

For a typical emulsion (Kodak NT4, the radiation length for which is 2·8 cm.) the cross section per unit volume neglecting screening is $1{\cdot}04\times10^{-2}$ cm^2 per cm^3. Since screening is a small effect the approximation is made that the cross sections for the various atoms of the emulsion are all decreased in the same ratio by screening, this ratio being that for $Z=40$, an average value. Using Racah's result for normalization it follows that the screened cross section per unit volume is $0{\cdot}98\times10^{-2}$ cm^2 per cm^3.

Pairs may also be produced in electron–electron collisions. If it is assumed that the cross section for this process is approximately $65\,r_0^2/(137)^2$, the cross section per unit volume for the emulsion is $2{\cdot}7\times10^{-4}$ cm^2 per cm^3. The collisions with atomic electrons thus contribute an additional 3% to the cross section per unit volume for nuclear collisions.

The characteristic length for pair production by a 1,000 MEV. electron is therefore 99 cm. or 35 radiation lengths.

For a 10,000 MEV. electron the results are : unscreened cross section $=180\,Z^2r_0^2/(137)^2$; decrease due to screening (method (*b*), $Z=40$) $\doteq 18\%$; characteristic length $=42$ cm. $=15$ radiation lengths.

Department of Mathematical Physics,
University of Birmingham.
14th July 1950.

D. G. RAVENHALL.

BRADT, H. L., KAPLON, M. F., and PETERS, B., 1950, *Helv. Phys. Acta*, **23,** 43.
BETHE, H. A., and HEITLER, W., 1934, *Proc. Roy. Soc.* A, **146,** 109.
BORSELLINO, A., 1947, *Nuovo Cim.*, **4,** 4.
HEITLER, W., and PENG, H. W., 1943, *Proc. R. Irish Acad.*, **54,** 107.
RACAH, G., 1937, *Nuovo Cim.*, **14,** 3.
WILLIAMS, E. J., 1935, *K. Danske Vidensk. Selsk.* **13,** 4.

---

* Remarks by Professor Occhialini at the Como Conference (1949) and Bradt *et al.* (1950).

Background Tracks in Electron-Sensitive Nuclear Emulsions

For many experiments in which electron-sensitive nuclear plates are used the background tracks are no serious disadvantage; there are, however, a number of experiments which could be done with these plates if the background could be eliminated or reduced.

The importance of the problem can be seen from the fact that in unshielded Ilford G5 plates kept at ground level, 250 electron tracks are produced per mm^2 of a 200 μ thick emulsion per day. This large background has been variously ascribed to cosmic radiation and to an internal contamination of the plates themselves. The experiments described below show that contamination plays a minor part.

As a preliminary experiment plates were left down a mine 600 metres below ground. At this depth the cosmic-ray intensity is completely negligible, yet these plates showed a density of background tracks almost identical with that found in plates kept at ground level. If however, the plates below ground were screened by 2 in. of lead on all sides, the number of background tracks was decreased by a factor of 9 (see Table). This made it clear that in the mine the majority of the tracks in the unscreened plates were due to γ-rays emitted by traces of radioactive material present in the surrounding rock. Although the γ-activity of the rock (a Silurian sandstone) could not be measured directly, the β-activity of a sample of the rock was investigated using a GM2 counter, and it was found to possess an activity of the order required to explain the results.

Next we shall consider whether the remaining background observed in shielded plates stored down the mine is due to contamination inherent in the plate, i.e. in the emulsion or in the glass support, or to γ-rays emitted by the container or in the lead shielding used. A lead screen 2 in. thick would, of course, be expected to cut down the total number of γ-rays by a much bigger factor than the observed decrease in number of background tracks.

The obvious contaminants to consider are the natural radio-elements of the uranium and thorium series. The degree of contamination of the emulsion itself can be seen at once to be exceedingly small from the very small number of α-particle tracks observed. $0{\cdot}040 \pm 0{\cdot}008$ α-tracks were observed to be produced per mm^2 per day in a G5 emulsion 200 μ thick. Since there will only rarely be β-particles emitted unassociated with α-particles, the electron tracks arising from such contamination constitute less than 0·1% of those observed in the screened plates.

A more serious possibility is radioactive contamination of the glass. This certainly contains thorium, presumably in approximate equilibrium with its products. The 'truncated stars' familiar to all workers with these plates demonstrate this. A count of alpha tracks arising from the glass showed that $0{\cdot}06 \pm 0{\cdot}007$ per mm^2 are produced per day. Although on the average about twice as many α- as β-particles are emitted for any of the natural radiaoctive series, this degree of contamination may not be negligible since the β-particles will have a much longer range in glass than their associated α-particles and will therefore be able to reach the emulsion from greater depths.

Experiments on some weakly contaminated zirconium oxide placed in contact with the emulsion surface enabled a measure to be made of the ratio of electron tracks to α-particle tracks observed under such conditions. A count of α- and β-tracks passing through the emulsion surface showed that in this case the ratio of β- to α-tracks observed was 15 ± 3. (The errors here do not represent normal statistical fluctuations so much as a certain non-uniformity of contamination.) The contamination of the zirconium was believed to be mainly uranium, on the basis of some subsidiary counter experiments. This would be in equilibrium with the two β-emitters ^{234}Th and ^{234}Pa which follow the decay of ^{238}U but would probably not be in equilibrium with the rest of the series. The glass contamination, being mainly of the complete thorium series, would give a greater ratio of α- to β-tracks as well as a higher average α-particle energy so that the ratio 15 : 1 may be regarded as an upper limit for the ratio of β- to α-tracks emerging from the glass.

Then the number of β-tracks entering the emulsion from the glass will not be more than approximately 1 track per mm^2 per day, or less than 3% of the total tracks in screened plates.

Gamma-radiation which would arise from even greater depths in the glass has still to be considered. The following argument shows, however, that this is not important.

In an infinite block of glass, the average number of γ-rays absorbed and giving rise to electron tracks in any small region will be equal to the number emitted in the same region apart from a factor of perhaps 3 or 4 arising from multiple scattering of γ-rays. As the number of γ-quanta emitted in passing down the radioactive series is comparable with the number of β-particles, the number of tracks crossing any small region of glass due to γ-rays will be roughly the same as that of β-particles directly emitted. Although the glass base used for the emulsion is of infinite thickness as far as electrons are concerned it is very far from this for γ-radiation which in consequence will not have built up a density which approaches the density to be expected in a thick block.

The only remaining contaminants which need to be considered are potassium 40 and carbon 14. To give the observed number of tracks in the screened emulsions, about 1·4% by weight of ordinary potassium would be required; this can at once be ruled out (Faust 1950). Allowing for the limited range of β-particles, probably some 10% of potassium might be needed in the glass to give the same effect. In fact, only about 0·15% is present, thus accounting for perhaps 1·5% of the number for which an explanation is needed. The effect of carbon 14 is of the same order; if the proportion of ^{14}C in carbon from biological sources is 1 in 10^{12} as found by Anderson *et al.* (1947) about 1 track per mm^2 will be produced per day in the emulsion, representing 3% of those observed.

It would then seem reasonable to hope for a reduction of background by a further factor of 10, in appropriate conditions, before the tracks arising from present plate materials become the main source of background. It is clear that most of the background tracks in the shielded plates are still due to γ-radiation arising outside the plate, presumably in the shielding itself. Attempts are being made to improve the situation by using 'cleaner' screening.

We are most grateful to the National Coal Board and to Mr. G. Morris, the manager of the Jubilee pit, for making possible the experiments described, and to Mr. Charles Parry for his very practical assistance throughout our operations underground.

Electron Tracks in G5 Emulsion, 200μ thick.

Plate	Date of development	No. of tracks per mm^2	Increase over 6 days
Control developed when plate 2 was taken down mine	20.6.50	435 ± 12	—
Plate kept in mine screened by 2 in. of lead	26.6.50	620 ± 15	183 ± 20
Plate kept above ground	26.6.50	2080 ± 70	1640 ± 70

Much of the necessary track-counting was done by Mrs. E. M. Munday.

Physics Department,
Birmingham University.
24th July 1950.

J. H. Fremlin.
Madeline C. Walters.

Anderson, E. C., *et al.*, 1947, *Phys. Rev.*, **72**, 931.
Faust, W. R., 1950, *Phys. Rev.*, **78**, 624 (L).

The Attainment of Very Low Temperatures by a Two-Stage Adiabatic Demagnetization Process

For the attainment of very low temperatures by adiabatic demagnetization of a paramagnetic salt, the initial magnetization process is normally carried out at a temperature of about 1° K. In order to remove most of the electron spin entropy at this temperature it is necessary to use very high magnetic fields (of the order of 20 kilogauss). To avoid the use of such large magnetic fields, we have thought it desirable to attempt to develop a two-stage apparatus in which the magnetization of the second stage is carried out at about 0·1° K., this temperature being produced by demagnetization of the first stage. In this way it is possible to remove almost the whole of the electron spin entropy by using a field of only a few kilogauss, such as can be provided by an ordinary air-cooled, low power electromagnet or by a permanent magnet.

The main obstacle to the successful realization of a two-stage process has been the construction of a satisfactory thermal switch for making and breaking thermal contact between the stages. A solution to this difficulty has been provided by the results of experiments on the thermal conductivity of superconductors in which it has been shown that, at low temperatures, the thermal conductivity of a superconductor may be very much lower than that of a normal metal but is restored to the normal value when the superconductivity is destroyed by a magnetic field (Hulm 1949, Rademakers 1949, Heer and Daunt 1949, Mendelssohn and Olsen 1950). The use of this property to provide a thermal switch between the stages has been suggested by Heer and Daunt (1949) and by Mendelssohn and Olsen (1950).

We have made some preliminary tests of the practicability of this method using the arrangement illustrated in Figure 1. The first stage A consisted of a compressed cylinder of iron ammonium alum and the second stage B was a cylinder, of similar size, of diluted copper potassium sulphate (mixed crystals of zinc potassium sulphate +10% copper potassium sulphate). The two stages were suspended in an enclosure which was cooled by liquid helium and were connected by a wire of very pure lead L which served as the thermal switch.

The procedure adopted was as follows : (*a*) Both stages were cooled to the temperature of the outer enclosure (0·9° K.) by means of helium exchange gas. (*b*) An electromagnet was symmetrically placed so that a field of about 4,200 gauss was applied to both stages. When the heat of magnetization had been removed, the exchange gas was pumped away. (*c*) The magnet was slowly lowered so that the upper stage was demagnetized while the lower stage remained in the field. During this procedure the lead wire was, at all times, in a field greater than the threshold value (800 gauss) so that there was good thermal contact between the stages and, as the cooling proceeded, heat was transferred in an approximately reversible way from the lower stage to the upper. In the final position of the magnet, the lower stage was still in a field of about 4,200 gauss, the lead wire was in a position where the stray field was about 1,000 gauss and the stray field on the upper stage was about 600 gauss. This latter field was then compensated by means of an auxiliary permanent magnet. (*d*) After waiting a few minutes for equilibrium to be established, the field was removed. As soon as the field on the lead wire fell below 800 gauss, the lower stage was effectively insulated from the upper.

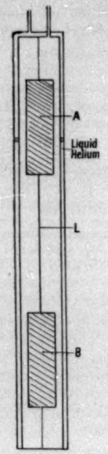

Figure 1.

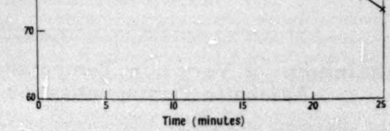

Figure 2.

The Curie temperature of the lower stage after demagnetization was found to be $T^* \sim 0{\cdot}01^\circ$ which is near the limit determined by the specific heat anomaly due to interaction between the nuclear moment and the electronic moment of the copper ion. The temperature of the upper stage was 0·12°.

The variation of $1/T^*$ with time for the lower stage is shown in Figure 2. Over the initial part of the curve where T^* is nearly constant, we are in the region of the specific heat anomaly where there is likely to be considerable difference between T^* and the true thermodynamic temperature. From the subsequent part of the curve we have attempted to estimate the rate of heat inflow assuming that T^* does not differ appreciably from T and that the specific heat can be extrapolated from high temperature measurements (Benzie and Cooke 1949) using a $1/T^2$ law. The result obtained is a heat inflow of the order of 100 ergs/min. There is no doubt that the insulation could be considerably improved by small modifications in the design of the apparatus.

One of us (J. H.) wishes to make grateful acknowledgment to the Pressed Steel Company Ltd., Cowley, for a Research Fellowship.

The Clarendon Laboratory,
Oxford.
4th July 1950.

J. Darby.
J. Hatton.
B. V. Rollin.

Benzie, R. J., and Cooke, A. H., 1949, *Nature, Lond.*, **164**, 837.
Heer, C. V., and Daunt, J. G., 1949, *Phys. Rev.*, **76**, 854.
Hulm, J. K., 1949, *Nature, Lond.*, **163**, 368.
Mendelssohn, K., and Olsen, J. L., 1950, *Proc. Phys. Soc.* A, **63**, 2.
Rademakers, A., 1949, *Physica*, **15**, 849.

Superconductivity of Lead Sulphide, Selenide and Telluride

During the course of some measurements on the electrical conductivity of lead telluride we recently had an opportunity to investigate, by magnetic measurements, whether superconductivity was exhibited by this compound at low temperatures. When it was found to be a superconductor, we thought it worth while also to examine lead selenide and lead sulphide by the same method. The measurements were only of a preliminary kind, but we feel that the results may be of some interest.

The electrical conductivity of lead sulphide at low temperatures has been investigated by a number of workers with conflicting results. The first measurements, made by McLennan *et al.* (1930), indicated that lead sulphide is a superconductor with a transition temperature near 4·2° K. In subsequent measurements by Meissner *et al.* (1933) it was found that, although some specimens exhibited superconductivity, others did not, and it was concluded that the superconductivity must be due to a trace of lead in some of the specimens. (Lead selenide was also found to be not superconducting.) In more recent measurements by Dunaev (1947) it was again found that lead sulphide was not a superconductor. In all these investigations measurements were made by observing the voltage drop across a specimen carrying a current, so that, except in the case of measurements on single crystals, the results would be obscured by the existence of contact resistance at grain boundaries.

We have recently carried out a series of measurements in which the specimen was mounted in the centre of a mutual inductance incorporated in an A.C. bridge. On reducing the temperature of the specimen, the onset of superconductivity could be detected by a change of mutual inductance due to the exclusion of magnetic field from the volume of the specimen, which caused an unbalance of the bridge. This method is independent of the existence of contact resistance between individual grains of the specimen.

A specimen of lead sulphide was prepared by heating the correct proportion of the pure elements together *in vacuo* to a temperature above the melting point (1,120° C.) and then cooling rapidly to room temperature. The ingot produced in this way was found to be superconducting with a transition temperature near 5° K. The threshold curve was measured at temperatures down to 1° K., and the limiting threshold field at this temperature was found to be about 750 gauss. As the threshold curve was significantly different from that of pure lead, and superconductivity was not observed at temperatures above 5° K., we conclude that the result was not due to contamination of the specimen with excess lead. Furthermore, from the magnitude of the bridge unbalance we were able to deduce that the measuring field was excluded from the whole bulk of the specimen and not merely from a small part of it. In order to eliminate the possibility that the result might be due to the existence of a surface film of superconducting material on the specimen, we repeated the measurements after the specimen had been powdered in a mortar and the powder compressed into a cylinder. Again superconductivity was exhibited. It is interesting to note that the electrical resistance of this compressed powder specimen obtained from normal current and voltage measurements at room temperature and at 90° K. indicated that it was a semiconductor with a large negative temperature coefficient of resistance. The semiconducting property is probably due to the presence of a surface layer on the grains due to the action of oxygen, which is known to have strong influence on the electrical properties of sulphides. The result indicates that measurements of current and voltage may be extremely unreliable as a test of superconductivity except in the case of single crystals. The superconducting property does seem to depend on the state of the material, since a cylinder pressed from commercial (B.D.H.) lead sulphide powder was not a superconductor.

Similar measurements were also made on specimens of lead selenide and telluride prepared in the same way as the sulphide ingot. In both cases superconductivity was observed, the transition temperature and threshold curve being nearly the same as for the sulphide.

We feel that these measurements make it seem probable that the sulphide, selenide and telluride may themselves be superconductors and that the results are not due merely to superconducting impurity in the specimens. The possibility that the results are due to the existence of a superconducting network throughout the specimen cannot be excluded, and it would be desirable to investigate this by a study of the Meissner effect in these compounds.

One of us (J.H.) would like to make grateful acknowledgment to the Pressed Steel Company Ltd., Cowley, for a Research Fellowship.

The Clarendon Laboratory,
Oxford.
4th July 1950.

J. Darby.
J. Hatton.
B. V. Rollin.

Dunaev, J. A., 1947, *C. R. Acad. Sci. U.R.S.S.*, **55**, 21.
McLennan, J. C., Allen, J. F., and Wilhelm, J. O., 1930, *Trans. Roy. Soc. Can.*, **53**, 111.
Meissner, W., Franz, H., and Westerhoff, H., 1933, *Ann. Phys., Lpz.*, **17**, 593.

Heat Flow in Superconductive Alloys

In our recent experiments on the heat transport in superconductors (Mendelssohn and Olsen 1950) it was found that whereas the heat conductivity of pure metals decreases on their becoming superconductive, in certain other cases an increase was observed. The decrease can be explained by the fact that the entropy of the superconductive electrons, i.e. those carrying the supercurrent, is zero (Daunt and Mendelssohn 1946). Consequently, as the temperature decreases a steadily increasing number of electrons is withdrawn from the conduction process. The increase in heat flow on the other hand seems to indicate some new process of heat transport competing with the decrease in the ordinary heat conduction of the metal. In one particular case, a specimen of columbium, the curves for the normal and the superconductive state were in fact found to cross over. The normal state can always be realized by applying a magnetic field greater than the threshold value and it was observed that, whereas between 8° and 4° K. the heat conduction was smaller in the superconductive state than in the normal one, below 4° K. the position was reversed. According to our conception of this new type of heat transport we expected this process to depend strongly on the purity of the specimen, and there were indeed indications that the columbium was less pure than some of the other metals investigated. An effort was therefore made to create artificially similar conditions by adding a small amount (0·1%) of bismuth to very pure lead. The results, while showing a deviation of the curves in the expected direction did not, however, produce a crossing over.

We have now measured the heat conduction of pure lead as well as that of alloys with 0·02%, 0·1%, 0·2% and 0·5% bismuth. While detailed analysis of the observations has to be left to a later communication, a brief summary of the main results seems indicated since they allow a decision on the problem mentioned above. The curves for the heat conduction of these alloys in the superconducting and in the normal state plotted against temperature are shown in the Figure. The curves for lead with 10% of bismuth and part of the superconductive curve of pure lead have also been added.

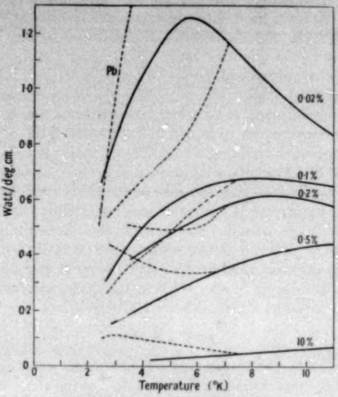

Heat conductivity of Pb–Bi alloys.

——— Normal state. – – – Superconductive state.

As was to be expected the absolute value of the heat conduction in the normal state decreases with increasing impurity content, and there are indications that the maximum in the heat conduction is shifted to progressively higher temperatures. In the specimens with the highest and the smallest bismuth content the superconductive curve departs from the normal one at a finite angle but in opposite directions. With the intermediate percentages, a gradual change of the superconductive curve from one extreme to the other can be observed, and in the case of PbBi 0·2% an actual crossing over of the two curves does occur.

The interpretation we have given for this new process of heat transport is that of a circulation of electrons in the superconductor somewhat similar to the mechanism causing the high heat flow in liquid helium II. The possibility of this circulation depends on a departure from the state of zero induction found in pure superconductors and the general change in behaviour with increasing impurity content is in good agreement with our model. The present results seem to rule out an alternative explanation proposed by Hulm (1949) who attributes the high heat flow in the superconducting state to an increased lattice conduction. Making the assumption that the Debye waves are not scattered by the superconductive electrons, an increased lattice conduction in the superconductive state may indeed be possible. However, as our results show, the superconductive curves for PbBi 0·5% and PbBi 0·2% intersect the curves for the heat conduction of the *purer* specimens. It is clearly very difficult to assume that lattice conduction in an impure superconductive specimen should exceed that in a purer one under similar conditions. In fact the values at 2·5° for superconductive PbBi 0·5% are of the same order as those of pure lead.

The Clarendon Laboratory,
Oxford.
10th July 1950.

K. Mendelssohn.
J. L. Olsen.

Daunt, J. G., and Mendelssohn, K., 1946, *Proc. Roy. Soc.* A, **185**, 225.
Hulm, J. K., 1949, *M.I.T. Int. Conf. Low Temp. Rep.*, p. 90.
Mendelssohn, K., and Olsen, J. L., 1950, *Proc. Phys. Soc.* A, **63**, 2.

The Dielectric Properties of some Alkaline Earth Titanates at Low Temperatures

1. STRONTIUM TITANATE.

Willis Jackson and Reddish (1945), and Coursey and Brand (1946) observed that solid solutions of $SrTiO_3$ in $BaTiO_3$ have ferroelectric Curie points at temperatures below the Curie point of pure $BaTiO_3$, the downward displacement of the Curie point increasing steadily as the amount of $SrTiO_3$ is increased. Von Hippel and others (1946) found that the dielectric constant of a polycrystalline specimen of pure $SrTiO_3$ increased from about 220 at room temperature to about 380 at −90° C. Since these results indicated that $SrTiO_3$ might itself be ferroelectric at very low temperatures, the dielectric properties were investigated in this laboratory down to liquid helium temperatures.

The sample was prepared by heating a mixture of Analar $SrCO_3$ and TiO_2 at 1,200° C. for 3 hours, grinding the resulting material into a fine powder, pressing the powder into disc form in a steel die and finally sintering the disc at 1,400° C. for 3 hours. This produced a hard, ceramic specimen, consisting of a mass of small crystallites and having a density about 20% less than that of a single crystal. In deriving the dielectric constant of the material from the measured capacity of the specimen, allowance was made for porosity with the aid of the formula obtained for ceramic specimens of $BaTiO_3$ by Rushman and Strivens (1947).

From room temperature down to about 50° K. the dielectric constant ϵ at 50 cycles per second, 5 volts per cm., followed the well-known Curie–Weiss law

$$\epsilon=C/(T-\theta) \qquad \ldots\ldots (1)$$

with $C=8{\cdot}3\times10^4$, $\theta=-35°$ K. At temperatures below 50° K., ϵ was smaller than predicted by equation (1) and tended to a steady value of about 1,300 as the absolute zero was approached. Hardly any change in ϵ occurred between 4·2° and 1·3° K., the lowest temperature of measurement. Since there was no evidence of the existence of a dielectric constant peak, and ϵ at 4° K. was independent of field strength for values of the latter up to 25,000 v/cm., it is reasonable to conclude that $SrTiO_3$ is not ferroelectric at low temperatures.

The above results do not support Smolenskii's (1950) recent conclusion that $SrTiO_3$ has a Curie point at 10° K.; this was apparently based on an application of equation (1) to the dielectric constant of $SrTiO_3$ at room temperature and above, which shows the danger of a too literal use of the Curie–Weiss law at temperatures greatly removed from the Curie temperature.

2. BARIUM TITANATE.

Since Merz (1949) has recently measured the spontaneous polarization of single domain $BaTiO_3$ crystals down to 90° K., it is of interest to note that we have extended dielectric measurements on multi-domain $BaTiO_3$ crystals, previously reported for high temperatures (Hulm 1947), down to liquid hydrogen temperatures. Above 90° K. the results were roughly in agreement with those of Merz, in that the spontaneous polarization changed suddenly at the minor transition points at about 280° K. and 200° K., and dropped to a value of about 10 micro-coulombs per cm^2 at 90° K. Below 90° K. we observed an interesting effect not previously reported for $BaTiO_3$, viz. that the coercive field strength of the ferroelectric hysteresis loop, which was practically constant from room temperature down to 90° K., rose at an ever increasing rate as the temperature was lowered, and at 20° K. was almost double the 90° K. value for a typical crystal. Although the observed maximum polarization for a given applied field dropped simultaneously from 10 to about 5 micro-coulombs per cm^2, there was no evidence of a genuine drop in the spontaneous moment of the crystal; it appears that the drop in maximum polarization was merely a secondary effect of the increase in coercive field, which made it increasingly difficult to align completely the spontaneous moment in the direction of the applied field.

The steep rise of the coercive field of $BaTiO_3$ at low temperatures, or in other words, the tendency of the spontaneous moment of each individual domain to 'freeze' into a given direction, brings to mind a similar effect in KH_2PO_4, reported by Busch and Ganz (1942). In a check measurement on a KH_2PO_4 crystal in the present work, the coercive field was practically constant at 2,600 v/cm. from 120° K. down to 60° K., and then rose steeply, reaching 18,000 v/cm. at 30° K. Although this ' freezing-in ' effect is probably a fairly general feature of ferroelectric behaviour at low temperature, no explanation of it appears to be offered by existing theories of ferroelectricity.

I wish to thank Dr. E. B. Mendoza for cooperating in the liquid helium measurements.

Royal Society Mond Laboratory,
Cambridge.
14th July 1950.

J. K. HULM.

BUSCH, G., and GANZ, E., 1942, *Helv. Phys. Acta*, **15**, 50.
COURSEY, P. R., and BRAND, K. G., 1946, *Nature, Lond.*, **157**, 297.
VON HIPPEL, A., BRECKENBRIDGE, R. G., CHESLEY, F. G., and TISZA, L., 1946, *Industr. Engng. Chem.*, **38**, 1097.
HULM, J. K., *Nature, Lond.*, 1947, **160**, 127.
JACKSON, WILLIS, and REDDISH, W., 1945, *Nature, Lond.*, **156**, 717.
MERZ, W. J., 1949, *Phys. Rev.*, **76**, 1221.
RUSHMAN, D. F., and STRIVENS, M. A., 1947, *Proc. Phys. Soc.*, **59**, 1011.
SMOLENSKII, G. A., 1950, *Doklady Akad. Nauk S.S.S.R.*, **70**, 405.

REVIEWS OF BOOKS

La théorie de la relativité restreinte, par O. COSTA DE BEAUREGARD. Pp. 173. (Paris : Masson et Cie, 1949.) No price.

During the last ten years the author has published nearly twenty papers containing many interesting and important ideas on the special theory of relativity. The present volume is an exposition of the theory from the point of view adopted in these researches and is intended primarily for readers who have previous knowledge of the subject. These readers will find the book well worth study, especially those who are unfamiliar with the author's original papers. On the other hand, I do not consider that M. de Beauregard has succeeded in his attempt to produce a book which also meets the needs of those wishing to read the subject for the first time. This is not important, however, as there is already in existence a large number of introductory expositions.

In both his researches and in this book the author presents the special theory of relativity in a general tensor form and, whenever possible, avoids consideration of sections of the Minkowski world at constant time. In a Foreword Prince Louis de Broglie discusses the implications of this point of view. While agreeing that the concept of simultaneity in space–time cannot be entirely abandoned, he points out that M. de Beauregard has succeeded in illuminating some facts which are obscure in the usual theory. The Foreword concludes with a list of the topics on which M. de Beauregard has produced original ideas.

Chapter I is divided into three sections which deal respectively with mechanics and optics from Newton to Einstein, tensors in pseudo-euclidean spaces, and repeated integrals. The usual theory of special relativity is presented in Chapter II, while the following chapter is devoted entirely to electromagnetism; it contains an account of the work of E. Henriot.

Chapter IV deals with several topics. Section A is given up to a discussion on the concept of force. It is well known that the classical equations

$$\mathbf{F}\,dt=d(m\mathbf{v}), \qquad \mathbf{F}\,.\,d\mathbf{r}=dW$$

are not covariant for a Lorentz transformation. M. de Beauregard introduces an anti-symmetrical tensor F^{ij} involving the components of a force $\mathbf{F}$ and a co-force $\mathbf{K}$, and by following closely the corresponding equations in electromagnetism obtains equations

$$(\mathbf{F}+\mathbf{K}_\wedge\mathbf{v})\,dt=d(m\mathbf{v}), \qquad \mathbf{F}\,.\,d\mathbf{r}=dW.$$

In Section B the dynamics of spin fluids and spin particles are considered. The equations of motion are obtained for a fluid with intrinsic angular momentum, and from these the equations of motion of a particle are deduced. It is shown that in a suitable reference frame the motion of a free particle is a uniform circular motion superposed on a uniform translation.

In Section C the concept of centre of mass of several particles is discussed. In the final Section, D of Chapter IV the author gives an account of relativistic thermodynamics.

Three distinct special problems are reviewed in the concluding chapter. The first section contains an account of Synge's theory of non-viscous fluids and the theory of integral invariants developed by Lichnerowicz. The second section considers again the mechanics of a material particle, the force being supposed derived from a four-potential as in magnetism. The book concludes with an exposition of de Broglie wave mechanics.

The author has taken considerable trouble in preparing the book for publication and in giving several references to original papers. G. L. C.

CONTENTS FOR SECTION B

PAGE
Dr. H. H. Hopkins and Mr. P. M. Barham. The Influence of the Condenser on Microscopic Resolution 737
Dr. H. Kuhn and Mr. B. A. Wilson. Reflectivity of Thin Silver Films and their Use in Interferometry 745
Dr. A. F. Gibson. The Absorption Spectra of Solid Lead Sulphide, Selenide and Telluride 756
Dr. M. S. B. Chaghtai. Note on the Electron Velocity Distribution in Low Voltage Arcs 768
Mr. M. R. Hopkins and Mr. T. C. Toye. The Determination of the Viscosity of Molten Metals 773
Dr. R. Millership and Mr. F. V. Webster. High Frequency Permeability of Ferromagnetic Materials 783
Mr. K. S. W. Chamption. The Production of Pulsed Magnetic Fields using Condenser Energy Storage 795
Dr. G. G. Macfarlane. A Theory of Contact Noise in Semiconductors . . 807
Dr. C. Dodd and Mr. G. N. Roberts. Dielectric Loss and Dielectric Constant Measurements in Supercooled Liquids 814

Letters to the Editor :

Mr. P. D. Lomer. The Dielectric Strength of Aluminium Oxide Films . 818
Mr. G. D. Adam and Dr. K. J. Standley. Ferromagnetic Resonance in Manganese Arsenide 820
Mr. J. T. Kendall. Electrical Conductivity of Gray Tin 821
Mr. G. Francis and Dr. A. von Engel. Development of the Low Pressure Electrodeless Discharge in a High-Frequency Electric Field 823
Reviews of Books 824
Contents for Section A 830
Abstracts for Section A 831

ABSTRACTS FOR SECTION B

The Influence of the Condenser on Microscopic Resolution, by H. H. Hopkins and P. M. Barham.

ABSTRACT. An expression is found for the distribution of light in the image of two small apertures which are illuminated by a condenser of numerical aperture equal to s times that of the imaging objective. The resolving power of the system is written $\rho = K\lambda/(\mathrm{N.A.})$, and K is found as a function of s. It is shown that precisely the same result obtains for both critical and Köhler illumination.

Reflectivity of Thin Silver Films and their Use in Interferometry, by H. Kuhn and B. A. Wilson.

ABSTRACT. A direct photoelectric method allowed the reflectivity R and the transmissivity T of partially reflecting films to be measured to an accuracy of 0·3% of the incident light intensity. For a large number of silver films, deposited on glass by evaporation *in vacuo*, the values of R and T measured for visible light of five different wavelengths, in the range of high reflectivities ($R > 0{\cdot}7$). The change of R as a function of time was also studied. With only moderate control of the conditions of surface cleaning and evaporation, the values of R were nearly always found to lie close to a ' standard ' curve giving R as a function of T, the wavelength and the age of the film. Possible causes of scatter from this standard curve were investigated. T was found not to obey an exponential law as a function of the thickness.

On the basis of these results, resolving power and brightness of etalon fringes were plotted as functions of T. The conclusion is reached that, in most practical cases, the resolving power of etalons for visible light is limited by imperfections of the surfaces rather than by the reflectivity of the silver films, if their thickness is properly chosen.

The Absorption Spectra of Solid Lead Sulphide, Selenide and Telluride, by A. F. Gibson.

ABSTRACT. Recent interest in lead sulphide, selenide and telluride as photoconductors makes information on their absorption spectra valuable. It is found that the absorption spectrum of each material is characterized by strong absorption in the visible and ultra-violet region, with a further band in the infra-red. The effects of temperature and oxidation are also studied.

In PbS the forbidden energy region between the filled and empty bands is found to be about 1·3 ev. in width, not 0·4 ev. as previously suggested. Hence photoconductivity in PbS cannot be associated with the main lattice. The corresponding energy gaps in PbSe and PbTe are found to be about 1·05 ev. and 0·9 ev. respectively.

Note on the Electron Velocity Distribution in Low Voltage Arcs, by M. S. B. Chaghtai.

ABSTRACT. An analysis has been made of a large number of hot cathode low voltage arc-type discharges in mercury vapour and hydrogen at low pressure by the cold probe methods of Langmuir and Mott-Smith. It has been verified that the space potential in the plasma near the filament is positive relative to anode potential, and it has been shown that consistent data for the space potential and concentrations of the slow (ultimate) electrons are obtainable from analyses of probe characteristics in both retarding and accelerating fields for electrons. The way in which the fast (primary) electrons develop a random motion has been traced by progressively confining them within the main discharge, firstly by using a cylindrical gauze anode with open ends, secondly by using a solid anode with open ends and lastly by using a solid anode with end caps.

The Determination of the Viscosity of Molten Metals, by M. R. Hopkins and T. C. Toye.

ABSTRACT. A method is described for the measurement of the viscosity of molten metals at temperatures up to about 900° c. The metal is contained in a cylindrical crucible which is allowed to oscillate about its axis under the control of the torsion in a suspension wire. The theory of the method is considered.

The viscosity of zinc has been determined in the temperature range 430° C. to 480° c. and the results are given.

High Frequency Permeability of Ferromagnetic Materials, by R. MILLERSHIP and F. V. WEBSTER.

ABSTRACT. Methods are described for the measurement of resistive and inductive permeabilities over a range of frequencies from 150 to 10,000 Mc/s. The measurements of the resistive permeabilities were carried out by comparing the attenuation of a coaxial transmission line with the ferromagnetic as the inner conductor with that of a coaxial line having a non-ferromagnetic as inner conductor. The inductive permeabilities were obtained from the wavelength in a coaxial line having the ferromagnetic as the inner conductor. The results show that at all frequencies the resistive permeability is greater than the inductive, and both decrease to unity at very high frequencies. The effective permeability, which is assumed to be complex, is deduced as a function of resistive and inductive permeabilities and plotted against frequency for a variety of materials. The experimental values are compared with theoretical values derived from two formal treatments.

The Production of Pulsed Magnetic Fields using Condenser Energy Storage, by K. S. W. CHAMPION.

ABSTRACT. An economical way of producing a pulsed magnetic field is to use condensers as the energy source and an air-cored magnet coil which, with the storage condensers, forms an oscillatory circuit. By means of a switch the coil is connected to the charged condensers and then disconnected precisely at the end of one cycle. In this way all the stored energy is used to produce the field, while most of it is recovered at the end of the pulse, the only appreciable losses being due to the resistance of the coil and switch.

The design of coils for use in the way described above is considered in detail. Expressions and curves are presented which enable the field produced by a specified coil and condenser combination to be readily calculated. Conversely, the data can be used to design the most satisfactory coil for any practical application. An example is given of the design and construction of an air-cooled coil.

A Theory of Contact Noise Semiconductors, by G. G. MACFARLANE.

ABSTRACT. A theory of contact noise is described in which the low-frequency noise is attributed to the random movement of adsorbed ions on the surface of a semiconductor from which an electron current is being drawn. Emission of electrons is assumed to take place only at localized patches on the surface and the adsorbed ions are assumed to give rise to a Schottky barrier layer, in which the potential maximum is linearly related to the concentration of ions. Diffusion of the ions over the surface gives rise to random fluctuations in the concentration of ions in a patch which results in random fluctuations in the height of the potential barrier and the emission current. It is shown that for a circular patch the spectral power density of the noise current varies with mean current j_0 and frequency f as $j_0^2 f^x$ over a small range of frequency and that x varies monotonically from $-0{\cdot}75$ at the lowest frequencies to $-1{\cdot}125$ at the highest frequencies. It is also shown that for a long thin rectangular patch the index x varies monotonically from $-0{\cdot}5$ to $-1{\cdot}5$ as the frequency is increased from zero. The dependence of the noise power density on temperature is also discussed.

Dielectric Loss and Dielectric Constant Measurements in Supercooled Liquids, by C. DODD and G. N. ROBERTS.

ABSTRACT. In order to provide further evidence in support of the structural change which takes place in a liquid when it is supercooled, measurements of dielectric loss at high frequencies and of dielectric constant have been made on various polar liquids. The evidence from the dielectric loss measurements is inconclusive but for the four liquids tested a significant discontinuity in the dielectric constant–temperature curve has been established at the melting point in each case.